INFORMATION TO USERS

This manuscript has been reproduced from the microfilm master. UMI films the text directly from the original or copy submitted. Thus, some thesis and dissertation copies are in typewriter face, while others may be from any type of computer printer.

The quality of this reproduction is dependent upon the quality of the copy submitted. Broken or indistinct print, colored or poor quality illustrations and photographs, print bleedthrough, substandard margins, and improper alignment can adversely affect reproduction.

In the unlikely event that the author did not send UMI a complete manuscript and there are missing pages, these will be noted. Also, if unauthorized copyright material had to be removed, a note will indicate the deletion.

Oversize materials (e.g., maps, drawings, charts) are reproduced by sectioning the original, beginning at the upper left-hand corner and continuing from left to right in equal sections with small overlaps.

Photographs included in the original manuscript have been reproduced xerographically in this copy. Higher quality 6" x 9" black and white photographic prints are available for any photographs or illustrations appearing in this copy for an additional charge. Contact UMI directly to order.

ProQuest Information and Learning
300 North Zeeb Road, Ann Arbor, MI 48106-1346 USA
800-521-0600

Finite Elements for Electrically Unbounded Piezoelectric Vibrations

by

Elena Antonova

A thesis submitted to the Faculty of Graduate Studies and
Research in partial fulfillment of the requirements
for the degree of Doctor of Philosophy

Department of Electrical and Computer Engineering
McGill University, Montréal
January, 2000

© Antonova Elena, 2000

National Library of Canada
Acquisitions and Bibliographic Services
395 Wellington Street
Ottawa ON K1A 0N4
Canada

Bibliothèque nationale du Canada
Acquisitions et services bibliographiques
395, rue Wellington
Ottawa ON K1A 0N4
Canada

Your file Votre référence

Our file Notre référence

The author has granted a non-exclusive licence allowing the National Library of Canada to reproduce, loan, distribute or sell copies of this thesis in microform, paper or electronic formats.

The author retains ownership of the copyright in this thesis. Neither the thesis nor substantial extracts from it may be printed or otherwise reproduced without the author's permission.

L'auteur a accordé une licence non exclusive permettant à la Bibliothèque nationale du Canada de reproduire, prêter, distribuer ou vendre des copies de cette thèse sous la forme de microfiche/film, de reproduction sur papier ou sur format électronique.

L'auteur conserve la propriété du droit d'auteur qui protège cette thèse. Ni la thèse ni des extraits substantiels de celle-ci ne doivent être imprimés ou autrement reproduits sans son autorisation.

0-612-64498-7

Canada

Abstract

In the modeling of piezoelectric vibrators, one of the universally used assumptions is that the exterior electroquasistatic field due to the electric flux leakage through the piezoelectric-air interface can be neglected. This approximation, valid for materials with large dielectric constants, can introduce a significant error in the simulation of piezoelectric crystals whose permittivity is comparable with that of free space. Because models that take into account the electric flux leakage are virtually non-existent, the objective of this thesis is to develop a solution of the three-dimensional piezoelectric problem which is referred to, by analogy with electromagnetics, as electrically unbounded.

To begin with, the general piezoelectric boundary-value problem with open electric boundaries is stated in the form of differential, variational, and projective equations. The latter formulation serves to construct the finite element solution of the system of piezoelectric equations. Tetrahedral elements of high order, assembled by means of universal matrices, are used to approximate the coupled mechanical and electric fields in the interior region. The exterior infinitely extending electric field is modeled by a single 'superelement', obtained by the ballooning method, and automatically compatible with the interior finite element discretization. After imposing electrical, static or homogeneous, boundary conditions on the matrix equations, the associated deterministic problem is solved for the full piezoelectric static capacitance using the preconditioned conjugate gradient method, while the eigenvalue problems are solved for the two resonant frequencies by a variant of the Lanczos method. Convergence and computer implementation of both methods, as well as of the associated data structures are described in detail.

The effect of the external electric field on static and motional parameters is studied for various types of rectangular piezoelectric vibrators. Illustrative examples involving different geometries, materials, electrode shapes and modes show that the leakage field increases the static capacitance, reduces the effective piezoelectric coupling and the spacing between the two resonant frequencies, and activates many spurious modes.

Résumé

Dans la modelisation des vibrateurs piézoélectriques l'une des suppositions universellement utilisée consiste à négliger le champ électroquasistatic exterieur dû à la fuite du déplacement électrique à travers l'interface piézoélectrique-air. Cette approximation, valide pour les matériaux avec des constantes diélectriques élevées, peut introduire une erreur importante dans la simulation des cristaux piézoélectriques dont les modules diélectriques sont comparables à celui du vide. Vu que les modèles qui tiennent compte de la fuite du déplacement électrique sont pratiquement non-existant, l'objectif de cette thèse consiste à développer une solution du problème piézoélectrique tridimensionnel qui est appelée ici, par analogie avec l'électromagnétique, électriquement illimité.

Pour commencer, le problème piézoélectrique général aux frontières électriques ouvertes est exposé en forme d'équations différentielles, variationnelles, est projectives. Cette dernière formulation sert à construire la solution du système des équations piézoélectriques en terme d'éléments finis. Les tétraèdres d'ordres élevés, assemblés par le moyen des matrices universelles, sont utilisés pour approximer les champs mécaniques et électriques couplés dans le domaine intérieur. Le champ électrique extérieur étendu à l'infini est modelé par un seul 'super-élément', obtenu par la méthode de ballonnement et automatiquement compatible avec la discrétisation en éléments finis du domain intérieur. Après l'imposition des conditions aux limites électriques — statiques ou homogènes — sur les équations matricielles, le problème associé du type défini est résolu pour la capacitance piézoélectrique statique complète en utilisant la méthode des gradients conjugués, tandis que les problèmes aux valeurs propres sont résolus pour les deux fréquences résonnantes par une variante de la méthode de Lanczos.

L'effect du champ électrique extérieur sur les paramètres statiques et dynamiques est étudié pour de divers types de vibrateurs piézoélectrique rectangulaires. Les examples explicatifs, impliquant de différents géométries, matériaux, formes d'électrodes et modes, démontrent que le champ de fuite électrique augmente la capacitance statique, réduit le coefficient du couplage piézoélectrique effectif et l'espacement entre les deux fréquences résonnantes, et active plusieurs modes parasits.

Original contributions to knowledge

(1) The three-dimensional piezoelectric problem is posed for the first time as a problem with open electric boundaries and stated in the form of differential, projective, and variational equations.

(2) A finite element method for solving the unbounded problem has been developed. The infinite exterior electroquasistatic field is modeled by a single 'superelement,' obtained from the three-dimensional ballooning method, and automatically compatible with the discretization of the interior piezoelectric region in tetrahedra of high order. Only a minor part of the superelement matrix is added to the global element assembly, since most of its entries are very small.

(3) It has been established numerically that the effect of the leakage field on piezoelectric vibrations consists in the reduction of the effective coupling coefficient and of the separation between the two resonant frequencies. This is attributed to the considerable increase in the resonator static capacitance and the respective decrease in the antiresonance frequency. The exterior electric field is also responsible for the appearance of many, normally inactive, spurious responses.

Although the above essential contributions constitute the solution of the piezoelectric problem with open electric boundaries, the following by-products of the research significantly improve its quality and are also claimed to be original work:

(a) The popular one-dimensional model of thickness vibrations is extended to include the electric flux leakage across the major surfaces of the piezoelectric plate so that the existing resonance and antiresonance equations can be obtained as special cases of a unique frequency equation.

(b) To avoid numerical integration, universal, or pre-computed, matrices used to assemble the piezoelectric stiffness matrices for high-order tetrahedral elements have been derived for the piezoelectric continuum.

(c) For three-dimensional rectangular piezoelectric vibrators, the superelement matrices are generated more economically by the developed block ballooning algorithm that exploits the symmetry of the region.

(d) The three-dimensional capacitance of a piezoelectric plate is determined from the solution of the full piezoelectric static problem by the preconditioned conjugate gradient method with a special stopping criterion.

(e) The Lanczos algorithm for the generalized eigenvalue problem was modified to avoid the factorization of the semi-definite mass matrix.

Acknowledgments

This research started under the supervision of Dr. P.Silvester whose wisdom, motivating spirit, and artistic style in science will never be forgotten. I shall remain profoundly indebted to him and I hope that this work demonstrates that some of his thirst for knowledge has rubbed off on me.

I am very grateful to Dr. J.P.Webb, who carefully read the thesis and made many valuable comments.

Table of contents

Introduction

In piezoelectric materials, the application of mechanical stress produces an electric polarization proportional to the stress and changing direction with it (direct piezoelectric effect); similarly, an applied electric field deforms the piezoelectric body, i.e. produces strain (converse piezoelectric effect). This phenomenon, experimentally discovered by the brothers Curie in 1880, is observed in some noncentrosymmetric ionic crystals, whose lattices of positive and negative ions are deformed differently under the action of external forces, thus leading to a separation of negative and positive charges. A straightforward application of piezoelectricity consisted in estimating pressure by measuring electric charges accumulated on the surfaces of the crystal. The piezoelectric effect was utilized in this minor way until Langevin proposed to use the mechanical resonance in quartz plates excited by an alternating electric field to generate ultrasound. Although as ultrasound transducers quartz crystals were subsequently abandoned in favor of stronger piezoelectrics, they still remain, due to their unique mechanical and electrical properties, irreplaceable for controlling stable frequency oscillators and in selective frequency filters. Besides being universally used in telecommunication, piezoelectric resonators serve as timing elements in most clocks, watches, microprocessors, and computers. Their characteristics such as a high quality factor, broad range of operating frequencies, time and temperature stability of parameters, small size, and low fabrication cost far exceed that of other types of electromechanical resonators or LC circuits. Piezoelectric materials have also been

widely used in sensors and actuators, in transducers for medical imaging and nondestructive evaluation, in acousto-optic delay lines, and in various surface acoustic wave devices. Most of the experimental and theoretical papers reporting progress in these fields are published in the *IEEE Transactions on Ultrasonics, Ferroelectrics, and Frequency Control* (formerly *IEEE Transactions on Sonics and Ultrasonics*), the Proceedings of the *Ultrasonics Symposium* and the *Annual Symposium on Frequency Control*.

The wide frequency range — from a few kilohertz to a gigahertz — is achieved by a great variety of piezoelectric device designs. In modern engineering, their development is often aided by computer simulation, typically used to predict the mechanical and electrical behavior of the piezoelectric device, to optimize its design, to evaluate new crystalline materials and to study new types of devices. The simulation of a piezoelectric device implies finding an approximate distribution of mechanical and electrical fields in the domain of interest, and recasting it in terms of practically important parameters. The mechanical and electrical fields are governed by the system of piezoelectrically coupled elastic equations of motion and Maxwell's equations of electromagnetism, and satisfy the imposed mechanical and electrical conditions. As any model of a real system, the piezoelectric boundary-value problem is typically based on some simplifying assumptions, made about the piezoelectric continuum (linearity, perfect insulation, absence of acoustical and electrical losses) or boundary conditions (perfectly conductive and infinitesimally thin electrodes, stress-free boundaries). One of the commonest assumptions consists in neglecting the electroquasistatic field distribution outside the piezoelectric crystal. Surely, ignoring the electric flux propagation through the uncovered surfaces of the piezoelectric is justified when the dielectric permittivity of the material ϵ is much greater than that of free space as in the case of piezoelectric ceramics; however, this condition does not hold for many crystals, particularly those used in high precision frequency control. Therefore, the approximation of a zero normal electric flux at the piezoelectric-air (vacuum) interface can introduce a significant error in the models of piezoelectric devices. The aim of this thesis is to develop a solution of the piezoelectric boundary-value problem that takes into account the nonzero electric flux leakage.

The problem of modeling finite regions surrounded by infinitely extending free space are frequently encountered in computational electromagnetics, and are

referred to as *open-boundary* or *unbounded* problems. In fact, the idea to formulate and solve the piezoelectric problem with open electric boundaries arose from a random visual association between the cross-section of a microstrip transmission line on a dielectric substrate and the cross-section of a strip-shaped piezoelectric resonator. A review of the literature (Chapter 2) showed that previous attempts to extend the problem domain beyond the boundary of the piezoelectric body were limited to the simplest one-dimensional models of extensional vibrations of piezoelectric rods; the extension of existing one-dimensional models of thickness vibrations to include the exterior field was developed as a by-product of this review. Although many conventional devices are well approximated by one- or two-dimensional models, with the modern tendency towards miniaturization, the use of composite materials and higher frequencies, most practical configurations require a full three-dimensional treatment. A numerical solution based on the three-dimensional *finite element* approximation of the coupled elastic and electric fields is developed in Chapter 1 and 3. Finite elements are well suited for piezoelectric problems because of their capability to handle anisotropic domains of complex shapes and complicated boundary conditions; moreover, special elements and techniques exist that model infinitely extending exterior regions. Since the algebraic equations resulting from the three-dimensional finite element discretization of the interior and exterior regions are very large, their solution required implementation of special data structures and modifications in existing numerical algorithms (Chapter 4). The effect of the electric field leakage on the static and modal solutions is illustrated on a variety of example problems (Chapter 5), involving different piezoelectric materials, crystal shapes, and electrode configurations.

1

The piezoelectric boundary-value problem

1. Introduction

This chapter was designed to provide the necessary theoretical background for the finite element analysis of the piezoelectric problem with open electric boundaries. Because no particular application has been aimed, the problem is formulated in the most general form of three-dimensional differential and projective piezoelectric equations. The latter is subsequently used to obtain the system of finite element equations, while the variational formulation is presented here as an alternative, and physically more meaningful, way of deriving them. The equivalent impedance and admittance representations, discussed at the end of this chapter for a general piezoelectric vibrator, allow the finite element approximate solutions to be recast in terms of lumped electrical parameters, thus providing a bridge to electric circuit analysis techniques.

A few points should be observed about the notation. In this chapter, all physical quantities are represented by bold face letter symbols, rather that indexed components. Dots and colons denote ordinary and double scalar products (i.e. summation over one and two subscripts respectively); the Hamilton (∇) notation is used to symbolically represent differential operations. Customary in modern electromagnetics, the described formalism is rarely employed in elasticity, where the trend is towards tensor subscript notation. One of the reasons for this is that symbolic notation fails to discriminate between vectors and tensors of higher rank, i.e. the rank of a variable can be established from its physical identity only. Nevertheless, this inconvenience was found to be outweighed by the compactness and clarity resulting from the reduced amount of detail in symbolic notation. This is particularly important given the concurrent system of variable subscripts arising

from the finite element discretization. Additionally, this formalism makes the analogy between electromagnetic and elastic quantities more explicit. Therefore, following Auld (1990a) who promoted its use in piezoelectric theory, all quantities and equations are written out and manipulated in symbolic notation. The subscript notation — full and abbreviated — appears in later chapters as more detailed calculations become necessary.

2. Governing equations of piezoelectromagnetism

The state of a piezoelectric body is characterized by the interaction of acoustical and electromagnetic fields governed by the elastic equation of motion (or equilibrium) and Maxwell's equations respectively. Mechanical and electromagnetic variables are coupled through the piezoelectric constitutive equations. Together with the field equations they form the governing equations of piezoelectromagnetism. This system is accompanied by the interface rules, used subsequently to derive boundary conditions required for the solution of the piezoelectric boundary-value problem.

2.1 *Field equations*

Acoustic and electromagnetic fields in an insulator can be described by the following basic state parameters:

mechanical displacement	$\mathbf{u}$	meter,
mechanical stress	$\mathbf{T}$	newton/meter^2,
mechanical strain	$\mathbf{S}$	unity,
electric field intensity	$\mathbf{E}$	volt/meter,
electric flux density	$\mathbf{D}$	coulomb/meter^2,
magnetic field intensity	$\mathbf{H}$	ampere/meter,
magnetic flux density	$\mathbf{B}$	weber/meter^2.

All parameters are functions of time t and Cartesian position vector $\mathbf{r}$. As is well known from the mathematical theory of elasticity (Love, 1926), the mechanical variables are related by the *stress equation of small motion*[1]

$$\nabla \cdot \mathbf{T} + \mathbf{F} = \rho \frac{\partial^2 \mathbf{u}}{\partial t^2}, \tag{2.1}$$

where ρ is the mass density, and $\mathbf{F}$ is the body force per unit volume; and the *compatibility equation for strain*

$$\nabla \times \mathbf{S} \times \nabla = 0. \tag{2.2}$$

---

[1] For a general displacement $\mathbf{u}$, the total time derivative $d^2\mathbf{u}/dt^2$ should be used in the inertia force term in (2.1). However, for infinitesimal deformations, a particle remains close to the mean position and one can approximate the total time derivative by $\partial^2\mathbf{u}/\partial t^2$.

Note that in Eq. (2.2), symbol $\mathbf{S} \times \nabla$ denotes the conjugate curl of the diadic **S**, i.e. $\epsilon_{ikj}\,\partial S_{kl}/\partial x_j$, where ϵ_{ikj} is the alternating tensor (Chou and Pagano, 1967). Electric and magnetic quantities adhere to the system of *Maxwell's equations*, written here for nonconducting media (i.e. **J** — the electric current density — is set to zero),

$$\nabla \times \mathbf{E} = -\frac{\partial \mathbf{B}}{\partial t}, \tag{2.3}$$

$$\nabla \cdot \mathbf{B} = 0, \tag{2.4}$$

$$\nabla \times \mathbf{H} = \frac{\partial \mathbf{D}}{\partial t}, \tag{2.5}$$

$$\nabla \cdot \mathbf{D} = \rho_e, \tag{2.6}$$

where ρ_e is the electric charge density.

Equation (2.1) is the differential form of the balance of linear momentum equation. The stress tensor **T** should also obey the *conservation law of the angular momentum* (Tiersten, 1969); in its differential form this requirement results in the symmetry condition for the stress tensor **T**:

$$\langle \mathbf{T} \rangle = 0, \tag{2.7}$$

where $\langle \mathbf{T} \rangle$ denotes the rotation vector of **T** (Nadeau, 1964). The symmetry of the strain tensor **S** follows from its definition as the symmetric part of the dyadic $\nabla\mathbf{u}$:

$$\mathbf{S} = \frac{1}{2}(\nabla\mathbf{u} + \mathbf{u}\nabla) \tag{2.8}$$

with $\mathbf{u}\nabla$ $(\partial u_j/\partial x_i)$ denoting the transpose of $\nabla\mathbf{u}$ $(\partial u_i/\partial x_j)$, i.e. the conjugate gradient of **u**. The strain **S** in (2.8) satisfies identically the compatibility equation (2.2), and can be seen as its general solution; in turn, Eq. (2.2) can be interpreted as the integrability condition for (2.8). Similarly, the electric field can be derived from the magnetic vector potential **A** and the electric scalar potential φ:

$$\mathbf{E} = -\frac{\partial \mathbf{A}}{\partial t} - \nabla\varphi, \tag{2.9}$$

so that (2.9) identically satisfies the first pair of Maxwell's equations[2]. It should be noted that neither the mechanical displacement **u** nor potentials **A** and φ are unique, i.e. any constant can be added to them without effect on **S** and **E**.

2.2 *Constitutive relations*

The constitutive relations describe the macroscopic properties of the piezoelectric medium, and represent an additional set of relationships between acoustic and electromagnetic field variables. These relations follow from the first law of thermodynamics

$$dU = \delta Q + \delta W, \tag{2.10}$$

that postulates the existence of the *internal energy density* function $U(\theta, \mathbf{S}, \mathbf{D}, \mathbf{B})$, with θ denoting the absolute temperature. The variation dU is given by the sum of the heat δQ transmitted to unit volume and the elementary work δW done by applied mechanical, electrical, and magnetic forces:

$$\delta W = \mathbf{T} : d\mathbf{S} + \mathbf{E} \cdot d\mathbf{D} + \mathbf{H} \cdot d\mathbf{B}. \tag{2.11}$$

For an adiabatic system ($\delta Q = 0$)

$$dU = \frac{\partial U}{\partial \mathbf{S}} : d\mathbf{S} + \frac{\partial U}{\partial \mathbf{D}} \cdot d\mathbf{D} + \frac{\partial U}{\partial \mathbf{B}} \cdot d\mathbf{B} \tag{2.12}$$

can be equated with δW, thus producing the first group of constitutive relations:

$$\mathbf{T} = \left(\frac{\partial U}{\partial \mathbf{S}}\right)_{\mathbf{D},\mathbf{B}}, \qquad \mathbf{E} = \left(\frac{\partial U}{\partial \mathbf{D}}\right)_{\mathbf{S},\mathbf{B}}, \qquad \mathbf{H} = \left(\frac{\partial U}{\partial \mathbf{B}}\right)_{\mathbf{S},\mathbf{D}}. \tag{2.13}$$

To use other sets of variables (different from **S**, **D**, **B**) as the independent ones, new thermodynamic functions have to be defined[3]:

$$G = U - \mathbf{S} : \mathbf{T} - \mathbf{E} \cdot \mathbf{D}, \tag{2.14}$$

---

[2] Traditionally, the system of mechanical equations is made up from Eqs. (2.1), (2.7) and (2.8). Here, the compatibility condition for **S** (2.2), not its definition (2.8), was used as a basic equation. This has been done for the sake of analogy with electromagnetic theory, where it is more customary to consider **E** in (2.9) as a general solution of Maxwell's equations rather than viewing (2.9) as the definition of **E**, and deducing (2.3) and (2.4) from it (e.g. Landau and Lifshitz, 1968).

[3] Because only *nonmagnetic* materials (i.e. $\mathbf{B} = \mu_0 \mathbf{H}$) will be considered further, the product $\mathbf{H} \cdot \mathbf{B}$ is not included in the thermodynamic functions.

$$G_1 = U - \mathbf{S} : \mathbf{T}, \tag{2.15}$$

$$G_2 = U - \mathbf{E} \cdot \mathbf{D}, \tag{2.16}$$

that under isothermal conditions ($d\theta = 0$) have the meaning of the *Gibbs free*, *elastic* and *electric energy* functions respectively. These functions give rise to three other sets of constitutive equations:

$$\mathbf{S} = -\left(\frac{\partial G}{\partial \mathbf{T}}\right)_{\mathbf{E}}, \qquad \mathbf{D} = -\left(\frac{\partial G}{\partial \mathbf{E}}\right)_{\mathbf{T}}, \tag{2.17}$$

$$\mathbf{S} = -\left(\frac{\partial G_1}{\partial \mathbf{T}}\right)_{\mathbf{D}}, \qquad \mathbf{E} = \left(\frac{\partial G_1}{\partial \mathbf{D}}\right)_{\mathbf{T}}, \tag{2.18}$$

$$\mathbf{T} = \left(\frac{\partial G_2}{\partial \mathbf{S}}\right)_{\mathbf{E}}, \qquad \mathbf{D} = -\left(\frac{\partial G_2}{\partial \mathbf{E}}\right)_{\mathbf{S}}, \tag{2.19}$$

that use (**T**, **E**), (**T**, **D**), and (**S**, **E**) as independent variables.

Which system is preferable depends on the particular boundary-value problem to be solved. Because the piezoelectric boundary conditions are more often given in terms of displacement **u** and potential φ, relations (2.8) and (2.9) privilege the set of variables (**S**, **E**). Assuming that one deal with a *linear* piezoelectric medium, the appropriate thermodynamic function — the Gibbs electric energy — is constructed as a homogeneous quadratic form

$$G_2 = \frac{1}{2}\mathbf{S} : \mathbf{c}^E : \mathbf{S} - \mathbf{E} \cdot \mathbf{e} : \mathbf{S} - \frac{1}{2}\mathbf{E} \cdot \boldsymbol{\epsilon}^S \cdot \mathbf{E}, \tag{2.20}$$

transforming the constitutive relations (2.19) into

$$\mathbf{T} = \mathbf{c}^E : \mathbf{S} - \mathbf{E} \cdot \mathbf{e}, \tag{2.21}$$

$$\mathbf{D} = \mathbf{e} : \mathbf{S} + \mathbf{E} \cdot \boldsymbol{\epsilon}^S. \tag{2.22}$$

For nonmagnetic materials Eqs. (2.21) and (2.22) should be supplemented by

$$\mathbf{B} = \mu_0 \mathbf{H}, \tag{2.23}$$

where μ_0 is the permeability of free space. The introduced coefficients are the

elastic stiffness tensor at constant electric field $\mathbf{c}^E = (c_{ijkl})$ newton/meter^2,
piezoelectric stress tensor $\mathbf{e} = (e_{ijk})$ coulomb/meter^2,
permittivity tensor at constant strain $\boldsymbol{\epsilon}^S = (\epsilon_{ij})$ farad/meter,

where subscripts i, j, k, l in the index notation of material tensors run from 1 to 3. Their symmetry properties

$$\left.\begin{aligned} &c_{ijkl} = c_{ijlk} = c_{jikl} = c_{klij}, \\ &e_{ijk} = e_{ikj}, \\ &\epsilon_{ij} = \epsilon_{ji} \end{aligned}\right\} \tag{2.24}$$

follow from the symmetry of tensors **T** and **S**, as well as from the independence of G_2's second derivatives with respect to **S** or **E** of the order of differentiation.

2.3 *Interface conditions*

The interface conditions for field variables are derived by integrating differential equations (2.1)–(2.6) over the surface (divergence equations) or loop (curl equations), enclosing an area or a boundary belonging to the discontinuity surface. Consequently, there are two mechanical and four electromagnetic conditions that must hold at the interface between two distinct materials. If by **n** one denotes the unit normal vector directed from medium 2 into medium 1, the boundary rules can be written as follows:

normal stress **T** (the traction force) is continuous,

$$\mathbf{n} \cdot (\mathbf{T}_1 - \mathbf{T}_2) = 0; \tag{2.25}$$

tangential strain **S** is continuous,

$$\mathbf{n} \times (\mathbf{S}_1 - \mathbf{S}_2) \times \mathbf{n} = 0; \tag{2.26}$$

normal electric flux **D** is discontinuous by the surface charge density σ,

$$\mathbf{n} \cdot (\mathbf{D}_1 - \mathbf{D}_2) = \sigma; \tag{2.27}$$

tangential electric field **E** is continuous,

$$\mathbf{n} \times (\mathbf{E}_1 - \mathbf{E}_2) = 0; \tag{2.28}$$

normal magnetic flux **B** is continuous,

$$\mathbf{n} \cdot (\mathbf{B}_1 - \mathbf{B}_2) = 0; \tag{2.29}$$

tangential magnetic field $\mathbf{H}$ is continuous at the interface between two nonconducting media,

$$\mathbf{n} \times (\mathbf{H}_1 - \mathbf{H}_2) = 0. \tag{2.30}$$

Taking into account expressions (2.8), (2.9) and the relation

$$\mathbf{B} = \nabla \times \mathbf{A}, \tag{2.31}$$

a similar integration of Eqs. (2.2) and (2.3) leads to the condition of continuity across the material interface of the displacement $\mathbf{u}$, scalar potential ϕ and tangential vector potential $\mathbf{A}$:

$$\mathbf{u}_1 = \mathbf{u}_2, \tag{2.32}$$

$$\phi_1 = \phi_2, \tag{2.33}$$

$$\mathbf{n} \times (\mathbf{A}_1 - \mathbf{A}_2) = 0. \tag{2.34}$$

These interface conditions for field variables and potentials will be used to derive conditions at the extremities of the piezoelectric boundary-value problem after choosing the boundary shape.

3. Wave equations

As shown in the previous section, the interaction between acoustic and electromagnetic fields in a piezoelectric body can be described by a system of six equations, i.e. Eqs. (2.1)–(2.6), in two mechanical variables **S** and **T**, and four electric variables **E**, **D**, **H**, **B**, all coupled by linear constitutive relations (2.21)–(2.23). For practical reasons it is desirable to reduce the number of equations and variables involved in the solution. One way of simplifying the boundary-value problem is to eliminate unnecessary variables by substituting constitutive relations in the system of field equations, and, therefore, to formulate the problem in terms of *wave equations*.

3.1 *Coupled field waves equations*

The Maxwell curl equations (2.3) and (2.5) can be combined into a single differential equation of second order in **E** and **D** by eliminating magnetic vector variables **B** and **H**:

$$\nabla \times \nabla \times \mathbf{E} = -\mu_0 \frac{\partial^2 \mathbf{D}}{\partial t^2}. \tag{3.1}$$

The substitution of linear constitutive relations (2.21)–(2.23) into the stress equation of motion (2.1) with no body forces ($\mathbf{F} = 0$) and into Eq. (3.1) yields the system of nonhomogeneous *piezoelectric wave equations* (Auld, 1990a) involving only two vector fields **u** and **E**:

$$\nabla \cdot (\mathbf{c}^E : \nabla \mathbf{u}) - \rho \frac{\partial^2 \mathbf{u}}{\partial t^2} = \nabla \cdot (\mathbf{E} \cdot \mathbf{e})^4, \tag{3.2}$$

$$\nabla \times \nabla \times \mathbf{E} + \mu_0 \boldsymbol{\epsilon}^S \cdot \frac{\partial^2 \mathbf{E}}{\partial t^2} = -\mu_0 \mathbf{e} : \nabla \frac{\partial^2 \mathbf{u}}{\partial t^2}. \tag{3.3}$$

For nonpiezoelectric materials ($\mathbf{e} = 0$) the system falls into two independent wave equations for **u** and **E** alone, governing the propagation of purely elastic and purely electromagnetic waves in an anisotropic crystal; otherwise, the two wave equations are coupled by the piezoelectric 'source' terms $\nabla \cdot (\mathbf{E} \cdot \mathbf{e})$ and

---

[4] The symmetry of the stiffness tensor **c** permits the double scalar dyadic product $\mathbf{c}^E : \mathbf{S} = \mathbf{c}^E : (\nabla \mathbf{u} + \mathbf{u}\nabla)/2$ to be simply recast as $\mathbf{c}^E : \nabla \mathbf{u}$.

$-\mu_0 \mathbf{e} : \nabla(\partial^2 \mathbf{u}/\partial t^2)$, and their solutions can be regarded as hybrid acousto-electromagnetic waves, having both the acoustic and electromagnetic field components. More specifically, the solutions of (3.2) and (3.3) are the acoustic waves propagating at speed V and accompanied by electromagnetic field — the 'slow' acousto-electromagnetic waves, as well as an electromagnetic wave propagating at speed $v \simeq 10^5$V and accompanied by mechanical deformation — the 'fast' acousto-electromagnetic wave (Baranskii, 1991; Dieulesaint and Royer, 1974). Because piezoelectric devices are conceived on the basis of either elastic wave propagation or resonance, attention will be subsequently focused only upon acoustic solutions of the piezoelectric wave equations which are considered in more detail in Section 3.3 of this chapter.

3.2 *Potential wave equations*

An alternative approach to simplifying the obtained wave equations is to formulate the problem in terms of potentials rather than fields themselves. Substituting (2.23) and (2.31) into the Maxwell's curl equation (2.5) for **H** gives a wave equation in **A**

$$\nabla \times \nabla \times \mathbf{A} = \mu_0 \frac{\partial \mathbf{D}}{\partial t}, \tag{3.4}$$

similar to (3.1). The piezoelectric term in the constitutive relation for **D** (2.22) couples (3.4), which can be rewritten in this case as

$$\nabla \times \nabla \times \mathbf{A} = \mu_0 \mathbf{e} : \nabla \frac{\partial \mathbf{u}}{\partial t} + \mu_0 \boldsymbol{\epsilon}^S \cdot \frac{\partial \mathbf{E}}{\partial t}, \tag{3.4a}$$

to the acoustic wave equation (3.2). The electric field **E** may be eliminated from both the acoustic (3.2) and electromagnetic (3.4a) wave equations, by substituting its value as derived from the potentials (2.9). The resulting system of nonhomogeneous potential wave equations in **u**, φ, and **A**

$$\nabla \cdot (\mathbf{c}^E : \nabla \mathbf{u}) - \rho \frac{\partial^2 \mathbf{u}}{\partial t^2} = -\nabla \cdot (\nabla \varphi \cdot \mathbf{e}) - \nabla \cdot \left(\frac{\partial \mathbf{A}}{\partial t} \cdot \mathbf{e} \right) \tag{3.5}$$

$$\nabla \times \nabla \times \mathbf{A} + \mu_0 \boldsymbol{\epsilon}^S \cdot \frac{\partial^2 \mathbf{A}}{\partial t^2} = -\mu_0 \boldsymbol{\epsilon}^S \cdot \nabla \frac{\partial \varphi}{\partial t} + \mu_0 \mathbf{e} : \nabla \frac{\partial \mathbf{u}}{\partial t} \tag{3.6}$$

can be used as an alternative to (3.2) and (3.3), especially when the boundary conditions are given in potentials rather than fields.

To fully define the vector potential **A** in a finite region of space, both its curl and divergence need to be specified. Equation (2.31) fixes only the curl of **A**, while the divergence of **A** is typically given by some *gauge condition* (Silvester and Ferrari, 1996). It is appropriate in the present case to use the gauge (Auld, 1990a)

$$\nabla \cdot \left(\boldsymbol{\epsilon}^S \cdot \frac{\partial \mathbf{A}}{\partial t} \right) = 0; \tag{3.7}$$

substituted into (2.6) with no body charge ($\rho_e = 0$), it produces an equation in **u** and φ :

$$\nabla \cdot \left(\mathbf{e} : \nabla \mathbf{u} - \boldsymbol{\epsilon}^S \cdot \nabla \varphi \right) = 0, \tag{3.8}$$

thus decoupling potentials **A** and φ. Variables **u**, **A**, and φ are now uniquely determined from the system formed by the pair of coupled wave equations (3.5)–(3.6), and the supplementary equation (3.8). The latter can be used to eliminate the potential φ from the system by expressing it in terms of mechanical displacement **u**. Substituted into Eqs. (3.5) and (3.6), it produces an acoustic wave equation for **u** with a source term in **A** alone and an electromagnetic wave equation for **A** with a source term in **u** alone. Borrowing the terminology from electromagnetics, the vector potential **A** produced by the gauge (3.7) may be referred to as the *modified* vector potential (Webb, 1995).

With this choice of gauge (3.7), the interface conditions (2.34) applicable to **A** must be supplemented by the requirement of the continuity of the normal components of $\left(\boldsymbol{\epsilon}^S \cdot \mathbf{A} \right)$ across the boundary:

$$\mathbf{n} \cdot \left(\boldsymbol{\epsilon}_1^S \cdot \mathbf{A}_1 - \boldsymbol{\epsilon}_2^S \cdot \mathbf{A}_2 \right) = 0. \tag{3.9}$$

This implies that at the interface between two regions with different permittivities $\left(\boldsymbol{\epsilon}_1^S \neq \boldsymbol{\epsilon}_2^S \right)$ the normal component of **A** is discontinuous. The tangential components of **A**, as well as the scalar potential φ, remain continuous under any choice of gauge.

3.3 *Coupled-wave behavior*

The representation of electric field $\mathbf{E}$ in terms of vector $\mathbf{A}$ and scalar φ potentials has yet another advantage: it allows separating $\mathbf{E}$ into rotational $\nabla \times \mathbf{E}^{(r)} \neq 0$ and irrotational $\nabla \times \mathbf{E}^{(i)} = 0$ parts

$$\mathbf{E} = \mathbf{E}^{(r)} + \mathbf{E}^{(i)}. \tag{3.10}$$

Now, the contribution of these two different types of electric fields that accompany the propagation of an acoustic wave in a piezoelectric medium — the rotational field $\mathbf{E}^{(r)} = -\partial\mathbf{A}/\partial t$, which is the characteristic of electromagnetic waves, and the irrotational, or potential, field $\mathbf{E}^{(i)} = -\nabla\varphi$, which is associated with the static bound electric charge distribution — can be considered individually.

According to the constitutive relation (2.22), the mechanical strain $\mathbf{S}$ (2.8) associated with a $\mathbf{u}$-polarized acoustic wave (Fig. 1.1) contributes through the piezoelectric part $\mathbf{D}^P = \mathbf{e} : \nabla\mathbf{u}$ of the total electric flux density

$$\mathbf{D} = \mathbf{D}^P + \mathbf{D}^{E^{(r)}} + \mathbf{D}^{E^{(i)}}, \tag{3.11}$$

where the last two terms constitute the electric contribution $\mathbf{E} \cdot \boldsymbol{\epsilon}^S$ to $\mathbf{D}$ from rotational and irrotational electric fields respectively. From the system of wave equations (3.6), (3.8) one can see that vector $\mathbf{D}^P$ is responsible for generating an electromagnetic wave, characterized by the vector potential $\mathbf{A}$, through the source term $\mu_0\left(\partial\mathbf{D}^P/\partial t\right) = \mu_0\mathbf{e} : \nabla(\partial\mathbf{u}/\partial t)$ in (3.6):

$$\nabla \times \nabla \times \mathbf{A} + \mu_0\boldsymbol{\epsilon}^S \cdot \frac{\partial^2\mathbf{A}}{\partial t^2} = \mu_0\frac{\partial\mathbf{D}^{E^{(i)}}}{\partial t} + \mu_0\frac{\partial\mathbf{D}^P}{\partial t}, \tag{3.12}$$

as well as a scalar potential wave, characterized by φ, through the 'charge' $\nabla \cdot \mathbf{D}^P = \nabla \cdot (\mathbf{e} : \nabla\mathbf{u})$ in (3.8):

$$\nabla \cdot \left(\boldsymbol{\epsilon}^S \cdot \nabla\varphi\right) = -\nabla \cdot \mathbf{D}^P. \tag{3.13}$$

The latter, piezoelectrically induced scalar field, can also contribute to the generation of an electromagnetic wave through the source term $\mu_0\left(\partial\mathbf{D}^{E^{(i)}}/\partial t\right) = -\mu_0\boldsymbol{\epsilon}^S \cdot \nabla(\partial\varphi/\partial t)$ in (3.6). In turn, the rotational and irrotational electric fields may alter the mechanical displacement $\mathbf{u}$ by means of 'body forces' $\nabla \cdot \mathbf{T}^{(i)} = -\nabla \cdot (\nabla\varphi \cdot \mathbf{e})$ and $\nabla \cdot \mathbf{T}^{(r)} = -\nabla \cdot ((\partial\mathbf{A}/\partial t) \cdot \mathbf{e})$ in (3.5):

$$\nabla \cdot (\mathbf{c}^E : \nabla \mathbf{u}) - \rho \frac{\partial^2 \mathbf{u}}{\partial t^2} = \nabla \cdot \mathbf{T}^{(i)} + \nabla \cdot \mathbf{T}^{(r)}, \tag{3.14}$$

thus coupling the acoustic wave with the static electric and electromagnetic fields.

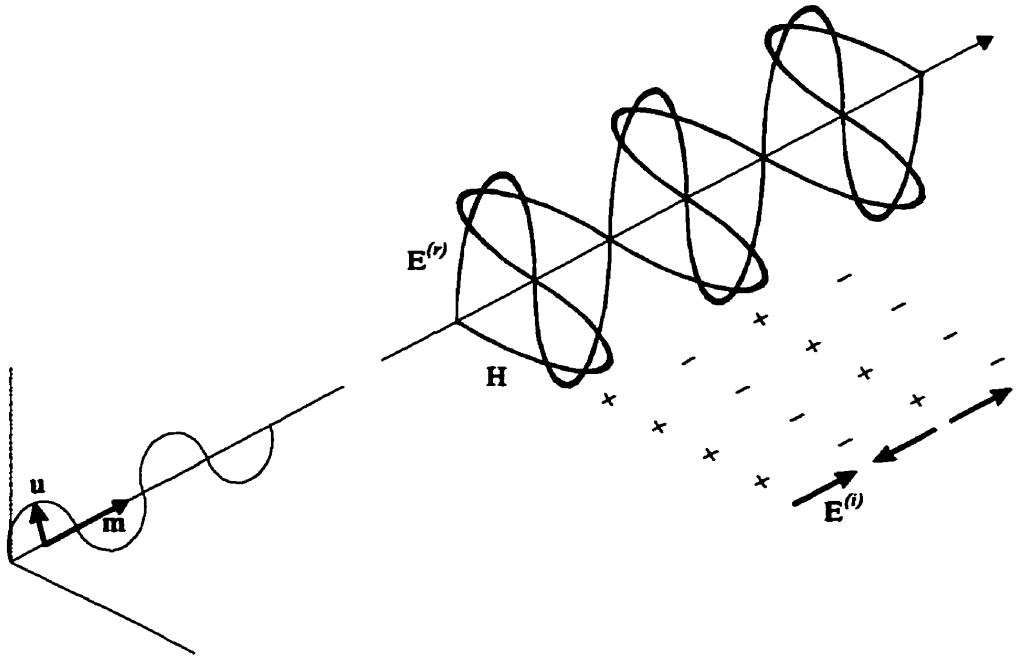

Fig 1.1 Electromagnetic wave and bound electric charge distribution associated with a **u**-polarized acoustic wave propagating in the direction given by the unit vector **m**.

Finally, when $\mathbf{D}^P$ reduces to zero, the displacement field **u** is not coupled to any type of electric field, and the piezoelectric hybrid wave degenerates into a purely acoustic one.

3.4 *Quasi-static approximation*

A very important case of the solution of coupled wave equations in the form of uniform plane waves has been considered in Appendix 1. These results are used here to introduce the quasi-static approximation in the piezoelectric boundary-value problem formulation. The analysis of mechanical characteristics of uniform plane waves demonstrated that the piezoelectric coupling between acoustic and electromagnetic waves is negligible in comparison with the effect of

piezoelectric stiffening, i.e. the coupling between the acoustic wave and the irrotational electric field. Equations (1.10) and (1.12) of Appendix 1 can be used to show a similar result for electric characteristics of coupled waves:

$$\frac{\|\mathbf{E}^{(r)}\|}{\|\mathbf{E}^{(i)}\|} = \left(\frac{\mathrm{V}}{v}\right)^2, \tag{3.15}$$

which proves that the rotational electric field in the quasi-acoustic wave is much weaker than the potential field in the stiffened wave:

$$\left\|\frac{\partial \mathbf{A}}{\partial t}\right\| \ll \|\nabla\varphi\| \tag{3.16}$$

Consequently, the varying magnetic flux **B**, created by the rotational electric field (2.3) propagating with acoustic velocity V, is negligible, and can be dropped, along with the magnetic field **H**, from the system of Maxwell's equations. Therefore, under assumption (3.16), the electric field is considered as being entirely irrotational $\mathbf{E} = \mathbf{E}^{(i)}$, in the sense that it can be derived from the scalar potential φ alone, as in electrostatics, and treated as satisfying the static field equations exactly. This field is not purely static but *electroquasistatic* because of the coupling with the time-varying acoustic wave. Thus, under the quasi-static approximation, the quasi-acoustic wave is regarded as nonpiezoelectric, or purely acoustic, while the stiffened acoustic wave (1.13) of Appendix 1 satisfies the quasi-static approximation exactly.

Although derived for uniform plane waves, assumption (3.16) can clearly be applied to most piezoelectric boundary-value problems. In problems dealing with wave propagation, the quasi-static approximation is justified by invoking the fact that acoustic and electromagnetic velocities differ by approximately five orders of magnitude. When piezoelectric resonance is considered, the same argument is typically given in terms of wavelength: the quasi-static approximation is valid because the elastic wavelength Λ, defined by the characteristic dimension of the bounded region, is much smaller than the electromagnetic wavelength $\lambda \approx 10^5\Lambda$ of the same frequency (Tiersten, 1969). In either case, the quasi-static approximation simplifies the formulation of the problem by allowing the magnetic vector potential **A** to be dropped from the system of wave equations.

4. Differential formulation

In the previous two sections, the basic equations of piezoelectromagnetism were introduced both in the form of field equations coupled by piezoelectric constitutive relations, and piezoelectric wave equations. It was also demonstrated that the quasi-static approximation, which considerably simplifies the problem by eliminating magnetic variables, is valid for the acousto-electromagnetic interaction in piezoelectric media. To complete the formulation of the piezoelectric boundary-values problem, it remains now to define the boundary shape and boundary conditions for field variables. The static and time-harmonic problems will be developed as specializations of the general problem given below.

4.1 *Finite piezoelectric body with open electric boundaries*

Consider a piezoelectric body of volume V, bounded by surface S, and surrounded by vacuum (or air) occupying the space $\tilde{V}$, as shown in Fig. 1.2. Let $\mathbf{n}$ be the unit normal vector pointing outward. In the absence of volume forces ($\mathbf{F} = 0$) and volume charges ($\rho_e = 0$), Eqs. (2.1) and (2.6) governing field variables $\mathbf{T}$ and $\mathbf{D}$ inside the volume V can be written as follows:

$$\nabla \cdot \mathbf{T} = \rho \frac{\partial^2 \mathbf{u}}{\partial t^2} \quad \text{in } V, \tag{4.1}$$

$$\nabla \cdot \mathbf{D} = 0 \quad \text{in } V. \tag{4.2}$$

The mechanical strain $\mathbf{S}$, as given by (2.8), and the quasi-static electric field $\mathbf{E}$ are directly expressed as spatial variations of the mechanical displacement $\mathbf{u}$ and scalar electric potential φ respectively:

$$\mathbf{S} = \frac{1}{2}(\nabla \mathbf{u} + \mathbf{u}\nabla) \quad \text{in } V, \tag{2.8}$$

$$\mathbf{E} = -\nabla \varphi \quad \text{in } V + \tilde{V}. \tag{4.3}$$

Constitutive equations (2.19) relates all four field variables by means of the Gibbs electric energy potential G_2:

$$\mathbf{T} = \left(\frac{\partial G_2}{\partial \mathbf{S}}\right)_{\mathbf{E}}, \quad \mathbf{D} = -\left(\frac{\partial G_2}{\partial \mathbf{E}}\right)_{\mathbf{S}} \quad \text{in } V.$$

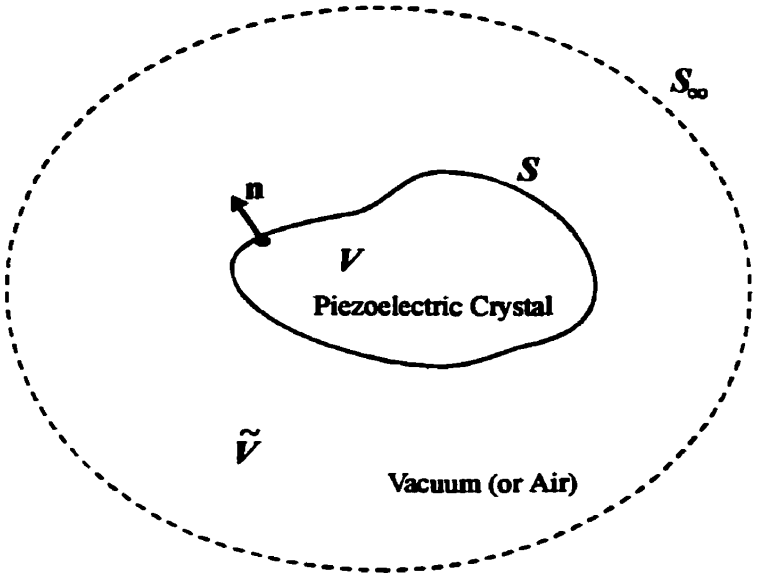

Fig 1.2 Piezoelectric body in unbounded free space.

Outside V — in $\tilde{V}$ — it is assumed that all mechanical variables vanish identically. The electric vectors **D** and **E** are governed by Eqs. (4.2) and (4.3) which are coupled through the constitutive equation

$$\mathbf{D} = \epsilon_0 \mathbf{E} \text{ in } \tilde{V}, \tag{4.4}$$

where ϵ_0 is the permittivity of the free space. Combining Eqs. (4.2) and (4.3), one obtains Laplace's equation for the electric potential in the outer space $\tilde{V}$:

$$\nabla^2 \varphi = 0 \text{ in } \tilde{V}. \tag{4.5}$$

To construct the boundary-value problem, mechanical and electric boundary conditions must be specified at every point of surface S. However, for electrical variables, the boundary S is, rather, an interface between the piezoelectric medium and the vacuum; an artificial boundary S_∞ (Fig. 1.2), that models the electrical extremities of the problem domain, must also be considered. Both the mechanical and electrical boundary conditions are derived from the interface conditions (2.25)–(2.28). They can be stated either in terms of prescribed surface tractions $\bar{\mathbf{t}}$ and charges $\bar{\sigma}$ — the *Neumann* boundary conditions:

$$\mathbf{n} \cdot \mathbf{T} = \bar{\mathbf{t}} \text{ on } S_{\mathbf{t}}, \tag{4.6}$$

$$\mathbf{n} \cdot [\mathbf{D}] = \overline{\sigma} \text{ on } S_{\overline{\sigma}}, \tag{4.7}$$

where $[\mathbf{D}]$ stands for the jump in the electric flux density vector $\left(\mathbf{D}^{\tilde{V}} - \mathbf{D}^{V}\right)$ across S, or in terms of prescribed surface displacements $\mathbf{u}$ or electric potentials φ — the *Dirichlet* boundary conditions:

$$\mathbf{u} = \overline{\mathbf{u}} \text{ on } S_{\overline{\mathbf{u}}}, \tag{4.8}$$

$$\varphi = \overline{\varphi} \text{ on } S_{\overline{\varphi}}, \tag{4.9}$$

where parts $S_{\overline{\mathbf{t}}}$ and $S_{\overline{\mathbf{u}}}$, $S_{\overline{\sigma}}$ and $S_{\overline{\varphi}}$ constitute the surface S: $S_{\overline{\mathbf{t}}} \cup S_{\overline{\mathbf{u}}} = S$ and $S_{\overline{\sigma}} \cup S_{\overline{\varphi}} = S$, but do not overlap: $S_{\overline{\mathbf{t}}} \cap S_{\overline{\mathbf{u}}} = \emptyset$ and $S_{\overline{\sigma}} \cap S_{\overline{\varphi}} = \emptyset$.

For linear piezoelectric materials equations (4.1) and (4.2) can be written more economically in the form of wave equations:

$$\nabla \cdot \left(\mathbf{c}^{E} : \nabla \mathbf{u}\right) + \nabla \cdot (\nabla \varphi \cdot \mathbf{e}) = \rho \frac{\partial^2 \mathbf{u}}{\partial t^2} \text{ in } V, \tag{4.10}$$

$$\nabla \cdot (\mathbf{e} : \nabla \mathbf{u}) - \nabla \cdot \left(\nabla \varphi \cdot \boldsymbol{\epsilon}^{S}\right) = 0 \text{ in } V. \tag{4.11}$$

Similarly, the Neumann boundary conditions (4.6)–(4.7) may be expressed directly in mechanical displacement $\mathbf{u}$ and electric potential φ:

$$\mathbf{n} \cdot \left(\mathbf{c}^{E} : \nabla \mathbf{u} + \nabla \varphi \cdot \mathbf{e}\right) = \overline{\mathbf{t}} \text{ on } S_{\overline{\mathbf{t}}}, \tag{4.12}$$

$$\mathbf{n} \cdot \left[\mathbf{e} : \nabla \mathbf{u} - \nabla \varphi \cdot \left(\boldsymbol{\epsilon}^{S} - \epsilon_0 \mathbf{I}\right)\right] = -\overline{\sigma} \text{ on } S_{\overline{\sigma}}. \tag{4.13}$$

The set of boundary conditions will be complete if one assumes that $\mathbf{E}$ and φ vanish at large distances from S, i.e. on S_{∞}:

$$\lim_{r \to \infty} \mathbf{E} = 0, \tag{4.14}$$

$$\lim_{r \to \infty} \varphi = 0. \tag{4.15}$$

The solution of the stated piezoelectric problem with *open electric boundaries*[5] consists in finding the distribution of the mechanical displacement $\mathbf{u}(\mathbf{r},t)$ in the

---

[5] When the piezoelectric boundary-value problem is regarded as a *closed boundary problem*, $\mathbf{D}$ and $\mathbf{E}$ are set to zero in $\tilde{V}$, and the boundary condition (4.7) transforms into $\mathbf{n} \cdot \mathbf{D}^{V} = \overline{\sigma}$ on $S_{\overline{\sigma}}$.

region V bounded by the surface S and of the electric potential $\varphi(\mathbf{r},t)$ in the infinitely extending region $V \cup \tilde{V}$, satisfying the governing equations in V and $\tilde{V}$, and boundary conditions imposed on S and S_∞. In general, the initial conditions for $\mathbf{u}$, $\partial\mathbf{u}/\partial t$, φ, $\partial\varphi/\partial t$ need also to be specified at all points of the body; in practice, for the two common problems considered below, their explicit imposition can be avoided.

4.2 *Static problem*

The static problem can be derived from the general formulation by assuming that the mechanical and electric field variables, as well as boundary conditions, are time-independent. The *equilibrium* equation is obtained from the equation of motion (4.1) by setting the inertia force to zero:

$$\nabla \cdot \mathbf{T} = 0 \text{ in } V. \tag{4.16}$$

The remaining equations given in the previous section still hold as do boundary conditions (4.6)–(4.15), where the driving terms $\bar{\mathbf{t}}$, $\bar{\sigma}$, $\bar{\mathbf{u}}$, and $\bar{\varphi}$ are now constant in time.

The boundary conditions can be further simplified to fit practical boundary configurations. Typically, the piezoelectric body is supported in such a way that its surface is traction-free, i.e. the mechanical boundary conditions are given as

$$\mathbf{n} \cdot \mathbf{T} = 0 \text{ on } S, \tag{4.17}$$

or, in terms of mechanical displacement and electric potential,

$$\mathbf{n} \cdot \left(\mathbf{c}^E : \nabla\mathbf{u} + \nabla\varphi \cdot \mathbf{e}\right) = 0 \text{ on } S. \tag{4.17a}$$

The piezoelectric body is assumed to be partially covered by one or several electrodes, occupying a portion of the surface S_e, as shown in Fig. 1.3.

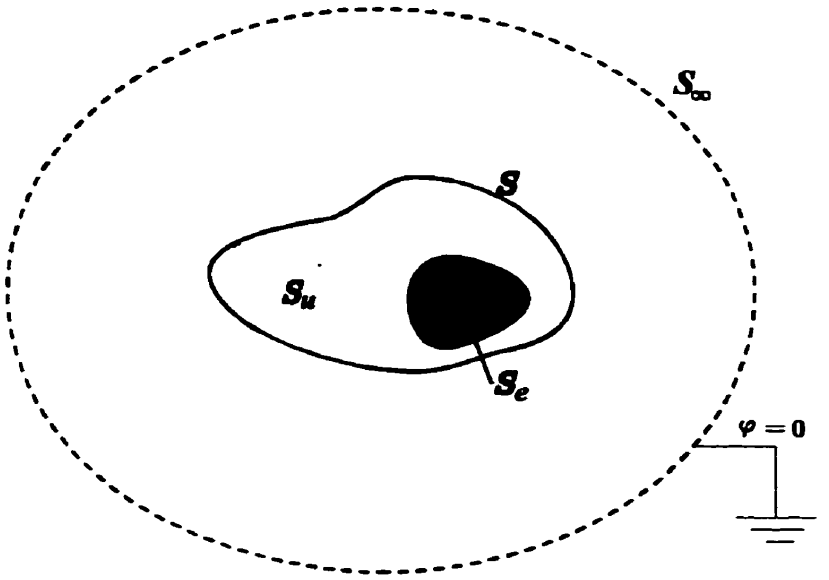

Fig 1.3 Partially plated piezoelectric body in unbounded free space.

This partition is relevant for the electrical boundary conditions only since the electrodes are considered to be infinitesimally thin and their mechanical properties nonexistent. Assuming that these electrodes behave as perfect conductors, it becomes possible to rewrite conditions (4.7) and (4.9) in terms of the total electric charge Q:

$$\int_{S_e} \mathbf{n} \cdot [\mathbf{D}] \, \mathrm{d}S = Q \,, \tag{4.18}$$

and of the electrode potential φ_e:

$$\varphi = \varphi_e \ \text{ on } S_e \tag{4.19}$$

respectively. Which of these boundary conditions should be used depends on the way the electrical energy is supplied to the driving electrode: the former is employed for a current source, while the latter for a voltage source. For linear materials, [**D**] in (4.18) can be expanded to yield

$$\int_{S_e} \mathbf{n} \cdot \left[\mathbf{e} : \nabla \mathbf{u} - \nabla \varphi \cdot \left(\boldsymbol{\epsilon}^S - \epsilon_0 \mathbf{I} \right) \right] \mathrm{d}S = -Q. \tag{4.20}$$

On the remaining, free of plating, part of the surface S_u, the continuity conditions for the normal electric flux density and the electric potential apply

$$\mathbf{n} \cdot \mathbf{D}^V = \mathbf{n} \cdot \mathbf{D}^{\tilde{V}} \text{ on } S_u, \tag{4.21}$$

$$\varphi^V = \varphi^{\tilde{V}} \text{ on } S_u. \tag{4.22}$$

As before, for linear materials condition (4.21) may be expressed in terms of mechanical displacement $\mathbf{u}$ and electric potential φ:

$$\mathbf{n} \cdot \left(\mathbf{e} : \nabla\mathbf{u} - \nabla\varphi \cdot \boldsymbol{\epsilon}^S\right) = -\mathbf{n} \cdot \nabla\varphi\, \epsilon_0 \text{ on } S_u. \tag{4.23}$$

Boundary conditions (4.14) and (4.15), that force the potential and its normal derivative to vanish on S_∞, must also be added to complete the formulation of the static boundary-value problem. The latter consists in finding the distributions $\mathbf{u}(\mathbf{r})$ and $\varphi(\mathbf{r})$ in the piezoelectric body in the state of equilibrium under the action of static voltages or static electric charges applied to the electroded parts of the traction-free surface S.

4.3 *Time-harmonic problem*

Another practically important type of boundary-value problem arises from the assumption that the displacement vector $\mathbf{u}$ and the scalar potential φ can be represented as products of two factors, one depending only upon the position vector $\mathbf{r}$ and the other - only upon time t:

$$\mathfrak{x}(\mathbf{r},t) = \mathfrak{X}(\mathbf{r})f(t), \tag{4.24}$$

where the generic symbol $\mathfrak{x}$ replaces either $\mathbf{u}$ or φ. Such a partition is possible for piezoelectric material with linear and time-invariant properties, so that the remaining field variables $(\mathbf{T}, \mathbf{S}, \mathbf{E}, \mathbf{D})$, derived from $\mathbf{u}$ and φ, can also be represented as (4.24). Indeed, substituting $\mathbf{u}$ in the form of (4.24) into the acoustic wave equation (4.10), and separating space- and time-dependent members, yields a time-harmonic solution for $f(t)$: $f(t) = e^{\pm i\omega t}$, where ω is the angular frequency. Therefore, $\mathbf{u}(\mathbf{r},t)$ and $\varphi(\mathbf{r},t)$ can be sought as real parts of $\mathbf{U}(\mathbf{r})e^{\pm i\omega t}$ and $\Phi(\mathbf{r})e^{\pm i\omega t}$ respectively, with spatial parts $\mathbf{U}(\mathbf{r})$ and $\Phi(\mathbf{r})$ obeying the following differential equations:

$$\nabla \cdot \left(\mathbf{c}^E : \nabla\mathbf{U}\right) + \nabla \cdot (\nabla\Phi \cdot \mathbf{e}) + \rho\omega^2\mathbf{U} = 0 \text{ in } V, \tag{4.25}$$

$$\nabla \cdot (\mathbf{e} : \nabla \mathbf{U}) - \nabla \cdot (\nabla \Phi \cdot \boldsymbol{\epsilon}^S) = 0 \text{ in } V, \tag{4.26}$$

$$\nabla^2 \Phi = 0 \text{ in } \tilde{V}. \tag{4.27}$$

According to the type of boundary condition, time-harmonic problems can be subdivided into *eigenvalue* and *deterministic*. The former corresponds to *free vibrations* of the piezoelectric body depicted in Fig. 1.3, the latter to *forced vibrations*. The solution of an eigenvalue problem, also referred to as a *resonance* problem, consists in finding the proper frequencies ω_n (eigenfrequencies) as well as the associated proper functions $(\mathbf{U}_n, \Phi_n)$ (eigenfunctions) that satisfy Eqs. (4.25)–(4.27) and homogeneous boundary conditions. As in the static case, the present formulation will be restricted to piezoelectric bodies with traction-free surfaces. This implies that the mechanical Neumann boundary conditions are always homogeneous on the entire surface S and given by Eqs. (4.17) or (4.17a). Keeping in mind that zero boundary conditions have been imposed on the outer surface S_∞, one can conclude that it is the zero electrical boundary conditions on S_e that set up conditions for free piezoelectric vibrations. Depending on which variable is zero on S_e, one can distinguish at least two types of resonance: the first occurs when the electrode potential is set to zero:

$$\varphi_e = 0 \text{ on } S_e, \tag{4.28}$$

while the second takes place for the zero total charge Q:

$$Q = 0 \text{ on } S_e. \tag{4.29}$$

Finally, the continuity of the normal electric flux (4.21) and electric potential (4.22) must be preserved across S_u, the unelectroded part of S.

Other eigenvalue problems can arise if the surface of the piezoelectric resonator (Fig. 1.3) is covered by more than one electrode, namely, those where zero potential is specified on some electrodes and zero total charge on the remainder. Note that for a piezoelectric problem with closed electric boundaries the reference potential can be associated with any of the electrodes. In this case, an eigenvalue problem is defined if a certain number of electrodes are *short-circuited* (zero potential), while the remainder are *open-circuited* (zero total charge) (Lloyd, 1967).

Deterministic, or *driven*, problems require non-homogeneous electric boundary conditions that must allow the separation of time and space variables, i.e. $Q = \mathrm{Q}\, e^{\pm i\omega t}$ or $\varphi_e = \Phi_e\, e^{\pm i\omega t}$ must be applied to S_e. However, there is no need to explicitly solve a deterministic problem for every ω. Because the eigenfunctions $(\mathbf{U}_n, \Phi_n)$ form an orthogonal set (Lewis, 1961; Lloyd, 1967), forced vibrations of a piezoelectric body can be expressed in terms of the eigensolutions ω_n and $(\mathbf{U}_n, \Phi_n)$, associated with any of the eigenvalue problems mentioned above. Such a representation is discussed in Section 7 of this thesis.

5 Projective formulation

The stated piezoelectric boundary-value problem can alternatively be represented in the form of projective equations. Projective formulations have the advantage of leading to approximate solutions that possess weaker continuity properties and fewer boundary constraints than those associated with differential formulations. Projective approximation techniques, and particularly Galerkin's approach, form the mathematical basis for the finite element method, adopted in this thesis to derive a numerical solution for the piezoelectric problem. Although in piezoelectricity the traditional approach to finite element analysis is variational, in this chapter, priority is given to the projective formulation since it allows the solution to be constructed without recourse to any variational principle.

5.1 *Weak approximation to the solution of the general piezoelectric boundary-value problem*

For equations (4.1) and (4.2) to hold in a *weak sense*, their left and right sides must have equal inner product projections onto any vector $\mathbf{w} \in \mathbf{W}^3$ and scalar $\theta \in \mathbf{W}$ functions respectively:

$$\int_V (\nabla \cdot \mathbf{T}) \cdot \mathbf{w}\, dV = \int_V \rho \frac{\partial^2 \mathbf{u}}{\partial t^2} \cdot \mathbf{w}\, dV, \qquad \forall\, \mathbf{w} \in \mathbf{W}^3 \tag{5.1}$$

$$\int_{V+\tilde{V}} (\nabla \cdot \mathbf{D})\theta\, dV = 0, \qquad \forall\, \theta \in \mathbf{W} \tag{5.2}$$

where $\mathbf{W}$ is a Hilbert space formed by square-integrable functions. This formulation allows the differentiation operator ∇ to be transferred from the unknown fields variables $\mathbf{T}$ and $\mathbf{D}$ to the chosen functions $\mathbf{w}$ and θ, thus relaxing the differentiability requirements for functions used to approximate the $\mathbf{u}$- and φ-field distributions. This operation is accomplished by applying the divergence theorem to volumes V and $V + \tilde{V}$

$$\int_V \nabla \cdot (\mathbf{T} \cdot \mathbf{w})\, dV = \int_S \mathbf{n} \cdot \mathbf{T} \cdot \mathbf{w}\, dS, \tag{5.3}$$

$$\int_{V+\tilde{V}} \nabla \cdot (\mathbf{D}\theta)\, dV = -\int_S \mathbf{n} \cdot [\mathbf{D}]\theta\, dS - \int_{S_\infty} \mathbf{n} \cdot \mathbf{D}\theta\, dS. \tag{5.4}$$

Since the electric field vanishes at infinity, the integral over S_∞ can be dropped from (5.4), simplifying it to:

$$\int_{V+\tilde{V}} \nabla \cdot (\mathbf{D}\theta)\, \mathrm{d}V = -\int_S \mathbf{n} \cdot [\mathbf{D}]\theta\, \mathrm{d}S. \tag{5.5}$$

Expressions (5.3) and (5.5) can be transformed by means of the following product differential rules

$$\nabla \cdot (\mathbf{T} \cdot \mathbf{w}) = (\nabla \cdot \mathbf{T}) \cdot \mathbf{w} + \mathbf{T} : \nabla \mathbf{w}^{6}, \tag{5.6}$$

$$\nabla \cdot (\mathbf{D}\theta) = (\nabla \cdot \mathbf{D})\theta + \mathbf{D} \cdot \nabla\theta \tag{5.7}$$

into

$$\int_V (\nabla \cdot \mathbf{T}) \cdot \mathbf{w}\, \mathrm{d}V + \int_V \mathbf{T} : \nabla \mathbf{w}\, \mathrm{d}V = \int_S \mathbf{n} \cdot \mathbf{T} \cdot \mathbf{w}\, \mathrm{d}S, \tag{5.8}$$

$$\int_{V+\tilde{V}} (\nabla \cdot \mathbf{D})\theta\, \mathrm{d}V + \int_{V+\tilde{V}} \mathbf{D} \cdot \nabla\theta\, \mathrm{d}V = -\int_S \mathbf{n} \cdot [\mathbf{D}]\theta\, \mathrm{d}S, \tag{5.9}$$

allowing equations (5.1) and (5.2) to be rewritten as

$$\int_V \mathbf{T} : \nabla \mathbf{w}\, \mathrm{d}V + \int_V \rho \frac{\partial^2 \mathbf{u}}{\partial t^2} \cdot \mathbf{w}\, \mathrm{d}V = \int_S \mathbf{n} \cdot \mathbf{T} \cdot \mathbf{w}\, \mathrm{d}S, \tag{5.10}$$

$$\int_{V+\tilde{V}} \mathbf{D} \cdot \nabla\theta\, \mathrm{d}V = -\int_S \mathbf{n} \cdot [\mathbf{D}]\theta\, \mathrm{d}S. \tag{5.11}$$

A similar system of projective equations has been obtained for the piezoelectric problem with closed electric boundaries by Naillon *et al* (1983). The present formulation is extended to include the external electric field by taking the volume integral in (5.11) over the entire space $V + \tilde{V}$ and replacing the electric flux **D** in the surface integral by its jump [**D**] across S. For linear piezoelectric materials, the substitution of constitutive Eqs. (2.21)–(2.22) makes Eqs. (5.10) and (5.11) into a projective version of the piezoelectric wave (4.10)–(4.11) and Laplace's (4.5) equations:

---

6 The symmetry of tensor **T** is implicitly assumed.

$$\int_V (\mathbf{c}^E : \nabla\mathbf{u} + \nabla\varphi \cdot \mathbf{e}) : \nabla\mathbf{w}\,\mathrm{d}V + \int_V \rho \frac{\partial^2 \mathbf{u}}{\partial t^2} \cdot \mathbf{w}\,\mathrm{d}V = \int_S \mathbf{n} \cdot \mathbf{T} \cdot \mathbf{w}\,\mathrm{d}S, \quad (5.12)$$

$$\int_V (\mathbf{e} : \nabla\mathbf{u} - \nabla\varphi \cdot \boldsymbol{\epsilon}^S) \cdot \nabla\theta\,\mathrm{d}V - \epsilon_0 \int_{\tilde{V}} \nabla\varphi \cdot \nabla\theta\,\mathrm{d}V = -\int_S \mathbf{n} \cdot [\mathbf{D}]\,\theta\,\mathrm{d}S. \quad (5.13)$$

To develop a numerical solution of (5.12)–(5.13), the unknown mechanical displacement $\mathbf{u}(\mathbf{r})$ and electric potential $\varphi(\mathbf{r})$ are approximated by the *basis*, or *trial*, functions $\{\alpha_i(\mathbf{r}) | i = 1,...,N\}$ and $\{\alpha'_i(\mathbf{r}) | i = 1,...,N'\}$ respectively. These functions form the spanning sets of N- and N'-dimensional linear subspaces of $\mathbb{W}$:

$$\mathbf{u}(\mathbf{r}) \simeq \sum_{i=1}^{N} \mathbf{u}_i\,\alpha_i(\mathbf{r}), \quad \mathbf{r} \in V, \quad (5.14)$$

$$\varphi(\mathbf{r}) \simeq \sum_{i=1}^{N'} \varphi_i\,\alpha'_i(\mathbf{r}), \quad \mathbf{r} \in V + \tilde{V}, \quad (5.15)$$

with vectors $\mathbf{u}_i$ and scalars φ_i in the role of the numerical coefficients to be determined from the solution. Similarly, functions $\mathbf{w}(\mathbf{r})$ and $\theta(\mathbf{r})$ may be expressed as linear combinations of *weighting*[7], or *testing*, functions $\{\beta_j(\mathbf{r}) | j = 1,...,M\}$ and $\{\beta'_j(\mathbf{r}) | j = 1,...,M'\}$, spanning M- and M'-dimensional linear subspaces of $\mathbb{W}$ respectively:

$$\mathbf{w}(\mathbf{r}) \simeq \sum_{j=1}^{M} \mathbf{w}_j\,\beta_j(\mathbf{r}), \quad \mathbf{r} \in V, \quad (5.16)$$

$$\theta(\mathbf{r}) \simeq \sum_{j=1}^{M'} \theta_j\,\beta'_j(\mathbf{r}) \quad \mathbf{r} \in V + \tilde{V}. \quad (5.17)$$

[7] The present formulation can be seen as a special case of the projective weighted residual method.

For approximations (5.14) and (5.15) to be the *weak solutions* of the governing equations with respect to subspaces $\mathbf{W}_M$ and $\mathbf{W}_{M'}$, Eqs. (5.12) and (5.13) must be satisfied for each function β_j and β'_j respectively. On substitution of (5.14)–(5.15), they turn into a system of M linear equations in $2N + N'$ coefficients $\mathbf{u}_i$, $\partial^2\mathbf{u}_i/\partial t^2$, and φ_i:

$$\sum_{i=1}^{N}\left(\int_V \nabla\alpha_i \cdot \mathbf{c}^E \cdot \nabla\beta_j \,\mathrm{d}V\right)\cdot \mathbf{u}_i + \sum_{i=1}^{N'}\left(\int_V \nabla\alpha'_i \cdot \mathbf{e} \cdot \nabla\beta_j \,\mathrm{d}V\right)\varphi_i + \sum_{i=1}^{N}\left(\rho\int_V \alpha_i\beta_j \,\mathrm{d}V\right)\frac{\partial^2\mathbf{u}_i}{\partial t^2} = \int_S \mathbf{n}\cdot\mathbf{T}\beta_j \,\mathrm{d}S, \qquad j = 1, \ldots, M \tag{5.18}$$

and M' linear equations in $N + N'$ coefficients $\mathbf{u}_i$ and φ_i:

$$\sum_{i=1}^{N}\left(\int_V \nabla\beta'_j \cdot \mathbf{e} \cdot \nabla\alpha_i \,\mathrm{d}V\right)\cdot \mathbf{u}_i - \sum_{i=1}^{N'}\left(\int_{V+\tilde{V}} \nabla\alpha'_i \cdot \boldsymbol{\epsilon} \cdot \nabla\beta'_j \,\mathrm{d}V\right)\varphi_i = -\int_S \mathbf{n}\cdot[\mathbf{D}]\,\beta'_j \,\mathrm{d}S, \qquad j = 1, \ldots, M' \tag{5.19}$$

where

$$\boldsymbol{\epsilon} = \begin{cases} \boldsymbol{\epsilon}^S & \text{in } V \\ \epsilon_0\mathbf{I} & \text{in } \tilde{V} \end{cases} \tag{5.20}$$

A few points should be observed about the properties of the basis and weighting functions. First, since Eqs. (5.18) and (5.19) involve only gradients of α_i (α'_i) and β_j (β'_j), both the basis and weighting functions need be only once differentiable. Second, the basis functions $\alpha_i(\alpha'_i)$ are chosen such that approximations $\mathbf{u}(\mathbf{r})$ and $\varphi(\mathbf{r})$ do not *a priori* satisfy the governing equations but do satisfy the Dirichlet boundary conditions (4.8)–(4.9)[8]; otherwise, the zero

[8] In the alternative approach, known as *boundary solution*, or Trefftz, procedure (Zienkiewicz *et al.*, 1977), the basis functions $\alpha_i(\alpha'_i)$ are chosen in such a manner that $\mathbf{u}(\mathbf{r})$ and $\varphi(\mathbf{r})$ *a priori* satisfy the governing equations. This method is typically used to model simple homogeneous structures for which Green's functions are derivable in closed form.

projections of the latter $\int_{S_{\bar{\mathbf{u}}}}(\mathbf{u}-\bar{\mathbf{u}})\cdot\mathbf{w}\,dS=0$ and $\int_{S_{\bar{\varphi}}}(\varphi-\bar{\varphi})\theta\,dS=0$ would have to be added to the system (5.12)–(5.13). To examine how the nonhomogeneous Neumann boundary conditions (4.6)–(4.7) are treated under the projective formulation, consider their weighted residuals

$$\int_{S_{\bar{\mathbf{t}}}}(\mathbf{n}\cdot\mathbf{T}-\bar{\mathbf{t}})\beta_j\,dS=\int_{S_{\bar{\mathbf{t}}}}\mathbf{n}\cdot\mathbf{T}\beta_j\,dS-\int_{S_{\bar{\mathbf{t}}}}\bar{\mathbf{t}}\beta_j\,dS, \tag{5.21}$$

$$-\int_{S_{\bar{\sigma}}}(\mathbf{n}\cdot[\mathbf{D}]-\bar{\sigma})\beta'_j\,dS=-\int_{S_{\bar{\sigma}}}\mathbf{n}\cdot[\mathbf{D}]\beta'_j\,dS+\int_{S_{\bar{\sigma}}}\bar{\sigma}\beta'_j\,dS. \tag{5.22}$$

Theoretically, to satisfy the Neumann boundary conditions in a projective sense, equations (5.18) and (5.19) must be supplemented by residuals (5.21) and (5.22), set to zero. However, in this formulation, this is not necessary. By choosing β_j and β'_j appropriately, integrals $\int_{S_{\bar{\mathbf{t}}}}\mathbf{n}\cdot\mathbf{T}\beta_j\,dS$ in (5.21) and $\int_{S_{\bar{\sigma}}}\mathbf{n}\cdot[\mathbf{D}]\beta'_j\,dS$ in (5.22) annihilate the boundary integrals over $S_{\bar{\mathbf{t}}}$ and $S_{\bar{\sigma}}$ in the right-hand sides of Eqs. (5.18) and (5.19), rewritten here as

$$\int_S\mathbf{n}\cdot\mathbf{T}\beta_j\,dS=\int_{S_{\bar{\mathbf{t}}}}\mathbf{n}\cdot\mathbf{T}\beta_j\,dS+\int_{S_{\bar{\mathbf{u}}}}\mathbf{n}\cdot\mathbf{T}\beta_j\,dS, \tag{5.23}$$

$$-\int_S\mathbf{n}\cdot[\mathbf{D}]\beta'_j\,dS=-\int_{S_{\bar{\sigma}}}\mathbf{n}\cdot[\mathbf{D}]\beta'_j\,dS-\int_{S_{\bar{\varphi}}}\mathbf{n}\cdot[\mathbf{D}]\beta'_j\,dS. \tag{5.24}$$

The remaining integrals over $S_{\bar{\mathbf{u}}}$ and $S_{\bar{\varphi}}$ in (5.23) and (5.24), on which $\mathbf{u}$ and φ are fixed while $\mathbf{n}\cdot\mathbf{T}$ and $\mathbf{n}\cdot[\mathbf{D}]$ are arbitrary, can be eliminated by forcing the weighting functions β_j and β'_j to vanish on the Dirichlet boundaries $S_{\bar{\mathbf{u}}}$ and $S_{\bar{\varphi}}$ respectively. By assigning zero 'weights' to these parts of S, the spatial derivatives $\nabla\mathbf{u}$ and $\nabla\varphi$, that enter the expressions for $\mathbf{n}\cdot\mathbf{T}$ and $\mathbf{n}\cdot[\mathbf{D}]$, are also eliminated from (5.23) and (5.24). As a consequence, the approximate solutions (5.14)–(5.15) are not required to satisfy the Neumann boundary conditions, which considerably simplifies the choice of the basis functions $\alpha_i(\alpha'_i)$. This distinguishes the weak solution from the strong one that requires functions $\mathbf{u}(\mathbf{r})$ and $\varphi(\mathbf{r})$ to satisfy all the boundary conditions besides of being twice differentiable.

As a result, the nonhomogeneous Neumann boundary conditions are solely represented by the integrals $\int_{S_{\bar{\mathbf{t}}}}\bar{\mathbf{t}}\beta_j\,dS$ and $\int_{S_{\bar{\sigma}}}\bar{\sigma}\beta'_j\,dS$. The surface traction $\bar{\mathbf{t}}$ and

charge $\bar{\sigma}$ in the latter are commonly approximated by the surface basis functions $\bar{\alpha}_i$ and $\bar{\alpha}'_i$ that form the subsets of $\{\alpha_i(\mathbf{r})|\, i = 1,...,N\}$ and $\{\alpha'_i(\mathbf{r})|\, i = 1,...,N'\}$ mentioned earlier:

$$\bar{\mathbf{t}} \simeq \sum_{i=1}^{N_S} \mathbf{t}_i \bar{\alpha}_i, \tag{5.25}$$

$$\bar{\sigma} \simeq \sum_{i=1}^{N'_S} \sigma_i \bar{\alpha}'_i, \tag{5.26}$$

where $\mathbf{t}_i$ and σ_i are known since $\bar{\mathbf{t}}$ and $\bar{\sigma}$ are prescribed. This permits projective equations (5.18) and (5.19) to be rewritten in the following form

$$\sum_{i=1}^{N} \left(\int_V \nabla \alpha_i \cdot \mathbf{c}^E \cdot \nabla \beta_j \, dV \right) \cdot \mathbf{u}_i + \sum_{i=1}^{N'} \left(\int_V \nabla \alpha'_i \cdot \mathbf{e} \cdot \nabla \beta_j \, dV \right) \varphi_i$$
$$+ \sum_{i=1}^{N} \left(\rho \int_V \alpha_i \beta_j \, dV \right) \frac{\partial^2 \mathbf{u}_i}{\partial t^2} = \sum_{i=1}^{N_S} \left(\int_{S_{\bar{\mathbf{t}}}} \bar{\alpha}_i \beta_j \, dS \right) \mathbf{t}_j,$$
$$j = 1, ..., M, \tag{5.27}$$

$$\sum_{i=1}^{N} \left(\int_V \nabla \beta'_j \cdot \mathbf{e} \cdot \nabla \alpha_i \, dV \right) \cdot \mathbf{u}_i - \sum_{i=1}^{N'} \left(\int_{V+\bar{V}} \nabla \alpha'_i \cdot \boldsymbol{\epsilon} \cdot \nabla \beta'_j \, dV \right) \varphi_i$$
$$= - \sum_{j=1}^{N'_S} \left(\int_{S_{\bar{\sigma}}} \bar{\alpha}'_i \beta'_j \, dS \right) \sigma_j,$$
$$j = 1, ..., M' \tag{5.28}$$

5.2 *Galerkin's approach*

In most cases, it is convenient to select the weighting functions β_j from the set of basis functions α_i (Galerkin's method). With this choice, the system of projective equations (5.27)–(5.28) becomes a symmetric matrix equation of order $N + N'$

$$\begin{bmatrix} \mathbf{K}^{uu} & \mathbf{K}^{u\varphi} \\ \mathbf{K}^{\varphi u} & -\mathbf{K}^{\varphi\varphi} \end{bmatrix} \begin{bmatrix} \mathbf{U} \\ \boldsymbol{\Phi} \end{bmatrix} + \begin{bmatrix} \mathbf{M} & 0 \\ 0 & 0 \end{bmatrix} \begin{bmatrix} \dfrac{\partial^2 \mathbf{U}}{\partial t^2} \\ 0 \end{bmatrix} = \begin{bmatrix} \mathbf{F} \\ -\mathbf{Q} \end{bmatrix}, \tag{5.29}$$

with vectors of unknowns $\mathbf{U} = (\mathbf{u}_i)_{i=1,\dots,N}$, $\mathbf{\Phi} = (\varphi_i)_{i=1,\dots,N'}$, and $\partial^2\mathbf{U}/\partial t^2 = (\partial^2\mathbf{u}_i/\partial t^2)_{i=1,\dots,N}$. The matrices $\mathbf{K}^{\mathbf{uu}}$, $\mathbf{K}^{\mathbf{u}\varphi}$, $\mathbf{K}^{\varphi\varphi}$ and $\mathbf{M}$ in (5.29) are respectively

- the *elastic stiffness* matrix made up of 3×3 matrix blocks

$$\mathbf{K}_{ij}^{\mathbf{uu}} = \left(\int_V \nabla\alpha_i \cdot \mathbf{c}^E \cdot \nabla\alpha_j \, \mathrm{d}V\right)_{i=1,\dots,N,\ j=1,\dots,N,} \tag{5.30}$$

- the *piezoelectric stiffness* matrix made up of 3×1 vector blocks

$$\mathbf{K}_{ij}^{\mathbf{u}\varphi} = \left(\int_V \nabla\alpha'_j \cdot \mathbf{e} \cdot \nabla\alpha_i \, \mathrm{d}V\right)_{i=1,\dots,N,\ j=1,\dots,N',} \tag{5.31}$$

- the *dielectric stiffness* matrix extended to the outer region $\tilde{V}$ with scalar elements

$$K_{ij}^{\varphi\varphi} = \left(\int_{V+\tilde{V}} \nabla\alpha'_i \cdot \boldsymbol{\epsilon} \cdot \nabla\alpha'_j \, \mathrm{d}V\right)_{i=1,\dots,N',\ j=1,\dots,N',} \tag{5.32}$$

- the *mass* matrix with 3×3 block elements

$$\mathbf{M}_{ij} = \mathbf{I}\left(\rho\int_V \alpha_i \, \alpha_j \, \mathrm{d}V\right)_{i=1,\dots,N,\ j=1,\dots,N,} \tag{5.33}$$

where $\mathbf{I}$ is a 3×3 identity matrix. The right-hand side vectors $\mathbf{F} = (\mathbf{f}_i)_{i=1,\dots,N}$ and $\mathbf{Q} = (\mathrm{q}_i)_{i=1,\dots,N'}$ contain respectively the components of the mechanical force acting upon $S_{\bar{\mathbf{t}}}$

$$\mathbf{f}_i = \sum_{j=1}^{N_S}\left(\int_{S_{\bar{\mathbf{t}}}} \overline{\alpha}_i \, \alpha_j \, \mathrm{d}S\right)\mathbf{t}_j, \tag{5.34}$$

and of the electric charges distributed over $S_{\bar{\sigma}}$

$$\mathrm{q}_i = \sum_{j=1}^{N'_S}\left(\int_{S_{\bar{\sigma}}} \overline{\alpha}'_i \, \alpha'_j \, \mathrm{d}S\right)\sigma_j. \tag{5.35}$$

Consider a piezoelectric body with traction-free, partially plated surface as shown in Fig. 1.3. This configuration, that had been used to formulate the static and time-harmonic piezoelectric problems, leads to a further simplifications of the projective matrix equation (5.29). First, the mechanical force term $\mathbf{F}$ disappears

from its right-hand side since homogeneous Neumann boundary condition (4.17) holds on the whole surface S. Second, only one variable — φ_e — is needed to characterize the N_e potential degrees of freedom on the electroded part of the surface S_e. The corresponding part $\mathbf{\Phi}_e$ of the vector of potential coefficient vector $\mathbf{\Phi} = (\mathbf{\Phi}', \mathbf{\Phi}_e)^{\mathrm{T}}$ can be written as $\mathbf{\Phi}_e = \varphi_e \mathbf{i}$, where $\mathbf{i} = (1, \ldots, 1)^{\mathrm{T}}$ is an N_e-dimensional vector with unit coordinates. Therefore, the N_e rows and columns of (5.29) associated with $\mathbf{\Phi}_e$ can be summed up to form a new matrix equation with a condensed electric part:

$$\begin{bmatrix} \mathbf{K}^{uu} & \mathbf{K}^{u\varphi'} & \mathbf{K}^{u\varphi_e}\mathbf{i} \\ \mathbf{K}^{\varphi' u} & -\mathbf{K}^{\varphi'\varphi'} & -\mathbf{K}^{\varphi'\varphi_e}\mathbf{i} \\ \mathbf{i}^{\mathrm{T}}\mathbf{K}^{\varphi_e u} & -\mathbf{i}^{\mathrm{T}}\mathbf{K}^{\varphi_e\varphi'} & -\mathbf{i}^{\mathrm{T}}\mathbf{K}^{\varphi_e\varphi_e}\mathbf{i} \end{bmatrix} \begin{bmatrix} \mathbf{U} \\ \mathbf{\Phi}' \\ \varphi_e \end{bmatrix} + \begin{bmatrix} \mathbf{M} & 0 & 0 \\ 0 & 0 & 0 \\ 0 & 0 & 0 \end{bmatrix} \begin{bmatrix} \dfrac{\partial^2 \mathbf{U}}{\partial t^2} \\ 0 \\ 0 \end{bmatrix} = \begin{bmatrix} 0 \\ 0 \\ Q \end{bmatrix}, \qquad (5.36)$$

where Q is the total charge on S_e. It should be noted that there is no charge vector $\mathbf{Q}'$ in the right-hand side of (5.36) associated with $\mathbf{\Phi}'$ as a result of the homogeneous Neumann boundary condition (4.21) imposed on the unelectroded part of the surface S_u.

As mentioned in Section 4, on the electroded part of the surface S_e either the total electric charge Q or the potential φ_e can be specified. In the first case, the electrode S_e can be seen as a Neumann electric boundary $S_e = S_{\overline{\sigma}}$. The matrix equation (5.36) applies to this situation with $Q = \overline{Q}$, and its solution provides the unknown $\mathbf{U}$, $\mathbf{\Phi}'$, and φ_e. In the second case, the Dirichlet boundary condition fixes the electric potential $\varphi_e = \overline{\varphi}_e$ on $S_e = S_{\overline{\varphi}}$, thus excluding the last equation containing the variable φ_e from the system (5.36), which has now the vector $\overline{\varphi}_e(-\mathbf{K}^{u\varphi_e}\mathbf{i}, \mathbf{K}^{\varphi'\varphi_e}\mathbf{i})^{\mathrm{T}}$ as driving term:

$$\begin{bmatrix} \mathbf{K}^{uu} & \mathbf{K}^{u\varphi'} \\ \mathbf{K}^{\varphi' u} & -\mathbf{K}^{\varphi'\varphi'} \end{bmatrix} \begin{bmatrix} \mathbf{U} \\ \mathbf{\Phi}' \end{bmatrix} + \begin{bmatrix} \mathbf{M} & 0 \\ 0 & 0 \end{bmatrix} \begin{bmatrix} \dfrac{\partial^2 \mathbf{U}}{\partial t^2} \\ 0 \end{bmatrix} = \overline{\varphi}_e \begin{bmatrix} -\mathbf{K}^{u\varphi_e}\mathbf{i} \\ \mathbf{K}^{\varphi'\varphi_e}\mathbf{i} \end{bmatrix} \qquad (5.37)$$

After solving (5.37) for $\mathbf{U}$ and $\mathbf{\Phi}'$, the total electric charge on S_e can be determined as

$$Q = \begin{bmatrix} \mathbf{i}^{\mathrm{T}}\mathbf{K}^{\varphi_e \mathbf{u}} & -\mathbf{i}^{\mathrm{T}}\mathbf{K}^{\varphi_e \phi'} & -\mathbf{i}^{\mathrm{T}}\mathbf{K}^{\varphi_e \varphi_e}\mathbf{i} \end{bmatrix} \begin{bmatrix} \mathbf{U} \\ \boldsymbol{\Phi}' \\ \overline{\varphi}_e \end{bmatrix} \tag{5.38}$$

from the last equation of (5.36).

The systems (5.36) and (5.37) are the two basic matrix equations that can be used to determine the approximations to the weak solution of the piezoelectric problem when either the total electric charge Q or the potential φ_e are specified on the plated part of the surface S_e. To adapt these equations to the static problem, the dynamic term $\mathbf{M}(\partial^2\mathbf{U}/\partial t^2)$ must be dropped from the system; in the case of time-harmonic field distributions $\mathbf{u}(\mathbf{r})$ and $\varphi(\mathbf{r})$, $\mathbf{M}(\partial^2\mathbf{U}/\partial t^2)$ is replaced by $-\omega^2\mathbf{M}\mathbf{U}$ and combined with the stiffness matrix. Thus, the time-harmonic counterparts of (5.36) and (5.37) are the equations:

$$\begin{bmatrix} \mathbf{K}^{\mathbf{u}\mathbf{u}} - \omega^2\mathbf{M} & \mathbf{K}^{\mathbf{u}\phi'} & \mathbf{K}^{\mathbf{u}\varphi_e}\mathbf{i} \\ \mathbf{K}^{\phi'\mathbf{u}} & -\mathbf{K}^{\phi'\phi'} & -\mathbf{K}^{\phi'\varphi_e}\mathbf{i} \\ \mathbf{i}^{\mathrm{T}}\mathbf{K}^{\varphi_e \mathbf{u}} & -\mathbf{i}^{\mathrm{T}}\mathbf{K}^{\varphi_e \phi'} & -\mathbf{i}^{\mathrm{T}}\mathbf{K}^{\varphi_e \varphi_e}\mathbf{i} \end{bmatrix} \begin{bmatrix} \mathbf{U} \\ \boldsymbol{\Phi}' \\ \Phi_e \end{bmatrix} = \begin{bmatrix} \mathbf{0} \\ \mathbf{0} \\ \overline{\mathbf{Q}} \end{bmatrix}, \tag{5.39}$$

and

$$\begin{bmatrix} \mathbf{K}^{\mathbf{u}\mathbf{u}} - \omega^2\mathbf{M} & \mathbf{K}^{\mathbf{u}\phi'} \\ \mathbf{K}^{\phi'\mathbf{u}} & -\mathbf{K}^{\phi'\phi'} \end{bmatrix} \begin{bmatrix} \mathbf{U} \\ \boldsymbol{\Phi}' \end{bmatrix} = \overline{\Phi}_e \begin{bmatrix} -\mathbf{K}^{\mathbf{u}\varphi_e}\mathbf{i} \\ \mathbf{K}^{\phi'\varphi_e}\mathbf{i} \end{bmatrix}, \tag{5.40}$$

solved for the spatial parts of functions $\mathbf{u}(\mathbf{r})$ and $\varphi(\mathbf{r})$ with time-harmonic driving charge $\overline{Q} = \overline{\mathbf{Q}}e^{i\omega t}$ or potential $\overline{\varphi}_e = \overline{\Phi}_e e^{i\omega t}$. If the boundary conditions are homogeneous, i.e. $\overline{\mathbf{Q}} = 0$ or $\overline{\Phi}_e = 0$ in (5.39) and (5.40) respectively, these matrix equations describe the two eigenvalue problems associated with the partially plated piezoelectric body from Section 4.3.

6. Variational formulation

An alternative way of obtaining the matrix equation (5.29) is to formulate the piezoelectric boundary-value problem in the form of variational equations, derived from a *variational principle*. The variational approach can be applied since the differential system (5.1)–(5.2) is *self-adjoint*. Governing equations and boundary conditions stem from the variational principle as stationary conditions of an energy related *functional*. Although Eq. (5.29), that furnishes the basis for the finite element analysis, has been already obtained by the Galerkin's method, the variational approach is also considered. It has the advantage of relying on the energy functions, thereby providing the mathematical procedure that led to (5.29) with a definite physical meaning.

6.1 *Variational principles*

In elasticity, the basis of variational formulation is the *principle of virtual work* (Washizu, 1968). According to this principle, the sum of all the virtual work done by external and internal forces applied to a mechanical system in equilibrium during an imaginary infinitesimal (virtual) displacement $\delta\mathbf{u}$ satisfying the prescribed constraint is zero:

$$\delta W_{ext} + \delta W_{int} = 0. \tag{6.1}$$

For dynamic problems, one must integrate (6.1) over the time interval $[t_0, t]$ and take into account the virtual work done by the inertia forces (d'Alembert's principle):

$$\delta W_{inert} = -\int_V \rho \frac{\partial^2 \mathbf{u}}{\partial t^2} \cdot \delta\mathbf{u}\, dV. \tag{6.2}$$

Since $\delta\mathbf{u}$ is required to vanish at t_0 and t, this work is equal, upon integration with respect to t, to the variation of the kinetic energy:

$$\delta T = \delta \int_V \frac{1}{2} \rho \frac{\partial \mathbf{u}}{\partial t} \cdot \frac{\partial \mathbf{u}}{\partial t}\, dV. \tag{6.3}$$

If it is further assumed that the internal forces are derived from a potential function $\mathfrak{U} = \mathfrak{U}(\mathbf{r}, t)$ such that

$$\delta W_{int} = -\delta \mathfrak{U}, \tag{6.4}$$

the dynamic principle of virtual work turns into the *Hamilton's principle*

$$\delta \int_{t_0}^{t} L \, \mathrm{d}t = \delta \int_{t_0}^{t} (T - \mathfrak{U} + W_{ext}) \, \mathrm{d}t = 0, \tag{6.5}$$

where the function $L = T - \mathfrak{U} + W_{ext}$ is the *Lagrangian* of the system. The principle states that the true motion makes the integral of the Lagrangian over the time interval $[t_0, t]$ stationary, provided the virtual displacement $\delta\mathbf{u}$ is consistent with the constraints, i.e. vanishes at t_0 and t, and at those parts of the piezoelectric on which $\mathbf{u}$ is prescribed.

The piezoelectric effect can be incorporated into the above principles by including the virtual work done by external and internal electrical charges. Consider, for example, the general problem defined in the differential form in Section 4.1. In the absence of volume forces ($\mathbf{F}$) and charges (ρ_e), the virtual work of external forces δW_{ext} reduces to the work done by the prescribed surface traction $\bar{\mathbf{t}}$ during a virtual displacement $\delta\mathbf{u}$ and by the surface charge $\bar{\sigma}$ during a variation of electrical potential $\delta\varphi$:

$$\delta W_{ext} = \int_{S_{\bar{\mathbf{t}}}} \bar{\mathbf{t}} \cdot \delta\mathbf{u} \, \mathrm{d}S - \int_{S_{\bar{\sigma}}} \bar{\sigma} \delta\varphi \, \mathrm{d}S,^{9} \tag{6.6}$$

where $\delta\mathbf{u}$ and $\delta\varphi$ are chosen such that they satisfy the Dirichlet boundary conditions (4.8) and (4.9), i.e. $\delta\mathbf{u} = 0$ on $S_{\bar{\mathbf{u}}}$ and $\delta\varphi = 0$ on $S_{\bar{\varphi}}$. The virtual work done by the constant internal volume $\nabla \cdot \mathbf{T}$ and surface stress $\mathbf{n} \cdot \mathbf{T}$ forces, as well as volume $\nabla \cdot \mathbf{D}$ and surface $\mathbf{n} \cdot [\mathbf{D}]$ charges during the same variations $\delta\mathbf{u}$ and $\delta\varphi$ is

$$\begin{aligned} \delta W_{int} = &- \int_V (-\nabla \cdot \mathbf{T}) \cdot \delta\mathbf{u} \, \mathrm{d}V - \int_{S_{\bar{\mathbf{t}}}} \mathbf{n} \cdot \mathbf{T} \cdot \delta\mathbf{u} \, \mathrm{d}S \\ &+ \int_{V+\tilde{V}} (\nabla \cdot \mathbf{D}) \delta\varphi \, \mathrm{d}V + \int_{S_{\bar{\sigma}}} \mathbf{n} \cdot [\mathbf{D}] \delta\varphi \, \mathrm{d}S, \end{aligned} \tag{6.7}$$

---

[9] The electrical part of the virtual work enters the expression with a negative sign because, as it will be shown subsequently, for a given pair of independent variables $\mathbf{S} = \mathbf{S}(\mathbf{u})$ and $\mathbf{E} = \mathbf{E}(\varphi)$ this is the the electric enthalpy G_2, not the internal energy U, that takes the place of the potential function $\mathfrak{U}$ (Tiersten, 1969).

where the work of internal forces is taken with the opposite sign compared to the virtual work of external forces. The volume integrals in (6.7) can be transformed by means of the integration by parts formulae for dyadics and vectors respectively

$$\int_V (\nabla \cdot \mathbf{T}) \cdot \delta\mathbf{u}\, \mathrm{d}V = -\int_V \mathbf{T} : \nabla\delta\mathbf{u}\, \mathrm{d}V + \int_S \mathbf{n} \cdot \mathbf{T} \cdot \delta\mathbf{u}\, \mathrm{d}S, \tag{6.8}$$

$$\int_{V+\tilde{V}} (\nabla \cdot \mathbf{D})\delta\varphi\, \mathrm{d}V = -\int_{V+\tilde{V}} \mathbf{D} \cdot (\nabla\delta\varphi)\, \mathrm{d}V - \int_S \mathbf{n} \cdot [\mathbf{D}]\delta\varphi\, \mathrm{d}S, \tag{6.9}$$

which indicate that the differential operators are formally self-adjoint (Gould, 1955). Taking into account that $\delta\mathbf{u}$ and $\delta\varphi$ vanish at those parts of the boundary S where $\mathbf{u}$ and φ are prescribed, the principle of virtual work for the given problem is written as

$$\int_{t_0}^{t} \Big[\delta \int_V \frac{1}{2} \rho \frac{\partial \mathbf{u}}{\partial t} \cdot \frac{\partial \mathbf{u}}{\partial t}\, \mathrm{d}V - \int_V \mathbf{T} : \delta\mathbf{S}\, \mathrm{d}V - \int_{V+\tilde{V}} \mathbf{D} \cdot \delta\mathbf{E}\, \mathrm{d}V + \int_{S_{\bar{\mathbf{t}}}} \bar{\mathbf{t}} \cdot \delta\mathbf{u}\, \mathrm{d}S - \int_{S_{\bar{\sigma}}} \bar{\sigma}\delta\varphi\, \mathrm{d}S \Big] \mathrm{d}t = 0, \tag{6.10}$$

where $\delta\mathbf{S} = 1/2\,(\nabla\delta\mathbf{u} + \delta\mathbf{u}\nabla)$ and $\delta\mathbf{E} = -\nabla\delta\varphi$. Since the present formulation uses the mechanical strain $\mathbf{S} = \mathbf{S}(\mathbf{u})$ and electric field $\mathbf{E} = \mathbf{E}(\varphi)$ as independent variables, the corresponding potential function is the Gibbs electric energy (electric enthalpy) G_2, whose density was defined by (2.16). Using constitutive relations (2.19), variational equation (6.10) leads to the Hamilton's principle for the dynamic piezoelectric problem

$$\int_{t_0}^{t} \Big[\delta(\mathrm{T} - G_2 + U_{ext}) + \int_{S_{\bar{\mathbf{t}}}} \bar{\mathbf{t}} \cdot \delta\mathbf{u}\, \mathrm{d}S - \int_{S_{\bar{\sigma}}} \bar{\sigma}\delta\varphi\, \mathrm{d}S \Big] \mathrm{d}t = 0, \tag{6.11}$$

which differs from the principle of virtual work by Tiersten (1969) by the additional exterior electric energy term

$$U_{ext} = \frac{1}{2} \epsilon_0 \int_{\tilde{V}} \nabla\varphi \cdot \nabla\varphi\, \mathrm{d}V. \tag{6.12}$$

An earlier version of the Lagrangian for piezoelectric vibrations is due to Eer Nisse (1967), Holland and Eer Nisse (1969), who claimed having derived it by 'trial and

error'. Lee (1990) extended (6.11) to include magnetic variables, thus obtaining a variational equation equivalent to the equations of piezoelectromagnetism given in Section 2.

The choice of independent variables determines which equations are derived from the variational principle, and which are considered as additional constraints. In the present example, the governing Eqs. (4.1), (4.2) and Neumann's boundary conditions (4.6), (4.7) follows from Hamilton's principle (6.11) as a condition of stationarity of the time integral (6.5) of the Lagrangian

$$L(\mathbf{u}, \varphi, t) = T - G_2 + U_{ext} + \int_{S_{\bar{\mathbf{t}}}} \bar{\mathbf{t}} \cdot \mathbf{u} \, \mathrm{d}S - \int_{S_{\bar{\sigma}}} \bar{\sigma} \varphi \, \mathrm{d}S, \tag{6.13}$$

provided the arbitrary variations $\delta\mathbf{u}$ and $\delta\varphi$ satisfy relations (2.8) and (4.3), and the Dirichlet boundary conditions (4.8) and (4.9). Therefore, the Neumann boundary conditions (4.6), (4.7) are implicit to the functional (6.13) and can be seen as *natural boundary conditions* (Hilderbrand, 1965), while the Dirichlet boundary conditions (4.8), (4.9) must be preassigned and, therefore, are *essential* to (6.13). Another feature of (6.13) is that its extremum, as pointed out by Eer Nisse (1967), is of a saddle point nature. This occurs because the electric enthalpy G_2 is not a positive definite function in contrast to the internal energy U which is part of the functional $\mathfrak{F}_1$ (Table 1.1), stationary under the variations of $\mathbf{S}$ and $\mathbf{D}$. As shown in Table 1.2, in this latter case, $\delta\mathbf{S}$ and $\delta\mathbf{D}$ satisfy Eqs. (2.8), (4.2), and boundary conditions (4.8), (4.7) respectively, while Eqs. (4.1), (4.3) and boundary conditions (4.6) and (4.9) result from the extremization of $\mathfrak{F}_1$. The two other stationary functionals, $\mathfrak{F}_2$ and $\mathfrak{F}_3$, based on the Gibbs free (G) and elastic (G_1) energy functions respectively, are drawn to demonstrate alternative combinations of governing equations and boundary conditions.

Table 1.1 Stationary functionals

Constitutive relations		Piezoelectric Lagrangian function
$\mathbf{T}=\dfrac{\partial U}{\partial \mathbf{S}}$	$\mathbf{E}=\dfrac{\partial U}{\partial \mathbf{D}}$	$\mathfrak{F}_1 = T-U-U^{ext}+\int_{S_{\bar{\mathbf{t}}}} \bar{\mathbf{t}}\cdot\mathbf{u}\,dS+\int_{S_{\bar{\varphi}}} \sigma\bar{\varphi}\,dS$
$\mathbf{S}=-\dfrac{\partial G}{\partial \mathbf{T}}$	$\mathbf{D}=-\dfrac{\partial G}{\partial \mathbf{E}}$	$\mathfrak{F}_2 = T-G+U^{ext}-\int_{S_{\mathbf{u}}} \mathbf{t}\cdot\bar{\mathbf{u}}\,dS-\int_{S_{\sigma}} \bar{\sigma}\varphi\,dS$
$\mathbf{S}=-\dfrac{\partial G_1}{\partial \mathbf{T}}$	$\mathbf{E}=\dfrac{\partial G_1}{\partial \mathbf{D}}$	$\mathfrak{F}_3 = T-G_1-U^{ext}-\int_{S_{\mathbf{u}}} \mathbf{t}\cdot\bar{\mathbf{u}}\,dS+\int_{S_{\bar{\varphi}}} \sigma\bar{\varphi}\,dS$
$\mathbf{T}=\dfrac{\partial G_2}{\partial \mathbf{S}}$	$\mathbf{D}=-\dfrac{\partial G_2}{\partial \mathbf{E}}$	$\mathfrak{F}_4 = T-G_2+U^{ext}+\int_{S_{\bar{\mathbf{t}}}} \bar{\mathbf{t}}\cdot\mathbf{u}\,dS-\int_{S_{\sigma}} \bar{\sigma}\varphi\,dS$

Table 1.2 Variational principles and equivalent equations and boundary conditions

Variational principle	Equations		Boundary conditions	
	imposed	derived	essential	natural
$\delta\mathfrak{F}_1=0$	$\mathbf{S}=\frac{1}{2}(\nabla\mathbf{u}+\mathbf{u}\nabla)$ $\nabla\cdot\mathbf{D}=0$	$\nabla\cdot\mathbf{T}=\rho\dfrac{\partial^2\mathbf{u}}{\partial t^2}$ $\mathbf{E}=-\nabla\varphi$	$\mathbf{u}=\bar{\mathbf{u}}$ $\mathbf{n}\cdot[\mathbf{D}]=\bar{\sigma}$	$\mathbf{n}\cdot\mathbf{T}=\bar{\mathbf{t}}$ $\varphi=\bar{\varphi}$
$\delta\mathfrak{F}_2=0$	$\nabla\cdot\mathbf{T}=\rho\dfrac{\partial^2\mathbf{u}}{\partial t^2}$ $\mathbf{E}=-\nabla\varphi$	$\mathbf{S}=\frac{1}{2}(\nabla\mathbf{u}+\mathbf{u}\nabla)$ $\nabla\cdot\mathbf{D}=0$	$\mathbf{n}\cdot\mathbf{T}=\bar{\mathbf{t}}$ $\varphi=\bar{\varphi}$	$\mathbf{u}=\bar{\mathbf{u}}$ $\mathbf{n}\cdot[\mathbf{D}]=\bar{\sigma}$
$\delta\mathfrak{F}_3=0$	$\nabla\cdot\mathbf{T}=\rho\dfrac{\partial^2\mathbf{u}}{\partial t^2}$ $\nabla\cdot\mathbf{D}=0$	$\mathbf{S}=\frac{1}{2}(\nabla\mathbf{u}+\mathbf{u}\nabla)$ $\mathbf{E}=-\nabla\varphi$	$\mathbf{n}\cdot\mathbf{T}=\bar{\mathbf{t}}$ $\mathbf{n}\cdot[\mathbf{D}]=\bar{\sigma}$	$\mathbf{u}=\bar{\mathbf{u}}$ $\varphi=\bar{\varphi}$
$\delta\mathfrak{F}_4=0$	$\mathbf{S}=\frac{1}{2}(\nabla\mathbf{u}+\mathbf{u}\nabla)$ $\mathbf{E}=-\nabla\varphi$	$\nabla\cdot\mathbf{T}=\rho\dfrac{\partial^2\mathbf{u}}{\partial t^2}$ $\nabla\cdot\mathbf{D}=0$	$\mathbf{u}=\bar{\mathbf{u}}$ $\varphi=\bar{\varphi}$	$\mathbf{n}\cdot\mathbf{T}=\bar{\mathbf{t}}$ $\mathbf{n}\cdot[\mathbf{D}]=\bar{\sigma}$

Note: For the sake of brevity, the time integral has been omitted in the first column, i.e. the variation of a functional $\delta\mathfrak{F}$ should be read as $\delta\int_{t_0}^{t}\mathfrak{F}$.

A more complete list of variational principles, derived especially for static piezoelectric problems, may be found in the review by Vekovischeva (1971). Among them, the most important are the generalized variational principle that considers all variables as being independent, and the piezoelectric Hellinger-Reissner principle, used in the theory of plates and shells (Shulga and Bolkisev,

1990). The former puts all the assumptions (governing equations, constitutive relations and boundary conditions) into the framework of the variational expression by means of Lagrange undetermined multipliers; any other principle can be derived from it by adding constraints to the field variables. In particular, in the Hellinger-Reissner principle, variables **S** and **E** are no longer considered independent, and are eliminated from the generalized principle by means of constitutive relations (1.18).

6.2 *Stationary functionals for static and time-harmonic problems*

Among the mentioned variational principles the one expressed by Eq. (6.11) has the most important practical application as a basis for the approximate solution techniques. Indeed, because this principle relies on the set of variables $\mathbf{S} = \mathbf{S}(\mathbf{u})$ and $\mathbf{E} = \mathbf{E}(\varphi)$ used in the differential formulation, it is convenient to use (6.11) to obtain the variational equation for the static and time-harmonic specializations of the general piezoelectric problem.

The static variational principle, derived by omitting the time integral and the kinetic energy term from (6.11), states that the Lagrangian

$$L(\mathbf{u}, \varphi) = G_2 - U_{ext} - \int_{S_t} \bar{\mathbf{t}} \cdot \mathbf{u} \, \mathrm{d}S + \int_{S_\sigma} \bar{\sigma} \varphi \, \mathrm{d}S, \tag{6.14}$$

is stationary for a piezoelectric body in equilibrium under the action of the constant surface traction $\bar{\mathbf{t}}$ and surface charge $\bar{\sigma}$. For the specific boundary conditions (4.17)–(4.19) considered in Section 4.2, this Lagrangian reduces to

$$L(\mathbf{u}, \varphi) = G_2 - U_{ext} + Q \varphi_e. \tag{6.15}$$

As in the differential and projective formulation, one will be interested in linear piezoelectric materials only; therefore, the electrical enthalpy G_2 in (6.15) is a quadratic function (2.20) of $\nabla \mathbf{u}$ and $\nabla \varphi$:

$$G_2 = \frac{1}{2} \int_V \left(\nabla \mathbf{u} : \mathbf{c}^E : \nabla \mathbf{u} + 2 \nabla \varphi \cdot \mathbf{e} : \nabla \mathbf{u} - \nabla \varphi \cdot \boldsymbol{\epsilon}^S \cdot \nabla \varphi \right) \mathrm{d}V, \tag{6.16}$$

while the energy density U_{ext} of the exterior electric field is given by (6.12).

For the time-harmonic fields, the spatial part of the Lagrangian, is written as

$$\mathrm{L}(\mathbf{U}, \Phi) = \mathrm{G}_2 - \mathrm{T} - \mathrm{U}_{ext} + \mathrm{Q} \Phi_e, \tag{6.17}$$

where G_2, U_{ext}, and $\mathrm{T} = 1/2\,\rho\omega^2\,\mathbf{U}\cdot\mathbf{U}$ are the time-averaged electric enthalpy G_2, exterior electric energy U_{ext}, and kinetic energy $T = 1/2\,\rho\,(\partial\mathbf{u}^*/\partial t)\cdot(\partial\mathbf{u}/\partial t)$ densities. Functional (6.17) is stationary for the true solution of the system (4.25)–(4.27) with time-harmonic driving charge $Q = \mathrm{Q}\,e^{i\omega t}$ or potential $\varphi_e = \Phi_e\,e^{i\omega t}$ applied to S_e. In particular, when the boundary conditions imposed on S_e are homogeneous ($\mathrm{Q} = 0$ or $\Phi_e = 0$), the solution of (4.25)–(4.27) makes the *Rayleigh quotient for free piezoelectric vibrations*

$$\lambda(\mathbf{U}, \Phi) = \frac{\mathrm{G}_2 - \mathrm{U}_{ext}}{\displaystyle\int_V \frac{1}{2}\rho\,\mathbf{U}\cdot\mathbf{U}\,dV}, \tag{6.18}$$

$\lambda = \omega^2$, stationary at the resonant frequencies ω_n of the piezoelectric vibrator.

After establishing the equivalence between the differential and variational formulations, the approximate solution of the piezoelectric problem can be obtained by performing a numerical extremization of stationary functionals. The usual procedure consists, first, in substituting the trial solutions (5.14) and (5.15) into the Lagrangian (6.14), which, due to (6.16) and (6.12), becomes a quadratic function of $N + N'$ unknown coefficients $\mathbf{u}_i$ and φ_j; and, second, in determining the stationary point of L from the system of linear equations

$$\left.\begin{aligned} \frac{\partial L}{\partial \mathbf{u}_i} &= 0, \qquad i = 1, 2, \ldots, N, \\ \frac{\partial L}{\partial \varphi_j} &= 0, \qquad j = 1, 2, \ldots, N'. \end{aligned}\right\} \tag{6.19}$$

It can be verified that system (6.19) leads to exactly the same matrix equations (5.29), obtained by means of the Galerkin method in Section 5.2.

6.3 *Energy relations for stationary solutions*

To conclude this section, several integral relations that characterize the balance of energy in the piezoelectric vibrator are derived for the stationary solutions.

Replacing $\delta\mathbf{u}$ with $\mathbf{U}$ and $\delta\varphi$ with Φ in (6.8) and (6.9) respectively, and taking into account that the exact solution $(\mathbf{U}, \Phi)$ satisfies the governing equations of

piezoelectric vibrations, $\nabla \cdot \mathbf{T} + \rho\omega^2\mathbf{U} = 0$ and $\nabla \cdot \mathbf{D} = 0$, the integration by part identities are recast as

$$-\int_V \rho\omega^2 \mathbf{U} \cdot \mathbf{U}\, dV = -\int_V \mathbf{T} : \mathbf{S}\, dV + \int_S \mathbf{n} \cdot \mathbf{T} \cdot \mathbf{U}\, dS, \tag{6.20}$$

$$0 = \int_{V+\tilde{V}} \mathbf{D} \cdot \mathbf{E}\, dV - \int_S \mathbf{n} \cdot [\mathbf{D}]\Phi\, dS. \tag{6.21}$$

As before, for the traction-free boundary surface and equipotential electrode, this system simplifies to

$$\int_V \rho\omega^2 \mathbf{U} \cdot \mathbf{U}\, dV = \int_V \mathbf{T} : \mathbf{S}\, dV, \tag{6.22}$$

$$\mathrm{Q}\,\Phi_e = \int_{V+\tilde{V}} \mathbf{D} \cdot \mathbf{E}\, dV. \tag{6.23}$$

Denoting the spatial parts of mechanical, dielectric, and mutual energies as

$$\mathrm{U}_{mech} = \frac{1}{2}\int_V \nabla\mathbf{U} : \mathbf{c}^E : \nabla\mathbf{U}\, dV, \tag{6.24}$$

$$\mathrm{U}_{diel} = \frac{1}{2}\int_V \nabla\Phi \cdot \boldsymbol{\epsilon}^S \cdot \nabla\Phi\, dV, \tag{6.25}$$

$$\mathrm{U}_{mut} = \frac{1}{2}\int_V \nabla\Phi \cdot \mathbf{e} : \nabla\mathbf{U}\, dV, \tag{6.26}$$

respectively, relations (6.22) and (6.23) can be rewritten in the form

$$\mathrm{T} = \mathrm{U}_{mech} - \mathrm{U}_{mut}, \tag{6.27}$$

$$\mathrm{Q}\,\Phi_e = \mathrm{U}_{mut} + \mathrm{U}_{diel} + \mathrm{U}_{ext}. \tag{6.28}$$

Addition of (6.27) and (6.28) yields the *equation of the conservation of energy*

$$\mathrm{Q}\Phi_e = \mathrm{U} + \mathrm{U}_{ext} - \mathrm{T}, \tag{6.29}$$

which states that the sum of potential energy, made up of interior $\mathrm{U} = \mathrm{U}_{mech} + \mathrm{U}_{diel}$ and exterior part U_{ext}, and the kinetic energy T is equal to the energy supplied by the applied voltage Φ_e or current $\mathrm{I} = j\omega\mathrm{Q}$.

For free vibrations ($Q = 0$ or $\Phi_e = 0$) there is no energy supply to the piezoelectric vibrator, and, consequently, the total stored energy is constant. From (6.29) it follows that the instantaneous potential energy is 180° out of phase with the instantaneous kinetic energy

$$U + U_{ext} = T, \tag{6.30}$$

and, therefore, the total energy stored in the vibrator can be calculated solely from its kinetic or potential form. Substituting (6.24) and (6.25) into (6.0), and rearranging terms, one obtain the *stationary value of the Rayleigh quotient* (6.18)

$$\omega_n^2 = \frac{\int_V \nabla \mathbf{U}_n : \mathbf{c}^E : \nabla \mathbf{U}_n \, dV + \int_{V+\tilde{V}} \nabla \Phi_n \cdot \boldsymbol{\epsilon} \cdot \nabla \Phi_n \, dV}{\int_V \rho \, \mathbf{U}_n \cdot \mathbf{U}_n \, dV}, \tag{6.31}$$

for free vibrations characterized by the set of eigenfrequencies ω_n and eigenfunctions $(\mathbf{U}_n, \Phi_n)$. With $\boldsymbol{\epsilon}$ defined by (5.20) over the entire space, equation (6.31) represents an open electric boundary analogue of the stationary Rayleigh quotient derived earlier by Lewis (1961) and Eer Nisse (1968) for piezoelectric vibrations.

6.4 *Electromechanical coupling coefficient*

The electromechanical coupling coefficients k, or simply coupling factors, are introduced to characterize the strength of the piezoelectric interaction between mechanical and electrical fields. Being dimensionless, they are particularly useful for the comparison of the piezoelectric efficiency of different materials. A critical review of various definitions of k can be found in Ikeda (1996).

The squared coupling coefficient k^2 is often defined as

$$k^2 = \frac{U_{mut}^2}{U_{mech} U_{diel}}. \tag{6.32}$$

Formally, it follows from (6.32), (6.27), and (6.28) that the static coupling coefficient ($T = 0$) is given by

$$k_{st}^2 = \frac{U_{mech}}{U_{diel} + U_{ext}}, \tag{6.33}$$

while the dynamic coefficient at resonance ($Q\Phi_e = 0$) is derived from

$$k_{dyn}^2 = \frac{U_{diel} + U_{ext}}{U_{mech}}. \tag{6.34}$$

In this thesis, however, the static and modal coupling coefficients are calculated using expressions

$$\bar{k}_{st}^2 = \frac{U_{mech}}{U_{total}}, \tag{6.35}$$

and

$$\bar{k}_{dyn}^2 = \frac{U_{diel} + U_{ext}}{U_{total}} \tag{6.36}$$

respectively, where U_{total} denotes the total (interior and exterior) energy $U + U_{ext}$. Equations (6.35) and (6.36) are more consistent with the latest (IEEE, 1987) definition of k as a measure of the capability of a piezoelectric crystal to convert energy from an electrical source to mechanical work (electrically-driven static piezoelectric problem), and from a mechanical source to electrical work (piezoelectric vibrations). Clearly, the coupling coefficients depends on the mechanical and electrical fields configurations, determined by the crystal geometry and boundary conditions. The dynamic coupling coefficient is typically smaller than the static one because the latter is associated with more uniform field distributions. Very often the dynamic coupling coefficient is calculated as

$$k_{eff}^2 = \frac{f_A^2 - f_R^2}{f_A^2}, \tag{6.37}$$

where f_R and f_A are the linear frequencies at resonance and antiresonance — the two characteristic electrical situations discussed in the following section.

7 Equivalent electrical parameters

Because the piezoelectric vibrators are typically used as two- or multi-terminal passive components, it is highly desirable to represent and analyze them in the form of an equivalent electrical circuit, i.e. a circuit consisting of frequency-independent inductors, capacitors and resistors, and possessing an identical impedance (admittance) function. The approximate solutions of the static and free-vibration problems discussed earlier can be utilized to determine the equivalent impedance (admittance) of forced piezoelectric vibrations. Their expansion in terms of static and proper solutions is based on integral relations derived from the piezoelectric reciprocity theorem considered in the next section.

7.1 *Reciprocity relation and mode orthogonality*

One of the most practically important integral relations between two possible solutions of the governing equations is the piezoelectric *reciprocity theorem* (Auld, 1990b). The reciprocity relation for the forced piezoelectric vibrations was first introduced by Lewis (1961), who used it as a principal tool for deriving the passive electrical circuit equivalent in its electrical behavior to the piezoelectric vibrator (Fig. 1.3).

For the body with a traction-free surface, in the absence of volume forces and charges, the reciprocity relation can be written as

$$(\omega_2^2 - \omega_1^2)\int_V \rho \mathbf{U}_1 \cdot \mathbf{U}_2 \, dV = \Phi_{e1} Q_2 - \Phi_{e2} Q_1, \tag{7.1}$$

where the indices 1 and 2 refer to two pairs of solution of forced piezoelectric vibrations; the static reciprocity relation may be seen as a special case of (7.1) with $\omega_1 = \omega_2 = 0$. In the case of free vibrations, (7.1) yields the *orthogonality condition*

$$\int_V \rho \mathbf{U}_1 \cdot \mathbf{U}_2 \, dV = 0 \tag{7.2}$$

for two different solutions ($\omega_1 \neq \omega_2$) of the same eigenset. Expression (7.2) constitutes the basis for the *modal analysis* of piezoelectric vibrators by allowing the expansion of an arbitrary forced vibration ($\mathbf{U}$,Φ) in terms of static ($\mathbf{U}_s$, Φ_s) and proper ($\mathbf{U}_n$, Φ_n) solutions:

$$\begin{pmatrix} \mathbf{U} \\ \Phi \end{pmatrix} = \begin{pmatrix} \mathbf{U}_s \\ \Phi_s \end{pmatrix} + \sum_{n=1}^{\infty} a_n \begin{pmatrix} \mathbf{U}_n \\ \Phi_n \end{pmatrix}. \tag{7.3}$$

The decomposition coefficient a_n is determined to satisfy the equation of motion $\nabla \cdot \mathbf{T} + \rho\omega^2\mathbf{U} = 0$ alone, and is found to be

$$a_n = \frac{\omega^2 \int_V \rho \mathbf{U}_s \cdot \mathbf{U}_n \, dV}{(\omega_n^2 - \omega^2) \int_V \rho \mathbf{U}_n \cdot \mathbf{U}_n \, dV}; \tag{7.4}$$

the remaining governing equation and boundary conditions are identically satisfied by (7.3). Applying (7.1) to the sets of solution $(\mathbf{U}_s, \Phi_s)$ and $(\mathbf{U}_n, \Phi_n, \omega_n)$, the numerator in (7.4) can be expressed in terms of static and proper electrode potential and charge: (Φ_{es}, Q_{en}) and (Φ_{en}, Q_{es}). For the two types of eigenvalue problem — when $\Phi_{en} = 0$ and $Q_{en} = 0$ — one obtain

$$a_n = \frac{\omega^2 \Phi_{es} Q_{en}}{(\omega_n^2 - \omega^2)T_n} \qquad (\Phi_{en} = 0), \tag{7.5}$$

and

$$a_n = -\frac{\omega^2 \Phi_{en} Q_{es}}{(\omega_n^2 - \omega^2)T_n} \qquad (Q_{en} = 0), \tag{7.6}$$

where $T_n = \omega_n^2 \int_V \rho \mathbf{U}_n \cdot \mathbf{U}_n \, dV$ denotes the double of the kinetic, i.e. total — see (6.0), energy of n-th mode of vibration.

7.2 *Electrical admittance and impedance matrices*

Before deriving an equivalent electrical admittance or impedance function for the forced piezoelectric vibrations, it would be convenient to view the piezoelectric vibrator as a multi-electrode structure. Configurations with one electrode, considered so far for the sake of simplicity, two electrodes (e.g. resonators) or several pairs of electrodes (e.g. monolithic crystal filters) represent special cases of the generalized resonator shown in Fig. 1.4.

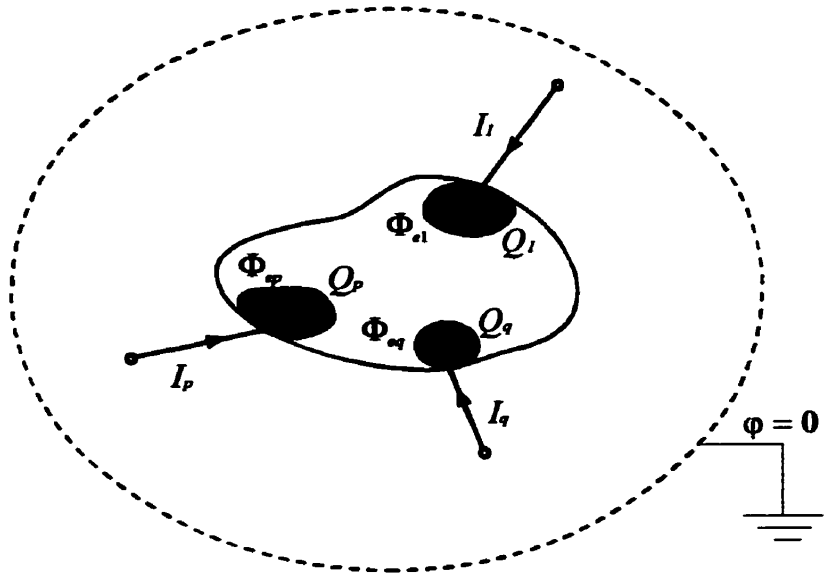

Fig 1.4 Piezoelectric vibrator with an arbitrary number of electrodes.

An L-terminal vibrator is driven now by the vectors of electrode potentials $\mathbf{\Phi} = (\Phi_{ep})_{p=1,\dots,L}$ and charges $\mathbf{Q} = (\mathrm{Q}_p)_{p=1,\dots,L}$; its electrical behavior can be characterized by the admittance and impedance matrices $\mathbf{Y}$ and $\mathbf{Z}$, defined respectively as

$$\mathbf{I} = \mathbf{Y}\,\mathbf{\Phi}, \tag{7.7}$$

and

$$\mathbf{\Phi} = \mathbf{Z}\,\mathbf{I}, \tag{7.8}$$

where $\mathbf{I} = j\omega\mathbf{Q}$. These matrices can be constructed by expressing the driving vectors $\mathbf{Q}$ and $\mathbf{\Phi}$ in terms of static and eigensolutions:

$$\begin{pmatrix} \mathbf{Q} \\ \mathbf{\Phi} \end{pmatrix} = \begin{pmatrix} \mathbf{Q}_s \\ \mathbf{\Phi}_s \end{pmatrix} + \sum_{n=1}^{\infty} a_n \begin{pmatrix} \mathbf{Q}_n \\ \mathbf{\Phi}_n \end{pmatrix}. \tag{7.9}$$

The decomposition coefficient a_n is the same as in (7.3), i.e.

$$a_n = \frac{\omega^2 \left(\mathbf{\Phi}_s^{\mathrm{T}} \mathbf{Q}_n - \mathbf{\Phi}_n^{\mathrm{T}} \mathbf{Q}_s \right)}{\left(\omega_n^2 - \omega^2 \right) \mathrm{T}_n} \tag{7.10}$$

because of the linearity of the piezoelectric material. In the form (7.10), a_n is applicable to any combination of homogeneous boundary conditions (i.e. when zero potential is specified on some electrodes $\Phi_{ep} = 0|_{p=1,\ldots,L'}$ and zero total charge $Q_p = 0|_{p=L'+1,\ldots,L}$ on the remainder), and represents a generalization of Eqs. (7.5)–(7.6). On the substitution of (7.10) into expansions (7.9), the latter become

$$\mathbf{Q} = \mathbf{Q}_s + \sum_{n=1}^{\infty} \frac{\omega^2 \mathbf{Q}_n \mathbf{Q}_n^{\mathrm{T}}}{(\omega_n^2 - \omega^2)\mathbf{T}_n} \mathbf{\Phi}_s - \sum_{n=1}^{\infty} \frac{\omega^2 \mathbf{Q}_n \mathbf{\Phi}_n^{\mathrm{T}}}{(\omega_n^2 - \omega^2)\mathbf{T}_n} \mathbf{Q}_s, \tag{7.11}$$

$$\mathbf{\Phi} = \mathbf{\Phi}_s - \sum_{n=1}^{\infty} \frac{\omega^2 \mathbf{\Phi}_n \mathbf{\Phi}_n^{\mathrm{T}}}{(\omega_n^2 - \omega^2)\mathbf{T}_n} \mathbf{Q}_s + \sum_{n=1}^{\infty} \frac{\omega^2 \mathbf{\Phi}_n \mathbf{Q}_n^{\mathrm{T}}}{(\omega_n^2 - \omega^2)\mathbf{T}_n} \mathbf{\Phi}_s. \tag{7.12}$$

Defining the symmetric matrix of static capacitance coefficients $\mathbf{C}_s$ as

$$\mathbf{Q}_s = \mathbf{C}_s \mathbf{\Phi}_s, \tag{7.13}$$

and using (7.7) and (7.8), one obtain the equivalent admittance $\mathbf{Y}$ and impedance $\mathbf{Z}$ matrices in the form

$$\mathbf{Y} = j\omega \left\{ \mathbf{C}_s + \sum_{n=1}^{\infty} \frac{\omega^2}{\omega_n^2 - \omega^2} (\mathbf{C}_n - \mathbf{E}_n \mathbf{C}_s) \right\}, \tag{7.14}$$

$$\mathbf{Z} = \frac{1}{j\omega} \left\{ \mathbf{C}_s^{-1} - \sum_{n=1}^{\infty} \frac{\omega^2}{\omega_n^2 - \omega^2} (\mathbf{F}_n - \mathbf{E}_n^{\mathrm{T}} \mathbf{C}_s^{-1}) \right\}. \tag{7.15}$$

In Eqs. (7.14)–(7.15), symbols $\mathbf{C}_n$, $\mathbf{F}_n$, $\mathbf{E}_n$ denote respectively the symmetric matrices

$$\mathbf{C}_n = \frac{\mathbf{Q}_n \mathbf{Q}_n^{\mathrm{T}}}{\mathbf{T}_n}, \tag{7.16}$$

and

$$\mathbf{F}_n = \frac{\mathbf{\Phi}_n \mathbf{\Phi}_n^{\mathrm{T}}}{\mathbf{T}_n}, \tag{7.17}$$

and the dimensionless matrix $\mathbf{E}_n$,

$$\mathbf{E}_n = \frac{\mathbf{\Phi}_n \mathbf{Q}_n^{\mathrm{T}}}{\mathbf{T}_n}. \tag{7.18}$$

Clearly, the matrix $\mathbf{E}_n$ vanishes identically for the two extreme cases of the eigenvalue problem associated with Fig. 1.4, i.e. when all electrodes are set to zero potential or when all are open circuited. For the former configuration ($\mathbf{\Phi}_n = 0\ \forall n$), the electrical behavior is represented solely by the symmetric admittance matrix

$$\mathbf{Y} = j\omega\left\{\mathbf{C}_s + \sum_{n=1}^{\infty} \frac{\omega^2 \mathbf{C}_n}{\omega_{Rn}^2 - \omega^2}\right\}, \tag{7.19}$$

where the corresponding eigenfrequencies ω_{Rn} are referred to as the *resonance* frequencies; the eigensolutions associated with the latter eigenproblem ($\mathbf{Q}_n = 0\ \forall n$) are used to expand the equivalent impedance matrix $\mathbf{Z}$ in a series about the *antiresonance* frequencies ω_{An}

$$\mathbf{Z} = \frac{1}{j\omega}\left\{\mathbf{C}_s^{-1} - \sum_{n=1}^{\infty} \frac{\omega^2 \mathbf{F}_n}{\omega_{An}^2 - \omega^2}\right\}. \tag{7.20}$$

Therefore, a lossless piezoelectric vibrator is characterized by two sets of critical frequencies: the resonance ω_{Rn}, at which the admittance tends to infinity and the impedance vanishes, and the antiresonance ω_{An}, at which the impedance is infinite while the admittance vanishes. In the form of (7.19) and (7.20), the equivalent $\mathbf{Y}$- and $\mathbf{Z}$-matrices have been obtained and analyzed by Lloyd (1967) as an extension of the work of Lewis (1961), who derived the admittance and impedance functions for a vibrator with one pair of electrodes. For this latter configuration, matrices $\mathbf{C}_s$ and $\mathbf{C}_n$ reduce to the ordinary static C_s and *motional* C_n capacitances between the driving electrodes.

By introducing a new matrix of *shunt* capacitances

$$\mathbf{C}_0 = \mathbf{C}_s - \sum_{n=1}^{\infty} \mathbf{C}_n \tag{7.21}$$

the admittance matrix (7.19) can be recast as

$$\mathbf{Y} = j\omega\left\{\mathbf{C}_0 + \sum_{n=1}^{\infty} \frac{\omega_{Rn}^2 \mathbf{C}_n}{\omega_{Rn}^2 - \omega^2}\right\}. \tag{7.22}$$

This allows its elements y_{pq} to be represented as an electrical network (second Foster form) as shown in Fig 1.5.

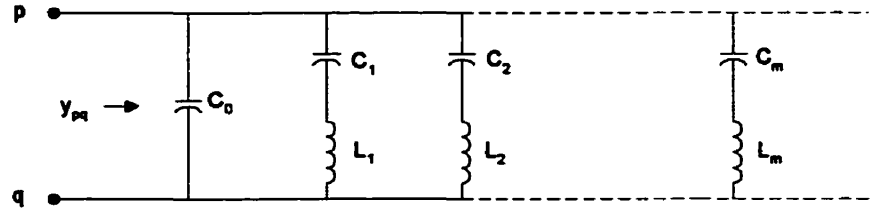

Fig 1.5 Network realization of the equivalent admittance function $\mathbf{Y} = (y_{pq})_{p,q=1,\ldots,L}$ in the form of the second Foster scheme. Here $C_0 = (C_0)_{pq}$, $C_m = (C_n)_{pq}$, $L_m = 1/(\omega_{Rm}^2 C_m)$.

Similarly, an element of the impedance matrix $\mathbf{Z}$ (7.20) — z_{pq} — can be realized through the first Foster form, with parameters defined in Fig. 1.6.

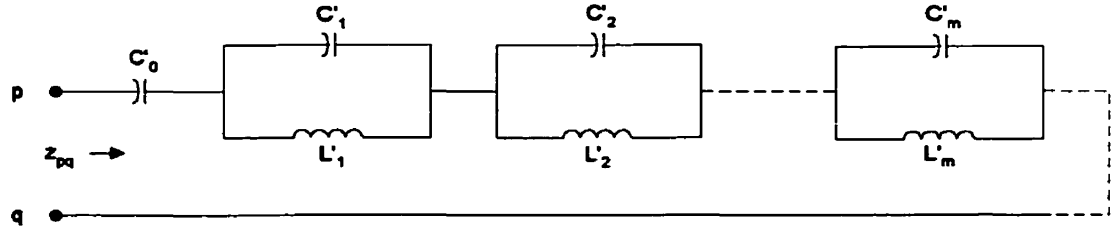

Fig 1.6 Network realization of the equivalent impedance function $\mathbf{Z} = (z_{pq})_{p,q=1,\ldots,L}$ in the form of the first Foster scheme. Here $C'_0 = 1/(C_s)_{pq}$, $C'_m = 1/(F_n)_{pq}$, $L'_m = 1/(\omega_{Am}^2 C'_m)$.

2

Waves and vibrations with open electric boundaries

1. Introduction

This chapter presents a short survey of past methods, or rather attempts, to model finite piezoelectric regions embedded in an infinitely extending free space. It shows how the external electric field has been taken into account for both wave propagation and resonance — the two basic phenomena that underlie the operation of all piezoelectric devices. The review is drawn to demonstrate that there is a demand for the solution of the piezoelectric problem referred to, by analogy with electromagnetics, as electrically unbounded.

Wave propagation is typically associated with relatively simple geometrical configurations such as a piezoelectric half-space or an infinite plate. Solution can often be sought as a superposition of uniform plane waves with amplitudes determined to satisfy mechanical and electrical boundary conditions. However, this approach is rarely suitable for the analysis of piezoelectric resonators. The modeling of external electric fields also becomes increasingly more complicated as the number of finite lateral dimensions grows. Except for a few special classes of problems that permit one-dimensional approximations of isolated modes (thickness and longitudinal), no serious attempt to take into consideration the leakage of the electric flux into the outer space has been reported in the literature. The most effective two-dimensional approximation technique — the Mindlin's power series expansion in the plate thickness — is not, by its very nature, compatible with the large sizes required by the 'openness' of the electric boundaries.

Because practical vibrator geometries are irreducibly three-dimensional, they can only be attacked by various numerical techniques, among which the *finite*

element method is by far the most popular. It has been widely used in piezoelectric analysis for its capacity to model anisotropic materials and arbitrary shapes. Although 'mechanically' open piezoelectric problems, such as the radiation from sonar transducers into an acoustic medium of infinite extent, have been a common application of the finite elements (Smith, Hunt, and Barach, 1973), there is no indication in the literature that this approach has been used in combination with any model of the exterior electric field. Special numerical techniques required to model the infinite exterior electric field distribution can be imported from engineering electromagnetics. A critical review of available methods is given in this chapter to provide ground for the choice of the method of *ballooning*, which has been retained for the use with the finite element model of the piezoelectric region.

2. Wave propagation

Plane waves propagating in an unbounded medium (Appendix 1) are of great importance because they are used as building blocks to construct solutions in bounded regions (Auld, 1981). In the method referred to as *superposition of partial waves*, all possible plane wave solutions having a common wave vector component along a given propagation direction — partial waves — are superimposed with amplitudes chosen to satisfy mechanical and electrical boundary conditions. Such a superposition of plane waves simultaneously satisfies the wave equations and the boundary conditions, i.e. is a correct solution of the boundary-value problem. The partial wave method, is suitable for analyzing planar structures such as a piezoelectric substrate, an infinite plate, or a layer over a substrate (Auld, 1990b). Because the problem of wave propagation is beyond the scope of this thesis, no attempts are made to survey in detail the influence of electrical boundary conditions encountered in practical configurations.

2.1 *Surface acoustic waves*

The surface acoustic wave (SAW) is defined as a wave propagating parallel to the surface of a solid (Fig. 2.1) with the amplitude of all the associated displacements and potential rapidly decreasing into the depth of the substrate ($x_2 \rightarrow \infty$).

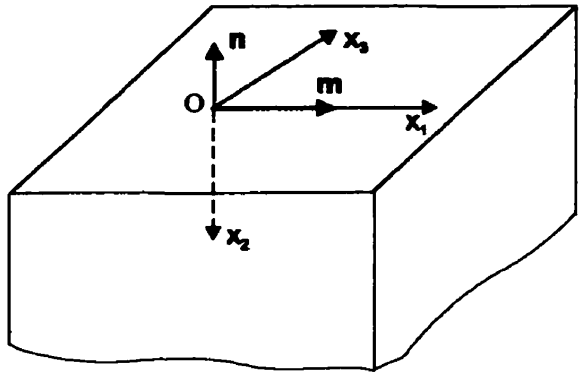

Fig 2.1 Coordinate system for the surface acoustic wave propagating in the direction **m**.

Because three mechanical and one electrical boundary conditions must be specified on the boundary of a piezoelectric substrate, the fields in the surface wave are

sought as a linear combination of four straight-crested (i.e. no dependence on the x_3 coordinate) waves propagating in the direction $\mathbf{m} = (1,\ m_2^{(r)},\ 0)^{\mathrm{T}}$:

$$\begin{pmatrix} \mathbf{u} \\ \varphi \end{pmatrix} = \sum_{r=1}^{4} \mathrm{A}_r \begin{pmatrix} {}^{\circ}\mathbf{u}^{(r)} \\ \varphi_{\circ}^{(r)} \end{pmatrix} e^{-i\beta_r x_2} e^{i\omega(t-\frac{x_1}{\mathrm{V}})}, \tag{2.1}$$

where $\beta_r = (\omega/\mathrm{V})m_2^{(r)}$ is the component of the wave vector in the depth direction. The electric potential above the substrate is taken as

$$\varphi = \varphi_s e^{\frac{\omega}{\mathrm{V}}x_2} e^{i\omega(t-\frac{x_1}{\mathrm{V}})},\quad x_2 < 0 \tag{2.2}$$

so that it satisfies Laplace's equation, vanishes as $x_2 \to -\infty$, and is equal to $\varphi_s = \varphi(x_1, 0, x_3)$ on the boundary $x_2 = 0$. The weighting coefficients A_r in (2.1), or amplitudes of the partial waves, are determined from the stress-free boundary condition and the condition of continuity of either electric potential or normal component of the electric flux density on the boundary. Substituting solution (2.1) into the boundary conditions gives a system of four homogeneous equations, whose determinant Δ^{SAW} must be zero in order for nontrivial solutions to exist. For instance, if the continuity of $\mathbf{D}$ is imposed, the elements of this *boundary-condition matrix* will be

$$\begin{aligned} \Delta_{ir}^{SAW} &= \left\{\mathbf{n}\cdot\mathbf{c}^{\mathrm{E}} : \left(\mathbf{m}^{(r)}{}^{\circ}\mathbf{u}^{(r)}\right) + \mathbf{m}^{(r)}\cdot\mathbf{e}\cdot\mathbf{n}\,\varphi_{\circ}^{(r)}\right\}_i,\quad i = 1,2,3 \\ \Delta_{4r}^{SAW} &= \mathbf{n}\cdot\mathbf{e} : \left(\mathbf{m}^{(r)}{}^{\circ}\mathbf{u}^{(r)}\right) - \mathbf{n}\cdot\left(\boldsymbol{\epsilon}^{S} - i\epsilon_{\circ}\mathbf{I}\right)\cdot\mathbf{m}^{(r)}\varphi_{\circ}^{(r)}, \end{aligned} \tag{2.3}$$

where $\mathbf{n} = (0, -1, 0)^{\mathrm{T}}$ is a unit vector normal to the surface. The component $m_2^{(r)}$ of the propagation vector $\mathbf{m}^{(r)}$ is determined from the full piezoelectric Christoffel equation[1] that can be regarded as an eighth-order algebraic equation with real coefficients in $m_2^{(r)}$; the phase velocity V enters this equation as a parameter. To insure that the displacement vanishes as $x_2 \to -\infty$, only four roots $m_2^{(r)}$ with negative imaginary parts and the associated eigenvectors $\left({}^{\circ}\mathbf{u}^{(r)}, \varphi_{\circ}^{(r)}\right)^{\mathrm{T}}$ are retained.

---

[1] The secular equation associated with the system in the form of Eq. (1.14) from Appendix 1 is not suitable for this purpose because the elimination of electric potential as an explicit variable gives rise to the stiffened constants defined by Eq. (1.16) of the same appendix. As demonstrated by Farnell (1970), stiffened constants are not valid for the analysis of SAW since the complex component m_2 of $\mathbf{m}$ is initially undefined and takes four different values.

Because it is rarely possible to analytically solve the Christoffel equation and express $m_2^{(r)}$, $^{\circ}\mathbf{u}^{(r)}$, and $\varphi_0^{(r)}$ as functions of V, the phase velocity is typically found from an automatic procedure that changes its value until the corresponding $m_2^{(r)}$, $^{\circ}\mathbf{u}^{(r)}$, and $\varphi_0^{(r)}$ make $\triangle^{SAW}$ equal zero. In general, the resulting phase velocity corresponds to a complex piezoelectric Rayleigh wave. However, when the sagittal plane (plane x_1–x_2 in Fig. 2.1) is perpendicular to a six-fold crystallographic axis, two velocities are acceptable. The first one is associated with a non-piezoelectric Rayleigh wave, while the second corresponds to a piezoelectric Bleustein-Gulyaev wave, created by two partial waves and polarized perpendicular to the sagittal plane. For the latter case both the Christoffel equation and Eq. (2.3) simplify considerably, so that analytical solution can be obtained (Dieulesaint and Royer, 1974). For example, the velocity of the x_3-polarized Blustein-Gulyaev wave propagating on an unplated surface is given by

$$\mathrm{V}_s^{BG} = \sqrt{\frac{c_{44}^D}{\rho}\left(1 - \frac{k^4}{\left(1+\epsilon_{11}^S/\epsilon_0\right)^2}\right)}, \tag{2.4}$$

with $k^2 = e_{15}^2/\left(\epsilon_{11}^S c_{44}^D\right)$ and $c_{44}^D = c_{44}^E + e_{15}^2/\epsilon_{11}^S$.

As it follows from the solution scheme outlined above, the propagation of SAW can always be viewed as a problem with open electric boundaries. The influence of the electrical boundary conditions is typically characterized by the coupling coefficient K_s for SAW

$$K_s^2 = \frac{2(\mathrm{V}_s - \mathrm{V}_o)}{\mathrm{V}_s}, \tag{2.5}$$

where V_s and V_o are the velocities of the waves on the free and fully metallized surfaces respectively; and the surface impedance Z_s defined by

$$\frac{\varphi_s}{\mathbf{n}\cdot\mathbf{D}_s} = i\frac{\mathrm{V}^2}{\omega}Z_s. \tag{2.6}$$

For some simple electrical boundary configurations analytical expressions for Z_s can be easily derived from (2.6). For example, if the space above the substrate is free or if an infinitesimally thin perfect conductor is placed at the distance h from the substrate, the impedance simplifies to $Z_s = i/(\mathrm{V}\epsilon_o)$, and $Z_s = (i/\epsilon_o)\tanh\left(\frac{\omega}{\mathrm{V}}h\right)$

respectively. An alternative definition of the coupling coefficient is due to Ingebrigtsen (1969):

$$K_\infty^2 = \frac{2(V_\infty - V_o)}{V_\infty}, \tag{2.7}$$

where the wave velocity V_∞ corresponds to the infinite surface impedance $Z_s = \infty$. According to (2.6), the condition of an infinite Z_s is met when the electric flux above the piezoelectric substrate is zero, i.e. when the fringing field is neglected. This means that K_∞ is associated with an electrically 'closed' model of SAW propagation, and, therefore, the ratio

$$\frac{K_\infty^2 - K_s^2}{K_\infty^2} = \frac{1}{1 + \epsilon_a/\epsilon_o} \tag{2.8}$$

can be regarded as a measure of the influence of the external portion of the electric field on SAW propagation, where $\epsilon_a = \sqrt{\epsilon_{11}\epsilon_{22} - \epsilon_{12}^2}$ is the effective permittivity of the anisotropic substrate in the given coordinate system (Morgan, 1985).

2.2 *Guided waves*

The partial wave approach can be extended directly, i.e. without increasing algebraic complexity, to the analysis of isotropic infinite plates. For the piezoelectric plates, however, this is possible only for cuts with special symmetries that allows the displacement to be separated into a shear horizontal (SH) wave and Lamb waves (the combination of shear vertical (SV) and longitudinal (P) waves), supported by isotropic plates (Auld, 1990b). These two families of modes are reflected at the two stress-free boundaries $x_2 = \pm h$ (Fig. 2.2) into waves of the same type, thus allowing the solution to be expressed in terms of a finite number of such waves.

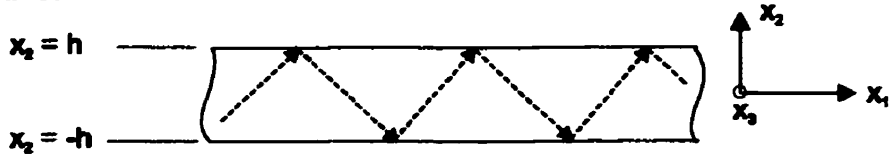

Fig 2.2 Partial wave reflection pattern in an infinite plate of thickness $2h$.

In this case, solution is constructed from partial waves (2.1) propagating within the plate with vectors $\mathbf{k} = (\alpha, \pm\beta_r, 0)^{\mathrm{T}}$, symmetric with respect to the medium plane. To satisfy the electrically open boundary conditions at $x_2 = \pm h$, the electric potential is taken outside the plate as

$$\varphi = \varphi_s e^{-\alpha|x_2-h|} e^{-i\alpha x_1}, \quad |x_2| \geq h, \tag{2.9}$$

thus obeying Laplace's equation and evanescent in the direction x_2.

The guided wave solution can be obtained from the procedure similar to that employed for SAW. However, the imposition of boundary conditions at the two boundaries of the plate fixes the *dispersion relation* between α and the frequency ω, which is determined by solving the Christoffel equation for wave numbers β_r simultaneously with the boundary-condition equation ($\Delta^G = 0$). Examples of such solutions in the plane with a *6mm* symmetry can be found in Auld (1990b) and Ikeda (1996). Dispersion relations in the form of transcendental equations are given for the electrical boundary conditions commonly encountered in planar problems (e.g. unplated and plated plate). In the high-frequency limit the guided wave velocity tends to that of the surface wave propagating in the same direction.

3 Piezoelectric vibrations

In general, the problem of piezoelectric vibrations of a three-dimensional body cannot be solved in terms of a finite number of partial waves: an arbitrary incident plane wave, when reflected back at the stress-free piezoelectric boundary, generates waves of other types that must be included into the analysis. Therefore, for a truly three-dimensional configuration it is always more practical to apply numerical methods, reviewed in a separate section below, rather than attempting to approximate the solution by an infinite series of partial waves. Nevertheless, the partial wave approach, or a mode-matching method, as it is often termed in resonator problems, can still be applied to the analysis of some simple geometries such as an infinite plate or a long narrow strip. The solution can then be represented as a superposition of standing waves which are formed from positive- and negative-traveling acoustic waves propagating in the thickness and length directions respectively. Explicit frequency equations are available for the resulting one-dimensional models of thickness and longitudinal vibrations, thus facilitating the estimation of the leakage field effect on the characteristic frequencies. As for the finite piezoelectric plates, Mindlin's two-dimensional approximation of combined modes remained the most powerful tool for modeling piezoelectric vibrations prior to using numerical methods. Although no applications of this theory to electrically open problems are known, this technique, being very important, is briefly outlined at the end of this section.

3.1 *Simple modes*

Piezoelectric resonators are typically fabricated in the form of rectangular or circular plates, strips and bars. As mentioned above, even resonators of such elementary shapes possess an infinite number of vibrations, many of which belong to the families of modes characterized by simple displacements shown in Table 2.1. Simple modes can often be realized if one of the dimension of the resonator differs significantly from the others, thus defining an isolated vibration which can be described by one-dimensional models. The piezoelectric boundary-value problem is then reduced to a system of ordinary differential equations with sets of mechanical and electrical boundary conditions at the two extremities of the characteristic size.

Because most of the resonators are designed to operate on one particular mode[2] and suppress all the other, unwanted, vibrations, such models have proved very useful in predicting the resonance frequency (Meeker, 1985). They considerably simplify the anisotropy analysis of the coupling and temperature coefficients of frequency for new piezoelectric materials (Détaint and Lançon, 1976; Fujiwara *et al.*, 1985), and are invaluable when material coefficients are determined from the resonance frequency measurements (IEEE, 1987).

Table 2.1 Principal types of vibrational modes

Mode	Shape	Frequency range
Flexure	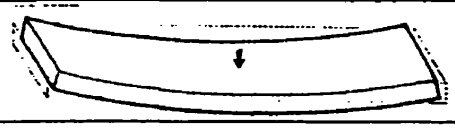	10–100 kHz
Torsional	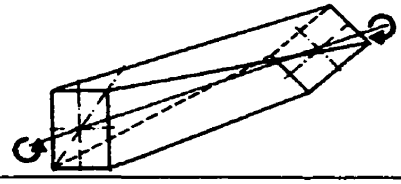	50–500kHz
Longitudinal	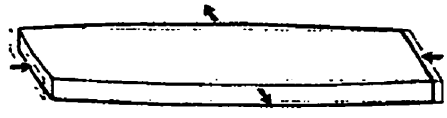	0.7–600 kHz
Contour (face-extensional + face-shear)	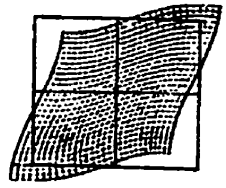	150–600 kHz
Thickness-shear	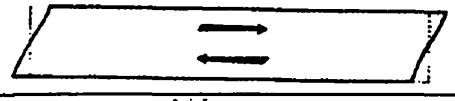	0.5–1600 MHz
Thickness-extentional	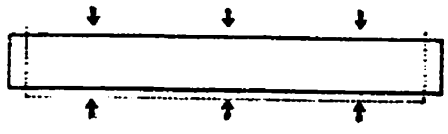	1 MHz – 6 GHz

[2] In some case the resonance is realized by 'coupling' two simple modes as it was done for the GT-cut quartz resonator to achieve a very high frequency stability over a wide temperature range.

The problem of electrical flux leakage is of different significance for the basic classes of resonance modes. As illustrated in Fig. 2.3 (a), in the case of contour vibrations, the two major surfaces are typically fully covered by electrodes, which minimize the fringing field. For other types of vibration, the size of the driving electrode is an important factor in the optimization of resonator parameters. For instance, for the thickness-shear vibrations of the strip-type resonator, shown in Fig. 2.3 (b), the electrode length is chosen to suppress the anharmonic overtones (Milsom *et al.*, 1983), and is often less than the half of the plate length. Moreover, the tendency is that the stronger the piezoelectric coupling, the shorter the electrode, thus leaving a considerable part of resonator major faces unplated. Partial electrodes are also typical for longitudinal and flexural vibrations. Hermann (1975) attributed the discrepancy of approximately 7% between the experimental and theoretical values of static capacitance to, in part, the neglect of the external electrostatic field in his model of flexural and length-extensional vibrations. The flux leakage through the plate surfaces is particularly serious when longitudinal or thickness modes are excited by a lateral electric field, as indicated in Fig. 2.3 (c).

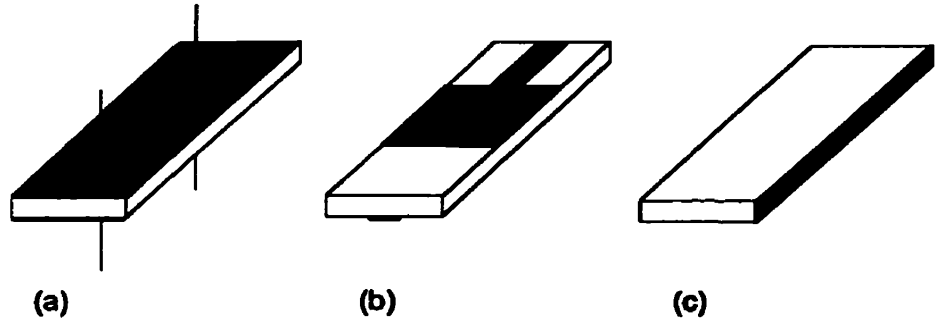

Fig 2.3 Typical electrode patterns: (a) contour vibrations; thickness-shear vibrations with perpendicular (b) and lateral (c) field excitations.

In principle, one-dimensional models of piezoelectric vibrations cannot take into account the influence of the electrode size, except maybe for a few configurations when, as for the longitudinal mode, the electrode is extended in the direction of the plate characteristic size (Zelenka, 1986). However, the two extreme cases of fully metallized and totally free plates, encountered in the models of surface and guided waves propagation, can still be treated within the scope of

one-dimensional approximations. To give an idea of how the electric field leakage may affect the frequency and the electromechanical parameters of the resonator, two types of vibrations — the longitudinal and the thickness — are considered in more detail.

A. Thickness vibration

The simple thickness-mode vibrations of a plate are characterized by the displacements that are functions of the plate thickness coordinate x_2 alone (Fig. 2.2); the governing wave equations[3] of the plate are therefore one-dimensional:

$$\left.\begin{aligned} c^E_{2jk2}\frac{d^2u_k}{dx_2^2} + e_{22j}\frac{d^2\varphi}{dx_2^2} - \rho\omega^2 u_j = 0, \\ e_{22k}\frac{d^2u_k}{dx_2^2} - \epsilon^S_{22}\frac{d^2\varphi}{dx_2^2} = 0. \end{aligned}\right\} \tag{3.1}$$

The general solution can be written as a linear combination of three positive- and negative traveling waves $\mathbf{k} = (0, \pm\beta_r, 0)^T$ propagating in the thickness direction of the plate with phase velocities V_r and amplitudes $^\circ\mathbf{u}^{(r)}$, or, as is more customary in resonator theory, in the form of a superposition of antisymmetric and symmetric solutions:

$$\begin{aligned} \mathbf{u} &= \sum_{r=1}^{3}\left(\mathbf{A}_r{}^\circ\mathbf{u}^{(r)}e^{i\beta_r x_2} + \mathbf{B}_r{}^\circ\mathbf{u}^{(r)}e^{-i\beta_r x_2}\right), \\ &= \sum_{r=1}^{3}\left(\mathbf{A}'_r{}^\circ\mathbf{u}^{(r)}\sin\beta_r x_2 + \mathbf{B}'_r{}^\circ\mathbf{u}^{(r)}\cos\beta_r x_2\right) \end{aligned} \tag{3.2}$$

with coefficients $\mathbf{A}'_r$, $\mathbf{B}'_r$ determined from the six stress-free boundary conditions $T_{2j} = 0$, $j = 1,2,3$ at $x_2 = \pm h$. The substitution of (3.2) into (3.1) yields the dispersion curves, which, in this case, are represented simply by three straight lines (nondispersive waves). To satisfy the two continuity conditions for D_2 and φ at $x_2 = \pm h$ within the scope of the one-dimensional model, it is not sufficient to take φ as a superposition of partial waves (Eq. (1.12), Appendix 1): a static

---

[3] In the following, the harmonic term $e^{i\omega t}$ is omitted from all variables and summation is assumed for repeated indices.

solution is also required. The electric potential is therefore obtained by integrating the second equation in (3.1):

$$\varphi = \frac{e_{22k}}{\epsilon_{22}^S} u_k + \mathrm{A}_i x_2 + \mathrm{B}_i, \tag{3.3}$$

with coefficient A_i, B_i determined from the electrical boundary conditions.

The frequency equations for the piezoelectric thickness vibrations of an infinite plate with electrodes coated on both surfaces was derived by Tiersten (1969). In his formulation, the resonance frequencies ($\varphi|_{x_2=\pm h} = 0$) of the three coupled thickness modes are determined from the transcendental equation

$$\left| \left(\bar{c}_{2jk2}\, \beta_r x_2 \cos \beta_r h - \frac{e_{22j} e_{22k}}{\epsilon_{22}^S} \sin \beta_r h \right) {}^{\circ}u_k^{(r)} \right| = 0, \tag{3.4}$$

while their antiresonance frequencies ($D_2|_{x_2=\pm h} = 0$) are obtained from

$$\cos \beta_r h = 0, \tag{3.5}$$

where $\beta_r = \omega\sqrt{\rho/\bar{c}_r}$, and $\bar{c}_r$ and ${}^{\circ}\mathbf{u}^{(r)}$ are respectively the rth eigenvalue and eigenvector of the Christoffel system with 'stiffened' elastic constants $\bar{c}_{2jk2} = c_{2jk2}^E + e_{22j}e_{22k}/\epsilon_{22}^S$. An alternative formulation reported by Yamada and Niizeki (1971), who derived the frequency equations in a slightly simpler form, compared to (3.4), from the electric admittance of the plate. Additionally, an admittance expression for the configuration with an air gap between the electrodes and the plate surface was also given. In the same paper, Yamada and Niizeki considered the case of a lateral field excitation, and obtained the corresponding frequency equations that were found to be reciprocal to the perpendicular field case. The résumé of characteristic equations for the two field orientations is given in Table 2.2.

The theory of thickness vibrations, even in its simplest one-dimensional version is very important for practical applications since most of the mass-produced crystal resonators operate on a thickness-shear mode. Although well documented, and being, along with the longitudinal vibrations, part of the IEEE Standard on Piezoelectricity (1987), the present models of thickness vibrations do not take into account the electric flux leakage. However, the imposition of open electric boundaries causes no difficulty in the one-dimensional case. Tiersten's approach outlined above was extended in this thesis to an uncoated piezoelectric plate by

setting D_2[4] equal to $\epsilon_o E_o$ at $x_2 = \pm h$, where E_o is the constant electrostatic field generated in the outer space $|x_2| > h$ by the thickness vibrations of the free piezoelectric plate. The constant A_i in (3.3) is determined from the continuity condition of electric potential $\varphi(\pm h) = \varphi_o(\pm h)$, where $\varphi_o(x_2) = \mathrm{A}_o x_2 + \mathrm{B}_o$ is a solution of the one-dimensional Laplace's equation outside the plate. Because there is no way to make this potential distribution evanescent, it is important to stress that the whole approximation is valid only when the thickness of the plate is small compared with other dimensions, i.e. when the plate is assumed infinite.

Table 2.2 Frequency equations for thickness vibrations

	Perpendicular (**E** ∥ **k**)	Lateral (**E** ⊥ **k**)
Electrode configuration	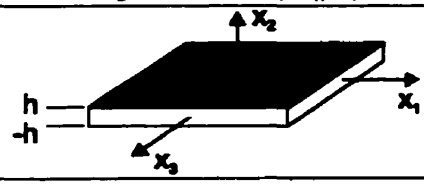	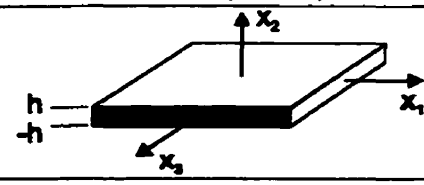
Dispersion relation	$\beta_r = \omega\sqrt{\dfrac{\rho}{\bar{c}_r}}$	
Resonance	$1 - \sum_{r=1}^{3} k_r^2 \dfrac{\tan\beta_r h}{\beta_r h} = 0$	$\cos\beta_r h = 0$
Antiresonance	$\cos\beta_r h = 0$	$1 + \sum_{r=1}^{3} k_r^2 \dfrac{\tan\beta_r h}{\beta_r h} = 0$
Coupling coefficient	$k_r^2 = \dfrac{\sum_{j=1}^{3}\left(e_{22j}\circ u_j^{(r)}\right)^2}{\bar{c}_r\,\epsilon_{22}^S}$	$k_r^2 = \dfrac{\sum_{j=1}^{3}\left(e_{32j}^*\circ u_j^{(r)}\right)^2}{\bar{c}_r\,\epsilon_{33}^*}$, with $e_{32j}^* = e_{32j} - \dfrac{e_{22j}\epsilon_{23}^S}{\epsilon_{22}^S}$, and $\epsilon_{33}^* = \epsilon_{33}^S - \dfrac{(\epsilon_{23}^S)^2}{\epsilon_{22}^S}$

The derivation of the frequency equation for an uncoated piezoelectric plate follows closely that of Tiersten for a totally metallized plate. Omitting details, the

---

[4] In order to satisfy the Gauss equation $\nabla \cdot \mathbf{D} = 0$, the electric flux component D_2 in one-dimensional piezoelectric problems can only be constant and uniform.

resulting equation that gives the three characteristic frequencies ω_s^r of the one-dimensional thickness vibrations with open electric boundaries can be written as

$$\left|\left(\bar{c}_{2jk2}\,\beta_r h\cos\beta_r h - \tau\frac{e_{22j}e_{22k}}{\epsilon_{22}^S}\sin\beta_r h\right)\circ u_k^{(r)}\right| = 0, \tag{3.6}$$

with

$$\tau = \frac{1}{1+\epsilon_{22}^S/\epsilon_o}. \tag{3.7}$$

Note that both the resonance and antiresonance frequency equations for a coated plate can be obtained as special cases of Eq. (3.6) by setting $\epsilon_o \to \infty$ (electrodes short-circuited, $E_2 = 0$) and $\epsilon_o = 0$ (electrodes open-circuited, $D_2 = 0$) respectively. Since $0 \le \tau \le 1$, the resonant frequency of a bare plate is $\omega_o \le \omega_s \le \omega_\infty$, where ω_o and ω_∞ denote, by analogy with SAW notation, the solutions of Eqs. (3.4) and (3.5) respectively, i.e. the resonance and antiresonance frequencies of a completely plated crystal.

For the purpose of analysis, it is more convenient to recast Eq. (3.6) into

$$1 - \sum_{r=1}^{3}\tau k_r^2\frac{\tan\beta_r h}{\beta_r h} = 0, \tag{3.8}$$

which makes it consistent with those of Table 2.2. For many practical crystal orientations, shown in Table 2.3, only one of the three thickness modes is piezoelectrically active ($k_r \neq 0$) or predominant. In this case, Eq. (3.8) simplifies to

$$\tan\beta h = \frac{\beta h}{\tau k^2}. \tag{3.9}$$

For a small piezoelectric coupling coefficient, the fundamental solution of Eq. (3.9) is well approximated by

$$\beta h = \frac{\pi}{2}\left(1 - \frac{4}{\pi^2}\tau k^2\right), \tag{3.10}$$

(Kantor, 1977) or, using the solution of Eq. (3.5) $\omega_\infty = \pi/(2h)\mathrm{V}$,

$$\omega_s = \left(1 - \frac{4}{\pi^2}\tau k^2\right)\omega_\infty. \tag{3.11}$$

Because the resonance frequency of a wholly coated plate ω_o is given by a similar expression $\omega_o = (1 - (4/\pi^2)k^2)\omega_\infty$ but without τ, the relative frequency shift due to the open electric boundaries can be approximated for materials with small piezoelectric coupling k^2 by

$$\frac{\omega_\infty - \omega_s}{\omega_\infty - \omega_o} = \tau. \tag{3.12}$$

Under the same assumptions, the relative decrease of the effective coupling coefficient is given by the expression

$$\frac{k_\infty^2 - k_s^2}{k_\infty^2} = \tau, \tag{3.13}$$

identical to Eq. (2.8) for SAW. As seen from Table 2.3, the shift for some typical crystal orientations ranges from 2 to 18 percent, and might be higher for materials with lower permittivity.

Table 2.3 Values of τ for common crystal cuts.

Material	Cut	τ
Quartz	AT (35.25°-rotated Y)	0.18
$GaPO_4$	AT (33.02°-rotated Y)	0.14
$Li_2B_4O_7$	51°-rotated Y	0.10
$LiTaO_3$	8.5°-rotated X	0.023
$LiNbO_3$	163°-rotated Y	0.023

Having a good estimate of ω_s is important for the design of resonator operating on *trapped-energy modes* (Onoe *et al.*, 1965; Shockley *et al.*, 1967). In such resonators the electrode size is chosen so that the energy distribution associated with the thickness vibration is concentrated almost entirely in the electroded region and rapidly decays in the uncoated portion of the plate, thus giving improved resonance characteristics. This phenomenon can be explained in terms of a guided propagation of thickness vibrations along the x_1- or x_3-axis of the plate (Fig. 2.2), characterized by a cut-off frequency below which their

amplitudes decrease exponentially with distance. Due to the mass-loading and different electrical boundary conditions, the coated and uncoated portions of the plate have different cut-off frequencies, equal respectively to ω_o and ω_s defined above. When the resonance frequency of a partially plated crystal ω is below ω_o or above ω_s, the thickness mode cannot propagate in either region; however, if ω falls in the range between ω_o and ω_s, the thickness mode propagates and forms standing waves in the electroded portion of the plate, but rapidly decays in the unelectroded part.

The resonance of the 'trapped' wave is determined not only by the relative decrease in frequency, or the plate back, defined by

$$\Delta_s = \frac{\omega_s - \omega_o}{\omega_s} \tag{3.14}$$

but also by the lateral dimension of the electroded region $2l_e$. Therefore, a whole series of resonances can occur between ω_o and ω_s. The optimization of a trapped-energy resonator consists in eliminating all the anharmonic resonances, except for the lowest, or fundamental, thickness mode. This condition is met when the electrode length satisfies the following condition

$$\left(\frac{l_e}{h}\right)_s \leq \frac{2}{\lambda\sqrt{\Delta_s}}, \tag{3.15}$$

where λ is a theoretical constant related to the wave number in the lateral direction. The calculation of the plate back Δ in (3.15) is typically based on frequency ω_∞, thus leading to a slightly lower estimate of $(l_e/h)_\infty = 2/(\lambda\sqrt{\Delta_\infty})$, where $\Delta_\infty = (\omega_\infty - \omega_o)/\omega_\infty$ is greater than ω_s. Ideally, this is ω_s that must be used as a cut-off frequency for the unplated region since it gives a more realistic upper bound for ω. If ω_s is not available, $(l_e/h)_\infty$ can be corrected using (3.12) to obtain $(l_e/h)_s$ as follows

$$\left(\frac{l_e}{h}\right)_s = \sqrt{1-\tau}\left(\frac{l_e}{h}\right)_\infty. \tag{3.16}$$

Finally, the most important electric flux leakage is expected in the case of thickness vibrations excited by a lateral electric field. Mindlin (1973) and later Lee (1988) studied the electromagnetic radiation from the face of an AT-cut quartz plate excited by face-shear traction and lateral electric field respectively. Because

only the wave solution was of interest, the authors did not consider the quasi-static electric field in the surrounding vacuum. By solving the one-dimensional equations of piezoelectromagnetism, they obtained an anticipated correction of the order of 10^{-5} to the wave numbers, thus measuring the effect of the quasi-static approximation on the thickness-shear mode. Yamada and Niizeki (1971) also neglected the electrostatic field outside the plate, when considering the lateral excitation. They assumed the applied electric field to be strictly parallel to the major faces of the plate, which represents a rough approximation for such an electrode configuration unless high permittivity crystals are used.

As earlier for the Tiersten's solution, the formulation by Yamada and Niizeki was modified here to include the external electrostatic field. In this case, the frequency equation for the piezoelectric resonance of the structure shown in Table 2.2 (column $\mathbf{E} \perp \mathbf{k}$), was found to be identical with Eq. (3.6). This result is consistent with the one-dimensional model of thickness vibrations since the lateral component E_3 of the electric field is considered constant across the plate (i.e. independent of x_3). Particularly, if E_3 is set to zero (resonance), the difference between the thickness vibrations excited by a lateral field and those of a free piezoelectric plate disappears. Because, under the assumption of a zero leakage field, the resonance frequency corresponding to the lateral electrode configuration is obtained from the same Eq. (3.5) as the antiresonance frequency of the totally coated plate, the resonance frequency shift due to the open electric boundaries is equal to $(\omega_\infty - \omega_s)$. To obtain the corresponding shift in the antiresonance frequency, the latter can be determined from the derived equation

$$\left| \left(\bar{c}_{2jk2}\, \beta_r h \cos \beta_r h + \left(\frac{\tilde{e}_{32j}\tilde{e}_{32k}}{\tilde{\epsilon}^S_{33}} - \tau \frac{e_{22j}e_{22k}}{\epsilon^S_{22}} \right) \sin \beta_r h \right) {}^{\circ}u_k^{(r)} \right| = 0, \tag{3.17}$$

where the corrected piezoelectric and dielectric constants are

$$\left.\begin{aligned} \tilde{e}_{32j} &= e_{32j} - (1-\tau)\frac{e_{22j}\epsilon^S_{23}}{\epsilon^S_{22}} = e^*_{32j} + \tau \frac{e_{22j}\epsilon^S_{23}}{\epsilon^S_{22}}, \\ \tilde{\epsilon}_{33} &= \epsilon^S_{33} - (1-\tau)\frac{(\epsilon^S_{23})^2}{\epsilon^S_{22}} = \epsilon^*_{33} + \tau \frac{(\epsilon^S_{23})^2}{\epsilon^S_{22}}. \end{aligned}\right\} \tag{3.18}$$

B. Longitudinal vibration

Simple longitudinal vibrations are realized when one of the plate dimensions is much larger that the others. In this case, the equation of motion becomes one-dimensional (x_1), and free-edge conditions for the only component of stress $T_{11}|_{\pm l} = 0$ can be satisfied by two partial waves $\mathbf{k} = (\pm\alpha, 0, 0)^{\mathrm{T}}$, traveling in the direction of the plate length ($2l$):

$$u_1 = \mathrm{A}\sin\alpha x_1 + \mathrm{B}\cos\alpha x_1. \tag{3.19}$$

The frequency equations (Mason, 1964) derived for two basic electrode configurations are summarized in Table 2.4.

Table 2.4 Frequency equations for longitudinal vibrations

	$\mathbf{E} \perp \mathbf{k}$	$\mathbf{E} \parallel \mathbf{k}$
Electrode configuration	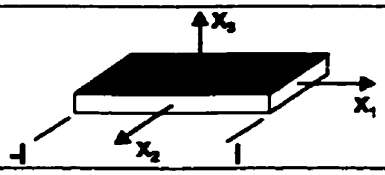	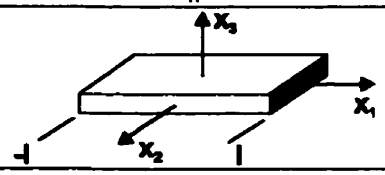
Dispersion relation	$\alpha = \omega\sqrt{\rho s_{11}^E}$	$\alpha = \omega\sqrt{\rho s_{11}^D}$
Resonance	$\cos\alpha l = 0$	$1 - \tilde{k}_{11}^2 \dfrac{\tan\alpha l}{\alpha l} = 0$
Antiresonance	$1 + \tilde{k}_{31}^2 \dfrac{\tan\alpha l}{\alpha l} = 0$	$\cos\alpha l = 0$
Coupling coefficient	$\tilde{k}_{31}^2 = \dfrac{k_{31}^2}{1 - k_{31}^2}$, with $k_{31}^2 = \dfrac{d_{31}^2}{\epsilon_{33}^T s_{11}^E}$	$\tilde{k}_{11}^2 = \dfrac{k_{11}^2}{1 + k_{11}^2}$, with $k_{11}^2 = \dfrac{g_{11}^2}{\beta_{11}^T s_{11}^D}$

Note: Material coefficients involved in the above equations are defined by the following systems of constitutive relations

$$\begin{cases} S_{11} = s_{11}^E T_{11} + d_{31} E_3 \\ D_3 = d_{31} T_{11} + \epsilon_{33}^T E_3 \end{cases}, \qquad \begin{cases} S_{11} = s_{11}^D T_{11} + g_{11} D_1 \\ E_1 = -g_{11} T_{11} + \beta_{11}^T D_1 \end{cases}.$$

They replace Eqs. (2.21)–(2.22) of Chapter 1 because for the given boundary conditions it is more convenient to use (T, E) and (T,D) instead of (S,E) as sets of independent variables.

It is more complicated to impose open electric boundary conditions in this model since the electric flux associated with longitudinal vibrations varies in the

direction of the length. Its exterior part is not uniform, as it was in the case of thickness vibrations; rather, it is described by Eq. (2.9), thus adding another dimension to the problem. Ogawa (1969) and, later, Ikeda (1996) treated the effect of flux leakage in terms of a *depolarization factor* N, defined as

$$E = -N\frac{P}{\epsilon_0}, \tag{3.20}$$

where E and P are respectively the scalar components of electric field and polarization in the piezoelectric plate. It takes into account the correction to the depolarization field $-P/\epsilon_0$ (Ikeda, 1996) due to the nonuniformity of P in the plate cross-section. An estimate of the two-dimensional factor N can be obtained if this cross-section is approximated by an ellipse, for which the polarization is uniform and assumed to be equal to P in the thickness-direction of the plate. For instance, if the thickness of the plate is not small, the electric flux will expand in the transverse direction x_2 (see Table 2.4, column $\mathbf{E} \perp \mathbf{k}$). In this situation, ϵ_{33} is replaced by ϵ_{33}/Γ, where the introduced factor Γ is given by

$$\Gamma = 1\Big/\left(1 + \frac{1-N}{N}\frac{\epsilon_0}{\epsilon_{33}}\right). \tag{3.21}$$

The admittance of the plate, from which the frequency equations analogous to those of column $\mathbf{E} \perp \mathbf{k}$ in Table 2.4 are derived, is transformed by means of the depolarizing factor into

$$Y = j\omega C_s'\left(1 + \hat{k}_{31}^2\frac{\tan\alpha l}{\alpha l}\right), \tag{3.22}$$

where $C_s' = C_s/\Gamma$ and $\hat{k}_{31}^2 = \tilde{k}_{31}^2\Gamma$ are the modified static capacitance and coupling coefficient respectively. It is seen from Eq. (3.22) that the resonance frequency is not affected by this modification, while the antiresonance frequency is decreased. The second field orientation ($\mathbf{E} \parallel \mathbf{k}$), for which both characteristic frequencies diminish in the presence of leakage field, can be treated in terms of a dynamic depolarization factor N'. Factor N', in contrast to the previous static depolarizing factor N, takes into account the sinusoidal field variation along the length direction, and is, therefore, function of the wavelength. Obviously, for $\omega \to 0$, $N' \to N$.

3.2 *Mindlin's theory*

Mindlin's approximation technique is best suited to predict resonances in thin piezoelectric plates. It consists in reducing the three-dimensional governing equations of piezoelectricity into two dimensions by, firstly, expanding the mechanical and electrical displacements in Cauchy's power series of the thickness coordinate of the plate x_2

$$\begin{pmatrix} \mathbf{u} \\ \mathbf{D} \end{pmatrix} = \sum_{n=0}^{\infty} x_2^n \begin{pmatrix} \mathbf{u}^{(n)} \\ \mathbf{D}^{(n)} \end{pmatrix}, \tag{3.23}$$

with coefficients $\mathbf{u}^{(n)}$ and $\mathbf{D}^{(n)}$ are independent of x_2. The series (3.23) are truncated after a small number of terms, typically $n = 0, 1, 2$, and then substituted into the three-dimensional equations in differential or variational forms. These equations are integrated with respect to the expansion variable x_2 to produce a series of two-dimensional (x_1, x_3) equations in stress- and electric-potential *resultants*

$$\begin{pmatrix} \mathbf{T}^{(n)} \\ \varphi^{(n)} \end{pmatrix} = \int_{-h}^{h} x_2^n \begin{pmatrix} \mathbf{T} \\ \varphi \end{pmatrix} dx_2, \tag{3.24}$$

with surface driving terms

$$\begin{pmatrix} \mathbf{F}^{(n)} \\ \Phi^{(n)} \end{pmatrix} = \left[x_2^n \begin{pmatrix} \mathbf{n} \cdot \mathbf{T} \\ \varphi \end{pmatrix} \right]_{-h}^{h} \tag{3.25}$$

respectively (Tiersten, 1969)[5]. This operation increases the number of parameters to be determined, but the resulting equations are simpler to solve, and closed form solutions are often available. Finally, to compensate, in part, for the truncation in (3.23), the material constants are premultiplied by some correction factors. The values of the latter are chosen from a comparison of a selected approximate solution, such as a thickness-shear mode, with a reference exact solution of three-dimensional equations (e.g. infinite plate).

---

[5] In contrast, a revised version of the same theory (Mindlin, 1972) starts with the expansion of the mechanical displacements $\mathbf{u}$ and electric potential φ in power series, which yields the two-dimensional equations in resultants $\mathbf{T}^{(n)}$ and $\mathbf{D}^{(n)} = \int_{-h}^{h} x_2^n \mathbf{D}\, dx_2$, and surface charges $\sigma^{(n)} = \left[x_2^{(n)} \mathbf{n} \cdot \mathbf{D} \right]_{-h}^{h}$.

The modes that Mindlin's approximation is able to encompass are determined by the displacement terms $\mathbf{u}^{(n)}$ retained in the expansion (3.23). The theory was initially developed to study the coupled flexure $\left(u_2^{(0)}\right)$ and thickness-shear $\left(u_1^{(1)}\right)$ modes in a rotated Y-cut quartz plate (Mindlin, 1952), as functions of one coordinate x_1 (the width of the plate was neglected) in the direction of the digonal axis of quartz. This approach has been subsequently extended to include resonances of the extension $\left(u_1^{(0)}\right)$, face-shear $\left(u_3^{(0)}\right)$, and thickness-twist $\left(u_3^{(1)}\right)$ modes propagating in both the directions x_1 and x_3 in a rectangular quartz plate (Mindlin and Spencer, 1967), as shown in Fig. 2.4, and, finally complemented by a thickness-stretch $\left(u_2^{(1)}\right)$ mode (Mindlin, 1984).

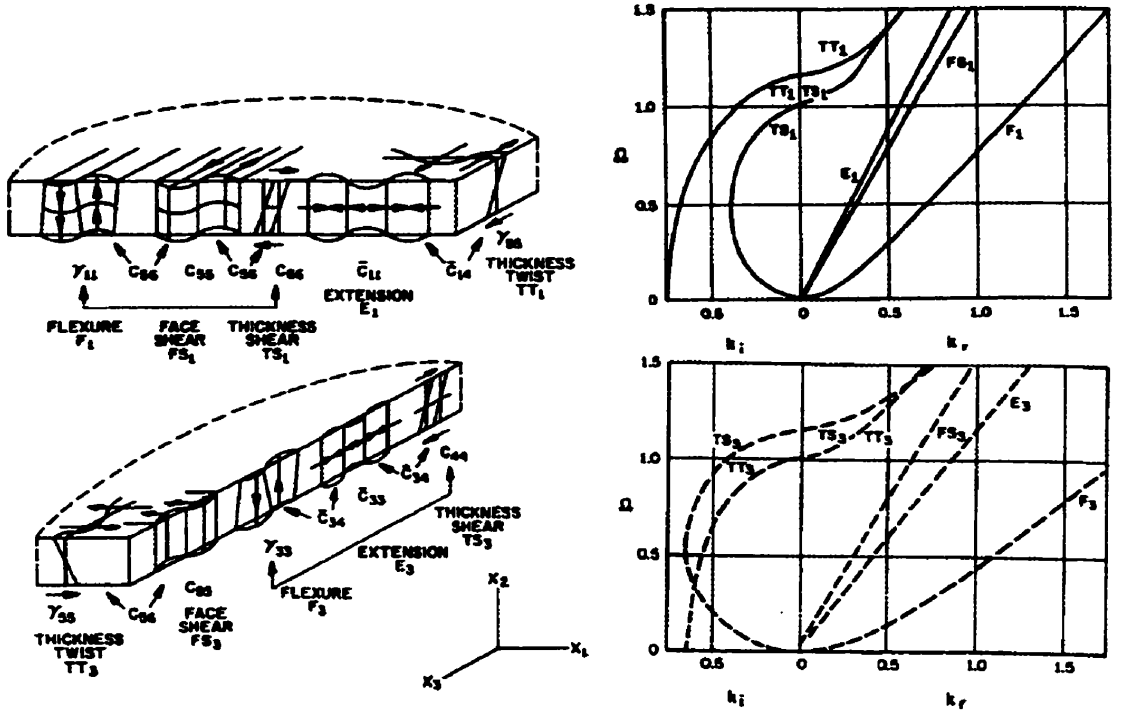

Fig 2.4 Displacements and dispersion curves for the five modes propagating along the x_1 and x_3 directions in an infinite AT-cut quartz plate (Mindlin and Spencer, 1967). Here, Ω is the normalized frequency, and k_r, and k_i are respectively the real and imaginary parts of the wave number.

Although resonance frequencies are well approximated by Mindlin's theory, the actual mode shapes cannot be determined because of the pre-assigned

displacement dependence (3.23) on x_2. Similarly, since the stress **T** and potential φ are not defined at a point but appear in the plate equations only as resultants (3.24), it becomes rather difficult to impose boundary conditions. The latter are now partitioned into the edge and interior boundary conditions, and involve the displacement coefficients, resultants and surface driving terms (3.23)–(3.25) (Tiersten and Mindlin, 1962). The mechanical effects of the electrodes (mass, stiffness, size), can be incorporated in the Mindlin's model by means of the surface loadings $\mathbf{t}^{(n)}$ (Mindlin, 1963; Mindlin and Lee, 1966; Tiersten, 1969). It is, meanwhile, more complicated to accommodate electrical boundary conditions for both the electric potentials and charges may be specified on the plate surfaces. Indeed, since the two-dimensional equations contain only the surface potential $\Phi^{(n)}$, a relation between $\Phi^{(n)}$ and the surface charges $\sigma|_{\pm h}$ is required; by the same token, if the surface charge densities $\sigma^{(n)}$ enter the equations (as in the revised version of the theory), it needs to be related to the surface potentials $\varphi|_{\pm h}$. Except for the simplest cases of a fully coated or totally free plate, such relationships are not easy to derive for the general electrical boundary conditions, no mention open electric boundaries.

4 Numerical solutions

The main advantage of the approximation techniques described in the previous section consists in their relative simplicity: frequency equations can often be obtained in a closed form, and solutions can be analyzed and interpreted as functions of frequency determining parameters. Although many resonator modes are well approximated by these methods, their applications are limited to simple geometries (e.g. thin plates or narrow thin bars) with trivial boundary conditions. Attempts to analyze a number of selected modes in three-dimensional resonators by partial waves methods lead to cumbersome expressions (Milsom *et al.*, 1983). In Mindlin's approach, it is difficult to impose complicated boundary conditions, whether mechanical or electrical.

Three-dimensional resonators or resonators with unconventional shapes and boundary conditions can only be tackled by some numerical method (e.g. finite differences, finite elements, and boundary elements) whose development was greatly stimulated by the growth of computer facilities. The first part of this section describes the evolution of the finite element method, which has been the principal numerical tool for modeling piezoelectric resonators since the early seventies. Because none of the described finite element applications is adapted to include the electric field induced in the outer space by the piezoelectric vibrations, the second part of this section reviews the corresponding methods that have been designed to cope with unbounded regions in electromagnetics.

4.1 *Piezoelectric problems*

The application of finite elements to piezoelectric problems is often said to date from the paper by Allik and Huges (1970), who reported a general formulation of piezoelectric vibrations in terms of tetrahedral finite elements. However, the underlying piezoelectric variational principle had been given earlier in the work by Eer Nisse (1967), and Holland and Eer Nisse (1968), who developed the variational technique to calculate the normal modes in ferroelectric ceramic parallelepipeds and in thick piezoelectric disks by approximating the mechanical displacement and electric potential with the products of sinusoidal and Bessel functions. The finite element formulation generalized this approach by replacing these globally defined, and therefore inconvenient for complex geometries, trial functions, by the interpolation functions defined on the finite

subregions, or elements. The choice of the latter, dictated by the geometry of the structure and the accuracy required, is very wide and has been constantly broadened with new applications.

Although the finite element method quickly gained popularity, it could not be immediately applied to model three-dimensional motion in piezoelectric resonators because of the large computational resources required, and has been preceded by various one- and two-dimensional approximations. An important contribution was made by Kagawa and his co-authors, who applied the finite element method to a large variety of piezoelectric structures. Starting from the one-dimensional analysis of flexural vibrations in composite electromechanical vibrators (Kagawa and Gladwell, 1970) and filters (Kagawa, 1971), he subsequently extended the finite element approach to approximate the lowest modes in partially plated rectangular ferroelectric ceramic plates (Kagawa and Yamabuchi, 1974) and the thickness vibrations in circular and plano-bevel quartz plates (Kagawa *et al.*, 1975). In the latter thin plate applications, the problem was reduced to two-dimensions by assuming the displacement is independent of the thickness coordinate or changes sinusoidally along the thickness direction respectively; the mechanical displacements in lateral directions were approximated on triangles of second order. The same type of elements was used more recently to predict the frequency-temperature characteristics of rectangular and plano-convex quartz plates and to model piezoelectric ceramic gyroscopes (Kagawa *et al.*, 1996). Kagawa was also the first to employ triangular ring elements for the axisymmetric vibrations of piezoelectric circular rods (Kagawa and Yamabuchi, 1976).

A significant number of publications arose from the combination of the finite element method and the Mindlin's approximation technique. In this approach, Mindlin's two-dimensional plate equations are not solved explicitly for a limited number of modes but, rather, written in a variational form, are discretized into finite elements. This facilitates the imposition of boundary conditions and broadens the range of geometries Mindlin's approximation can be applied to. Cowley and Willis (1974) used triangular elements to discretize a circular AT-cut quartz plate with partial electrodes and calculated resonance frequencies around the fundamental thickness-shear mode. Mochizuki (1978) employed triangular prism elements to obtain the frequency spectrum for a variety of circular and rectangular quartz plates. More recently, the finite element method based on Mindlin's plate

equations was used to study the frequency shift in quartz plates due to the electrode mass-loading and shape (Lee *et al.*, 1982), temperature (Yong, 1987a), acceleration (Lee and Tang, 1987; Lee and Guo, 1991), or the piezoelectric effect itself (Yong and Zhang, 1993) if the basic model was purely mechanical. An interesting approach that combines the finite element, Mindlin's and the partial wave methods was described by Sekimoto and his associates. They proposed to satisfy the two-dimensional Mindlin's equations by a linear combination of eigenmodes (partial waves) guided in the width direction of the plate, while their amplitudes being approximated by one-dimensional finite elements in the length direction. This technique, that appears to be both computationally efficient and accurate, was employed to study spurious resonances and their equivalent electrical parameters in the miniature rectangular quartz resonators (Sekimoto *et al.*, 1990, 1992).

As mentioned earlier, the full three-dimensional simulation of piezoelectric resonators represents a challenging task. Since most resonators operate with high frequency thickness modes, a large number of finite elements is required to capture the mechanical and electrical field distributions along the lateral dimensions of the plate. Problems with 10^4–10^5 degrees of freedom (Lobitz *et al.*, 1990; Trümpy and Zingg, 1993) are routinely encountered. For this reason, three-dimensional finite elements have been principally used to model low-frequency piezoelectric devices such as tuning forks for wrist-watch resonators (Tomikawa *et al.*, 1978; Yong, 1987b) and other flexure-type quartz vibrators (Söderkvist, 1990), ultrasonic transducers for sonar applications (Allik *et al.*, 1974; Decarpigny *et al.*, 1985) and medical imaging (Boucher *et al.*, 1981; Naillon *et al.*, 1983, Lerch, 1990), as well as composite transducers with periodic structure (Hossack and Hayward, 1991; Huang and Boucher, 1994). In many cases, the authors carried out the entire piezoelectric analysis using existing commercial finite element packages with added piezoelectric capabilities such as ANSYS (Ostergaard and Pawlak, 1986), NASTRAN (McDearmon, 1984), or ATILA (Decarpigny *et al.*, 1985); or adapted their code to the solver, pre- and post-processing parts of PATRAN, ABAQUS, MODULEF (Chalande, 1990), and FINEL (Guo *et al.*, 1992) finite element software. In other cases, self-developed piezoelectric programs based on either standard tetrahedron and hexahedron elements with polynomial interpolation or custom designed elements (Raoelijaona and Dulmet, 1994) have been developed.

In any case, because most transducers are typically made of materials with very high permittivity constants, the problem of modeling the fringing electric field has never been raised in the context of three-dimensional finite element analysis.

To conclude this section, some alternative numerical methods should also be mentioned. The method of finite differences was used in the late sixties to study low frequency contour modes in quartz plates (Lloyd and Redwood, 1966), but has subsequently given way to a more versatile finite element method. It has the advantage of yielding linear systems that are much more sparse, and is still applied from time to time to two-dimensional structures with regular boundaries (Campbell and Weber, 1992) or to the time-domain models of acoustic wave propagation (Kostek and Randall, 1994) or vibrations (Yamada and Sato, 1998). The boundary element method represents a potential interest for the piezoelectric problem with open electric boundaries since it is ideally suited to modeling infinite regions. However, its application implies the knowledge of the Green's function and its first spatial derivatives which are difficult to obtain in a closed form for piezoelectric solids, and were evaluated so far only numerically (Chen and Lin, 1995). More appropriate for complex piezoelectric structures is the hybrid finite element–boundary integral method, applied in the early seventies to study the vibrations of sonar transducers immersed in an infinite acoustic medium (Smith *et al.*, 1973); unfortunately, such methods often lead to unsymmetric global matrices in contrast to the pure finite element analysis (Lerch, 1992).

4.2 *Open-boundary electromagnetic problems*

Many efficient numerical methods have been developed in electromagnetics to model open-boundary problems. It is, therefore, natural to choose among them an appropriate one that could be used in conjunction with the finite element representation of the piezoelectric part of the problem. Several good surveys of these methods (Emson, 1988; Silvester and Pelosi, 1995; Webb, 1995) facilitate the selection. Although all methods are very different both from the point of view of the underlying mathematical principles and computing requirements, one can typically distinguish

- the methods suited for *quasi-static* and *wave* problems. The range of techniques that can model the smoothly decaying quasi-static field is, clearly, much

wider than that of methods designed to approximate the wave behavior at infinity. Only the former will be considered here;

- the *global* and *local*, or elemental, methods. The authors of the surveys attribute different meaning to these terms which leads not only to a confusion but to, sometimes mutually exclusive, grouping of methods. Webb (1995) related this classification with the sparsity of the system coefficient matrix $\mathbf{K}^{ext}$ arising from the modeling of the exterior region. With this approach, global methods are those that couple the surface unknowns thus yielding a dense matrix $\mathbf{K}^{ext}$, while the local methods keep it sparse.

Various, more detailed, schemes of classification exist. Loosely, the numerical techniques suitable for modeling the unbounded exterior quasi-static fields can be grouped into the following families:

a) In the *simple truncation or simple constraint* methods the hypothetical boundary Γ, that separates the interior and exterior parts of the problem (Fig 2.5), is placed far enough from the sources to allow setting all fields to zero or assuming a decay outside of Γ according to a predetermined (e.g. exponential) law. The extended interior region is modeled by a finite element mesh.

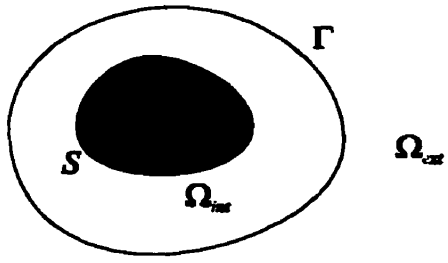

Fig 2.5 Partitioning of the problem domain into interior and exterior parts.

b) *Hybrid* methods represent the field outside of Γ in terms of an integral expression, while the interior region Ω_{int} is modeled by finite elements. Silvester and Pelosi (1995) classified various hybrid methods according to the type of basis functions (polynomials or eigenfunctions) employed to approximate the exact boundary conditions on Γ expressed in terms of the free-space Green function and its derivatives. For this reason, this family of methods includes not only the

'classical' hybrid finite element–boundary integral method reported in the papers by Silvester and Hsieh (1971) for the two-dimensional Laplace equation and by McDonald and Wexler (1972) for the Helmholtz equation, but also the semi-analytical *transfinite element method* (Lee and Cendes, 1987) that employs the expansion in Fourier series for approximating the continuity condition for the electric potential and its normal derivative on a circular (spherical) boundary Γ.

c) The *recursive condensation* methods treat the exterior region as a single 'superelement', obtained from the successive enlargement of the boundary Γ to infinite size Γ_∞ by attaching geometrically similar layers of elements until zero-potential boundary conditions can be applied to Γ_∞. This boundary increase is accompanied by an elimination of all nodes between adjacent layers leaving only those on Γ, so that the total number of the variables remains unchanged. The first method of this group appeared under the name of 'ballooning' (Silvester *et al.*, 1977), in which a very remote boundary Γ_∞ was reached after a few iterations. This method was refined to its limiting cases by the 'infinite substructuring' (Dasgupta, 1984) and the 'infinite scaling' (Hurwitz, 1984) techniques that improved its numerical accuracy by using an infinite number of recursive steps and an infinite sequence of infinitesimal steps respectively.

d) The *transformation* methods use special coordinate transformations to map the exterior unbounded region onto the region of finite volume that can be subdivided into regular finite elements in the same way as the interior problem. The shape of the inner boundary Γ, transformed into itself in this operation, determines, in part, the transformation rule. The simplest circular or spherical boundary Γ is associated with the well known Kelvin transformation, used by Freeman and Lowther (1989) to solve axisymmetric and three-dimensional problems; a general mapping that corresponds to an arbitrary star-shaped Γ was described by Stochniol (1992).

All these techniques are sufficiently documented in the mentioned references, and no attempts are made here to discuss them in more detail; instead, their principal features are summarized in Table 2.5 to explain the choice of method suitable for the use with the finite element model of piezoelectric structures.

Table 2.5 The features of numerical techniques of modeling the exterior unbounded quasi-static fields

Methods	Advantages	Disadvantages
Local		
–Simple constraint –Transformation	–sparse coefficient matrix –simple to implement –compatible with existing FE codes –potential values calculated or recovered at all points	–introduce additional degrees of freedom –accuracy depends on the choice of Γ
Global		
All	–allow an arbitrary choice of Γ (shape and closeness to S) –additional variables may be avoided	–full coefficient matrix
–Hybrid (polynomial)	–no iterative calculation involved	–evaluation of Green's integrals with strong singularities
–Ballooning	–algorithm is simple to implement	–exterior potentials not calculated –matrix inversion at each step of recursion
–Infinite substructuring	–exterior potentials can be recovered from the solution	–solution of a quadratic eigenvalue problem
–Infinitesimal scaling	–high accuracy in the modeling of exterior region	–solution of a nonlinear ordinary differential matrix equation

Initially, the method of ballooning was selected as one of the easiest to program. Its implementation allowed performing rapid tests to demonstrate the substantial influence of the exterior quasi-static field on piezoelectric vibrations. Subsequently, the choice a global method was confirmed when some of the free space was includes into the interior domain Ω_{int} to visualize the fringe field. Numerical tests showed that even an element-thick layer between Γ and the surface of the piezoelectric region considerably increases the size of the finite element equations, which limits the spectrum of problems that can be modeled at the present level of computer facilities. Therefore, for reasons of storage economy, the numerical techniques belonging to the category of local methods were

temporarily put aside since they inevitably introduce additional degrees of freedom. The hybrid methods, in which the placement of boundary Γ is also arbitrary, represent an alternative to the recursive condensation techniques. However, the calculation of the exterior element implies a numerical or symbolic evaluation of integrals with Green's functions kernel, which cannot be done accurately unless special measures that alleviate the associated singularities are taken. It was judged that obtaining the exterior element by the method of ballooning was computationally more straightforward than adapting these special schemes to various functions that might be used to approximate the boundary potential. As for other recursive condensation methods, only the infinite restructuring offers a real improvement compared to ballooning: it allows the exterior electric potential distribution to be recovered from the solution but, unfortunately, at the price of an increased computational complexity. Taking all these considerations into account, it was decided to keep the ballooning technique as a principal tool for solving Laplace's equation in the unbounded space surrounding the piezoelectric solid.

5 Statement of problem

The above review shows that for problems with simple planar boundaries the exterior potential distribution constitutes an integral part of the analytical solution for either surface or guided waves. For practical vibrator configurations, the piezoelectric problem with open electric boundaries must be tackled as a three-dimensional one, whose solution can only be accomplished by applying some numerical technique. No such method had been developed yet. The reported three-dimensional finite element models do not take into account the quasi-static electric field that surrounds the deformed piezoelectric solid. This can be explained, in part, by the fact that most of these models deal with materials possessing high relative permittivity coefficients, such as piezoelectric ceramics for transducer applications. In this case, the neglect of the fringing field can be justified; however, it can introduce a significant error in the analysis of crystals with low ϵ^S/ϵ_0. Such materials are predominant in devices for frequency control, where high precision is required not only at the design stage but also while modeling parameters of these devices.

As was demonstrated, previous attempts to include the exterior electric field were limited to one-dimensional models of piezoelectric vibrations. Even these simples models suggest that the equivalent electrical parameters (C_s, C_n), coupling coefficient k^2, and antiresonance frequency f_a, i.e. those characteristics that depend on electrical boundary conditions, can be especially inaccurate if approximate solutions neglect the external electric field. Moreover, some modes, piezoelectrically inactive for a given electrode configuration, can be excited electrically by this fringing field. It is, therefore, felt that if the latter were included into the problem domain, a more realistic model of piezoelectric vibrations would result. The objective of this thesis is to develop a finite-element based numerical solution of the three-dimensional piezoelectric problem with open electric boundaries.

3

Finite element formulation

1. Introduction

This chapter develops an approximate solution based on the finite element representation of projective equations derived in Chapter 1. In this approach, the unknown quantities are, first, approximated on geometrical subregions, or *elements*, of the problem domain. Second, an approximate solution for the entire region is built up by enforcing some or full continuity requirements between the elements. One of the main advantages of this approach is that the resulting stiffness and mass matrices, formed on the element-by-element basis, are sparse, which is crucial for a fast computer solution of the associated system of equations.

However, the numerical properties of assembled, large scale finite element models will be addressed in the next chapter; the present one deals with *local*, or element, matrices, i.e. with the matrix representations of individual elements. Such matrices are constructed for the tetrahedral elements in the piezoelectric part of the problem domain, and for the bordering 'toblerone' elements, used to discretize some of the surrounding free space prior to starting the process of recursive condensation. Because the piezoelectric problem always allows a formulation in terms of 'potential' functions $\mathbf{u}$ and φ, both continuous across material interfaces, the scalar, or *nodal*, finite elements seems to be the most appropriate. The method of universal matrices, extended here for piezoelectric media, is used to derive local matrices for high-order tetrahedra; the bordering elements are formed by ordinary numerical integration.

2. Finite element modeling of the unbounded problem

In this section, the symmetric matrices (5.30)–(5.33) of Chapter 1 arising from the Galerkin approach are recast to integrate the finite element method of approximating the mechanical and electrical field distributions. Different types of finite elements are employed for the inner and outer parts of the problem domain, i.e. for the piezoelectric body and the infinitely extending free space around it. The interior region is modeled by conventional tetrahedral elements with interpolative approximation. The exterior quasi-static electric field is represented by a single infinite element, or *superelement*, resulting from a recursive condensation process described in this section.

2.1 *The finite element approximation*

In the expansions (5.14) and (5.15) of Chapter 1 it was tacitly assumed that functions $\alpha_i(\mathbf{r})$ and $\alpha_i'(\mathbf{r})$ had been defined on the entire problem space — V and $V + \tilde{V}$ respectively. In contrast to this global approach, the finite element method uses piecewise basis functions, defined on a union of non-overlapping subregions, or *elements*, V_e that fill the problem domain: $V + \tilde{V} = \sum_{(e)} V_e$. The unknown quantities $\mathbf{u}$ and φ are uniquely represented within each element as:

$$\mathbf{u}^{(e)}(\mathbf{r}) \simeq \sum_{m=1}^{M} \mathbf{u}_m^{(e)} \alpha_m^{(e)}(\mathbf{r}), \tag{2.1}$$

$$\varphi^{(e)}(\mathbf{r}) \simeq \sum_{m=1}^{M} \varphi_m^{(e)} \alpha_m^{(e)}(\mathbf{r}), \tag{2.2}$$

where M is the number of basis functions $\alpha_m^{(e)}(\mathbf{r})$, $\mathbf{r} \in V_e$. Equations (2.1)–(2.2) ensure that as soon as parameters $\mathbf{u}_m^{(e)}$ and $\varphi_m^{(e)}$ are determined from the solution, the approximated quantities $\mathbf{u}$ and φ can be calculated everywhere in V and $V + \tilde{V}$ respectively.

Because the present finite element modeling is based on nodal simplex elements (Appendix 3), the numerical coefficients $\mathbf{u}_m^{(e)}$ and $\varphi_m^{(e)}$ in (2.1) and (2.2) have the physical meaning of field values at node $\mathbf{r}_m$, provided the interpolative polynomial $\alpha_m^{(e)}$ has unity value at $\mathbf{r}_m$ and vanishes at the rest of the element nodes: $\alpha_m^{(e)}(\mathbf{r}_n) = \delta_{mn}$. If the same order of polynomial interpolation is used in all

elements, the interelement continuity of the approximated quantities $\mathbf{u}$ and φ is, therefore, enforced by setting equal values to the unknown $\mathbf{u}_m^{(e)}$ and $\varphi_m^{(e)}$ associated with nodes shared by several elements. This is accomplished by assigning the same *global* index ig to the common node m. The integer function $ig = ig(e, m)$ maps the local, i.e. proper to the element e, index $m = 1, ..., M$ onto a unique global node number $ig = 1, ..., n$[1] so that approximations (2.1) and (2.2) can be rewritten as

$$\mathbf{u}^{(e)}(\mathbf{r}) \simeq \sum_{m=1}^{M} \mathbf{u}_{ig(e,m)} \alpha_m^{(e)}(\mathbf{r}), \tag{2.3}$$

$$\varphi^{(e)}(\mathbf{r}) \simeq \sum_{m=1}^{M} \varphi_{ig(e,m)} \alpha_m^{(e)}(\mathbf{r}), \tag{2.4}$$

where $\mathbf{u}_{ig}$ and φ_{ig} are the globally numbered quantities from the projective equation (5.29) in Chapter 1.

The global stiffness $\mathbf{K}$ and mass $\mathbf{M}$ matrices in (5.29) can now be assembled from E local, or element, matrices $\mathbf{K}^{(e)}$ and $\mathbf{M}^{(e)}$ as follows

$$\mathbf{K}_{ig(i),ig(j)} = \sum_{e=1}^{E} \sum_{i=1}^{M} \sum_{j=1}^{M} \mathbf{K}_{ij}^{(e)}, \tag{2.5}$$

$$M_{ig(i),ig(j)} = \sum_{e=1}^{E} \sum_{i=1}^{M} \sum_{j=1}^{M} \mathbf{M}_{ij}^{(e)}. \tag{2.6}$$

The local matrices $\mathbf{K}^{(e)}$ and $\mathbf{M}^{(e)}$ are defined as their global counterparts (5.30)–(5.33) of Chapter 1, except that the integrals are now taken over the element volume V_e:

$$\mathbf{K}_{ij}^{(e)} = \left(\int_{V_e} \nabla \alpha_i \cdot \mathbf{t} \cdot \nabla \alpha_j \, dV \right)_{i=1,...,M,\ j=1,...,M,} \tag{2.7}$$

---

[1] Because Eqs. (2.1) and (2.2) imply that the sets of basis functions α_i' and α_i used to approximate the mechanical displacement and electric potential in Eqs. (5.14)–(5.15) of Chapter 1 are identical, it follows that $N = N' = n$, and the array of global indexes ig is the same for both field variables.

$$\mathbf{M}_{ij}^{(e)} = \mathbf{I}\left(\rho \int_{V_e} \alpha_i \alpha_j \, dV\right)_{i=1,\ldots,M,\ j=1,\ldots,M,} \tag{2.8}$$

where a generic tensor $\mathbf{t}$ stands for tensors $\mathbf{c}^E$, $\mathbf{e}$, and $\boldsymbol{\epsilon}^S$ in the elastic, piezoelectric, and dielectric stiffness matrices respectively, and $\mathbf{I}$ is a 3×3 identity matrix. Because the nodal variables $\mathbf{u}_m$ and φ_m are directly linked only to the nodal variables of the same element (through the local matrix) or neighboring elements (through global indexing), the element-by-element assembly in (2.5) and (2.6) yields *sparse* and, provided an efficient global numbering is used, *banded* stiffness and mass matrices.

The dielectric stiffness matrix $\mathbf{K}^{\varphi\varphi}$ is formed in two steps. First, its interior part, i.e. the part associated with the piezoelectric material, is made up of element matrices of type (2.7) with $\mathbf{t} = \boldsymbol{\epsilon}^S$:

$$K_{ig(i),ig(j)}^{\varphi\varphi} = \sum_{(e)} \sum_{i=1}^{M} \sum_{j=1}^{M} \left(K_{ij}^{\varphi\varphi}\right)^{(e)}. \tag{2.9}$$

Second, the symmetric superelement matrix $\mathbf{S}_{n_S \times n_S}$[2] is added to the part of $\mathbf{K}^{\varphi\varphi}$ that corresponds to the surface nodes:

$$K_{igs(i),igs(j)}^{\varphi\varphi} = K_{igs(i),igs(j)}^{\varphi\varphi} + \sum_{i=1}^{n_S} \sum_{j=1}^{n_S} S_{ij}, \tag{2.10}$$

where array $igs(i)$ maps the surface node index $i = 1, \ldots, n_S$ onto the global index igs. The recursive condensation process, that produces the superelement matrix S, is described below.

2.2 *The superelement for the exterior region*

The three-dimensional version of the recursive condensation is a straightforward extension of its two-dimensional ballooning method described in Silvester *et al* (1977). The strengths and weaknesses of this technique have been discussed in Section 4.2, Chapter 2 in connection with other methods of modeling large empty spaces. In particular, the recursive condensation process, although

---

[2] Starting from this chapter the symbol S, used earlier to denote the mechanical strain tensor, will be reserved for the superelement matrix.

reducing the sparsity of the global dielectric stiffness matrix (2.10), has the advantage of not adding new degrees of freedom to the problem.

The most significant difference between the two- and three-dimensional implementations of the balloon algorithm is the size of matrices to be recursively inverted during the process of condensation. Since no interface separates the interior region from the superelement, the dimension of such matrices is exactly equal to the number of surface nodes n_S, which tends to be large for many geometries. It is, therefore, not very practical to attempt to generate the superelement matrix without seeking simplifying assumptions. The latter will be discussed in Chapter 4 along with the convergence properties of the three-dimensional balloon recursion. The algorithm itself is described in great details in Silvester and Ferrari (1996) so that only the main stages that lead to the matrix S are outlined below.

1. The construction of the superelement starts with an enlargement of the interior part of the problem domain Ω by a bordering region $\Omega_{(1)}$, whose outer surface $\partial\Omega_{(1)}$ is obtained by scaling the boundary $\partial\Omega$ by a factor $\eta > 1$ about the point $O \in \Omega$, as shown in Fig. 3.1.

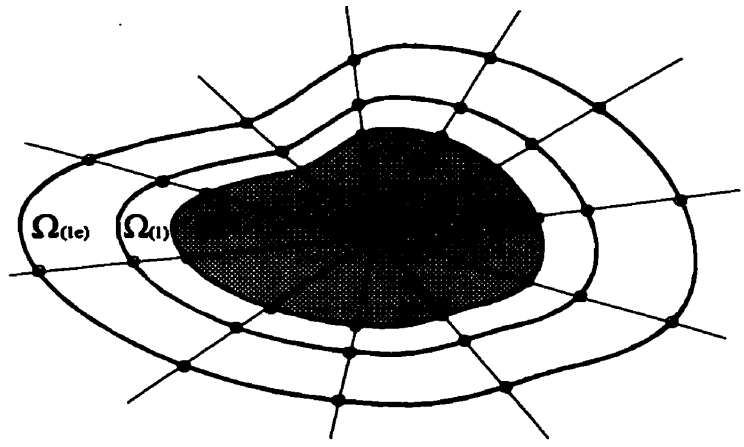

Fig 3.1 Cross-section of the interior region Ω of volume V enlarged by two successive concentric shells $\Omega_{(1)}$ and $\Omega_{(1e)}$.

To ensure the continuity of electric potential φ across the boundary $\partial\Omega$, the region $\Omega_{(1)}$ must be made up of elements compatible with those in Ω, i.e. the

approximating functions over $\partial\Omega$ must be the same for adjoin elements from regions Ω and $\Omega_{(1)}$. An example of such elements is considered in Section 4 of this chapter. If elements of high order are used to build $\Omega_{(1)}$, all interior nodes between $\partial\Omega$ and $\partial\Omega_{(1)}$ are to be eliminated by the process of static condensation. If no condensation of unwanted potentials associated with interior nodes is to be performed, $\mathbf{S}^{(1)}$ can be viewed as a global matrix (2.9) for the space bounded by $\partial\Omega$ and $\partial\Omega_{(1)}$. In either case, the assembly of elements in $\Omega_{(1)}$ produces the first superelement matrix $\mathbf{S}^{(1)}$.

2. The bordering region $\Omega_{(1)}$ is augmented by a layer $\Omega_{(1e)}$ — an enlarged copy of $\Omega_{(1)}$ obtained by scaling the boundary $\partial\Omega_{(1)}$ by η. Because the new region $\Omega_{(1e)}$ is geometrically similar to $\Omega_{(1)}$, the corresponding matrix $\mathbf{S}^{(1e)}$, as an inspection of (2.7) shows, can be obtained from $\mathbf{S}^{(1)}$ as follows:

$$\mathbf{S}^{(1e)} = \eta\mathbf{S}^{(1)}. \tag{2.11}$$

3. Regions $\Omega_{(1)}$ and $\Omega_{(1e)}$ are combined into a larger one $\Omega_2 = \Omega_{(1)} \cup \Omega_{(1e)}$, and unwanted potentials $\Phi_{\partial\Omega_1}$ associated with nodes on $\partial\Omega_1$ are eliminated (static condensation) from the system

$$\left(\begin{bmatrix} \mathbf{S}_{11}^{(1)} & \mathbf{S}_{12}^{(1)} & 0 \\ \mathbf{S}_{21}^{(1)} & \mathbf{S}_{22}^{(1)} & 0 \\ 0 & 0 & 0 \end{bmatrix} + \eta \begin{bmatrix} 0 & 0 & 0 \\ 0 & \mathbf{S}_{11}^{(1)} & \mathbf{S}_{12}^{(1)} \\ 0 & \mathbf{S}_{21}^{(1)} & \mathbf{S}_{22}^{(1)} \end{bmatrix}\right) \begin{bmatrix} \Phi_{\partial\Omega} \\ \Phi_{\partial\Omega_1} \\ \Phi_{\partial\Omega_2} \end{bmatrix} = \begin{bmatrix} 0 \\ 0 \\ 0 \end{bmatrix} \tag{2.12}$$

to produce the element matrix $\mathbf{S}^{(2)}$ that approximates Laplace's equation in region Ω_2:

$$\begin{bmatrix} \mathbf{S}_{11}^{(2)} & \mathbf{S}_{12}^{(2)} \\ \mathbf{S}_{21}^{(2)} & \mathbf{S}_{22}^{(2)} \end{bmatrix} \begin{bmatrix} \Phi_{\partial\Omega} \\ \Phi_{\partial\Omega_2} \end{bmatrix} = \begin{bmatrix} 0 \\ 0 \end{bmatrix}. \tag{2.13}$$

The new dense matrix $\mathbf{S}^{(2)}$ inherits the size $n_S \times n_S$ and the symmetry of the original matrix $\mathbf{S}^{(1)}$, so that $\mathbf{S}_{21}^{(2)} = \mathbf{S}_{12}^{(2)\mathrm{T}}$.

4. Steps 2 and 3 are repeated iteratively until the outer boundary $\partial\Omega_{(k+1)}$ is moved far enough from $\partial\Omega$. At the kth iteration, the distance from the origin O to a point on $\partial\Omega_{(k+1)}$ increases in the power series

$$\sigma = \eta^{2^k}, \tag{2.14}$$

so that, even for a scaling factors η close to unity, typically six or seven iterations suffice to impose the infinity boundary condition (Eq. (4.15), Chapter 1) on $\partial\Omega_{(k+1)}$. At every successive condensation, the superelement matrix $\mathbf{S}^{(k)}$ is replaced by $\mathbf{S}^{(k+1)}$ which models a larger portion of the exterior empty space. Its submatrices can be are expressed in terms of submatrices of $\mathbf{S}^{(k)}$ and the distance (2.14) as follows:

$$\mathbf{S}_{11}^{(k+1)} = \mathbf{S}_{11}^{(k)} - \left[\mathbf{D}^{-1}\mathbf{S}_{12}^{(k)\mathrm{T}}\right]^{\mathrm{T}}\left[\mathbf{D}^{-1}\mathbf{S}_{12}^{(k)\mathrm{T}}\right], \tag{2.15}$$

$$\mathbf{S}_{12}^{(k+1)} = -\sigma\left[\mathbf{D}^{-1}\mathbf{S}_{12}^{(k)\mathrm{T}}\right]^{\mathrm{T}}\left[\mathbf{D}^{-1}\mathbf{S}_{12}^{(k)}\right], \tag{2.16}$$

$$\mathbf{S}_{22}^{(k+1)} = \sigma\,\mathbf{S}_{22}^{(k)} - \sigma^2\left[\mathbf{D}^{-1}\mathbf{S}_{12}^{(k)}\right]^{\mathrm{T}}\left[\mathbf{D}^{-1}\mathbf{S}_{12}^{(k)}\right], \tag{2.17}$$

where $\mathbf{D}$ is the Choleski factor of the matrix

$$\mathbf{S}_{22}^{(k)} + \sigma\,\mathbf{S}_{11}^{(k)} = \mathbf{D}\mathbf{D}^{\mathrm{T}}. \tag{2.18}$$

5. At the last iteration, only submatrix $\mathbf{S}_{11}$ needs to be calculated and stored. Submatrices $\mathbf{S}_{12}$ and $\mathbf{S}_{22}$ are of no practical interest unless other than zero potential boundary conditions are imposed at infinity. Therefore, $\mathbf{S}_{11}$ represents the final superelement matrix $\mathbf{S}$ that models the exterior quasi-static field:

$$\mathbf{S}\boldsymbol{\Phi}_{\partial\Omega} = 0. \tag{2.19}$$

Because the recursive node condensation leads to a dense matrix $\mathbf{S}$, all surface electric potentials $\boldsymbol{\Phi}_{\partial\Omega}$ are coupled to each other. It will be shown in Chapter 4 that no significant error is introduced in the solution by neglecting the coupling between distant nodes. Therefore, many entries of $\mathbf{S}$ can be discarded, and only a small part of $\mathbf{S}$ is added to the interior dielectric global matrix $\mathbf{K}^{\varphi\varphi}$ in (2.10).

3. Tetrahedral elements for the interior region

Scalar tetrahedral elements have been chosen to discretize the interior piezoelectric region. Tetrahedra inherit all the geometrical and algebraic virtues of simplex elements among which the most important are the following:

– any polyhedral shape can be represented as a union of tetrahedra;

– interpolation polynomials of any degree N are easily constructed on simplex elements (Appendix 3). These polynomials form a complete set, so that any polynomial of degree N and lower can be expressed as a linear combination of its elements. This results in the 'geometric isotropy' of simplex elements — a property of being independent (e.g. from the point of view of the accuracy of approximation) of the orientation within the global coordinate system (Silvester and Ferrari, 1996);

– the continuity of approximating functions is automatically satisfied between elements of the same order for sets of regularly spaced interpolation nodes coincide for adjacent faces or edges;

– because differential and integration operations involved in the construction of simplex elements are carried out in homogeneous coordinates, a considerable part of algebraic calculations (Appendix 3) can be done only once — for a generic tetrahedron — and applied afterwards to any element. This property is best illustrated on the example of universal matrices considered below.

3.1 *Stiffness and mass matrices*

The traditional way of evaluating matrices (2.7) and (2.8), inherited from structural mechanics, is by numerical integration, using quadrature formulae for tetrahedra (e.g. Hammer, Marlowe, and Stroud, 1956). Since products $\nabla\alpha_i \cdot \mathbf{t} \cdot \nabla\alpha_j$ and $\alpha_i \alpha_j$ have to be recomputed at many integration points, this approach is computationally costly and potentially inaccurate, particularly for elements of high-order. With advances in symbolic algebra packages, it became possible to derive closed-form expressions for (2.7) and (2.8) (Moetakef, Lawrence, Joshi *et al*, 1995). In this approach, the calculation of the mass matrix causes no problem since the result is purely numerical. Moreover, for the first two orders of tetrahedra, having explicit expressions for the stiffness matrix elements reduces the computation time and round-off error as against the numerical integration. However, for tetrahedra of order higher that two, the symbolic

generation of the stiffness matrix takes a lot of time and produces very lengthy expressions that are handled with difficulty by the symbolic computation programs themselves, and, later, by some compilers, when integrated with the finite element code. This suggests that both the numerical and the analytic integrations of the entire stiffness matrix are not very practical for high-order tetrahedra.

An alternative approach to setting up tetrahedral elements, is to use the pre-computed, or *universal*, matrices. Very popular in electromagnetic finite element applications, the pre-computed matrices had proved helpful in acoustic problems as well, soon after their introduction by Silvester (1969). Stone (1973) used five different types of matrices to assemble high-order triangular elements for modeling the surface acoustic wave propagation in isotropic guiding structures. Although Stone's work clearly demonstrated the elegance and efficiency of this approach, to the best of the author's knowledge, no further applications of universal matrices in acoustic problems, and all the more in the piezoelectric finite element analyses, have been reported since. The object of this section is to derive such matrices for piezoelectric tetrahedra of high order.

The idea behind this method is to separate material properties, as well as geometric coefficients and volume of the tetrahedron, from terms containing interpolation polynomials and their derivatives. The former are problem specific and can be combined into the *weighting* coefficients; the latter are independent of the tetrahedron shape and size, and, when integrated in local coordinates, form purely numerical (universal) matrices that can be pre-computed and tabulated. The element matrices are then generated as weighted row and column permutations of universal matrices with exactly the same computational efforts for elements of any order.

Consider first the element stiffness matrix (2.7). The gradient operator in local coordinates has been derived in Eq. (3.2), Appendix 3 and is given by

$$\nabla\alpha_i = \frac{1}{6V}\sum_{m=1}^{4}\mathbf{g}^{(m)}\frac{\partial\alpha_i}{\partial\zeta_m}, \tag{3.1}$$

where V is the tetrahedron volume, and $\mathbf{g}^{(m)}$ denotes the array of geometric coefficients $[b_m \quad c_m \quad d_m]^{\mathrm{T}}$, defined by Eq. (1.4) of the same appendix. The block-element of the stiffness matrix is now represented in the discrete form

$$\mathbf{K}_{ij}^{(tet)} = \frac{1}{(6V)^2}\sum_{m=1}^{4}\sum_{n=1}^{4}\mathbf{W}^{(mn)}\int_V \frac{\partial\alpha_i}{\partial\zeta_m}\frac{\partial\alpha_j}{\partial\zeta_n}\,dV, \tag{3.2}$$

where the weighting coefficient $\mathbf{W}^{(mn)}$ is defined by the double scalar product of geometric and material parameters

$$\mathbf{W}^{(mn)} = \mathbf{g}^{(m)} \cdot \mathbf{t} \cdot \mathbf{g}^{(n)}. \tag{3.3}$$

Factor $\mathbf{W}^{(mn)}$ is respectively a 3×3 matrix, a 3-dimensional vector, and a scalar when $\mathbf{t}$ stands for tensors $\mathbf{c}^E$, $\mathbf{e}$, and $\boldsymbol{\epsilon}^S$; expanded expressions (3.3) are tabulated in Appendix 4 for all these tensors. The weighting factors $\mathbf{W}^{(mn)}$ are linearly dependent:

$$\sum_{n=1}^{4}\mathbf{W}^{(mn)} = 0, \quad m = 1, \ldots, 4, \tag{3.4}$$

just as the geometric coefficients b_m, c_m, d_m are (Eq. (1.6) of Appendix 3). Another property of $\mathbf{W}^{(mn)}$ follows immediately from its definition (3.3):

$$\mathbf{W}^{(nm)} = \mathbf{W}^{(mn)\mathrm{T}}. \tag{3.5}$$

On combining equations (3.4) and (3.5), it becomes clear that only six out of sixteen factors $\mathbf{W}^{(mn)}$ are 'independent', and need to be calculated for every tetrahedron; the remaining coefficients can be found from the system

$$\left.\begin{aligned}
&\mathbf{W}^{(11)} + \mathbf{W}^{(12)} + \mathbf{W}^{(13)} + \mathbf{W}^{(14)} = 0,\\
&\mathbf{W}^{(12)\mathrm{T}} + \mathbf{W}^{(22)} + \mathbf{W}^{(23)} + \mathbf{W}^{(24)} = 0,\\
&\mathbf{W}^{(13)\mathrm{T}} + \mathbf{W}^{(23)\mathrm{T}} + \mathbf{W}^{(33)} + \mathbf{W}^{(34)} = 0,\\
&\mathbf{W}^{(14)\mathrm{T}} + \mathbf{W}^{(24)\mathrm{T}} + \mathbf{W}^{(34)\mathrm{T}} + \mathbf{W}^{(44)} = 0,
\end{aligned}\right\} \tag{3.6}$$

and Eq. (3.5).

The integral in (3.2) can be made independent of the tetrahedron shape and volume by performing the integration with respect to the local coordinates. For tetrahedra this transformation requires premultiplying (3.2) by $6V$ (Eq. (4.2), Appendix 3). The block-elements of the stiffness matrix $\mathbf{K}$ can therefore be calculated as a weighted combination

$$\mathbf{K}_{ij}^{(tet)} = \frac{1}{6V}\sum_{m=1}^{4}\sum_{n=1}^{4}\mathbf{W}^{(mn)}\mathfrak{A}_{ij}^{(mn)}, \tag{3.7}$$

of purely numerical matrices $\mathfrak{A}^{(mn)}$ whose elements are evaluated by integrating polynomials $(\partial\alpha_i/\partial\zeta_m)(\partial\alpha_j/\partial\zeta_n)$ over a tetrahedron Ω of unit volume

$$\mathfrak{A}_{ij}^{(mn)} = \int_{\Omega}\frac{\partial\alpha_i}{\partial\zeta_m}\frac{\partial\alpha_j}{\partial\zeta_n}\,\mathrm{d}\zeta_1\mathrm{d}\zeta_2\mathrm{d}\zeta_3. \tag{3.8}$$

Equation (3.7) can be written in matrix notation by invoking the *tensor product*[3] of two matrices:

$$\mathbf{K}^{(tet)} = \frac{1}{6V}\sum_{m=1}^{4}\sum_{n=1}^{4}\mathbf{W}^{(mn)}\otimes\mathfrak{A}^{(mn)}. \tag{3.9}$$

This implies that if the weighting factor $\mathbf{W}^{(mn)}$ is a $p\times q$ matrix and $\mathfrak{A}^{(mn)}$ is a $M\times M$ one, the resulting $pM\times qM$ stiffness matrix $\mathbf{K}^{(tet)}$ will be partitioned into M^2 blocks $\mathbf{K}_{ij}^{(tet)}$ of size $p\times q$ each, defined by Eq. (3.7).

The number of terms in (3.9) can be reduced by eliminating one of the four local coordinates (e.g. ζ_4) using Eq. (1.3) of Appendix 3. The discrete form of the gradient operator (3.1) can now be replaced by

$$\nabla\alpha_i = \frac{1}{6V}\sum_{m=1}^{3}\mathbf{g}^{(m)}\left(\frac{\partial\alpha_i}{\partial\zeta_m}-\frac{\partial\alpha_i}{\partial\zeta_4}\right), \tag{3.10}$$

according to Eq. (3.4) of Appendix 3. This change turns (3.9) into a nine-term summation

$$\mathbf{K}^{(tet)} = \frac{1}{6V}\sum_{m=1}^{3}\sum_{n=1}^{3}\mathbf{W}^{(mn)}\otimes\mathfrak{B}^{(mn)}, \tag{3.11}$$

and gives rise to a new set of numerical matrices $\mathfrak{B}^{(mn)}$ defined by

$$\mathfrak{B}_{ij}^{(mn)} = \int_{\Omega}\left(\frac{\partial\alpha_i}{\partial\zeta_m}-\frac{\partial\alpha_i}{\partial\zeta_4}\right)\left(\frac{\partial\alpha_j}{\partial\zeta_n}-\frac{\partial\alpha_j}{\partial\zeta_4}\right)\mathrm{d}\zeta_1\mathrm{d}\zeta_2\mathrm{d}\zeta_3. \tag{3.12}$$

---

[3] This kind of matrix operation is also referred to as *Kronecker* or *direct* product (M.Marcus and H. Minc, 1964).

An alternative way of condensing the discrete representation of the stiffness matrix is to eliminate diagonal members $m = n$ from (3.9) by expressing them in terms of off-diagonal ones using system (3.6). After some rearrangement, this yields a twelve-term expansion

$$\mathbf{K}^{(tet)} = \frac{1}{6V}\sum_{m=1}^{3}\sum_{n=m+1}^{4}\left(\mathbf{W}^{(mn)} \otimes \mathfrak{C}^{(mn)} + \mathbf{W}^{(mn)\mathrm{T}} \otimes \mathfrak{C}^{(nm)}\right) \tag{3.13}$$

with numerical matrices $\mathfrak{C}^{(mn)}$ whose elements are determined as follows

$$\mathfrak{C}_{ij}^{(mn)} = -\int_{\Omega} \frac{\partial \alpha_i}{\partial \zeta_m}\left(\frac{\partial \alpha_j}{\partial \zeta_m} - \frac{\partial \alpha_j}{\partial \zeta_n}\right) \mathrm{d}\zeta_1 \mathrm{d}\zeta_2 \mathrm{d}\zeta_3. \tag{3.14}$$

A similar approach led Silvester (1972) to define a symmetric numerical matrix $\mathbf{Q}^{(mn)}$ (Eq. (2.3), Appendix 4) that was employed in the solution of the three-dimensional scalar Helmholtz equation for isotropic media; the weighting coefficient matrix reduces then to a scalar symmetric array $W^{(mn)} = b_m b_n + c_m c_n + d_m d_n = W^{(nm)}$. Because for the piezoelectric tetrahedral elements the weighting factors $\mathbf{W}^{(mn)}$ are, in general, neither scalar nor symmetric, nonsymmetric matrices $\mathfrak{C}^{(mn)}$ and $\mathfrak{C}^{(nm)}$ in (3.13) cannot be combined to form one symmetric matrix $\mathbf{Q}^{(mn)}$. The relationship between matrices $\mathbf{Q}$ and $\mathfrak{C}$ is given by Eq. (2.4) of Appendix 4.

Finally, the mass matrix (2.8) is easily obtainable from the numerical matrix $\mathfrak{T}$,

$$\mathfrak{T}_{ij} = \int_{\Omega} \alpha_i \alpha_j \, \mathrm{d}\zeta_1 \mathrm{d}\zeta_2 \mathrm{d}\zeta_3, \tag{3.15}$$

also called a *metric* of the interpolation polynomial basis $\{\alpha_i\}$, as

$$\mathbf{M}^{(tet)} = 6V\rho\mathfrak{T} \otimes \mathbf{I}. \tag{3.16}$$

As it follows from the above discussion, to generate the tetrahedral elements, only two types matrices are needed — the metric matrix $\mathfrak{T}$ and one of the matrices $\mathfrak{A}$, $\mathfrak{B}$, and $\mathfrak{C}$; in principle, either of the three equations (3.9), (3.11), and (3.13) can be employed to assemble the stiffness matrix $\mathbf{K}^{(tet)}$. However, the symmetry properties of $\mathfrak{A}$, $\mathfrak{B}$, and $\mathfrak{C}$, that are discussed in the following section, may be decisive in the choice of the numerical matrix to be retained for the computer implementation of the finite element analysis.

3.2 *Symmetry and permutation properties of universal matrices*

The numerical matrices $\mathfrak{A}$, $\mathfrak{B}$, $\mathfrak{C}$, and $\mathfrak{T}$, defined in the previous section, are all universal in the sense that their elements are exactly the same for any real tetrahedral element. They can be computed up to any reasonable order of interpolation polynomials and stored in the form of integer numbers with a common integer denominator. By explicitly writing $\{\alpha_i\}$ in terms of auxiliary polynomials (Eq.(2.1), Appendix 3), the integrals (3.8), (3.12), (3.14), and (3.15) are best evaluated analytically using a symbolic algebra program. Alternatively, the matrices $\mathfrak{A}$, $\mathfrak{B}$, and $\mathfrak{C}$ can be derived from a basic set of universal matrices (Silvester, 1982a; Silvester, Minhas, and Csendes, 1981), which counts among its members the already known metric matrix $\mathfrak{T}$ and the finite differential operator $\mathfrak{D}$, formed by the derivatives of polynomials α_i with respect to the local coordinates $\partial\alpha_i/\partial\zeta_m$ evaluated at the interpolation nodes P_j ($\alpha_i(P_j) = 1$ for $i = j$, and $\alpha_i(P_j) = 0$ for $i \neq j$):

$$\mathfrak{D}_{ij}^{(m)} = \left.\frac{\partial\alpha_i}{\partial\zeta_m}\right|_{P_j}. \tag{3.17}$$

Equations (3.8), (3.12), (3.14) may now be rewritten in matrix form

$$\mathfrak{A}^{(mn)} = \mathfrak{D}^{(m)}\mathfrak{T}\mathfrak{D}^{(n)\mathrm{T}}, \tag{3.18}$$

$$\mathfrak{B}^{(mn)} = \left(\mathfrak{D}^{(m)} - \mathfrak{D}^{(4)}\right)\mathfrak{T}\left(\mathfrak{D}^{(n)} - \mathfrak{D}^{(4)}\right)^{\mathrm{T}}, \tag{3.19}$$

$$\mathfrak{C}^{(mn)} = -\mathfrak{D}^{(m)}\mathfrak{T}\left(\mathfrak{D}^{(m)} - \mathfrak{D}^{(n)}\right)^{\mathrm{T}}. \tag{3.20}$$

Therefore, as soon as the fundamental matrices $\mathfrak{D}^{(m)}$ and $\mathfrak{T}$ are calculated and tabulated, any of the matrices $\mathfrak{A}$, $\mathfrak{B}$, and $\mathfrak{C}$ can be generated from them at will. It is also evident from the above equations that the matrices $\mathfrak{B}$ and $\mathfrak{C}$ are related to $\mathfrak{A}$:

$$\mathfrak{B}^{(mn)} = \mathfrak{A}^{(mn)} - \mathfrak{A}^{(4n)} - \mathfrak{A}^{(m4)} + \mathfrak{A}^{(44)} \tag{3.21}$$

$$\mathfrak{C}^{(mn)} = \mathfrak{A}^{(mn)} - \mathfrak{A}^{(mm)} \tag{3.22}$$

It follows from (3.18) and (3.19) that the property (3.5) of weighting coefficients applies to the universal matrices $\mathfrak{A}$ and $\mathfrak{B}$ as well

$$\begin{aligned} \mathfrak{A}^{(nm)} &= \mathfrak{A}^{(mn)\mathrm{T}}, \\ \mathfrak{B}^{(nm)} &= \mathfrak{B}^{(mn)\mathrm{T}} \end{aligned} \tag{3.23}$$

Taking into account that $(\mathbf{A} \otimes \mathbf{B})^{\mathrm{T}} = \mathbf{A}^{\mathrm{T}} \otimes \mathbf{B}^{\mathrm{T}}$, this observation leads to the following relation

$$\begin{aligned} \mathbf{W}^{(nm)} \otimes \mathfrak{A}^{(nm)} &= \left(\mathbf{W}^{(mn)} \otimes \mathfrak{A}^{(mn)}\right)^{\mathrm{T}}, \\ \mathbf{W}^{(nm)} \otimes \mathfrak{B}^{(nm)} &= \left(\mathbf{W}^{(mn)} \otimes \mathfrak{B}^{(mn)}\right)^{\mathrm{T}}, \end{aligned} \tag{3.24}$$

which reduces the number of numerical matrices $\mathfrak{A}^{(mn)}$ or $\mathfrak{B}^{(mn)}$ that enter into expansions (3.9) and (3.11) to ten and six respectively.

Because summations (3.9) and (3.11) involve fewer terms than (3.13) it might seem that it is more economical to use the matrices $\mathfrak{A}$ or $\mathfrak{B}$ to construct the stiffness matrix $\mathbf{K}^{(let)}$. At this stage, storage requirement should be considered more closely. Indeed, not all the universal matrices need to be calculated and tabulated: most of them are obtainable from one another by applying various permutation operators associated with a regular tetrahedron (Silvester, 1982b) such as

– rotation about the tetrahedron centroid (cyclic permutation of all four vertices);

– rotation about one of the tetrahedron three-fold axes (cyclic permutation of three vertices lying in the plane perpendicular to this axis);

– mirroring or 'flip' permutation (exchange of two vertices).

One way of deriving permutation rules for universal matrices is to identify them with tetrahedron vertices and edges (Silvester and Ferrari, 1990). Using this geometric analogy, it becomes evident that the symmetric matrices $\mathfrak{A}^{(mm)}$ can be generated from one matrix $\mathfrak{A}^{(11)}$ by applying any permutation operation that maps vertex 1 onto vertex m; the nonsymmetric matrices $\mathfrak{A}^{(mn)}$, $m \neq n$, associated with the edge $\overrightarrow{mn}$ can be obtained from one matrix, e.g. $\mathfrak{A}^{(12)}$, by employing tetrahedron permutations that transform the edge $\overrightarrow{12}$ into edge $\overrightarrow{mn}$. The same geometric argument applies to matrices $\mathfrak{B}^{(mn)}$. This means that in both cases at

least two starting matrices need to be tabulated in order to generate complete sets of universal matrices $\mathfrak{A}$ and $\mathfrak{B}$ from expansion (3.9) and (3.11).

In contrast, Eq. (3.13) does not contain any diagonal term ($m = n$); in other words, the universal matrices involved in this expansion are associated with tetrahedron edges only. This suggest that all the required matrices $\mathfrak{C}^{(mn)}$ can be generated from the basic matrix $\mathfrak{C}^{(12)}$ alone by successively applying the same permutations that relate edges $\overrightarrow{mn}$ to the edge $\overrightarrow{12}$. An example of such permutations is shown in Fig. 3.2.

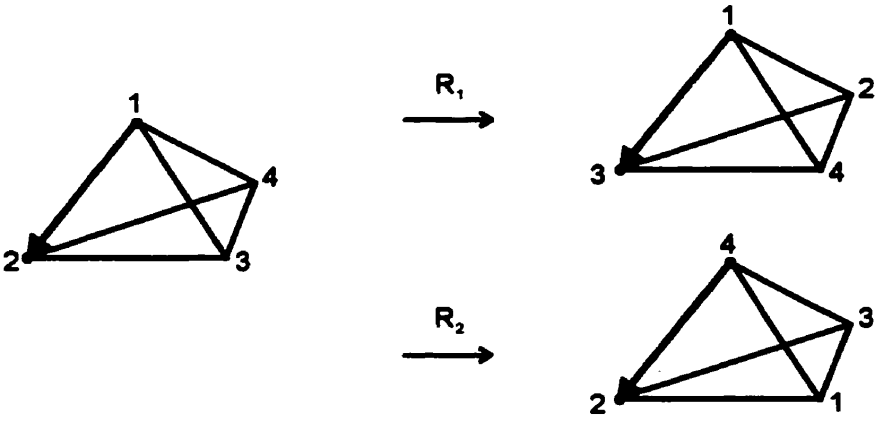

Fig 3.2 Right-handed rotations $\mathbf{R}_1$ and $\mathbf{R}_2$ of the tetrahedron about ζ_1- and ζ_2-axes respectively.

Rotations $\mathbf{R}_1$ and $\mathbf{R}_2$, that map the edge $\overrightarrow{12}$ onto edges $\overrightarrow{13}$ and $\overrightarrow{42}$ respectively, relabel the tetrahedron vertices according to the following matrices

$$\mathbf{R}_1 = \begin{bmatrix} 1 & 0 & 0 & 0 \\ 0 & 0 & 0 & 1 \\ 0 & 1 & 0 & 0 \\ 0 & 0 & 1 & 0 \end{bmatrix}, \qquad \mathbf{R}_2 = \begin{bmatrix} 0 & 0 & 1 & 0 \\ 0 & 1 & 0 & 0 \\ 0 & 0 & 0 & 1 \\ 1 & 0 & 0 & 0 \end{bmatrix}. \tag{3.25}$$

Matrices (3.25) can be used directly for tetrahedra of first order to obtain the matrices $\mathfrak{C}^{(13)}$ and $\mathfrak{C}^{(42)}$ as row and column permutations of $\mathfrak{C}^{(12)}$:

$$\mathfrak{C}^{(13)} = \mathbf{R}_1 \mathfrak{C}^{(12)} \mathbf{R}_1^{\mathrm{T}}, \qquad \mathfrak{C}^{(42)} = \mathbf{R}_2 \mathfrak{C}^{(12)} \mathbf{R}_2^{\mathrm{T}}. \tag{3.26}$$

The diagram in Fig. 3.3 shows that these two rotations are sufficient to obtain the remaining universal matrices.

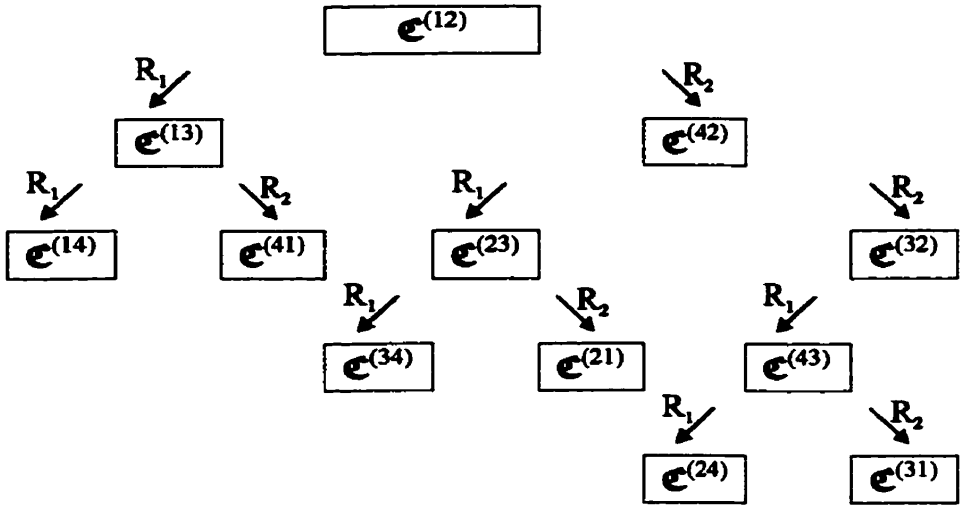

Fig 3.3 Derivation of numerical matrices $\mathfrak{C}^{(mn)}$, $m \neq n$, from matrix $\mathfrak{C}^{(12)}$.

For elements of order higher than the first, rotation matrices must take into account the relabeling of all the tetrahedron nodes. Such matrices have been generated up to the forth order and compactly stored in the form of one-dimensional arrays R_1 and R_2 whose entries indicate the column numbers of the nonzero element in each row of $\mathbf{R}_1$ and $\mathbf{R}_2$ respectively. Examples of such arrays for a tetrahedron of second order are given in Section 3, Appendix 4.

Following the described scheme, the stiffness matrix $\mathbf{K}^{(tet)}$ can be derived from the row and column permutations of only one numerical matrix $\mathfrak{C}^{(12)}$, and six weighting coefficients $\mathbf{W}^{(12)}$, $\mathbf{W}^{(13)}$, $\mathbf{W}^{(14)}$, $\mathbf{W}^{(23)}$, $\mathbf{W}^{(24)}$, $\mathbf{W}^{(34)}$. While $\mathfrak{C}^{(12)}$ is constant for a given order of interpolation, the weighting factors are recalculated for every real tetrahedral element. Using the permutation arrays R_1 and R_2, the element of the stiffness matrix is calculated as shown in Eq. (3.27). The number of operations involved in (3.27) is fixed, and does not depend on the element order. This sets practically no limit on the order of tetrahedra used in the analysis, which distinguishes the method of universal matrices from other methods of computing element matrices.

Equations (3.16) and (3.27) were implemented in the actual finite element code. The required universal matrices $\mathfrak{C}^{(12)}$ and $\mathfrak{T}$ were calculated and tabulated

up to the fourth order. Example of these matrices for tetrahedral elements of second order are given by Equations (2.1) and (2.2) of Appendix 4.

$$
\begin{aligned}
\mathbf{K}_{ij}^{(tet)} = \frac{1}{6V}\Big\{ & \mathbf{W}^{(12)}\mathfrak{C}_{ij}^{(12)} \\
& + \mathbf{W}^{(12)\mathrm{T}}\mathfrak{C}^{(12)}_{R_2(R_1(R_2(i))),R_2(R_1(R_2(j)))} \\
& + \mathbf{W}^{(13)}\mathfrak{C}^{(12)}_{R_1(i),R_1(j)} \\
& + \mathbf{W}^{(13)\mathrm{T}}\mathfrak{C}^{(12)}_{R_2(R_1(R_2(R_2(i)))),R_2(R_1(R_2(R_2(j))))} \\
& + \mathbf{W}^{(14)}\mathfrak{C}^{(12)}_{R_1(R_1(i)),R_1(R_1(j))} \\
& + \mathbf{W}^{(14)\mathrm{T}}\mathfrak{C}^{(12)}_{R_2(R_1(i)),R_2(R_1(j))} \\
& + \mathbf{W}^{(23)}\mathfrak{C}^{(12)}_{R_1(R_2(i)),R_1(R_2(j))} \\
& + \mathbf{W}^{(23)\mathrm{T}}\mathfrak{C}^{(12)}_{R_2(R_2(i)),R_2(R_2(j))} \\
& + \mathbf{W}^{(24)}\mathfrak{C}^{(12)}_{R_1(R_1(R_2(R_2(i)))),R_1(R_1(R_2(R_2(j))))} \\
& + \mathbf{W}^{(24)\mathrm{T}}\mathfrak{C}^{(12)}_{R_2(i),R_2(j)} \\
& + \mathbf{W}^{(34)}\mathfrak{C}^{(12)}_{R_1(R_1(R_2(i))),R_1(R_1(R_2(j)))} \\
& + \mathbf{W}^{(34)\mathrm{T}}\mathfrak{C}^{(12)}_{R_1(R_2(R_2(i))),R_1(R_2(R_2(j)))}\Big\}
\end{aligned}
\tag{3.27}
$$

4. Bordering elements

The basic requirement for elements in the bordering region $\Omega_{(1)}$ is that they be compatible with tetrahedral elements used to subdivide the interior piezoelectric region. The skew triangular prism, or skew 'toblerone' element, shown in Fig. 3.4, arises naturally from the enlargement of border $\partial\Omega$. The element shape is defined by two similar triangles ABC and $A'B'C'$ connected by straight edges A–A', B–B', C–C'. Because vertices $A(x_1, y_1, z_1)$, $B(x_2, y_2, z_2)$, and $C(x_3, y_3, z_3)$ of the surface triangle are also common to an interior tetrahedron $ABCD$ (Fig. 3.4), the continuity of approximating functions across the surface is automatically guaranteed, provided the same order of interpolation over ABC is employed.

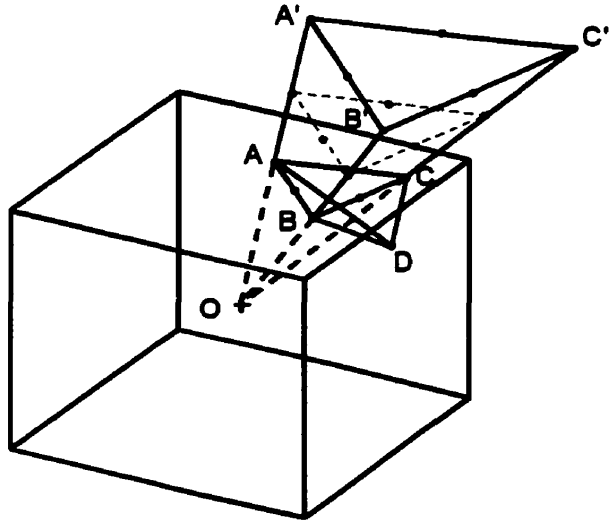

Fig 3.4 Skew 'toblerone' element — the building block for the bordering region $\Omega_{(1)}$.

Nodes $A'(x_4, y_4, z_4)$, $B'(x_5, y_5, z_5)$, and $C'(x_6, y_6, z_6)$ are generated by the mapping

$$\frac{OA'}{OA} = \frac{OB'}{OB} = \frac{OC'}{OC} = \eta \tag{4.1}$$

with respect to the point $O(x_o, y_o, z_o)$ so that their coordinates are derived from their surface counterparts as

$$\left.\begin{aligned} x_{i+3} &= \eta(x_i - x_o) + x_o, \\ y_{i+3} &= \eta(y_i - y_o) + y_o, \\ z_{i+3} &= \eta(z_i - z_o) + z_o, \end{aligned}\right\} \qquad i = 1, 2, 3. \tag{4.2}$$

To construct the bordering element, it is possible to further subdivide the described triangular prism into four tetrahedra, and to employ approximating functions already derived for the interior region. However, this would imply using the same order of interpolation on the surface, which is determined by the interior tetrahedra, and in the radial direction. This could be particularly inconvenient if high-order interpolation is needed to model the field variations inside the piezoelectric domain, while lower degree polynomials might be sufficient to approximate the electric field decay near the surface; moreover, high-order interpolation generates nodes inside the bordering region $\Omega_{(1)}$ which must be removed by the computationally costly procedure of static condensation. Instead, it was decided to define the basis function over the whole prism. This allow combining different interpolation orders over triangles ABC and $A'B'C'$, and along the radial edges A–A', B–B', and C–C', thus providing for more flexibility in modeling the interior and exterior field distributions.

4.1 *Approximation on the 'toblerone' element*

Let the Lagrangian polynomials $\alpha^t(\zeta_1, \zeta_2, \zeta_3)$ of degree N_t and $\alpha^s(\xi_1, \xi_2)$ of degree N_s be associated with the line segment and base triangle respectively. Because both shapes are special cases of simplexes, the interpolation polynomials α^t and α^s can be expressed in terms of auxiliary polynomials R_m using the multi-index numbering:

$$\alpha^t_{mno}(\zeta_1, \zeta_2, \zeta_3) = R_m(N_t, \zeta_1) R_n(N_t, \zeta_2) R_o(N_t, \zeta_3), \qquad m + n + o = N_t, \tag{4.3}$$

$$\alpha^s_{mn}(\xi_1, \xi_2) = R_m(N_s, \xi_1) R_n(N_s, \xi_2), \quad m + n = N_s. \tag{4.4}$$

As is evident from the definition of R_m (Eq. (2.2), Appendix 3), functions α^t and α^s have zeros at $M_t = (N_t + 1)(N_t + 2)/2$ and $M_s = (N_s + 1)$ equispaced points (Fig. 3.4) respectively. In a single-index notation, the Lagrangian interpolation on the 'toblerone' element can be defined as a product of polynomials α^t and α^s:

$$\alpha_i(\zeta_1, \zeta_2, \zeta_3, \xi_1, \xi_2) = \alpha_j^t(\zeta_1, \zeta_2, \zeta_3)\, \alpha_k^s(\xi_1, \xi_2), \tag{4.5}$$

where the correspondence between the index $i = 1, ..., M_t M_s$ and indices j and k may be established in the following manner

$$i = (k-1)\, M_t + j, \qquad j = 1, ..., M_t, \;\; k = 1, ..., M_s. \tag{4.6}$$

The unknown potential can thus be approximated in terms of independent interpolation functions α^t and α^s by

$$\varphi(x, y, z) = \sum_{i=1}^{M_t M_s} \Phi_i\, \alpha_j^t(\zeta_1, \zeta_2, \zeta_3)\, \alpha_k^s(\xi_1, \xi_2) \tag{4.7}$$

The same type of functions (4.5) is used to approximate the element shape transformation, required subsequently to express the Jacobian J associated with the element. Because all the prism edges are straight, it is sufficient to employ linear (with respect to each local variable) interpolating polynomials

$$\alpha_i = \begin{cases} \zeta_i \xi_1, & i = 1, 2, 3, \\ \zeta_{i-3} \xi_2, & i = 4, 5, 6. \end{cases} \tag{4.8}$$

The element geometric shape is, therefore, approximated similarly to Eq. (4.7), where the potential nodal values Φ_i are replaced by the prism's vertex coordinates (x_i, y_i, z_i):

$$\left.\begin{aligned} x &= (x_1\zeta_1 + x_2\zeta_2 + x_3\zeta_3)\xi_1 + (x_4\zeta_1 + x_5\zeta_2 + x_6\zeta_3)\xi_2, \\ y &= (y_1\zeta_1 + y_2\zeta_2 + y_3\zeta_3)\xi_1 + (y_4\zeta_1 + y_5\zeta_2 + y_6\zeta_3)\xi_2, \\ z &= (z_1\zeta_1 + z_2\zeta_2 + z_3\zeta_3)\xi_1 + (z_4\zeta_1 + z_5\zeta_2 + z_6\zeta_3)\xi_2, \end{aligned}\right\}. \tag{4.9}$$

If orders N_t or N_s in (4.7) are greater then one, which is typically the case, the constructed 'toblerone' can be seen as a subparametric element.

4.2 *Stiffness matrix*

On setting $\epsilon = \epsilon_0 \mathbf{I}$ in Eq. (5.32) of Chapter 1, the elements of the stiffness matrix becomes

$$K_{ij}^{(tob)} = \epsilon_0 \int_V \nabla\alpha_i \cdot \nabla\alpha_j \, \mathrm{d}V, \tag{4.10}$$

where the gradients of interpolating functions $\nabla\alpha_i$ are expressed with respect to the Cartesian or global coordinates x, y, z. Because functions α_i are given in terms of local, or simplex, coordinates $\zeta_1, \zeta_2, \zeta_2, \xi_1, \xi_2$, among which only the three ζ_1, ζ_2, ξ_1 will be considered as independent, it is easier to perform the differentiation with respect to ζ_1, ζ_2, ξ_1 by invoking the Jacobian $\mathbf{J}$ of the coordinate transformation:

$$\nabla\alpha_i = \mathbf{J}^{-1}\left[\frac{\partial\alpha_i}{\partial\zeta_1} \quad \frac{\partial\alpha_i}{\partial\zeta_2} \quad \frac{\partial\alpha_i}{\partial\xi_1}\right]^{\mathrm{T}} = \mathbf{J}^{-1}\nabla_{\zeta_1\zeta_2\xi_1}\alpha_i. \tag{4.11}$$

Taking into account that $\zeta_1 + \zeta_2 + \zeta_3 = 1$ and $\xi_1 + \xi_2 = 1$, the stiffness matrix can be evaluated in local coordinates as

$$K_{ij}^{(lob)} = \epsilon_0 \int_0^1 \mathrm{d}\xi_1 \int_0^1 \mathrm{d}\zeta_2 \int_0^{1-\zeta_2} \mathrm{d}\zeta_1 (\nabla_{\zeta_1\zeta_2\xi_1}\alpha_i)^{\mathrm{T}} \mathbf{J}^{-\mathrm{T}}\mathbf{J}^{-1}\nabla_{\zeta_1\zeta_2\xi_1}\alpha_j |\mathbf{J}|. \tag{4.12}$$

The gradient $\nabla_{\zeta_1\zeta_2\xi_1}\alpha_i$ can be expressed in terms of partial derivatives of the basis functions $\alpha_j^t(\zeta_1, \zeta_2, \zeta_3)$ and $\alpha_k^s(\xi_1, \xi_2)$ by applying the chain rule of differentiation to (4.5), and, subsequently, to Eqs. (4.3)–(4.4):

$$\begin{aligned}\nabla_{\zeta_1\zeta_2\xi_1}\alpha_i &= \left[\frac{\partial\alpha_j^t}{\partial\zeta_1}\alpha_k^s \quad \frac{\partial\alpha_j^t}{\partial\zeta_2}\alpha_k^s \quad \alpha_j^t\frac{\partial\alpha_k^s}{\partial\xi_1}\right]^{\mathrm{T}} \\ &= \begin{bmatrix} \left(\dfrac{\partial R_m}{\partial\zeta_1}R_nR_o - R_mR_n\dfrac{\partial R_o}{\partial\zeta_1}\right)\alpha_k^s \\ \left(R_m\dfrac{\partial R_n}{\partial\zeta_2}R_o - R_mR_n\dfrac{\partial R_o}{\partial\zeta_2}\right)\alpha_k^s \\ \alpha_j^t\left(\dfrac{\partial R_m}{\partial\xi_1}R_n - R_m\dfrac{\partial R_n}{\partial\xi_1}\right) \end{bmatrix},\end{aligned} \tag{4.13}$$

where indices m, n, o refer to the multi-index notation, while the single indices i, j, k are related by Eq. (4.6). Derivatives of the auxiliary polynomials R were obtained in Appendix 3, Eq. (3.5).

4.3 *Calculation of the Jacobian*

The substitution of Eqs. (4.2) and (4.9) into the Jacobian matrix $\mathbf{J} = \partial(x, y, z)/\partial(\zeta_1, \zeta_2, \xi_1)$ and some rearrangement yields

$$\mathbf{J} = \begin{bmatrix} (x_1 - x_3)\bar{\xi} & (y_1 - y_3)\bar{\xi} & (z_1 - z_3)\bar{\xi} \\ (x_2 - x_3)\bar{\xi} & (y_2 - y_3)\bar{\xi} & (z_2 - z_3)\bar{\xi} \\ -(\eta - 1)\bar{x} & -(\eta - 1)\bar{y} & -(\eta - 1)\bar{z} \end{bmatrix}, \tag{4.14}$$

where the introduced variables are

$$\left.\begin{aligned} \bar{\xi} &= \xi_1 + \eta\xi_2, \\ \bar{x} &= \zeta_1 x_1 + \zeta_2 x_2 + \zeta_3 x_3, \\ \bar{y} &= \zeta_1 y_1 + \zeta_2 y_2 + \zeta_3 y_3, \\ \bar{z} &= \zeta_1 z_1 + \zeta_2 z_2 + \zeta_3 z_3. \end{aligned}\right\} \tag{4.15}$$

Note that the last three equations of (4.15) represent the approximation of the shape of the surface triangle ABC (Fig. 3.4). The determinant of the Jacobian, i.e. its magnitude, is readily expressed as

$$|\mathbf{J}| = -(\bar{\xi})^2(\eta - 1)(|\mathbf{A}| - |\mathbf{B}|), \tag{4.16}$$

with $|\mathbf{A}|$ and $|\mathbf{B}|$ denoting the determinants

$$|\mathbf{A}| = \begin{vmatrix} x_1 & y_1 & z_1 \\ x_2 & y_2 & z_2 \\ x_3 & y_3 & z_3 \end{vmatrix}, \qquad |\mathbf{B}| = \begin{vmatrix} x_1 - x_3 & y_1 - y_3 & z_1 - z_3 \\ x_2 - x_3 & y_2 - y_3 & z_2 - z_3 \\ x_o & y_o & z_o \end{vmatrix}. \tag{4.17}$$

It is evident from (4.15)–(4.17) that, since $|\mathbf{A}|$ and $|\mathbf{B}|$ are constant, the determinant $|\mathbf{J}|$ is a function of the local coordinate ξ_1 alone.

The Jacobian of the inverse transformation $\partial(\zeta_1, \zeta_2, \xi_1)/\partial(x, y, z)$, equal to the inverse of the Jacobian of the forward transformation $\mathbf{J}^{-1}$, can be evaluated analytically which is due to the relatively simple form of $|\mathbf{J}|$:

$$\mathbf{J}^{-1} = \frac{1}{|\mathbf{A}| - |\mathbf{B}|} \begin{bmatrix} \dfrac{c_{11}}{\bar{\xi}} & \dfrac{c_{12}}{\bar{\xi}} & \dfrac{c_{13}}{\bar{\xi}} \\ \dfrac{c_{21}}{\bar{\xi}} & \dfrac{c_{22}}{\bar{\xi}} & \dfrac{c_{23}}{\bar{\xi}} \\ \dfrac{c_{31}}{-(\eta - 1)} & \dfrac{c_{32}}{-(\eta - 1)} & \dfrac{c_{33}}{-(\eta - 1)} \end{bmatrix}, \tag{4.18}$$

where elements of the auxiliary matrix $\mathbf{C}$ are given by

$$\left.\begin{aligned}
c_{11}^{-1} &= (y_2 - y_3)\overline{z} - (z_2 - z_3)\overline{y}, \\
c_{12}^{-1} &= -(x_2 - x_3)\overline{z} + (z_2 - z_3)\overline{x}, \\
c_{13}^{-1} &= (x_2 - x_3)\overline{y} - (y_2 - y_3)\overline{x}, \\
c_{21}^{-1} &= (y_1 - x_3)\overline{z} - (z_1 - z_3)\overline{y}, \\
c_{22}^{-1} &= (x_1 - x_3)\overline{z} - (z_1 - z_3)\overline{x}, \\
c_{23}^{-1} &= -(x_1 - x_3)\overline{y} + (y_1 - y_3)\overline{x}, \\
c_{31}^{-1} &= (y_1 - y_3)(z_2 - z_3) - (z_1 - z_3)(y_2 - y_3), \\
c_{32}^{-1} &= (z_1 - z_3)(x_2 - x_3) - (x_1 - x_3)(y_2 - y_3), \\
c_{33}^{-1} &= (x_1 - x_3)(y_2 - y_3) - (y_1 - y_3)(x_2 - x_3).
\end{aligned}\right\} \tag{4.19}$$

4.4 *Numerical integration over the 'toblerone'*

Although closed-form expressions have been derived for Jacobian matrices (4.14) and (4.18), associated with the forward and inverse coordinates transformations respectively, they are not constant as their simplex counterparts (Eqs. (1.7) and (1.8) of Appendix 3). Attempts to evaluate the stiffness matrix (4.12) symbolically or establish some kind of universal matrices proved to be not very practical; it is more efficient to perform the integration numerically, using Gaussian integration formulae.

The examination of Eq. (4.12) reveals that the integrand represents a polynomial in coordinates ζ_1, ζ_2, and ξ_1 for which the Gaussian scheme with an appropriate number of points yields exact integration. Indeed, it can be seen from Eqs. (4.15), (4.18) and (4.19) that the matrix $\mathbf{J}^{-1}$ can be partitioned as follows

$$\mathbf{J}^{-1} = \frac{1}{|\mathbf{A}| - |\mathbf{B}|} \begin{bmatrix} \dfrac{1}{\bar{\xi}}\mathbf{C}_1 \\ -\dfrac{1}{(\eta - 1)}\mathbf{C}_2 \end{bmatrix}, \tag{4.20}$$

where the matrix $\mathbf{C}_1$ is function of local coordinates ζ_1, ζ_2, while entries of $\mathbf{C}_2$ are constant for a given element. Collecting all the Jacobian related terms, the following matrix is obtained:

$$\mathbf{J}^{-\mathrm{T}}\mathbf{J}^{-1}|\mathbf{J}| = -\frac{(\eta - 1)}{|\mathbf{A}| - |\mathbf{B}|}\left[\mathbf{C}_1^{\mathrm{T}}\mathbf{C}_1 + \left(\frac{\bar{\xi}}{\eta - 1}\right)^2 \mathbf{C}_2^{\mathrm{T}}\mathbf{C}_2\right] \tag{4.21}$$

whose elements are the linear combinations of polynomial terms $\left(\zeta_1^i \zeta_2^j\right)^2$, $i+j=1$, and ξ_1^2.

The minimum number of integration points I_s and I_t required for an exact numerical integration over the line segment and triangle is also determined from the order of interpolation functions α_j^t and α_k^s. According to (4.13), the components of $\nabla_{\zeta_1\zeta_2\xi_1}\alpha_i$ are formed by the polynomials $\zeta_1^m \zeta_2^n \xi_1^o$, $m+n+o \le N_t + N_s - 1$, with $\max(m+n) = N_t$ and $\max(o) = N_s$. Taking into account (4.21), the degree of the polynomial function

$$P_{ij} = (\nabla_{\zeta_1\zeta_2\xi_1}\alpha_i)^{\mathrm{T}} \mathbf{J}^{-\mathrm{T}} \mathbf{J}^{-1} \nabla_{\zeta_1\zeta_2\xi_1}\alpha_j \, |\mathbf{J}|, \tag{4.22}$$

is at most $2N_t + 2$ in both variables ζ_1 and ζ_2, and at most $2N_s + 2$ in ξ_1. The number of integration point along with their weights w and coordinates x, α, β, γ are supplied in Section 4, Appendix 4 for the first few N_t and N_s. Elements of the stiffness matrix $\mathbf{K}^{\varphi\varphi}$ are then evaluated by successively applying Gaussian integration formulae for the line segment and triangle:

$$K_{ij}^{\varphi\varphi} = \epsilon_0 \sum_{m=1}^{I_s} \sum_{n=1}^{I_t} w_m^s w_n^t P_{ij}(x_m, \alpha_n, \beta_n, \gamma_n) \tag{4.23}$$

4

Computer implementation

1. Introduction

Numerical solution of the three-dimensional piezoelectric problem with open electric boundaries is accomplished in two stages: the generation of a suitable superelement matrix S and subsequent solution of the piezoelectric — static or vibrational — problem itself. Once matrix S is generated by a separate program, it can be applied to a great variety of interior problems provided that the continuity of electric potential across the boundary is preserved. The overall solution is computationally very demanding because of large matrices arising from the three-dimensional finite element discretization of both the interior and exterior domains. It is typically very difficult to isolate the numerical methods from the rest of the application. Therefore, most of the research efforts were devoted to finding appropriate data structures and selecting methods of implementation that suit best the computing algorithms used. It was also found important to exploit the symmetry properties of the region and the special structure of matrices whenever possible.

This chapter describes practical computational aspects of the numerical solution, which comprises the following stages:

- generation of the finite element mesh;
- assembly of the global finite element matrices from their local representations — expressed by Eqs. (3.16), (3.27) of Chapter 3 and the superelement matrix S — accompanied by a simultaneous imposition of boundary conditions;
- solution of the finite element equations associated with the deterministic (static) and eigenvalue (vibration) problems.

2. Mesh generation

An automatic mesh generation program was designed to discretize a three-dimensional rectangular region into high order tetrahedral elements. Rectangular shapes are typical for piezoelectric vibrators and also most convenient from the point of view of programming simplicity. The number of elements E_x, E_y, E_z along the edges and the order of interpolation N are the only input parameters required. The very same procedure is used by the program that implements the ballooning algorithm to create the inner boundary of the superelement. Indeed, a set of surface triangles arises naturally from the discretization of the interior region into tetrahedra. Provided the input parameters are the same for both programs, the identical element topologies on the surface of the rectangular region automatically guarantee the continuity of approximating functions across the surface when the superelement is combined with the interior model.

The program starts by generating a set of uniformly distributed nodes that partition the interior region into $E_x \times E_y \times E_z$ rectangular prisms, or 'brick' elements, as shown in Fig. 4.1.

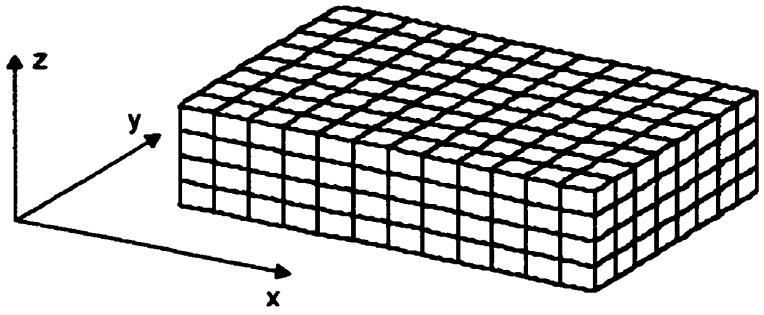

Fig 4.1 Rectangular region subdivided into $E_x \times E_y \times E_z$ (here $E_x = 12$, $E_y = 8$, $E_z = 4$) 'brick' elements.

Each 'brick' is then dissected into five tetrahedra according to one of the two basic schemes (Fig. 4.2), which must be properly alternated in the mesh in order to preserve the continuity of approximating functions across the element faces. Therefore, the division of the whole region involves $E_V = 5E_xE_yE_z$ tetrahedral elements for the solution of the interior problem and $E_S = 4(E_xE_y + E_xE_z + E_yE_z)$ triangular elements on the surface to build the

superelement. For a given order of interpolation N, each tetrahedron is represented by $M = (N+1)(N+2)(N+3)/6$ nodes, thus producing the total of ME_V nodes over the entire set of elements. Their Cartesian (global) coordinates (x_i, y_i, z_i), $i = 1, ..., M$ are easily determined from the local coordinates $\zeta_1^i, \zeta_2^i, \zeta_3^i, \zeta_4^i$ and the tetrahedron vertex coordinates by using Eq. (1.5), Appendix 3. Because the nodes homogeneous coordinates ζ_m^i, $m = 1, ..., 4$ are independent of the tetrahedron shape and size, they can be calculated once (Eq. (2.3), Appendix 3) and stored as arrays of integer quotients of the type j/N, where $j = 0, ..., N$.

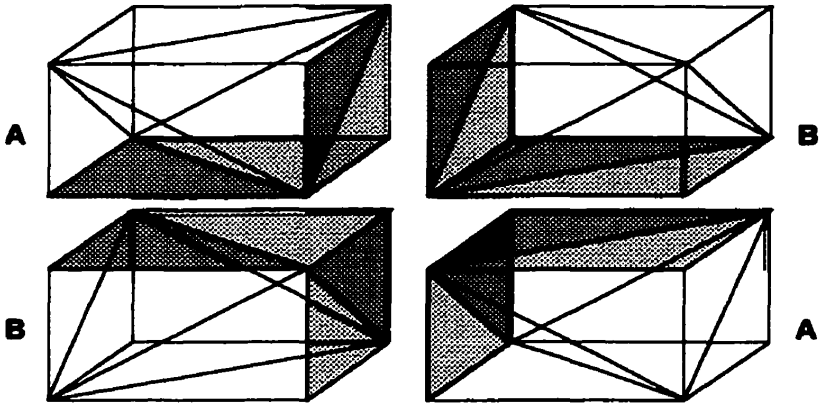

Fig 4.2 Brick partition into two types (A and B) of tetrahedra arrangements and their respective position in the mesh.

The obtained elements are disjoint in the sense that a shared node has as many different indexes as the number of tetrahedra it belongs to. This means that several sets of variables $(\mathbf{u}, \varphi)$ may be associated with the same node. To create the finite element mesh (i.e. an assembled set of elements and nodes), and to enforce the continuity of approximated physical values across the element boundaries, a conjoint, or global, node numbering must be employed. This can be accomplished by hashing the list of 'disjoint' nodes $idis = 1, ..., ME_V$ by their Cartesian position $\mathbf{r} = (x_{idis}, y_{idis}, z_{idis})^T$ in order to eliminate those with identical $\mathbf{r}$. A possible hashing function is

$$h(idis) = \sum_{k=1}^{3} p_k r_{ie(k)}, \tag{2.1}$$

where p_1, p_2, p_3 are the weighting coefficients, and ie is the index table of the array (E_x, E_y, E_z), rearranged into ascending order. For example, if $E_x = 6$, $E_y = 4$, $E_z = 8$, then $ie(1) = 2$, $ie(2) = 1$, $ie(3) = 3$, and (2.1) becomes $h(idis) = p_1 y_{idis} + p_2 x_{idis} + p_3 z_{idis}$. On sorting the array h, those nodes $idis$ that have the same value of h, i.e. the same location r, are assigned a common global index $ig(idis)$. The global node numbering $ig = 1, \ldots, n$ is then used to update the lists of E_V tetrahedra and E_S surface triangles so that they be defined by uniquely numbered nodes.

However, the role of function h is not limited to interconnecting elements. Its second objective is to order nodes, and therefore variables, in a way to reduce the bandwidth of the finite element matrices for the interior problem. By making a special choice of weighting coefficients p_i, so that they satisfy, in particular, condition $p_1 < p_2 < p_3$, the rearrangement of array h in ascending order gives priority to nodes located in the direction characterized by the minimum number of elements $E_{ie(1)}$ along the edge, while those in the direction of the maximum number of elements $E_{ie(3)}$ are numbered last, i.e. with the highest indices. This guarantees that nodes are indexed in a consistent, though not necessarily optimal, manner and the maximum node number difference does not exceed $N^2(E_{ie(1)} + 1)(E_{ie(2)} + 1)$. Obviously, such an approach favors meshes elongated in one particular direction (strip geometry) for which $E_{ie(3)} \gg E_{ie(2)} \approx E_{ie(1)}$.

3 Block ballooning method for rectangular regions

The general three-dimensional ballooning algorithm for modeling Laplace's equation was described in Chapter 3. As soon as the global finite element matrix for the bordering region $\Omega_{(1)}$ is assembled from the 'toblerone' matrices and all the interior nodes are eliminated by the process of static condensation, the method amounts to implementing Eqs. (2.14)–(2.18) of the same chapter. For the mesh size n_S (i.e. the number of surface nodes), the overall storage requirement includes:

- two symmetric matrices $\mathbf{S}_{11}$, $\mathbf{S}_{22}$: $2 \times n_S(n_S+1)/2$,
- one unsymmetric matrix $\mathbf{S}_{12}$: n_S^2,
- one triangular matrix $\mathbf{D}$: $n_S(n_S+1)/2$,
- two unsymmetric matrices $\mathbf{D}^{-1}\mathbf{S}_{12}$, $\mathbf{D}^{-1}\mathbf{S}_{12}^{\mathrm{T}}$: $2 \times n_S^2$,

i.e. $9n_S^2/2$ locations in total. In practice, there is no need to keep all these matrices in the fast-access memory. Indeed, inspection of Eqs. (2.14)–(2.17) of Chapter 3 shows that, without impairing computational efficiency, it suffices to allocate only $5n_S^2/2$ memory to store two unsymmetric matrices and one linear array to house a symmetric matrix. The greatest storage requirement $\left(2n_S^2\right)$ is due to matrices $\mathbf{D}^{-1}\mathbf{S}_{12}$ and $\mathbf{D}^{-1}\mathbf{S}_{12}^{\mathrm{T}}$ that are accessed simultaneously at each step of the ballooning recursion. The lower triangles of symmetric matrices $\mathbf{S}_{11}$ and $\mathbf{S}_{22}$ are alternately generated in the one-dimensional array $\left(n_S^2/2\right)$, and subsequently copied to a secondary storage device (disk) to be retrieved during the next iteration. The same array is used to house the triangular factor $\mathbf{D}$. On calculation, the matrix $\mathbf{S}_{12}$ overwrites one of the unsymmetric matrices, and can immediately be used to form the new matrices $\mathbf{D}^{-1}\mathbf{S}_{12}$ and $\mathbf{D}^{-1}\mathbf{S}_{12}^{\mathrm{T}}$.

The computing time for each iteration is proportional to the total number of floating-point operations, or *flops*[1], required for

---

[1] In this chapter a 'traditional' definition of a flop, as one floating-point multiplication and one addition or substraction (Watkins, 1991), is used. If the new definition of flop was used (Golub and Van Loan, 1989), the number of arithmetic operations would double.

- one Choleski factorization of $\sigma\mathbf{S}_{11}+\mathbf{S}_{22}$: $n_S^3/6$,
- two forward substitutions $\mathbf{D}^{-1}\mathbf{S}_{12}^{\mathrm{T}}$, $\mathbf{D}^{-1}\mathbf{S}_{12}$: $2\times(n_S^2/2\times n_S)$,
- two symmetric $\left[\mathbf{D}^{-1}\mathbf{S}_{12}^{(k)\mathrm{T}}\right]^{\mathrm{T}}\left[\mathbf{D}^{-1}\mathbf{S}_{12}^{(k)\mathrm{T}}\right]$ and $\left[\mathbf{D}^{-1}\mathbf{S}_{12}^{(k)}\right]^{\mathrm{T}}\left[\mathbf{D}^{-1}\mathbf{S}_{12}^{(k)}\right]$, and one unsymmetric $\left[\mathbf{D}^{-1}\mathbf{S}_{12}^{(k)\mathrm{T}}\right]^{\mathrm{T}}\left[\mathbf{D}^{-1}\mathbf{S}_{12}^{(k)}\right]$ matrix multiplications : $2\times(n_S^3/2)+n_S^3$.

Therefore, if applied directly, the algorithm would require $5n_S^2/2$ memory and $19n_S^3/6\times iter\approx 3n_S^3\times iter$ computing time, where *iter* is the number of iterations, typically six or seven. These core memory requirements and computing time estimates increase rapidly with n_S but can be minimized significantly for rectangular regions. In this case, superelement matrices possess certain symmetries, so that only a part of the matrix needs to be calculated and stored.

3.1 *Handling of symmetry*

A rectangular parallelepiped has at least three symmetry planes that subdivide it into eight equivalent parts, or octants, numbered as shown in Fig. 4.3. If the origin point $\mathbf{r}_o=\mathbf{r}_o(x_o,y_o,z_o)$ (i.e. the point with respect to which the successively ballooned boundaries are concentric) is placed at the geometric center of the region of interest and the numbers of elements along edges E_x, E_y, E_z are even, the mesh of nodes inherits the same symmetry. Nevertheless, it is not sufficient to consider only one octant of the problem domain as can be done for isotropic problems. Because the interior piezoelectric region is always anisotropic, symmetry must be imposed explicitly on the whole superelement matrix. This leads to a block balloon recursion procedure described below.

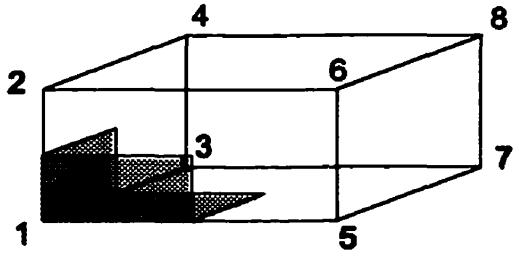

Fig 4.3 Basic one-eighth part of a rectangular region.

Based on their Cartesian position **r**, all nodes can be partitioned into eight equivalent sets, corresponding to the eight symmetrical parts of the surface (Fig. 4.3). With this node ordering, a generic submatrix **S** (e.g. $\mathbf{S}_{11}$, $\mathbf{S}_{12}$, or $\mathbf{S}_{22}$) involved in the ballooning recursion is composed of eight independent blocks $\mathbf{G}^{(1)}$, $\mathbf{G}^{(2)}$,..., $\mathbf{G}^{(8)}$ distributed inside **S** according to the permutation table shown in Fig. 4.4. Because an element S_{ij} of matrix **S** can be interpreted as the potential at node i due to the source located at node j, these submatrices have the following meanings: $\mathbf{G}^{(1)}$ incorporates electrostatic interactions between nodes within the same symmetrical parts 1–1,..., 8–8; the block $\mathbf{G}^{(2)}$ — between octants 1–2, 3–4, 5–6, 7–8, and so on; finally, $\mathbf{G}^{(8)}$ reflects the interaction between parts 1–8, 2–7, 3–6, 4–5, symmetric about the origin point. Moreover, the blocks $\mathbf{G}^{(ioct)}$, $ioct = 1, ..., 8$ of symmetric matrices $\mathbf{S}_{11}$ and $\mathbf{S}_{22}$ are also symmetric, while for the unsymmetric matrix $\mathbf{S}_{12}$ they are respectively unsymmetric.

1	2	3	4	5	6	7	8
2	1	4	3	6	5	8	7
3	4	1	2	7	8	5	6
4	3	2	1	8	7	6	5
5	6	7	8	1	2	3	4
6	5	8	7	2	1	4	3
7	8	5	6	3	4	1	2
8	7	6	5	4	3	2	1

Fig 4.4 The structural symmetry of matrices $\mathbf{S}_{11}$, $\mathbf{S}_{12}$, and $\mathbf{S}_{22}$ arising from a special node numbering. Only the shadowed part needs to be calculated and stored.

The equivalence between nodes belonging to different octants is established by means of a $|\mathbf{r} - \mathbf{r}_o|$–based hashing function. Because symmetrical nodes are located at equal distances from the origin, they are easily identified on sorting the associated hashing array as those having identical value of this function. A surface node *igs* and its seven symmetrical counterparts are assigned the same index *iloc*, referred to as 'local' by analogy with the assembly of the global matrix **S** from the element matrices, which, in this case, are represented by the blocks $\mathbf{G}^{(ioct)}$. A special two-dimensional array $i8(1..n_S, 1..2)$ maps the global surface node index *igs* onto the

- octant number $ioct = 1,...,8$:

$$i8(igs, 1) = ioct; \tag{3.1}$$

- local node index $iloc = 1,...,n_{oct}$:

$$i8(igs, 2) = iloc, \tag{3.2}$$

where n_{oct} is the number of 'independent' nodes that belongs to the first, for instance, octant shown in Fig. 4.3. The index array $i8$ and the permutation matrix $\mathbf{P}$, which is an exact replica of the table shown in Fig. 4.4, allow reconstituting the entire matrix $\mathbf{S}$ from its eight independent blocks $\mathfrak{S}^{(ioct)}$ as follows:

$$\begin{aligned} &\text{for } igs = 1, ..., n_S \\ &\quad \Big[\text{for } jgs = 1, ..., n_S \\ &\qquad \Big[\begin{array}{ll} ioct = i8(igs, 1), & joct = i8(jgs, 1) \\ iloc = i8(igs, 2), & jloc = i8(jgs, 2) \end{array} \\ &\qquad\quad S_{igs,jgs} = \mathfrak{S}^{P(ioct,joct)}_{iloc,jloc}. \end{aligned} \tag{3.3}$$

Since the number of nodes in one octant n_{oct} is roughly equal to $n_S/8$, matrices $\mathbf{S}_{11}$, $\mathbf{S}_{12}$, and $\mathbf{S}_{22}$ occupy approximately one eighth of the storage required had their symmetry not been exploited.

3.2 *Block recursive process*

The structural symmetry of ballooning matrices allows also minimizing the computing time, evaluated at $3n_S^3$ per iteration for the general algorithm. First, this reduction is related to the very same fact that only one eighth of matrices $\mathbf{S}_{11}$, $\mathbf{S}_{12}$, and $\mathbf{S}_{22}$ entries needs to be calculated thus diminishing the amount of operations associated with matrix multiplications by $1/8$. Another, less obvious, simplification arises from the observation that the inverse symmetric matrix $(\mathbf{S}_{22} + \sigma\,\mathbf{S}_{11})^{-1}$, represented by its Choleski factorization $\mathbf{D}^{-\mathrm{T}}\mathbf{D}^{-1}$, possesses the symmetry of matrices $\mathbf{S}_{11}$ and $\mathbf{S}_{22}$.[2] However, no attempt to invert $\mathbf{S}_{22} + \sigma\,\mathbf{S}_{11}$ blockwise will be made here; rather, this fact is used to conclude that the matrices $(\mathbf{D}^{-\mathrm{T}}\mathbf{D}^{-1})\mathbf{S}_{12}^{\mathrm{T}}$ and $(\mathbf{D}^{-\mathrm{T}}\mathbf{D}^{-1})\mathbf{S}_{12}$ also inherit the symmetry pattern shown in Fig. 4.4, both being products of matrices with identical block structures. They are thereby

[2] This can easily be verified by generalizing the Frobenious formula for the 2×2 block inverse (Gantmacher, 1988) to an 8×8 block matrix.

characterized by the same permutation matrix $\mathbf{P}$ and index array $i8$, that are used to describe the distribution of elements in $\mathbf{S}_{11}$, $\mathbf{S}_{12}$, and $\mathbf{S}_{22}$ (Eq. (3.3)).

It becomes more convenient to recast Eqs. (2.14)–(2.16) from Chapter 3 as

$$\mathbf{S}_{11}^{(k+1)} = \mathbf{S}_{11}^{(k)} - \mathbf{S}_{12}^{(k)}\left[\mathbf{D}^{-\mathrm{T}}\mathbf{D}^{-1}\mathbf{S}_{12}^{(k)\mathrm{T}}\right], \tag{3.4}$$

$$\mathbf{S}_{12}^{(k+1)} = -\sigma\mathbf{S}_{12}^{(k)}\left[\mathbf{D}^{-\mathrm{T}}\mathbf{D}^{-1}\mathbf{S}_{12}^{(k)}\right], \tag{3.5}$$

$$\mathbf{S}_{22}^{(k+1)} = \sigma\,\mathbf{S}_{22}^{(k)} - \sigma^2\mathbf{S}_{12}^{(k)\mathrm{T}}\left[\mathbf{D}^{-\mathrm{T}}\mathbf{D}^{-1}\mathbf{S}_{12}^{(k)}\right], \tag{3.6}$$

since matrices $\mathbf{D}^{-1}\mathbf{S}_{12}^{(k)\mathrm{T}}$ and $\mathbf{D}^{-1}\mathbf{S}_{12}^{(k)}$ are never formed explicitly, which would inevitably destroy the block structure of Eqs. (3.4)–(3.6). Therefore, all the matrix multiplications in (3.4)–(3.6), as well as the forward elimination and back substitution $\mathbf{D}^{-\mathrm{T}}\mathbf{D}^{-1}\mathbf{S}_{12}^{(k)\mathrm{T}}$ and $\mathbf{D}^{-\mathrm{T}}\mathbf{D}^{-1}\mathbf{S}_{12}^{(k)}$ can be performed only on a one-eighth of matrix $\mathbf{S}_{12}^{(k)}$, i.e. on its eight independent blocks $\mathbf{S}_{12}^{(ioct)}$, as shown in Fig. 4.5.

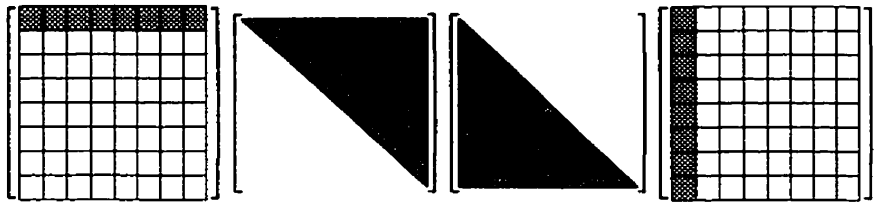

Fig 4.5 Accessed parts of matrices used to form the products $\mathbf{S}_{12}^{(1,\mathrm{T})}\left[\mathbf{D}^{-\mathrm{T}}\mathbf{D}^{-1}\mathbf{S}_{12}^{(1,\mathrm{T})}\right]$.

In this new recursion scheme, the core memory is redistributed among the

- eight symmetric blocks $(n_S^2/16)$ to store alternately $\mathbf{S}_{11}^{(ioct)}$ and $\mathbf{S}_{22}^{(ioct)}$, $ioct = 1, \ldots, 8$;
- two sets of eight unsymmetric blocks $(2 \times n_S^2/8)$ to simultaneously access the 'old' (k) and store 'new' $(k+1)$ submatrices $\mathbf{S}_{12}^{(ioct)}$;
- triangular factor $\mathbf{D}$ $(n_S^2/2)$,

which gives the total of $13n_S^2/16 \approx 3n_S^2/4$ data elements — approximately one third of the initial $5n_S^2/2$. Note that one auxiliary n_S–vector is now sufficient to house the result of the forward elimination and back substitution $\mathbf{D}^{-\mathrm{T}}\mathbf{D}^{-1}\mathbf{S}_{12}^{(1,\mathrm{T})}$

since it is used only once during an iteration and needs not be generated in a matrix.

Except for the Choleski factorization of $\sigma \mathbf{S}_{11} + \mathbf{S}_{22}$, for which the arithmetic $(n_S^3/6)$ remains unaltered, the amount of work required to execute one loop of the ballooning recursion (3.4)–(3.6) is composed now of the cost of two partial, i.e. involving $n_S/8$ columns, forward eliminations and back substitutions $(2 \times n_S^2/2 \times n_S/8)$, and of two (also partial) symmetric $(2 \times n_S^3/16)$ and one unsymmetric $(n_S^3/8)$ matrix multiplications. As a result, the overall computing time for the block balloon recursion reduces to $2n_S^3/3$ per iteration, which is approximately five times less than that required if the full matrices $\mathbf{S}_{11}$, $\mathbf{S}_{12}$, and $\mathbf{S}_{22}$ were handled. For instance, on a Pentium II 400 MHz computer, the time required to generate a final $\mathbf{S}_{11}$ matrix after seven iterations ranges from 12 minutes for the mesh size $n_S = 866$ to 12 hours for $n_S = 3458$ respectively.

It is also important to note that in the developed computer programs single precision (32-bit) arithmetic was employed to store arrays of data, while all the dot product operations were performed in double precision (64-bit) to diminish the roundoff error.

4 Assembly of global matrices

Each node ig of the finite element mesh of n nodes is associated with four variables: the three components of mechanical displacement u_{ig}^1, u_{ig}^2, u_{ig}^3 and one electric potential φ_{ig}. If all the mechanical variables $\mathbf{U}$ are numbered first, and all the electrical potentials $\mathbf{\Phi}$ — last, i.e. when the mapping between the nodal set of variables $(\mathbf{u}, \varphi)_{ig}$ and the vector $\mathbf{x} = (\mathbf{U}, \mathbf{\Phi})^{\mathrm{T}}$ of all the unknowns is

$$\begin{pmatrix} u_{ig}^1 \\ u_{ig}^2 \\ u_{ig}^3 \\ \varphi_{ig} \end{pmatrix} = \begin{pmatrix} x_{ig} \\ x_{ig+n} \\ x_{ig+2n} \\ x_{ig+3n} \end{pmatrix}, \tag{4.1}$$

the $4n \times 4n$ global stiffness $\mathbf{K}$ and mass $\mathbf{M}$ matrices[3] can be partitioned respectively as

$$\mathbf{K} = \begin{bmatrix} \mathbf{K}_{uu} & \mathbf{K}_{u\varphi} \\ \mathbf{K}_{u\varphi}^{\mathrm{T}} & -\mathbf{K}_{\varphi\varphi} \end{bmatrix}, \tag{4.2}$$

$$\mathbf{M} = \begin{bmatrix} \mathbf{M}_{uu} & 0 \\ 0 & 0 \end{bmatrix}. \tag{4.3}$$

In (4.3) the size of the nonsingular submatrix $\mathbf{M}_{uu}$ of the mass matrix is $3n \times 3n$, and, in fact, the term 'mass matrix' will be employed in the present section to denote precisely $\mathbf{M}_{uu}$. For n typically ranging in a three-dimensional mesh from 10^3 to 10^4, the dimensions of the unconstrained stiffness $n_K = 4n$ and mass $n_M = 3n$ matrices are quite large. Moreover, because (4.2) and (4.3) are assembled from the element matrices, they are very sparse, so that it is impractical, and often impossible, to store them fully.

The choice of data structures for large sparse symmetric matrices is intimately related to the numerical techniques employed for solving the finite element equations. Both the storage mode and numerical methods must exploit the special structure of the global matrices to minimize the computing time and storage requirements. That is why the two conventional storage schemes — *sparse* and

---

[3] Note that indices $\mathbf{u}$ and φ have been shifted to the lower position since in the present chapter the elastic, piezoelectric, and dielectric submatrices will not be addressed elementwise.

profile — considered in the present section are best regarded integrally with the conjugate gradient and Lanczos methods described in Section 5.

A point to note is that, among other factors discussed below, the number of elements in the global stiffness matrix **K** depends on the material properties of the piezoelectric crystal. Although it varies only slightly with materials and crystal orientations, it should still be mentioned that, for the sake of consistency, all the illustrative examples given throughout this and the following sections were generated for the AT-cut of quartz.

4.1 *Sparse storage*

The sparse scheme stores only nonzero elements of matrix **A** of size $n \times n$ in a one-dimensional array sa, and some additional, or overhead, information about the location of these elements. Typically the sparse storage is used in conjunction with iterative algorithms that regard **A** as an operator: **A** is frequently referenced through the matrix-vector product **Ax** but never modified in the course of iterations. A speedy retrieval of **A**'s elements from its compact storage is best accomplished by storing indices of the nonzero elements in an integer one-dimensional array ija, thus avoiding an expensive searching through sa by means of some indexing function (Silvester, 1993). In this respect, the *row-indexed sparse storage mode* (Press *et al.*, 1992) is one of the most economical and also most commonly used.

In the sparse storage mode,

- the first n locations of sa store **A**'s diagonal entries; location $n+1$ is not used. Starting from position $n+2$, the array houses **A**'s nonzero off-diagonal elements, ordered by rows, and, within each row, ordered by columns. For **A** symmetric, only the nonzero entries from its lower triangular part need to be stored;
- the first n locations of ija store pointers to array sa, i.e. indices of sa where the new row begins; as follows from the description of sa, $ija(1) = n+2$, and $ija(n+1)$ equals the total number of nonzero elements in **A**. Starting from position $n+2$, the array ija stores the column number of the corresponding element in sa.

If the nonzero elements of **A** are stored in sa as 4-byte real numbers, and the corresponding column indices — as 2-byte integers, the overhead storage for the above scheme (array ija) is half the storage required for sa. The described data structure is best illustrated on the example of a symmetric matrix-vector multiplication $\mathbf{y} = \mathbf{Ax}$:

$$
\begin{array}{l}
\text{for } i = 1, \ldots, n \\
\quad \left[\begin{array}{l}
y(i) = sa(i)x(i) \\
\text{for } k = ija(i), \ldots, ija(i+1) - 1 \\
\quad \left[\begin{array}{l}
j = ija(k) \\
y(i) = y(i) + sa(k)x(j) \\
y(j) = y(j) + sa(k)x(i).
\end{array} \right.
\end{array} \right.
\end{array}
\tag{4.4}
$$

Typically, the global matrices are so large that not only do they need to be manipulated in sparse format, but have to be generated directly in this format, thus bypassing the full storage mode. As will be clear from the next section that deals with the superelement, the sparsity patterns of **K** is not known in advance, and, therefore, the element matrices cannot be simply embedded in the connected (global) assembly of elements as shown in Eq. (2.5) of Chapter 3. Thus, a generic global matrix **A** must be assembled one row at a time, or variable-by-variable, so that for each row i, all the corresponding nonzero positions $ija(i), \ldots, ija(i+1) - 1$ are filled prior to starting row $i + 1$. Because the number of nonzero locations in **A** does not depend on the variable numbering, i.e. the mapping between the variable $\left(u_{ig}^1, u_{ig}^2, u_{ig}^3 \text{ or } \varphi_{ig}\right)$ at node ig and the unknown $x(i)$ is irrelevant for the sparse format, this is equivalent to performing matrix assembly in a *node-by-node* fashion.

To assemble the row corresponding to a given node, the contribution from all the elements that contain this node must be taken into account. This implies that for each node ig, one must determine the set of elements $e_1, e_2, \ldots, e_k$ the node belongs to. This task is, in a sense, inverse to that of interconnecting elements by assigning a global node index ig to the node shared by k elements. It is, therefore, natural to invoke the 'disconnected' node indices $idis$ because of the unique correspondence between them and the elements. In particular, in the regular mesh described in Section 2, index $idis$ is assigned in a consistent manner

$idis = eM - 1 + m$ to a node occupying position m among the M nodes of the element e. This indicates that values m and e can easily be recovered from $idis$ as

$$\left.\begin{aligned} m &= idis \bmod M \\ e &= \frac{idis - m}{M} + 1 \end{aligned}\right\}. \tag{4.5}$$

The sparse assembly of row ig of the global matrix **A** amounts to looping over the list of disconnected nodes $idis = 1, ..., ME_V$, and, for all $idis$ that share the same global index ig, collecting nonzero elements from the row m of e's local matrix, where m and e are determined as in (4.5). As they arrive, the nonzero elements are first accumulated in a separate array *srow* along with the corresponding column numbers jg, stored in a parallel integer array *icol*. After scanning all the elements that meet at node ig, i.e. elements which contribute to the row ig of the global matrix, *icol* is sorted in ascending order and attached to the indexing array *ija*. Then, elements $srow(icol(i))$, $i = 1, ..., s_{ig}$, where s_{ig} is the total number of nonzeros in row ig, are added to the array *sa*, and $ija(ig + 1)$ is set to $ija(ig) + s_{ig}$. If the fastest sorting technique *quicksort* is used, the process of sorting the array *icol* requires $O(s_{ig}\log(s_{ig}))$ work; therefore, the assembly of the entire matrix is least a $O(ns\log(s))$ process, where s denotes the average number of nonzero elements per row.

The value of s is an important characteristic of the sparse storage mode. As follows from the description of the indexing array *ija*, it can be calculated for a given matrix as

$$s = \frac{ija(n + 1)}{n}. \tag{4.6}$$

Through the sparsity structure of the element matrices, s depends on the tetrahedron order N (Table 4.1) and, in the case of the stiffness matrix, on material properties. For meshes which are large enough to have the number of interior (fully connected) nodes clearly superior to that of surface nodes (partially connected), s is practically independent of the variable numbering. It is interesting to note, that there is almost no increase in s for the mass matrix as the element order changes from 2 to 3. This is explained by the fact that the tetrahedral mass matrix for $N = 3$ has a certain amount of zero entries, in contrast to other

practical element orders (at least the first five), for which the local mass matrices are full. This suggests that if higher accuracy needs to be achieved without increasing the sparse storage of the mass matrix, this peculiarity of tetrahedra of third order can prove useful!

Table 4.1 Average number of nonzeros s per row.

Order of tetrahedron N	s	
	Stiffness matrix **K**	Mass matrix **M**
1	27	6
2	48	12
3	80	13
4	121	32

Table 4.1 also demonstrates that since the nodal variables u^1, u^2, u^3 are related in the local stiffness matrix by the elastic tensor $\mathbf{c}^E$ and coupled to φ by piezoelectric coefficients $\mathbf{e}$, the average number of nonzero entries per row s_K and s_M for matrices **K** and **M**, respectively, are approximately in the ratio 4:1 (except for elements of order $N = 3$). Because s is independent of the mesh configuration, for a given element order N the number of elements in the sparse storage of global matrices $\mathbf{K}_{4n\times 4n}$ and $\mathbf{M}_{3n\times 3n}$ are functions of the number of nodes n alone (Fig. 4.6).

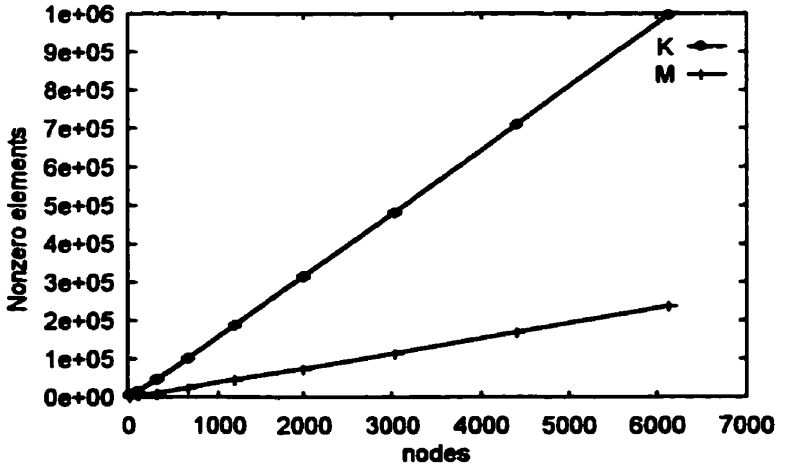

Fig 4.6 The number of nonzero elements in global matrices for the element order $N = 2$.

It should be noted that despite the elastic and piezoelectric coupling of variables in the stiffness matrix, its sparse storage is so economical that for a wide range of n it occupies less than 1% of the full matrix storage.

4.2 *Inclusion of the superelement matrix*

The superelement, represented by the final matrix $\mathbf{S}_{11}$ of the ballooning recursion, is added to the global stiffness matrix $\mathbf{K}$ as a regular element defined by the set of the surface nodes n_S. For each node ig belonging to the surface, the corresponding row is of matrix $\mathbf{S}_{11}$ is appended to $\mathbf{K}$ along with the contribution from tetrahedral elements that also share the node ig. Because the surface node number $is = 1, ..., n_S$ is found by searching (quicksort) the array igs (Chapter 3, Section 2.1) for index ig, the addition of the whole superelement is a $O(n_S^2 \log(n_S))$ process.

The eight independent blocks of matrix $\mathbf{S}_{11}$ are retrieved to an auxiliary array from the disk, where they have been previously stored by the program that performs the recursive condensation. Any element of the whole matrix $\mathbf{S}_{11}$ can be restored from its independent blocks according to Eq. (3.3). However, it soon becomes clear that a considerable part of $\mathbf{S}_{11}$'s elements can be discarded on the basis of their magnitude without any significant impact on the solution of the open-boundary problem. Therefore, it is impractical to add the full matrix $\mathbf{S}_{11}$ to the element assembly since, for typical n_S, its storage requirements outweighs that for $\mathbf{K}$ for the interior problem. To discard or retain $\mathbf{S}_{11}$'s elements in a systematic way, a threshold value *thres* is introduced for their normalized, with respect to the average $\overline{S} = \sum_{i=1}^{n_S} S_{ii}^{11}/n_S$ of diagonal entries, magnitudes. In other words, only those entries of matrix $\mathbf{S}_{11}$ are allowed into $\mathbf{K}$ whose relative magnitude exceeds *thres*, i.e.

$$\frac{|S_{ij}^{11}|}{\overline{S}} > thres. \tag{4.7}$$

The influence of *thres* on the numerical solution is demonstrated on the example of the static capacitance of a quartz cube with top and bottom surfaces are half-covered by electrodes, as shown in Fig. 4.7*(a)*.

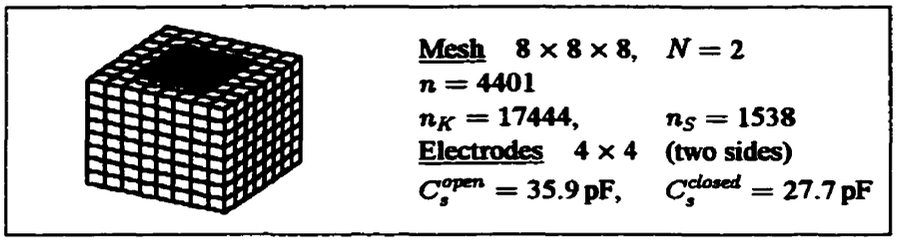

(a)

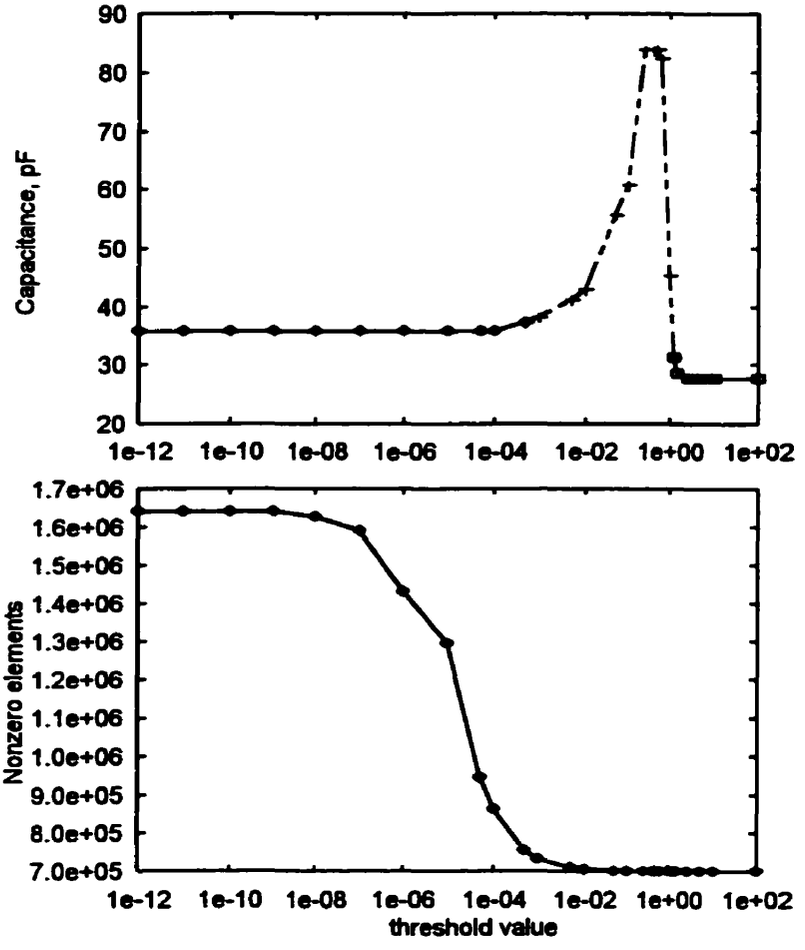

(b)

(c)

Fig 4.7 Parameters of the piezostatic problem as functions of the threshold value *thres* for the elements of the ballooning matrix $\mathbf{S}_{11}$. *(a)* Problem description. *(b)* Static capacitance of the open-boundary problem. *(c)* Sparse storage requirements for the global stiffness matrix.

The problem was initially solved with open and closed electric boundaries, i.e. with and with no matrix $\mathbf{S}_{11}$ added, and, subsequently, for several intermediate fill levels

of $\mathbf{S}_{11}$ prescribed by *thres*. Figure 4.7 shows how the static capacitance C_s *(b)* and the number of nonzero locations in $\mathbf{K}$ *(c)* change as the threshold value increases and more elements of $\mathbf{S}_{11}$ are discarded. The capacitance curve begins with C_s^{open}, and maintains this level until *thres* reaches the value of approximately 10^{-4}. For the same *thres* interval, the storage requirements for the stiffness matrix $\mathbf{K}$ drop from $1.64 \cdot 10^6$ to $0.86 \cdot 10^6$ words, thus diminishing by almost 50%. Between $thres = 10^{-4}$ and $thres = 1$ the solution has no physical meaning: the curve behavior simply reflects how the numerical value of static capacitance deteriorates as larger elements disappear from $\mathbf{S}_{11}$. Starting from $thres = 1$, the capacitance becomes that of a closed-boundary problem C_s^{closed}, which indicates that no elements from $\mathbf{S}_{11}$ are left in $\mathbf{K}$. The storage requirements for $\mathbf{K}$ stabilize at the level of a closed-boundary problem, i.e. $0.7 \cdot 10^6$ locations, even earlier — at $thres = 10^{-2}$. This means that the entries of matrix $\mathbf{S}_{11}$ whose magnitude lies within $10^{-2} < |S_{ij}^{11}|/\overline{S} < 1$ are either diagonal, or fit into the sparsity pattern of the 'closed' global matrix.

The above example demonstrates that only $0.16 \cdot 10^6$ out of $1.18 \cdot 10^6$ locations, i.e. 14% of matrix $\mathbf{S}_{11}$, need to be added to the global matrix to achieve the full accuracy in calculating the capacitance of the open-boundary problem. All the elements S_{ij}^{11}, $|S_{ij}^{11}|/\overline{S} < 10^{-4}$, associated with electrostatic interaction between relatively distant nodes, can be discarded without altering C_s^{open}. For the element order $N = 2$, the remaining entries of $\mathbf{S}_{11}$ increase the average number on nonzeros in the stiffness matrix $\mathbf{K}$ from $s_{closed} = 48$ to $s_{open} = 59$, thus leaving $\mathbf{K}$ largely sparse. Experiments with other ballooning matrices suggest that $thres = 10^{-4}$ seems to be a reasonable compromise between accuracy and storage requirements, and is adopted further as a default value for numerical tests and illustrative problems.

4.3 *Profile storage*

In the profile, also termed *envelope* or *skyline*, storage mode the symmetric matrix $\mathbf{A}$ is written into an one-dimensional array *env* so that for each row i of its lower triangle, only entries located between the leftmost nonzero element $il(i)$ and the diagonal i are stored. Therefore, the method allocates storage for all the members of the *envelope* $\{(i,j)|\ i = 1,...,n;\ j = il(i),...,i\}$, even though some of them are zero. This approach implies solving the systems of linear equations by

some sort of elimination (direct method) which involves a complete factorization of matrix **A**. Indeed, although the **A**'s triangular factor **L** will have a different sparsity pattern because of the *fill-in* during the factorization, it will have the same profile so that it can overwrite **A**. Moreover, for **A** stored in *env* by rows, the *bordered* form of the factorization (Watkins, 1991) is the most appropriate.

The data structure associated with the profile storage scheme is much simpler than its sparse counterpart. It requires

- an array *env* whose first n positions store the diagonal entries of **A**, and — starting from position $n+1$ — **A**'s envelope, one row after the other;
- an integer array *il* of length n to house the column number $il(i)$ of the first nonzero element in the row i;
- an integer array *ienv* of length $n+1$ to store pointers to *env*: its element $ienv(i)$ indicates the position in *env* where the first nonzero entry of row i is stored. If the row is represented only by its diagonal element, then $ienv(i) = ienv(i+1)$. It also follows from the above that $ienv(1) = n+1$ and $ienv(n+1)$ equals the total number of locations in *env*.

Again, a pseudocode for the symmetric matrix-vector product $\mathbf{y} = \mathbf{Ax}$ is drawn to illustrate the described storage:

$$
\begin{array}{l}
\text{for } i = 1, \ldots, n \\
\quad \left[\begin{array}{l}
y(i) = env(i)x(i) \\
k = ienv(i) \\
\text{for } j = il(i), \ldots, i-1 \\
\qquad \left[\begin{array}{l}
y(i) = y(i) + env(k)x(j) \\
y(j) = y(j) + env(k)x(i) \\
k = k+1
\end{array} \right.
\end{array} \right.
\end{array}
\tag{4.8}
$$

Because the last stored element of row i is always diagonal, the components of array *ienv* can be derived from *il* as follows

$$ienv(i+1) = ienv(i) + i - il(i), \tag{4.9}$$

so that, in principle, it suffices to have the array *il* alone. However, it is convenient to record *ienv* to avoid recalculating (4.9) any time matrix **A** is accessed.

Therefore, the profile scheme can be implemented with a fixed overhead storage of $2n + 1$ integer locations, which is negligible compared to the primary storage for the array *env*. The assembly of global matrices is also considerably simplified. Indeed, array *il*, and consequently *ienv*, can be determined in advance (e.g. by running a dummy loop over all elements), so that the global matrices are formed in a usual, *element-by-element*, manner.

The envelope of a symmetric matrix **A** is characterized by the average semiband width p, calculated as

$$p = \frac{ienv(n+1)}{n}. \tag{4.10}$$

With this definition of p, the envelope size becomes a linear function np of the problem dimension n, and can be compared to the sparse storage (ns). In contrast to the average number of nonzero elements per row (s), p depends on the order in which unknowns are numbered. In Section 2, a special hashing function was designed to help ordering nodes in a way to minimize the maximal node number difference over all elements. These efforts would be fruitless if the variables were numbered as shown in (4.1). Fortunately, this was required only for the purpose of partitioning matrices **K** and **M** into physically meaningful blocks (Eqs. (4.2)–(4.3)); in practice, mechanical and electrical variables are intermixed within the global matrices according to the following scheme

$$\begin{pmatrix} u_{ig}^1 \\ u_{ig}^2 \\ u_{ig}^3 \\ \varphi_{ig} \end{pmatrix} = \begin{pmatrix} x_{4ig-3} \\ x_{4ig-2} \\ x_{4ig-1} \\ x_{4ig} \end{pmatrix}. \tag{4.11}$$

In this way, the variable number difference taken over all elements and, respectively, **A**'s envelope are minimized simultaneously with the node number difference.

Table 4.2 illustrates some typical values of p obtained with the variable numbering (4.11) for square plate and strip geometries. The two problems were discretized with tetrahedra $(N = 2)$ in a way to make the number of nodes n in the meshes alike. Because the adopted node numbering favors the strip configuration, the corresponding storage requirements is almost less by half than

that of the square plate. Bearing in mind that for the same element order the sparse storage mode — for which the variable numbering is immaterial — produces an average of 48 elements per row, one can see that even for the 'optimal' strip geometry only one-eighth of the envelope is filled; clearly, **K**'s envelope becomes sparser as elements of the ballooning matrix are added.

Table 4.2 The average semiband width p of global matrices.

Mesh	Nodes	**K**			**M**	
$E_x \times E_y \times E_z$	n	n_K	p	electric boundary	n_M	p
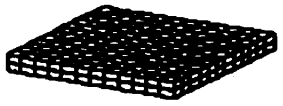 $12 \times 12 \times 2$	2837	11348	690 1105	*closed* *open*	8511	517
 $24 \times 6 \times 2$	2897	11588	374 633	*closed* *open*	8691	281

The proportion of 'wasted' space is even greater for the profile of the mass matrix **M**, for which the average number of nonzeros per row is only 12. To reduce the memory requirements, Yong and Zhang (1994) proposed a storage scheme that exploits the special structure of **M**. They observed that the associated fill-in happens along the same discrete subdiagonals where the few **M**'s nonzero elements are initially located. In three-dimensional finite element models (Yong and Cho, 1994), this *a priori* knowledge of the fill-in pattern allows allocating storage only for the one third of the mass matrix envelope. However, as it will be demonstrated later in this chapter, by modifying the Lanczos algorithm the factorization of the mass matrix, and therefore its profile storage and handling, can be avoided, thus giving way to a more efficient sparse scheme.

4.4 *Imposition of boundary conditions*

The finite element matrix equations were derived from the projective and variational formulations under which all the boundary conditions fell into essential and natural. This constitutes one of the principal advantages of the finite element

method since only essential boundary conditions need to be explicitly imposed on the nodal variables. The homogeneous natural conditions are satisfied approximately, in a weighted sense, while the nonhomogeneous natural conditions make up the driving terms, i.e. the right-hand side of the finite element equations.

The choice of functional $\mathfrak{F}_4$ in the variational formulation (Section 6.1, Chapter 1) makes the Dirichlet boundary conditions to act as essential, and the Neumann conditions — as natural. The former are enforced by constraining the mechanical displacements and electric potentials on some parts of the surface. Because it was agreed to consider only problems with traction-free boundaries, and also because at any point of the surface the Dirichlet and Neumann conditions are mutually exclusive, the mechanical conditions are purely homogeneous Neumann, and no driving term is associated with them. Therefore, only the electric Dirichlet and nonhomogeneous Neumann boundary conditions need to be taken into account. In the framework of the present finite element model, this amounts to prescribing either electric potentials or electric charge densities at some of the boundary nodes.

To introduce boundary conditions into the finite element equations, the problem variables $\mathbf{x}$ and, correspondingly, the source terms $\mathbf{q}$ must be numbered in a way to distinguish prescribed nodal potentials or charge densities, from their free counterparts. Clearly, numbering (4.11) is suitable only if all the nodal values are unconstrained; otherwise, it needs to be modulated in order to fit specific types of boundary constraints. For instance, all the electric boundary conditions, discussed in Section 5.2 Chapter 1, involve electrodes. Due to the conducting nature of the latter, only one electric variable should be associated with each electrode. In this way, the boundary conditions are imposed on all the electrode nodes collectively, either in terms of the total electrode charge $Q = \overline{Q}$ (Neumann) or electrode potential $\Phi_e = \overline{\Phi}_e$ (Dirichlet), thus giving rise to matrix equations (5.39) or (5.40) of Chapter 1. Therefore, the first step in the variable numbering would consist in identifying nodes that belongs to the same electrode, and assigning a unique index to the corresponding nodal potentials (or charges).

The way in which these electrode's variables are handled is problem specific. If solution is sought in the form of proper vibrations[4], either $\overline{\Phi}_e$ or $\overline{\mathbf{Q}}$ is zero. In particular, when the problem is solved for resonance ($\Phi_e = 0$), the electrode potentials are simply eliminated from, or rather not included in, $\mathbf{x}$, so that no rows of the stiffness matrix are associated with them. To obtain the antiresonance solution $(\overline{\mathbf{Q}} = 0)$, the electrode potentials are treated as one unknown, and the corresponding rows of $\mathbf{K}$'s lower triangle of the stiffness matrix are summed up to form a unique row. In either case, the right-hand side vector $\mathbf{q}$ is zero, and the numerical solution is determined from an eigenvalue problem. In contrast, the static problem requires a driving vector which is formed by assigning a constant nonzero values to either $\overline{\Phi}_e$ or $\overline{\mathbf{Q}}$. Because the static solution is typically recast in the form of capacitance C_S (or, in the case of multiple electrodes, in the matrix of capacitance coefficients $\mathbf{C}_S$), it is convenient, following the definition of C_S, to specify opposite charges of equal amounts on the electrodes $\overline{\mathbf{Q}} = (+\mathrm{Q}, -\mathrm{Q})^{\mathrm{T}}$, and determine their potentials by solving the corresponding system of linear equations. Therefore, among the four possible combinations of electrical boundary conditions summarized in Table 4.3, only three (nonshaded) are implemented in the present analysis.

Table 4.3 Vectors of unknowns $\mathbf{x}$ and sources $\mathbf{q}$ for different types of boundary conditions

Vector of unknowns	Boundary conditions	homogeneous	nonhomogeneous
$\mathbf{x} = \begin{bmatrix} \mathbf{U} \\ \boldsymbol{\Phi}' \end{bmatrix}$	Dirichlet	*resonance* $\mathbf{q} = 0$	$\mathbf{q} = \boldsymbol{\Phi}_e \begin{bmatrix} -\mathbf{K}_{\boldsymbol{\Phi}'\mathbf{U}} \\ \mathbf{K}_{\boldsymbol{\Phi}'\boldsymbol{\Phi}'} \end{bmatrix} \mathbf{1}$
$\mathbf{x} = \begin{bmatrix} \mathbf{U} \\ \boldsymbol{\Phi}' \\ \boldsymbol{\Phi}_e \end{bmatrix}$	Neumann	*antiresonance* $\mathbf{q} = 0$	*static* $\mathbf{q} = \begin{bmatrix} 0 \\ 0 \\ \overline{\mathbf{Q}} \end{bmatrix}$

[4] As in Chapter 1, for the sake of simplicity the imposition of boundary conditions is discussed for a system with one electrode.

5 Numerical solution of finite element equations

After assembling the global matrices **K** and **M** and imposing boundary conditions, the finite element procedure amounts to solving either the generalized eigenvalue problem

$$\mathbf{Kx} = \lambda \mathbf{Mx}, \tag{5.1}$$

or the system of linear equations

$$\mathbf{Kx} = \mathbf{q} \tag{5.2}$$

for the vibration and static problems respectively. The global matrices **K** and **M** of size n, partitioned as shown in Eqs. (4.2) and (4.3), are both *real* and *symmetric* since they were assembled from symmetric element matrices with real entries. As mentioned in the previous chapter, the interface conditions for variables **x** are enforced by the continuity of approximating functions across element interfaces, including the superelement, so that no additional, possibly unsymmetric, coupling terms are introduced during the matrix assembly.

Among other characteristics that determine numerical properties of systems (5.1) and (5.2), it is important to mention that the stiffness matrix **K** is *indefinite* as the underlying energy function — the electric enthalpy G_2 — is. Its submatrices $\mathbf{K}_{uu}$ and $\mathbf{K}_{\varphi\varphi}$ are both positive definite which is directly related to the positiveness of the strain $\frac{1}{2}\mathbf{U}^{\mathrm{T}}\mathbf{K}_{uu}\mathbf{U}$ and dielectric $\frac{1}{2}\mathbf{\Phi}^{\mathrm{T}}\mathbf{K}_{\varphi\varphi}\mathbf{\Phi}$ energies for any nontrivial displacement **U** and potential $\mathbf{\Phi}$. The matrix **K** is singular unless electrical boundary conditions, in one of the forms shown in Table 4.3, are introduced into it. In contrast, the mass matrix **M** is always singular since no time-derivative is associated with the scalar electric potential. The kinetic energy $\frac{1}{2}\mathbf{U}^{\mathrm{T}}\mathbf{M}_{uu}\mathbf{U}$ being positive, the **M**'s nonsingular submatrix $\mathbf{M}_{uu}$ is positive definite, and the whole matrix **M** is said to be *positive semi-definite*.

For the computer implementation, it is especially relevant that the global matrices **K** and **M** are typically *large* and very *sparse*. In other words, it is important to use algorithms that take advantage of **K** and **M**'s sparsity because the latter are large. To date, the most efficient algorithms for solving (5.2) and (5.1) are the preconditioned conjugate gradient and the Lanczos methods respectively. After a brief review of alternative approaches, the application of both techniques to

the piezoelectric static and vibration problems are considered at greater length in this section.

5.1 *Review of past methods*

The earliest solution to the piezoelectric problem was that of Allik and Hughes (1970), and consisted in reducing the latter to the ordinary structural dynamics equations by a static condensation of electrical degrees of freedom. Removing the unspecified electric potentials $\mathbf{\Phi}'$ from Eq. (5.39), Chapter 1

$$\mathbf{\Phi}' = \mathbf{K}_{\varphi'\varphi'}^{-1}\left(\mathbf{K}_{\varphi' u}\mathbf{U} - \mathbf{K}_{\varphi'\varphi_e}\mathbf{i}\,\Phi_e\right), \tag{5.3}$$

recasts the vibration problem into

$$\begin{bmatrix} \mathbf{H}_{uu} - \lambda\mathbf{M}_{uu} & \mathbf{H}_{u\varphi_e}\mathbf{i} \\ \mathbf{i}^{\mathrm{T}}\mathbf{H}_{u\varphi_e}^{\mathrm{T}} & -\mathbf{i}^{\mathrm{T}}\mathbf{H}_{\varphi_e\varphi_e}\mathbf{i} \end{bmatrix} \begin{bmatrix} \mathbf{U} \\ \Phi_e \end{bmatrix} = \begin{bmatrix} \mathbf{0} \\ \mathbf{Q} \end{bmatrix} \tag{5.4}$$

where

$$\mathbf{H}_{uu} = \mathbf{K}_{uu} + \mathbf{K}_{u\varphi'}\,\mathbf{K}_{\varphi'\varphi'}^{-1}\,\mathbf{K}_{u\varphi'}^{\mathrm{T}} \tag{5.5}$$

$$\mathbf{H}_{u\varphi_e} = \mathbf{K}_{u\varphi_e} - \mathbf{K}_{u\varphi'}\,\mathbf{K}_{\varphi'\varphi'}^{-1}\,\mathbf{K}_{\varphi'\varphi_e} \tag{5.6}$$

$$\mathbf{H}_{\varphi_e\varphi_e} = \mathbf{K}_{\varphi_e\varphi_e} - \mathbf{K}_{\varphi'\varphi_e}^{\mathrm{T}}\,\mathbf{K}_{\varphi'\varphi'}^{-1}\,\mathbf{K}_{\varphi'\varphi_e} \tag{5.7}$$

are the condensed stiffness, piezoelectric and dielectric matrices respectively.

The resonant frequencies ω, $\lambda = \omega^2$, and mode shapes $\mathbf{U}$ has always been of prime interest to piezoelectric device designers. For free vibrations, system (5.4) transforms into the generalized eigenvalue problem

$$\mathbf{H}'_{uu}\mathbf{U} = \omega^2\mathbf{M}_{uu}\mathbf{U}, \tag{5.8}$$

where $\mathbf{H}'_{uu} = \mathbf{H}_{uu}$ for $\Phi_e = 0$ and $\mathbf{H}'_{uu} = \mathbf{H}_{uu} + \mathbf{H}_{u\varphi_e}\mathbf{i}\mathbf{i}^{\mathrm{T}}\mathbf{H}_{u\varphi_e}^{\mathrm{T}}/(\mathbf{i}^{\mathrm{T}}\mathbf{H}_{\varphi_e\varphi_e}\mathbf{i})$ for $\bar{\mathbf{Q}} = 0$. Because $\mathbf{M}_{uu}$ is positive-definite, it admits the Choleski decomposition $\mathbf{M}_{uu} = \mathbf{L}\mathbf{L}^{\mathrm{T}}$, and (5.8) can be recast into an equivalent standard symmetric eigenvalue problem

$$\mathbf{L}^{-1}\mathbf{H}'_{uu}\mathbf{L}^{-\mathrm{T}}\mathbf{Y} = \omega^2\mathbf{Y} \tag{5.9}$$

with same eigenvalues and the transformed eigenvectors $\mathbf{Y} = \mathbf{L}^{\mathrm{T}}\mathbf{U}$. If required, the condensed potentials $\boldsymbol{\Phi}'$ can be recovered from (5.3) after obtaining $\mathbf{U}$ (and Φ_e, if solved for the antiresonance) from the numerical solution of (5.9).

An obvious drawback of this approach is that sparsity is destroyed in the process of static condensation. The Householder reduction to tridiagonal form followed by the bisection method applied to the Sturm sequence (Watkins, 1991) is typically the best way to determine a few specified eigenvalues of a dense matrix. The static condensation is, therefore, useful for three-dimensional problems of modest size, as those associated with low frequency transducer modeling. In an attempt to alleviate the solution, Boucher *et al.* (1981), and more recently Yong and Zhang (1993), proposed to solve (5.9) for purely mechanical modes ($\mathbf{H}'_{uu} = \mathbf{K}_{uu}$) and treat piezoelectricity as a perturbation — a method barely suitable for materials with strong piezoelectric coupling. In general, large systems of piezoelectric equations are better solved directly by numerical methods that preserve the sparsity or profile of their matrices. At this point it is important to note that because $\mathbf{M}$ is singular, problem (5.1) has only n_M eigenvalues, where n_M is the size of $\mathbf{M}_{uu}$; the remaining $n_K - n_M$ eigenvalues associated with electrical degrees of freedom are regarded as infinite. For the same reason, the generalized eigenvalue problem (5.1) cannot be reduced to the form (5.9). This difficulty is typically overcome by applying the standard reduction to the reciprocal problem

$$\mathbf{M}\mathbf{x} = \frac{1}{\lambda}\mathbf{K}\mathbf{x}. \tag{5.10}$$

With this substitution, the infinite eigenvalues are mapped onto zeros, and the problem (5.10) has the full set of n_K eigenvalues.

Among the numerous techniques (Parlett, 1980; Pissanetsky, 1984) suitable for finding a few lowest eigenvalues and eigenvectors of large sparse symmetric generalized eigenvalue problems in the form (5.10), the *inverse iteration*, *subspace iteration*, and *Lanczos method* are most widely used in the finite element applications; all these methods can be combined with shifting (σ) to determine the eigenpairs in any specified region of the spectrum.

Starting from a given vector $\mathbf{x}_0$, the inverse iteration finds and scales (to avoid overflow or underflow) the new approximation to the eigenvector $\mathbf{x}_{k+1}$:

$$\begin{cases} (\mathbf{K}-\sigma\mathbf{M})\mathbf{x}_{k+1} = \mathbf{M}\mathbf{x}_k, \\ \mathbf{x}_{k+1} = \mathbf{x}_{k+1}/\|\mathbf{x}_{k+1}\|_2. \end{cases} \quad k = 0, 1, 2... \tag{5.11}$$

The procedure is repeated until the corresponding approximation to the eigenvalue λ_k satisfies some convergence criterion. The ith eigenpair converges linearly with the rate $|(\lambda_i - \sigma)/(\lambda_{i+1} - \sigma)|$ (Watkins, 1991), which is rapid only if $|\lambda_i - \sigma| \ll |\lambda_{i+1} - \sigma|$, i.e. when shift σ is a good approximation to λ_i. To accelerate the process (5.11), the shift can be refined and set equal to the Rayleigh quotient $\sigma_{k+1} = \mathbf{x}_k^{\mathrm{T}}\mathbf{K}\mathbf{x}_k/(\mathbf{x}_k^{\mathrm{T}}\mathbf{M}\mathbf{x}_k)$ at each step, thus giving rise to the *Rayleigh-Ritz iteration* characterized by cubic convergence. The subspace iteration method (Bathe and Wilson, 1973) can be viewed as a generalization of the Rayleigh-Ritz procedure to the subspace of M-orthogonal vectors $\mathbf{X}_k$. In this case, the convergence rate of the first q eigenpairs $|\lambda_q/\lambda_{b+1}|$ is determined by the subspace dimension b, and can be hastened by choosing a larger block of $\mathbf{X}_k$. However, the increase of b also increases both the number of matrix-vector operations and storage requirements, which may render the method inefficient if b is not properly selected. A careful choice of the starting block $\mathbf{X}_0$ is also very important since convergence can be very fast if $\mathbf{X}_0$ is close to the least dominant subspace. The subspace iteration method has been very popular among engineers, including the piezoelectric community (Yong, 1987b; Lerch, 1990; Trümpy and Zingg, 1993), since its introduction in the early seventies, and has been a standard eigenvalue solver for many finite element programs. Nowadays, however, it is progressively replaced by the rival Lanczos method, which is superior to simultaneous iteration in both speed and storage (Nour-Omid *et al.*, 1983). Although the algorithm is still often associated with instability and ghost eigenvalues, many piezoelectric engineers adopted it, largely through the finite element packages available to them, as a tool for solving the eigenvalue problems arising in their applications (Decarpigny *et al.*, 1991; Yong and Stewart, 1991; Guo *et al.*, 1992).

In contrast to the frequently encountered modal analyses of piezoelectric structures, the literature is mute on the numerical solution of the full piezostatic problem under electric load. It is very likely that what is buried under the name of 'static analysis' in the finite element packages, supplemented with piezoelectricity, performs this task (Söderkvist, 1998). However, the review of technical papers (Boucher *et al.*, 1981; Naillon *et al.*, 1983; Johnson, 1990) indicates that, at best,

the static solution ($\omega = 0$) in the form of static capacitance C_s is obtained as a by-product of the vibration problem as

$$C_s = \mathbf{H}_{\varphi_e\varphi_e}. \tag{5.12}$$

In the modern piezoelectric finite element analysis such an approach to calculating C_s is untenable for several reasons. First, on using sparse eigensolvers, the dense matrix $\mathbf{K}^{-1}_{\phi'\psi'}$ in (5.7), and therefore $\mathbf{H}_{\varphi_e\varphi_e}$, are never formed explicitly. Second, the inspection of the electrical equation in (5.4)

$$(\mathbf{i}^{\mathrm{T}}\mathbf{H}^{\mathrm{T}}_{\mathbf{u}\varphi_e})\mathbf{U} - (\mathbf{i}^{\mathrm{T}}\mathbf{H}_{\varphi_e\varphi_e}\mathbf{i})\,\Phi_e = \mathbf{Q} \tag{5.13}$$

reveals that (5.12) takes into account only the dielectric contribution to the static capacitance. The neglect of the static displacement $\mathbf{U}$ in (5.13) can introduce a large error in C_s for materials with strong piezoelectric coupling. Finally, the external electric field has never been taken into account by any existing approximation to the static capacitance, although among other electrical parameters it is precisely C_s that is most affected by it.

Clearly, from computational and physical considerations, Eq. (5.12) is not an adequate way of calculating the static capacitance of a piezoelectric structure; the 'true' $C_s = \mathrm{Q}/\Phi_e$ can be obtained only from the solution of (5.2) for Φ_e given Q. When solving linear systems, one can choose between direct (elimination) and iterative methods. Typically, iterative techniques, such as *the preconditioned conjugate gradient method*, work very well for static problems, so that no recourse to the costly factorization of the coefficient matrix is needed. As will be shown below, the electrically driven piezoelectric static problem is no exception to this rule. Because the computational experience related to the numerical solution of the piezostatic problem (with closed or open electric boundaries) has never been reported in the literature, the following section is drawn to fill this lacuna.

5.2 *The preconditioned conjugate gradient method for the static problem*

The standard conjugate gradient method (Golub and Van Loan, 1989) iteratively solves the symmetric and positive-definite $n \times n$ system of linear equations

$$\mathbf{A}\mathbf{x} = \mathbf{b} \tag{5.14}$$

by finding the minimum (if **A** is positive-definite) or the stationary point (if **A** is indefinite) of the corresponding quadratic form

$$\mathbf{F}(\mathbf{x}) = \frac{1}{2}\mathbf{x}^{\mathrm{T}}\mathbf{A}\mathbf{x} - \mathbf{x}^{\mathrm{T}}\mathbf{b}. \tag{5.15}$$

The *gradient* of the function F can be expressed in terms of the *residual* vector

$$\mathbf{r} = \mathbf{b} - \mathbf{A}\mathbf{x}, \tag{5.16}$$

namely $\nabla \mathbf{F} = -\mathbf{r}$. Because $\mathbf{r} = 0$ for $\mathbf{x}$ satisfying (5.14), finding the zero of ∇F is equivalent to solving Eq. (5.14). At each k-th iteration of the method, the search direction vectors $\mathbf{p}_k$ along gradient lines are chosen

- to be *conjugate* to each other with respect to the matrix **A**

$$\mathbf{p}_{k+1}^{\mathrm{T}}\mathbf{A}\mathbf{p}_k = 0, \tag{5.17}$$

- to make the residual orthogonal to the preceding search direction

$$\mathbf{p}_k^{\mathrm{T}}\mathbf{r}_{k+1} = 0, \tag{5.18}$$

- to make successive residuals orthogonal to each other

$$\mathbf{r}_{k+1}^{\mathrm{T}}\mathbf{r}_k = 0. \tag{5.19}$$

In exact arithmetic, the conjugate gradient method is guaranteed to converge to the solution in at most n iteration, provided **A** is positive-definite. However, for indefinite matrices, as in the piezoelectric case, the algorithm can break-down. Indeed, if the search direction happens to be self-conjugate

$$\mathbf{p}_k^{\mathrm{T}}\mathbf{A}\mathbf{p}_k = 0, \tag{5.20}$$

it will be trapped along the asymptote of the saddle-shaped n-dimensional energy functional. Hopefully, the roundoff error in finite precision arithmetic prevents the search vector $\mathbf{p}_k$ from satisfying condition (5.20) exactly, and can delay convergence rather than break the algorithm. In the author's experience of applying the conjugate gradient method to a wide range of piezostatic problems (5.2), it never failed, so that no recourse to either its robust *bi-conjugate* variant (Press *et al*,1992) or *symmetric squaring* $\mathbf{A}\mathbf{A}^{\mathrm{T}}$ (Saad, 1988) was ever required.

The convergence rate of the conjugate method is known to depend on the entire spectrum of **A**. The closer **A** is to identity matrix **I** — either in the sense of having few distinct or many clustered eigenvalues — the fewer iterations are required for the method to converge. This observation is behind the idea of premultiplying, or *preconditioning*, the system (5.14) by a matrix **P** in order to 'improve' the spectrum of its operator, and thereby hasten convergence. The resulting preconditioned conjugate gradient method (PCG) solves the system

$$\mathbf{PAx} = \mathbf{Pb} \tag{5.21}$$

instead of (5.14). For positive-definite matrices the boundaries of **A**'s spectrum can be combined to form the spectral condition number $k_2(\mathbf{A}) = \lambda_{max}(\mathbf{A})/\lambda_{min}(\mathbf{A})$, where λ_{max} and λ_{min} are the largest and smallest eigenvalues of **A**. This makes it possible to estimate the convergence rate of the conjugate gradient method in terms of $k_2(\mathbf{A})$. Because the upper bound for the solution error is a function of $\sqrt{k_2(\mathbf{A})}$ (Golub and Van Loan, 1989), $k_2(\mathbf{A}) \approx 1$, i.e. a well-conditioned matrix, is a *sufficient* condition for a fast convergence of the conjugate gradient method. Therefore, in order to perform better than the standard algorithm ($\mathbf{P} = \mathbf{I}$), the PCG method should use such a preconditioner **P** that **PA** 'approximates' the identity matrix **I**, and $k_2(\mathbf{PA})$ be close to unity.

Among a great variety of preconditioners between **I** and the full inverse $\mathbf{A}^{-1}$, finding the one that suits best a specific problem is not a trivial task. It was not meant in the present thesis to find an optimal preconditioner for the piezoelectric stiffness matrices. Instead, attention was turned to the most widely used type of preconditioning, i.e. by incomplete factorization $\tilde{\mathbf{A}}$ of matrix **A**:

$$\mathbf{A} \approx \tilde{\mathbf{A}} = \tilde{\mathbf{L}}\tilde{\mathbf{D}}\tilde{\mathbf{L}}^{\mathrm{T}}, \tag{5.22}$$

where $\tilde{\mathbf{L}}$ is constructed by ignoring some of the fill-in elements that would be nonzero in an exact factorization. The specific criteria used to suppress that fill can be based on either a preassigned set of matrix positions, e.g. sparsity pattern of **A** (Greenbaum and Rodrigue, 1989), or on the magnitude of nonzero elements (Ajiz and Jennings, 1984). Since most often the PCG method is used in conjunction with the sparse storage of matrices **A** and $\tilde{\mathbf{A}}$, the majority of preconditioners fall into the first category. A very economical storage scheme is obtained when all fill is discarded, or rather not calculated at all. In this case, the approximate factor $\tilde{\mathbf{L}}$ has

the same sparsity pattern as **A** and only one indexing array ija is needed to describe both $\tilde{\mathbf{L}}$ and **A**. This type of incomplete factorization is also very inexpensive, and requires only $ns^2/2$ work, where s is the average number of nonzeros in the row of $\tilde{\mathbf{L}}$ and **A**.

In this approach, the preconditioner is set to $\tilde{\mathbf{A}}^{-1}$, $\mathbf{P} = \tilde{\mathbf{A}}^{-1}$, and the conjugate gradient algorithm is applied to matrix $\tilde{\mathbf{A}}^{-1}\mathbf{A}$ (Fig. 4.8). The latter has a smaller condition number than **A** alone (Manteuffel, 1980), and produces $\tilde{\mathbf{A}}^{-1}$-orthogonal residual vectors $\mathbf{r}$: $\mathbf{r}_{k+1}^{\mathrm{T}}\tilde{\mathbf{A}}^{-1}\mathbf{r}_k = 0$.

<u>Initialization:</u>

Guess $\mathbf{x}_0$

Set $\mathbf{r}_0 = \mathbf{b} - \mathbf{A}\mathbf{x}_0$

$\mathbf{d}_0 = \tilde{\mathbf{A}}^{-1}\mathbf{r}_0$ (Solve $\tilde{\mathbf{A}}\mathbf{d}_0 = \mathbf{r}_0$ for $\mathbf{d}_0$)

$\rho_0 = \mathbf{r}_0^{\mathrm{T}}\mathbf{d}_0$

$\mathbf{p}_0 = \mathbf{d}_0$

<u>CG Step:</u>

For $k = 0, 1, 2, \ldots$

1. $\mathbf{q}_k = \mathbf{A}\mathbf{p}_k$
2. $\alpha_k = \rho_k / \mathbf{p}_k^{\mathrm{T}}\mathbf{q}_k$
3. $\mathbf{x}_{k+1} = \mathbf{x}_k + \alpha_k\mathbf{p}_k$
4. $\mathbf{r}_{k+1} = \mathbf{r}_k - \alpha_k\mathbf{q}_k$
5. If ($\|\mathbf{r}_{k+1}\|_2 \leq tol\|\mathbf{b}\|_2$ or $iter > iter_{max}$) Stop
6. $\mathbf{d}_{k+1} = \tilde{\mathbf{A}}^{-1}\mathbf{r}_{k+1}$ (Solve $\tilde{\mathbf{A}}\mathbf{d}_{k+1} = \mathbf{r}_{k+1}$ for $\mathbf{d}_{k+1}$)
7. $\rho_{k+1} = \mathbf{r}_{k+1}^{\mathrm{T}}\mathbf{d}_{k+1}$
8. $\beta_{k+1} = \rho_{k+1}/\rho_k$
9. $\mathbf{p}_{k+1} = \mathbf{d}_{k+1} + \beta_{k+1}\mathbf{p}_k$

End loop

Fig 4.8 The preconditioned conjugate gradient algorithm.

Since the matrix $\tilde{\mathbf{A}}^{-1}\mathbf{A}$ is never formed explicitly, applying it as an operator implies solving the auxiliary system

$$\tilde{\mathbf{A}}\mathbf{d} = \mathbf{r} \tag{5.23}$$

at each iteration (step 6, Fig. 4.8), where $\tilde{\mathbf{A}}$ is given by (5.22), besides calculating the matrix-vector product $\mathbf{q} = \mathbf{A}\mathbf{p}$ (step 1, Fig. 4.8). Each of these operations costs $2ns$ flops, so that the bulk of arithmetic involved in the solution is estimated at $4ns \times iter$, where *iter* is the number of PCG iterations required to reach the preassigned tolerance *tol* (step 5, Fig. 4.8). Typically, for piezoelectric problems the number of iterations *iter* is such that the amount of work associated with the PCG iterations outweighs that of the incomplete factorization: $ns^2/2 < 4ns \times iter$. In contrast, for the direct solution with exact factor $\mathbf{L}$ stored in the profile of matrix $\mathbf{A}$, the cost of the solution itself by forward elimination and back substitution ($2np$) is negligible compared to the complete factorization of $\mathbf{A}$ ($np^2/2$). This was taken into account when summarizing the operation count, along with the storage requirements, for the PCG and direct methods (Table 4.4).

Table 4.4 Operation count and storage requirement for the direct and iterative solutions of the system of linear equations.

Method	Arithmetic, flops	Storage, bytes
PCG	$ns^2/2 + 4ns \times iter$	$10ns$
Direct	$np^2/2$	$4np$
floating-point format	double (8 bytes)	single (4 bytes)

For the PCG algorithm the storage is made up of $8ns$ bytes to house the $2ns$ locations of matrix $\mathbf{A}$ and the preconditioner $\tilde{\mathbf{A}}$ in single precision (4-bytes), and of additional $2ns$ bytes to store their common indexing array ija in the form of 2-byte integers, thus giving the total of $10ns$ bytes.[5] However, it is not unusual in three-dimensional finite element analysis that the number of problem variables n exceeds the upper numeric limit of the 2-byte integer. The latter depends on the programming language used. For instance, it equals 32767 for the INTEGER*2 data type in FORTRAN, while in a more flexible C, the `unsigned int` allows

[5] Note that this estimate does not include the six n-vectors $\mathbf{r}_k$, $\mathbf{r}_{k+1}$, $\mathbf{d}_k$, $\mathbf{d}_{k+1}$, $\mathbf{p}_k$, $\mathbf{q}_k$ used by the algorithm (Fig. 5.1).

reaching 65535. To go beyond these numbers, one has no choice but to store the column indices as 4-byte integers, so that array ija will occupy as much space as arrays sa and sp for the principal matrices **A** and $\tilde{\mathbf{A}}$ respectively, raising the overall storage to $12ns$ bytes. At the same time, Gaussian elimination requires np locations to store the profile of the symmetric matrix, which, in single precision, amounts to $4np$ bytes of memory. Since for most practical meshes (Table 4.5), p is such that $4p > 10s$, one can conclude that the PCG method handles data in a more efficient manner than Gaussian elimination.

Table 4.5 Ratios of storage requirements for the PCG and direct solutions of large scale piezostatic problems.

Shape	Mesh $E_x \times E_y \times E_z$	n	s	p	Storage ratio Direct / PCG
cube	$8 \times 8 \times 8$	17444	48	1560	3.8
plate	$16 \times 16 \times 2$	19156	44	887	2.4
strip	$30 \times 8 \times 2$	18264	43	474	1.3

Note: All the considered regions were discretized in elements of second order ($N = 2$), had their electric boundaries closed, and the top and bottom surfaces half-covered by electrodes.

The convergence behavior of the PCG method applied to piezostatic problems was studied on some of the geometries used to illustrate the sparse storage scheme. To reduce the roundoff error, all tests were performed using double precision arithmetic, with matrices **A** and $\tilde{\mathbf{A}}$ stored in single precision format (Table 4.4). Theoretically, the algorithm should be considered converged when the static capacitance C_s stops changing. In practice, however, C_s is evaluated only after the PCG iteration has been terminated by some numerical, and often application independent, norm-based condition. In the piezoelectric case, the latter must be chosen with care, particularly when the PCG solver is used as a 'black box.' Indeed, the piezoelectric stiffness matrix represents a typical example of the so-called 'artificial ill-conditioning' — the term attributed to Lanczos, but borrowed here from Fried (1970) — resulting from the difference in the order of magnitude between elastic and dielectric moduli:

$$\begin{bmatrix} \mathbf{K}_{uu} & \mathbf{K}_{u\varphi} \\ \mathbf{K}_{u\varphi}^{T} & -\mathbf{K}_{\varphi\varphi} \end{bmatrix} \sim \begin{bmatrix} 10^{10} & 1 \\ 1 & -10^{-10} \end{bmatrix}. \tag{5.24}$$

This type of ill-conditioning is not pathological, and can easily be removed by, e.g. diagonal, scaling. Unless used alone as a simplest form of preconditioning, the latter is not required since the incomplete factorization–conjugate gradient procedure is invariant to diagonal scaling (Manteuffel, 1980). However, as demonstrated on the numerical examples below, it is important to scale or 'precondition' the stopping criteria; otherwise, the difference in the orders of magnitude among the components of the residual vector $\mathbf{r}$ inherited from (5.24) will make its norm $\|\mathbf{r}\|_2$ converge very slowly. The convergence rate of the PCG method under two different stopping criteria is illustrated on the example of the problem described in Fig. 4.7*(a)*. In both cases, the iteration started from a zero vector $\mathbf{x}_0 = 0$, i.e. $\mathbf{r}_0 = \mathbf{b}$. In the first experiment, the termination criterion (step 5, Fig. 5.1) required relative residual norm err_1 be less than the input tolerance *tol*:

$$\frac{\|\mathbf{r}\|_2}{\|\mathbf{b}\|_2} < tol; \tag{5.25}$$

in the second experiment, the iteration was stopped when the *preconditioned* relative residual err_2 was less than the tolerance *tol*:

$$\frac{\left\|\tilde{\mathbf{A}}^{-1}\mathbf{r}\right\|_2}{\left\|\tilde{\mathbf{A}}^{-1}\mathbf{b}\right\|_2} < tol. \tag{5.26}$$

As can be seen in Fig. 4.9 *(a)* and *(b)*, the number of iterations stops augmenting only after the value of *tol* has been tightened to 10^{-8} and 10^{-10} respectively. Nevertheless, the method can be considered converged for a relatively loose tolerance on the error $tol = 10^{-3}$, when the values of $C_s^{closed} = 27.7$ pF and $C_s^{open} = 35.9$ pF are reached. In either case, no change in the sixth significant digit of C_s^{closed} and C_s^{open} is observed after some 10–15 iterations, which is quite remarkable considering the problem size $n = 17444$. However, if the quantity $\|\mathbf{r}\|_2/\|\mathbf{b}\|_2$ is monitored (Fig. 4.9*(a)*), 300–320 iterations are required to achieve $err_1 < 10^{-3}$, thus giving a false impression that the solution keeps improving.

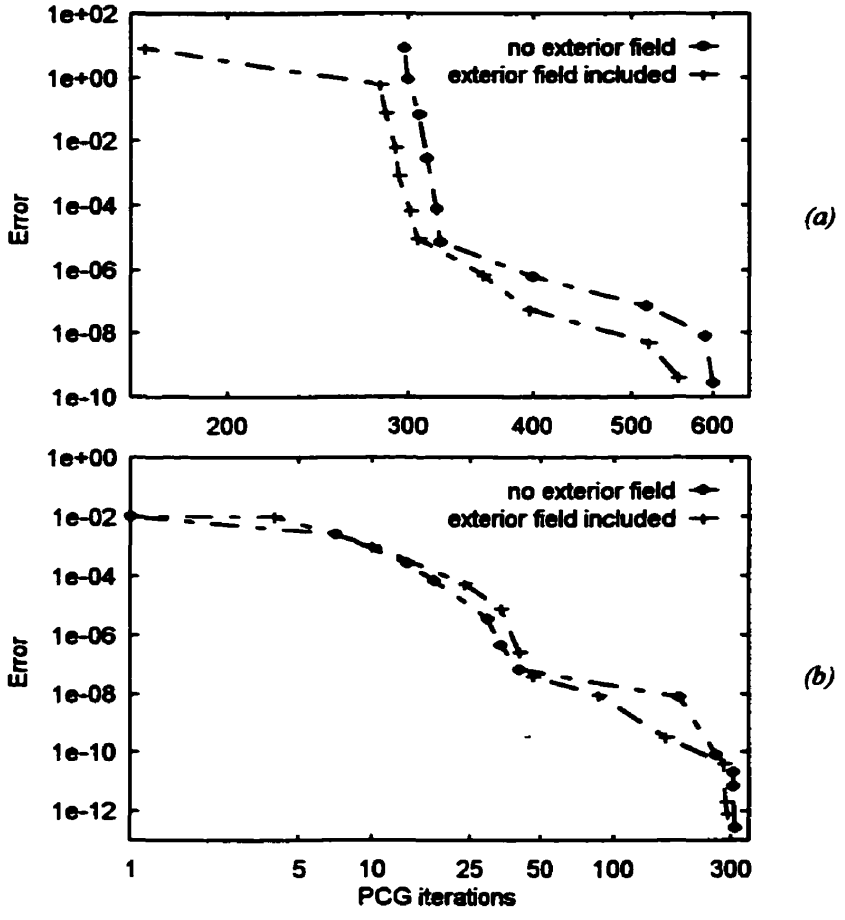

Fig 4.9 Relative residual *err* as function of PCG iterations. *(a)* $err = \|\mathbf{r}\|_2/\|\mathbf{b}\|_2$. *(b)* $err = \left\|\tilde{\mathbf{A}}^{-1}\mathbf{r}\right\|_2/\left\|\tilde{\mathbf{A}}^{-1}\mathbf{b}\right\|_2$

This slow convergence rate is typical for a purely mechanical problem $\mathbf{K} = \mathbf{K}_{uu}$, which is known to be worse conditioned than its dielectric counterpart $\mathbf{K}_{\varphi\varphi}$. Moreover, because the condition number $k_2(\mathbf{K}_{uu})$ depends on the fundamental frequency of the shape[6] (Fried, 1972), i.e. of a fictitious structure having resonator's geometry but unit density, the err_1-convergence deteriorates as linear dimensions diverge (Table 4.6). For strip geometries, it can be so poor that it

[6] This statement is better assimilated by evoking Eqs. (3.18)–(3.20) of Chapter 3 which demonstrate that the element stiffness matrices embed the metric matrix $\mathfrak{T}$— the mass matrix for unit density.

renders the PCG method almost useless, unless low memory requirements are imperative.

Table 4.6 Performance ratios for the direct and PCG iterative solutions of the piezostatic problems from Table 5.2.

Shape	Region $l_x \times l_y \times l_z$				PCG iterations err_1	PCG iterations err_2	Arithmetic ratio Direct / PCG err_1	Arithmetic ratio Direct / PCG err_2
cube	$1 \times 1 \times 1$				320	14	200	317
plate	$8 \times 8 \times 1$				1031	24	2	70
strip	$15 \times 4 \times 1$				1212	22	0.5	24

Note: In the PCG solution, the tolerance on both the err_1 and err_2 was $tol = 10^{-3}$.

In contrast, the PCG method demonstrates a spectacular convergence (Fig. 4.9*(b)*) for the electrically-driven piezostatic problems, provided the error is measured in the $\tilde{\mathbf{A}}^{-1}$-norm (Golub and Van Loan, 1989). Indeed, quantity $err_2 = \left\|\tilde{\mathbf{A}}^{-1}\mathbf{r}\right\|_2 / \left\|\tilde{\mathbf{A}}^{-1}\mathbf{b}\right\|_2$ converges simultaneously with the capacitance C_s, and no drastic increase in the number of iterations is observed as the ratio of linear dimensions grows. As the last column of Table 4.6 demonstrates, the PCG method remains superior to the Gaussian elimination for a wide range of crystal geometries. Its convergence rate corresponds to that of an electrostatic problem of the same size, and can be related to the condition number $k_2(\mathbf{K}_{\varphi\varphi})$. The closeness of the two curves in Fig. 4.9*(b)* indirectly indicates that the latter is little affected by the addition of the superelement. It inevitably deteriorates with an increased number of variables (Fig. 4.10), i.e. when the discrete model approaches the continuum, for which $k_2 \to \infty$.

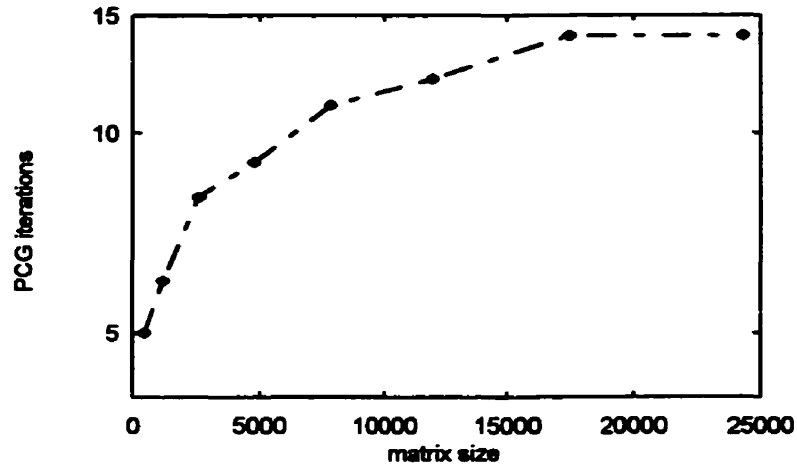

Fig 4.10 Number of PCG iterations for various matrix sizes. Here, $tol = 10^{-3}$.

The number of iterations also increases slightly as the difference between dielectric moduli ϵ^S becomes greater. For instance, for lithium niobate, the same problem configuration is resolved in 20 iterations compared to the already mentioned 10–15 iterations for quartz.

5.3 *The Lanczos algorithm for the vibration problem*

The Lanczos method finds a few extremal (largest and smallest) eigenvalues λ of a real symmetric $n \times n$ matrix $\mathbf{A}$

$$\mathbf{A}\mathbf{x} = \lambda\mathbf{x}, \tag{5.27}$$

by generating a sequence of symmetric tridiagonal $k \times k$ matrices $\mathbf{T}_k$

$$\mathbf{T}_k = \begin{bmatrix} \alpha_1 & \beta_2 & & & & \\ \beta_2 & \alpha_2 & \beta_3 & & & \\ & \beta_3 & \cdot & \cdot & & \\ & & \cdot & \cdot & \cdot & \\ & & & \cdot & \cdot & \beta_k \\ & & & & \beta_k & \alpha_k \end{bmatrix}, \tag{5.28}$$

whose extremal eigenvalues provide good approximations to the extremal eigenvalues of $\mathbf{A}$ (Parlett, 1980; Golub and Van Loan, 1989). For $k = n$ such a matrix $\mathbf{T}_n$ could have been obtained from a similarity transformation (e.g. Householder reduction)

$$\mathbf{T}_n = \mathbf{Q}_n^{\mathrm{T}} \mathbf{A} \mathbf{Q}_n, \tag{5.29}$$

where $\mathbf{Q}_n$ is an orthogonal matrix:

$$\mathbf{Q}_n^{\mathrm{T}} \mathbf{Q}_n = \mathbf{I}_n. \tag{5.30}$$

The eigenvalues of the similar matrix $\mathbf{T}_n$ are those of $\mathbf{A}$, but can be recovered more easily (e.g. QR algorithm or bisection method) since $\mathbf{T}_n$ is tridiagonal. However, the goal is to avoid such explicit transformations because they inevitably destroy the sparsity of $\mathbf{A}$. Instead, the Lanczos algorithm, starting from a given vector $\mathbf{q}_1$, calculates the elements of $\mathbf{T}_n$ directly, i.e. from Eq. (5.29) rewritten in the form

$$\mathbf{A} \mathbf{Q}_n = \mathbf{Q}_n \mathbf{T}_n, \tag{5.31}$$

and Eq. (5.30). The generated orthonormal columns of matrix $\mathbf{Q}_n = (\mathbf{q}_1, \ldots, \mathbf{q}_n)$ are the *Lanczos vectors*.

Reducing the whole matrix ($k = n$) to tridiagonal form was the original use of the Lanczos algorithm. However, for practical applications, these are the eigenvalues and eigenvectors of matrix $\mathbf{T}_k$ at step $k \ll n$, i.e. long before the tridiagonalization process is completed, that are of interest. For $k < n$, Eq. (5.31) is not exact any longer and should be rewritten as

$$\mathbf{A} \mathbf{Q}_k = \mathbf{Q}_k \mathbf{T}_k + \mathbf{R}_k, \tag{5.32}$$

where $\mathbf{Q}_k$ is an $n \times k$ submatrix of $\mathbf{Q}_n$,

$$\mathbf{Q}_k^{\mathrm{T}} \mathbf{Q}_k = \mathbf{I}_k, \tag{5.33}$$

and $\mathbf{R}_k = (0, 0, \ldots, 0, \mathbf{r}_k)$ is an $n \times k$ matrix with the *residual vector*

$$\mathbf{r}_k = \mathbf{q}_{k+1} \beta_k \tag{5.34}$$

in the last column. Equations (5.33)–(5.34) suggest that, provided $\mathbf{r}_k$ is available from the previous Lanczos iteration, β_k and $\mathbf{q}_{k+1}$ can be obtained by normalizing $\mathbf{r}_k$. This corresponds to steps 1 and 6, respectively, of the simple Lanczos algorithm, shown in Fig. 4.11. The residual vector itself

$$\mathbf{r}_k = \mathbf{A} \mathbf{q}_k - \mathbf{q}_{k-1} \beta_{k-1} - \mathbf{q}_k \alpha_k \tag{5.35}$$

is calculated in two steps. First, a partial residual is found (steps 2 and 3, Fig. 4.11) and used to compute the diagonal entries of matrix $\mathbf{T}_k$

$$\alpha_k = \mathbf{q}_k^{\mathrm{T}} \mathbf{A} \mathbf{q}_k; \tag{5.36}$$

then, vector $\mathbf{r}_k$ is updated (step 5) to produce a complete residual. As follows from Eqs. (5.34)–(5.36), $\mathbf{q}_k$, α_k, β_k are computed in such a way that in exact arithmetic the Lanczos vectors satisfy explicitly the following orthogonality conditions:

$$\mathbf{q}_k^{\mathrm{T}} \mathbf{q}_{k+1} = 0, \quad \mathbf{q}_k^{\mathrm{T}} \mathbf{q}_{k-1} = 0, \quad \|\mathbf{q}_k\|_2 = 1 \tag{5.37}$$

as well as

$$\mathbf{q}_k^{\mathrm{T}} \mathbf{r}_k = 0 \tag{5.38}$$

at each step of the algorithm. Consequently, the current Lanczos vector $\mathbf{q}_k$ and the residual vector $\mathbf{r}_k$ are orthogonal to all previous Lanczos vectors $\mathbf{Q}_{k-1}$.

<u>Initialization:</u>

Guess $\mathbf{r}_0 \neq 0$

Set $\beta_0 = \|\mathbf{r}_0\|_2$

$\mathbf{q}_0 = 0$

<u>Lanczos Step:</u>

For $k = 1, 2, \ldots$

1. $\mathbf{q}_k = \mathbf{r}_{k-1}/\beta_{k-1}$
2. $\mathbf{r}_k = \mathbf{A}\mathbf{q}_k$
3. $\mathbf{r}_k = \mathbf{r}_k - \beta_{k-1}\mathbf{q}_{k-1}$
4. $\alpha_k = \mathbf{r}_k^{\mathrm{T}}\mathbf{q}_k$
5. $\mathbf{r}_k = \mathbf{r}_k - \alpha_k\mathbf{q}_k$
6. $\beta_k = \|\mathbf{r}_k\|_2$
7. Compute θ_i, $\mathbf{s}_i$, $\mathbf{y}_i$, $i = 1, \ldots, k$, if needed.
8. If ($\forall$ Ritz pairs (θ_i, $\mathbf{y}_i$), $i = 1, \ldots, m$ are satisfactory) Stop

End loop

Fig 4.11 The basic Lanczos algorithm.

At each step of the Lanczos iteration, the extremal eigenvalues of matrix $\mathbf{T}_k$ turn out to be increasingly good approximations to **A**'s extremal eigenvalues. These approximations to **A**'s eigenpairs, i.e. the *Ritz pairs* $(\theta_i, \mathbf{y}_i)$, can be obtained by solving a small $(k \ll n)$ tridiagonal eigenproblem

$$\mathbf{T}_k \mathbf{s}_i = \theta_i \mathbf{s}_i, \quad i = 1, ..., k, \tag{5.39}$$

with normalized eigenvectors $\mathbf{s}_i$, $\|\mathbf{s}_i\|_2 = 1$, and then computing the Ritz vector as

$$\mathbf{y}_i = \mathbf{Q}_k \mathbf{s}_i, \quad i = 1, ..., k. \tag{5.40}$$

However, the accuracy of the Ritz pair can be established without forming $\mathbf{y}_i$ explicitly until θ_i becomes an accepted eigenvalue of **A**. As shown in Parlett (1980), an error bound on the residual can be computed as

$$\|\mathbf{A}\mathbf{y}_i - \mathbf{y}_i \theta_i\|_2 = \beta_k |s_{i,k}|, \quad i = 1, ..., k \tag{5.41}$$

where $s_{i,k}$ denotes the bottom (kth) component of vector $\mathbf{s}_i$, thus making quantity $\beta_{ki} = \beta_k |s_{i,k}|$ essential in assessing the accuracy of **A**'s eigenpair. The Cauchy's interlace theorem states that for any real number θ and any vector $\mathbf{x}$, such that $\|\mathbf{x}\|_2 = 1$, there is an eigenvalue λ of **A** satisfying

$$|\lambda - \theta| \leq \|\mathbf{A}\mathbf{x} - \mathbf{x}\theta\|_2. \tag{5.42}$$

Setting $\theta = \theta_i^{(k)}$, one can conclude that each Ritz interval $\left[\theta_i^{(k)} - \beta_{ki}, \theta_i^{(k)} + \beta_{ki}\right]$ contains the Ritz value $\theta_i^{(k+1)}$ at the next step $k+1$

$$\left|\theta_i^{(k+1)} - \theta_i^{(k)}\right| \leq \beta_{ki}, \quad i = 1, ..., k, \tag{5.43}$$

and that the same error bound applies to an eigenvalue λ of matrix **A**:

$$\left|\lambda - \theta_i^{(k)}\right| \leq \beta_{ki}, \quad i = 1, ..., k \tag{5.44}$$

since $\|\mathbf{y}\|_2 = \sqrt{\mathbf{s}^T \mathbf{Q}_k^T \mathbf{Q}_k \mathbf{s}} = \|\mathbf{s}\|_2 = 1$ in exact arithmetic. For well separated eigenvalues this error bound can be refined (Parlett, 1980; Parlett and Nour-Omid, 1985), so that the Ritz intervals are less likely to overlap; the eigenvector error bound is also available from the above references. Finally, the Ritz value $\theta_i^{(k)}$ is considered converged to an eigenvalue λ of matrix **A** if its error bound $\tilde{\beta}_{ki}$ is less than the tolerance *tol*:

$$\tilde{\beta}_{ki} \leq tol \left| \theta_i^{(k)} \right|. \tag{5.45}$$

As the conjugate gradient method, the Lanczos algorithm access matrix **A** only through a function that computes **Ax** for a given vector **x**, which makes it well suited for large and sparse matrices. In exact arithmetic, the simple Lanczos method (Fig. 4.11) requires only three vectors $\mathbf{r}_k$, $\mathbf{q}_k$, $\mathbf{q}_{k-1}$ of length n; an implementation of the algorithm with just two n-vectors can be found in Golub and Van Loan (1989). However, in finite precision, additional storage is needed to hold some old Lanczos vectors used to enforce orthogonality against the newly computed vectors. Indeed, it is well known that a global loss of orthogonality among the Lanczos vectors occurs as a result of roundoff error. What is more, in floating-point arithmetic this constitutes a necessary and sufficient condition for convergence of $\mathbf{T}_k$'s eigenvalues to that of **A**. Therefore, if the 'practical' conjugate gradient algorithm is almost identical to its exact arithmetic version (Fig. 4.8), the Lanczos process, if implemented as shown in Fig. 4.11, will never converge, computing more and more redundant copies of the extremal eigenvalues. This earned it the reputation of 'unstable' and delayed its acceptance as a very effective method of finding some of the extremal eigenpairs. The following modifications are required to turn the simple recurrence of Fig. 4.11 into a *practical* Lanczos algorithm:

- limited *reorthogonalization* of Lanczos vectors, e.g. *selective* (Parlett and Scott, 1979), *partial* (Simon, 1984) or *external selective* (Grimes *et al.*, 1994), to prevent the appearance of spurious eigenpairs;
- *block* form of Lanczos method to find multiple or clustered eigenvalues;
- using the Lanczos method *iteratively*, i.e. restarting it after a good approximation to an eigenvector was found;
- efficient *stopping criteria* for identifying converged Ritz pairs.

Creating a program that would efficiently combine some of or all the above modifications is not straightforward. In resent years, a lot of research has been devoted to the development of a reliable Lanczos eigensolver (Parlett and Nour-Omid, 1989; Grimes *et al.*, 1994) that could be used as a 'black box' inside an

application code. Nevertheless, no standard Lanczos-based software, such as EISPACK for dense matrices, exists yet. A few stand alone FORTRAN programs developed by matrix experts are outlined in Parlett (1984). The programs typically count several thousand lines of code, and differ, in particular, by the level of orthogonalization (if any) maintained among the Lanczos vectors. Only Scott's program LASO2, which implements the *block version of selective reorthogonalization*, is distributed independently of its author. The double precision version of LASO2 comes in two flavors — DNLASO and DILASO: the former computes a specified number of eigenpairs m at one end of the spectrum of the symmetric matrix **A**, while the latter finds all the eigenpairs outside a user defined interval. With some modifications described later in this section, the DNLASO program was adopted as an eigensolver and integrated with the piezoelectric modal analysis code. Although this version uses only half the power of the Lanczos algorithm, which determines eigenvalue at both ends of **A**'s spectrum, it was found more practical to have control over the number of wanted eigenpairs rather than adjusting the excluded interval for every specific case.

The selective reorthogonalization scheme (Parlett and Scott, 1979) exploits the fact that orthogonality is lost in the direction of converged Ritz vectors, so that any newly computed Lanczos vector is orthogonalized only against this selected set, not against all the previous Lanczos vectors. The block version of the algorithm replaces the single Lanczos vector $\mathbf{q}_k$ by an orthonormal block of b vectors and matrix $\mathbf{T}_k$ is block tridiagonal. To calculate this block at each step of the recurrence, the simple orthonormalization of the residual vector (steps 6 and 1, Fig. 4.11) is replaced by the modified Gram-Schmidt process (Watkins, 1991) which produces a QR decomposition of the $n \times b$ block of residual vectors $\mathbf{r}_k$. In a sense, the block variant of the Lanczos algorithm is to the simple Lanczos recursion what the subspace iteration is to the inverse iteration. A large block size improves convergence, but because the amount of work is proportional to b^2 (Golub and Van Loan, 1989), it is not very practical to have it larger than the maximal multiplicity of any eigenvalue sought. One should note, in passing, that the capability to adjust the block size was very appreciated when calculating the spectrum of strip piezoelectric vibrators which often required $b > 2$. To run LASO2, the user must supply two subroutines OP and IOVECT. The first returns the block product **AX** for an $n \times b$ input array **X**, while the second stores the

selected Lanczos vectors on a secondary storage device and periodically recalls them when needed. Overall, the program requires approximately $3n \times b$ storage in addition to $n \times m$ locations reserved for the computed eigenvectors. If some good guesses at **A**'s wanted eigenvectors are available, it is possible to supply them as a starting block; otherwise, the algorithm starts with b randomly generated vectors.

The convergence rate (or, as it is often called, the emergence rate) of the eigenvalue λ_i is determined by the gap ratio $|\lambda_{i+1} - \lambda_i|/|\lambda_n - \lambda_1|$ (Grimes *et al.*, 1994), where the eigenvalues are indexed in ascending order $|\lambda_1| \leq ... \leq |\lambda_n|$. Because for the vibration problem they have the physical meaning of squared natural frequencies, the largest eigenvalues λ_n are typically very large compared to λ_1, $\lambda_n \gg \lambda_1$. Therefore, in the sense of relative separation, the largest eigenvalues are said to be better separated than the smallest, even though $|\lambda_{i+1} - \lambda_i|$ could be of the same order of magnitude in either case. This means that convergence to small eigenvalues $\lambda_i \approx \lambda_1$, which are usually of interest in modal analysis, will be very slow. Although the Lanczos method produces eigenvalues at both ends of **A**'s spectrum, the larger eigenpairs will emerge sooner than the small ones: according to Parlett (1984), the algorithm will find some 50 eigenvalues near λ_n for every eigenvalue near λ_1. Unfortunately, preconditioning cannot be directly applied to the eigenvalue problem since it changes the eigenpairs sought. The cure of the convergence problem is the same as for the power method — to give the algorithm the inverse operator $\mathbf{A}^{-1}$ (Scott, 1982). As in the case of inverse iteration (inverse power method), the smallest eigenvalues of **A** are mapped onto the largest eigenvalues of $\mathbf{A}^{-1}$, and the convergence ratio is correspondingly inverted. This approach can turn out to be expensive since, to deliver $\mathbf{A}^{-1}$, a factorization of **A** is typically required; however, experience shows that this strategy pays by a very rapid convergence.

In general, to improve convergence of eigenvalues in any part of the spectrum, e.g. in the neighborhood of a specified number σ, the method is applied to the shifted and inverted operator $(\mathbf{A} - \sigma\mathbf{I})^{-1}$, whose eigenvalues μ are related to the original eigenvalues λ of **A** by the *spectral transformation* relation

$$\mu = \frac{1}{\lambda - \sigma}. \tag{5.46}$$

The latter maps the eigenvalues λ close to the *shift* σ onto large eigenvalues μ, which are delivered first by the Lanczos algorithm. In the context of a generalized eigenvalues problem (5.1), the spectral transformation amounts to applying the Lanczos algorithm to the inverted and shifted problem

$$\mathbf{W}^{\mathrm{T}}(\mathbf{K}-\sigma\mathbf{M})^{-1}\mathbf{W}\mathbf{z}=\frac{1}{\lambda-\sigma}\mathbf{z}, \tag{5.47}$$

where it was assumed that $\mathbf{M}$ could be factored as

$$\mathbf{M}=\mathbf{W}\mathbf{W}^{\mathrm{T}}, \tag{5.48}$$

and $\mathbf{z}$ is the transformed eigenvector

$$\mathbf{z}=\mathbf{W}^{\mathrm{T}}\mathbf{x}. \tag{5.49}$$

It can be rewritten in the form of a standard eigenvalue problem

$$\mathbf{A}\mathbf{z}=\mu\mathbf{z}, \tag{5.50}$$

with symmetric operator

$$\mathbf{A}=\mathbf{W}^{\mathrm{T}}(\mathbf{K}-\sigma\mathbf{M})^{-1}\mathbf{W}, \tag{5.51}$$

whose eigenvalues and eigenvectors are related to those of (5.1) by (5.46) and (5.49) respectively. Because $\mathbf{A}$ in (5.51) is never formed explicitly, calculating the matrix-vector product $\mathbf{A}\mathbf{q}$ implies solving the linear system

$$(\mathbf{K}-\sigma\mathbf{M})\mathbf{r}=\mathbf{W}\mathbf{q}. \tag{5.52}$$

Although the spectral transformation is naturally used by the subspace iteration technique, it took Ericsson and Ruhe (1980) to emphasize its much more effective combination with the powerful Lanczos method. Ericsson and Ruhe applied the Lanczos algorithm to the symmetric operator (5.51) and employed the $\mathbf{LDL}^{\mathrm{T}}$ factorization of $\mathbf{K}-\sigma\mathbf{M}$ to solve (5.52). They also proposed a sophisticated shifting strategy (i.e. using many shifts, and, consequently, many factorizations of matrix $\mathbf{K}-\sigma\mathbf{M}$, to obtain the solution in few Lanczos steps, or using few shifts but accepting longer Lanczos runs), and derived the error bound for the original eigenvalue λ:

$$\left|\lambda-\left(\sigma+1/\theta_i^{(k)}\right)\right|\leq\beta_{ki}/\left(\theta_i^{(k)}\right)^2,\quad i=1,\ldots,k. \tag{5.53}$$

Inequality (5.53) shows how the spectral transformation loosens the error bound (5.44): when λ is close to the shift σ, only a 'moderately' small β_{ki} is sufficient to guarantee a good approximation of λ by $\sigma + 1/\theta_i^{(k)}$ since $\theta_i^{(k)}$ in the denominator is large.

In the form (5.46)–(5.52), the spectral transformation Lanczos method was applied to large two- and three-dimensional piezoelectric vibration problems, where the system (5.52) has been solved by some variants of Gaussian elimination such as substructuring technique (Yong and Zhang, 1994), modified Crout's factorization (Yong and Cho, 1994), or $\mathbf{LDL}^{\mathrm{T}}$ factorization (Yong, 1995). In all these cases the solution implied another factorization — that of matrix $\mathbf{M}$ — as part of the transformation (5.47). With $\mathbf{M}$ semi-definite, the factor $\mathbf{W}$ in (5.48) is rectangular with linearly independent column:

$$\mathbf{W} = \begin{bmatrix} \mathbf{L} \\ 0 \end{bmatrix}, \tag{5.54}$$

where $\mathbf{L}$ is the Choleski factor of matrix $\mathbf{M}_{uu} = \mathbf{LL}^{\mathrm{T}}$. In principle, (5.52) could be solved by an iterative (e.g. PCG) method, but, as will be shown below, the conditioning of matrix $\mathbf{K} - \sigma\mathbf{M}$ deteriorates rapidly as σ grows, leading to long iterations. Given the fact that (5.52) is to be solved as many times as the product $\mathbf{Ax}$ is calculated, a direct solution is clearly preferred. Therefore, in the framework of Ericsson and Ruhe's spectral transformation, two costly factorizations are typically required.

However, it is a misconception that matrix $\mathbf{M}$ should always be factored in order to maintain the symmetry of the operator $\mathbf{A}$ given to the Lanczos program. A small but practically very important variant of spectral transformation described in Nour-Omid *et al.* (1987) suggests applying Lanczos algorithm to the generalized eigenvalue problem rewritten in the form

$$(\mathbf{K} - \sigma\mathbf{M})^{-1}\mathbf{Mx} = \mu\mathbf{x}, \tag{5.55}$$

where μ is the shifted and inverted eigenvalue (5.46), and $\mathbf{x}$ is the original eigenvector of system (5.1). Working with the nonsymmetric operator

$$\mathbf{A} = (\mathbf{K} - \sigma\mathbf{M})^{-1}\mathbf{M} \tag{5.56}$$

may seem extravagant, but after observing that it is self-adjoint in the **M** semi-inner product:

$$(\mathbf{Ax}, \mathbf{y})_{\mathbf{M}} = (\mathbf{x}, \mathbf{Ay})_{\mathbf{M}} = \mathbf{y}^{\mathrm{T}}\mathbf{MAx}, \tag{5.57}$$

it becomes clear that the standard Lanczos algorithm can be applied directly to (5.56) provided all the inner products are replaced by the **M** semi-inner products (Fig. 4.12).

<u>Initialization:</u>

Guess $\mathbf{q}_0 \neq 0$

Set $\mathbf{p}_0 = \mathbf{M}\mathbf{q}_0$

Solve $(\mathbf{K} - \sigma\mathbf{M})\mathbf{r}_0 = \mathbf{p}_0$ for $\mathbf{r}_0$

$\mathbf{p}_0 = \mathbf{M}\mathbf{r}_0$

$\beta_0 = \sqrt{\mathbf{r}_0^{\mathrm{T}}\mathbf{p}_0}$

$\mathbf{q}_0 = 0$

<u>Lanczos Step:</u>

For $k = 1, 2, \ldots$

1. $\mathbf{q}_k = \mathbf{r}_{k-1}/\beta_{k-1}$
2. $\mathbf{p}_k = \mathbf{M}\mathbf{q}_k$
3. Solve $(\mathbf{K} - \sigma\mathbf{M})\mathbf{r}_k = \mathbf{p}_k$ for $\mathbf{r}_k$
4. $\mathbf{r}_k = \mathbf{r}_k - \beta_{k-1}\mathbf{q}_{k-1}$
5. $\alpha_k = \mathbf{r}_k^{\mathrm{T}}\mathbf{p}_k$
6. $\mathbf{r}_k = \mathbf{r}_k - \alpha_k\mathbf{q}_k$
7. $\mathbf{p}_k = \mathbf{M}\mathbf{r}_k$
8. $\beta_k = \sqrt{\mathbf{r}_k^{\mathrm{T}}\mathbf{p}_k}$
9. Compute $\theta_i, \mathbf{s}_i, \mathbf{y}_i, i = 1, \ldots, k$
10. If ($\forall$ Ritz pairs $(\theta_i, \mathbf{y}_i)$, $i = 1, \ldots, m$ are satisfactory) Stop

End loop

Fig 4.12 The modified Lanczos algorithm for vibration problems.

In exact arithmetic, the modified Lanczos recurrence generates M-orthogonal Lanczos vectors $\mathbf{Q}_k$:

$$\mathbf{q}_k^{\mathrm{T}}\mathbf{M}\mathbf{q}_{k+1} = 0, \quad \mathbf{q}_k^{\mathrm{T}}\mathbf{M}\mathbf{q}_{k-1} = 0, \quad \|\mathbf{q}_k\|_{\mathbf{M}} = 1 \tag{5.58}$$

by calculating α_k as

$$\alpha_k = \mathbf{q}_k^{\mathrm{T}}\mathbf{M}\mathbf{A}\mathbf{q}_k = \mathbf{q}_k^{\mathrm{T}}\mathbf{M}(\mathbf{K} - \sigma\mathbf{M})^{-1}\mathbf{M}\mathbf{q}_k. \tag{5.59}$$

It also follows from the above that the residual vector is M-orthogonal to the current Lanczos vector

$$\mathbf{q}_k^{\mathrm{T}}\mathbf{M}\mathbf{r}_k = 0, \tag{5.60}$$

as well as to the previous ones. Expression (5.59) reveals that the modified Lanczos algorithm can be viewed as the standard one with respect to the generalized eigenvalue problem

$$\mathbf{M}(\mathbf{K} - \sigma\mathbf{M})^{-1}\mathbf{M}\mathbf{x} = \mu\mathbf{M}\mathbf{x}, \tag{5.61}$$

which has the same eigenpairs as (5.55) but is symmetric. Therefore, their is no drawback associated with the application of the Lanczos recurrence to the nonsymmetric operator (5.56), while the advantages are substantial.

First, no factorization of matrix M is needed, thus saving $n_M p_M^2/2$ work, where n_M and p_M are the size and semiband width of M respectively; consequently, the storage requirements can be reduced by $n_M(p_M - s_M)$, where s_M is the average number of nonzeros per row, by switching to a more efficient sparse storage of M. Furthermore, the M-factorization is not required even when evaluating the residual norm

$$\|\mathbf{M}(\mathbf{K} - \sigma\mathbf{M})^{-1}\mathbf{M}\mathbf{y}_i - \theta_i\mathbf{M}\mathbf{y}_i\|_{\mathbf{M}^{-1}} = \beta_{ki}, \quad i = 1, \ldots, k, \tag{5.62}$$

since $\mathbf{M}^{-1}$ cancels in (5.62). The generalized Cauchy's interlace theorem states that for any real scalar θ and any vector $\mathbf{x}$, such that $\|\mathbf{M}\mathbf{x}\|_{\mathbf{M}^{-1}} = 1$, there is an eigenvalue λ of A satisfying

$$|\lambda - \theta| \leq \|\mathbf{A}\mathbf{x} - \theta\mathbf{M}\mathbf{x}\|_{\mathbf{M}^{-1}}. \tag{5.63}$$

Using the above and the fact that Lanczos vectors are **M**-orthogonal in exact arithmetic, so that the Ritz vector **y** in (5.62) satisfies $\|\mathbf{My}\|_{\mathbf{M}^{-1}} = 1$, the error bound for the transformed eigenvalue μ is given by (5.44), i.e.

$$\left|\mu - \theta_i^{(k)}\right| \leq \beta_{ki}, \quad i = 1, ..., k, \tag{5.64}$$

and for the original λ by (5.53); as in the case of the standard Lanczos procedure, these bounds can be improved. Although at each step of the modified Lanczos algorithm an auxiliary vector $\mathbf{p} = \mathbf{Mx}$ (steps 2 and 7, Fig. 4.12) is to be computed twice, requiring $2n_M s_M$ flops, this is still cheaper than performing the forward elimination and back substitution ($2n_M p_M$) involved in the computation of **Ax**, with **A** from Eq. (5.51) since $s_M \leq p_M$; for the total number of Lanczos iterations *iter*, the amount of work diminishes therefore by $2n_M(p_M - s_M) \times iter$. Finally, there is no need to back transform the computed eigenvectors as in (5.49) since they are the original eigenvectors of (5.1).

At each iteration, the modified Lanczos algorithm requires solving system

$$(\mathbf{K} - \sigma\mathbf{M})\mathbf{r} = \mathbf{Mq} \tag{5.65}$$

for **r** given **q**. As already mentioned in connection with the similar system (5.52), the PCG method is not very useful to this end. Because the price to pay for this is high (i.e. the cost of complete factorization of $\mathbf{K} - \sigma\mathbf{M}$), the performance, or rather 'misperformance', of the PCG algorithm applied to (5.65) merits some comment. Figure 4.13 shows how the number of PCG iterations changes as the shift σ grows. The curve was obtained for a cubic shape discretized as in Fig.4.7(a), but the behavior is characteristic for other geometries and meshes as well. First, even for $\sigma = 0$ the convergence is not that of an electrically-driven piezostatic problem (Table 4.6): some 270–300 PCG steps are required to achieve the tolerance $tol = 10^{-3}$, no matter which error estimate, (5.25) or (5.26), is used. Indeed, the multiplication by the mass matrix **M** purges all electrical coordinates from the right-hand side of (5.65), which results in purely 'mechanical' convergence. The latter is governed by the conditioning of the shifted matrix $k_2(\mathbf{K}_{uu} - \sigma\mathbf{M}_{uu})$, which degrades rapidly as σ increases — a behavior well known to many finite element specialists.

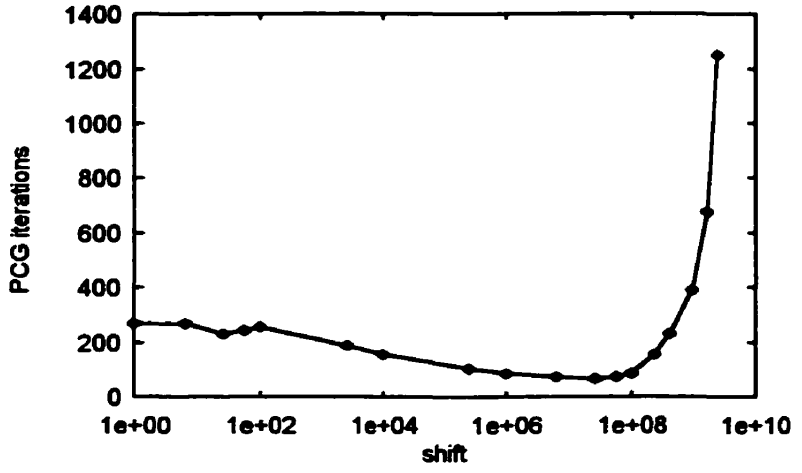

Fig 4.13 Number of PCG iterations for the operator $\mathbf{K} - \sigma\mathbf{M}$ as function of shift σ.

The minimum in the number of PCG iterations in the neighborhood of the lowest eigenvalue $\lambda_1 = 10^8$ (fundamental frequency ω_1 squared) of (5.1) does not come out of the blue. It is tempting to explain its location by means of the computable bounds on the spectral condition numbers of the global stiffness and mass matrices[7] derived by Fried (1972, 1973). They are useful in many respects (e.g. to study the influence of the discretization parameters on the PCG convergence), but what is relevant at this point is that the bounds on $k_2(\mathbf{K}_{uu})$ are related to λ_1, whereas the bounds on $k_2(\mathbf{M}_{uu})$ do not involve λ_1 at all. The former fact — used earlier to substantiate the ill-conditioning of matrix $\mathbf{K}_{uu}$ as the vibrator shape elongates — distinguishes the shift $\sigma \approx \lambda_1$ among other values. It is therefore natural to assume that the 'balance' between matrices $\mathbf{K}_{uu}$ and $\sigma\mathbf{M}_{uu}$, i.e. the lowest condition number $k_2(\mathbf{K}_{uu} - \sigma\mathbf{M}_{uu})$, is achieved for σ close to $\lambda_1 = \omega_1^2$.

As follows from the above, the complete $\mathbf{LDL}^T$ factorization of matrix $\mathbf{K} - \sigma\mathbf{M}$ in (5.65) is inevitable. Its cost $(n_K p_K^2/2)$ has been included in the arithmetic estimates for the two schemes of spectral transformation Lanczos algorithm (Table 4.7).

---

[7] Fried's bounds are expressed in terms of the extremal eigenvalues of the element stiffness and mass matrices, the maximal number of elements sharing a nodal point and the fundamental frequency of the structure. It is felt, however, that they can be further refined for tetrahedral elements to include weighting coefficients and extremal eigenvalues of the universal matrices.

Table 4.7 Operation count and storage requirements for the spectral transformation Lanczos method.

Operator **A**	Arithmetic, flops	Storage, words
$\mathbf{W}^{\mathrm{T}}(\mathbf{K}-\sigma\mathbf{M})^{-1}\mathbf{W}$	$(n_K p_K^2 + n_M p_M^2)/2$ $+ 2(n_K p_K + n_M p_M) \times iter$	$n_K p_K + n_M p_M$
$(\mathbf{K}-\sigma\mathbf{M})^{-1}\mathbf{M}$	$n_K p_K^2/2$ $+ 2(n_K p_K + n_M s_M) \times (iter+1)$	$n_K p_K + n_M s_M$
floating-point format	double (8-byte)	single (4-byte)
$\Delta_{arithm} = n_M p_M^2/2 - 2(n_K p_K + n_M s_M) + 2n_M(p_M - s_M) \times iter$ (flops) $\Delta_{storage} = n_M(p_M - s_M)$ (words)		

The operation count corresponds to the simplified exact arithmetic versions of the algorithms presented in Fig. 4.11 (with symmetric operator (5.51)) and Fig. 4.12 respectively, for which the block size is $b = 1$. Nevertheless, because the additional storage and work associated with practical implementations of both schemes (e.g. selective reorthogonalization) is almost the same, it is sufficient to conclude that the second scheme is unconditionally better in terms of both storage and computing time. The latter is actually proportional to the calculated arithmetic cost since both global matrices are stored in core memory, and no additional work is associated with accessing secondary storage (except for some negligible traffic of Lanczos vectors carried out by the subroutine IOVECT).

The **M**-orthogonal Lanczos algorithm — although well known to matrix experts (Parlett, 1980; Scott, 1982), integrated with some professional Lanczos eigensolvers (Jones and Patrick, 1993; Grimes *et al.*, 1994), and certainly embedded in many finite element packages — seems to be sometimes overlooked by engineers, as attempts to optimize the factorization of the mass matrix suggest. Meanwhile, its deliberate use is particularly important in conjunction with large scale finite element models of novel problems, not solved by commercial packages, or of problems whose demand of core storage is so high that one cannot afford any inefficiency in the handling of data. The problem of piezoelectric vibrations with open electric boundaries is a perfect example of both these specifics. The fact that in this case the mass matrix **M** is singular does not invalidate the **M**-orthogonal Lanczos recurrence. Yes, computing the semi-norm $\|\mathbf{r}_k\|_{\mathbf{M}} = \sqrt{\mathbf{r}_k^{\mathrm{T}}\mathbf{M}\mathbf{r}_k}$ (steps 7

and 8, Fig. 4.12) with **M** semi-definite can lead to a zero β_k for a nontrivial residual vector $\mathbf{r}_k$. This only indicates — through Eqs. (5.32) and (5.34) — that all the *finite* (mechanical) eigenvalues of (5.1) computed at the kth step are exact. As pointed out by Scott (1982) and explained in greater detail in Nour-Omid *et al.* (1987), the eigenvector associated with these finite eigenvalues, i.e. the desired eigenvectors, lie in the range of operator $(\mathbf{K}-\sigma\mathbf{M})^{-1}\mathbf{M}$. The Lanczos vectors must also be confined to this subspace, otherwise the computed Ritz vectors will contain unwanted components in the null space of $(\mathbf{K}-\sigma\mathbf{M})^{-1}\mathbf{M}$. When working with operator (5.51) this condition was satisfied automatically since the multiplication by $\mathbf{W}^{\mathrm{T}}(\mathbf{K}-\sigma\mathbf{M})^{-1}\mathbf{W}$ purges any vector from components in the direction of infinite (electrical) eigenvalues; however, in the **M**-orthogonal spectral transformation Lanczos algorithm the finite subspace must be enforced explicitly. This is accomplished by choosing the starting vector $\mathbf{q}_0$ from the range of $(\mathbf{K}-\sigma\mathbf{M})^{-1}\mathbf{M}$, e.g. by applying the latter to a random n-vector (Initialization step, Fig. 4.12), so that in exact arithmetic all the generated Lanczos vectors will belong to the range of $(\mathbf{K}-\sigma\mathbf{M})^{-1}\mathbf{M}$.

This and the previously described modifications associated with the **M**-orthogonal Lanczos algorithm have been incorporated into the DNLASO code. Namely, the Euclidean dot products (norms) of vectors have been replaced, where required, by their **M**-products (norms); the modified Gram-Schmidt orthogonalization has been made **M**-orthogonal (Nour-Omid and Clough, 1985). Therefore, the resulting Lanczos solver, let call it DNLASO_M, can be seen as a variant of Scott's program DNLASO, fine tuned to find extreme eigenvalues of the vibration problem in the form (5.55) with **M** semi-definite. Before being definitively integrated with the piezoelectric application, DNLASO_M was applied concurrently with the original DNLASO to solve several test problems. The numerical behavior of DNLASO_M with nonsymmetric operator (5.56) was practically indistinguishable from the performance of DNLASO with symmetric operator (5.51). In all tests, the programs were identical in both accuracy of the eigenpairs and the number of Lanczos iterations required, apart from the obvious difference that DNLASO_M consumed less storage and computing time (Table 4.7) to deliver the same information.

The convergence behavior of the spectral transformation Lanczos method is illustrated in Fig. 4.14 for two types of eigenvalue distribution associated with a square plate and a strip respectively.

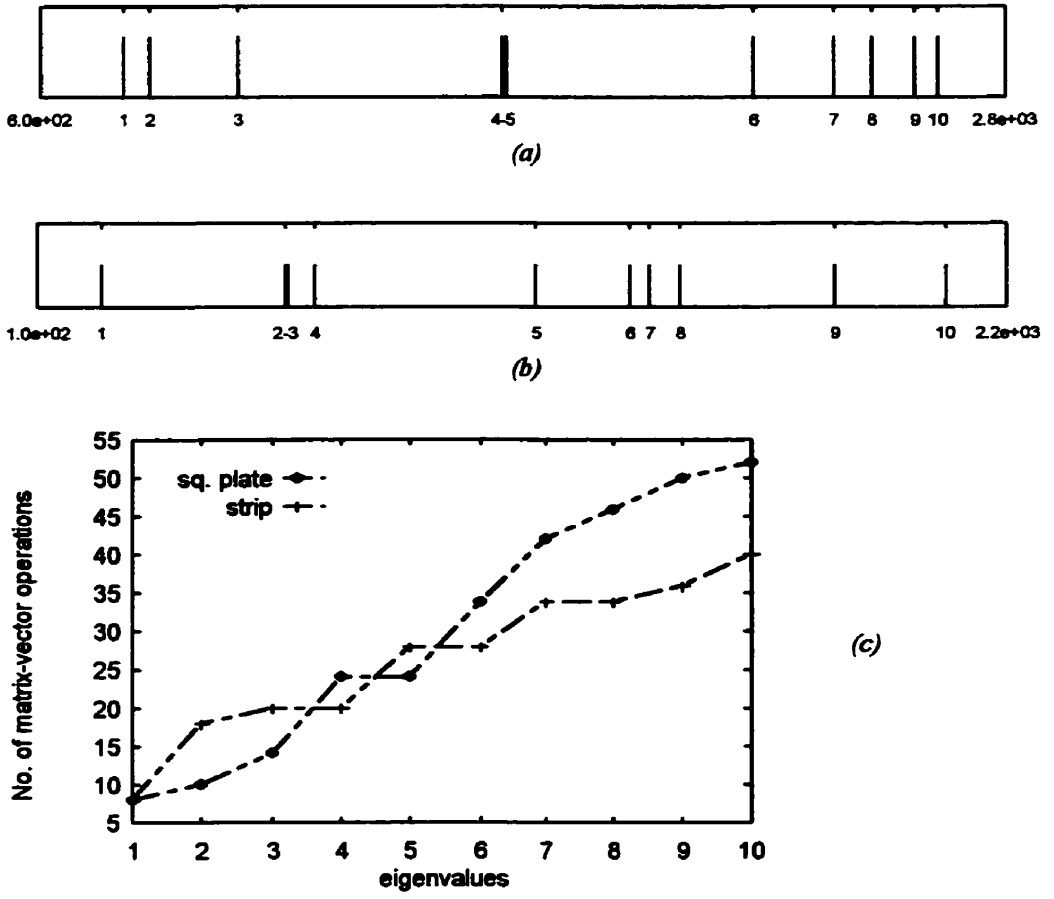

Fig 4.14 Distribution of the first ten eigenfrequencies ω: *(a)* square plate 6 : 6 : 1; *(b)* strip 12 : 3 : 1. *(c)* The number of matrix-vector operations **Ax** required by the spectral transformation block Lanczos algorithm as function of the number of wanted eigenpairs.

The two geometries were modeled by meshes of elements of second order shown in Table 4.2. In this example, the shift was taken slightly lower than the first eigenvalue $\sigma \approx \omega_1^2$; the block size was $b = 2$, so that the actual number of matrix-vector operations **Ax** (or the 'effective' number of Lanczos iterations $\overline{iter}$) was calculated as being twice the number of calls to the subroutine OP that delivers the

block **AX**. The curves in Fig. 4.14*(c)* correspond to problems with closed electric boundaries, but experiments with open boundaries demonstrate that convergence is practically the same. The vibrator geometry has also little influence on the number of Lanczos steps which does not exceed $\overline{iter} = 40$–50 for ten eigenvalues. In fact, the latter could have been obtained in fewer steps should the DILASO version of the Scott's program be used: with DNLASO-based Lanczos solver, one finds the specified number of eigenvalues that lie only to the right side of the shift σ, thus wasting half the power of the algorithm. In either case, for practical numbers of wanted eigenvalues (typically 5 to 10 per shift), the convergence of the spectrally transformed eigenpairs is so fast that the initial cost of factorizing $\mathbf{K} - \sigma\mathbf{M}$ always eclipses the total cost of Lanczos iterations.

5

Illustrative problems

1. Introduction

In this chapter, several examples are presented to illustrate the application of the ballooning method to various practical problems, and to study the influence of the exterior electric field on piezoelectric vibrations. The large systems of equations associated with the three-dimensional modeling of piezoelectric structures impose severe limitations on geometries and modes that can be tackled at the present level of computer facilities. Therefore, the considered examples do not aim at any specific application and by no means intend to be used for the optimization of vibrator design. Nevertheless, the illustrative problems were chosen to be as close as possible to the practical piezoelectric configurations in terms of geometry, crystal cut, electrode shape or operating mode.

Piezoelectric vibrators, as precision devices, are very sensitive to various perturbations such as acceleration, temperature gradients, mechanical stresses caused by crystal defects, electrodes or mounting. All of them can produce changes in resonant frequencies or equivalent electrical parameters. It was judged that the best way to evaluate the influence of the exterior field on a vibrator's parameters was to compare it to changes resulting from the variations in electrical boundary conditions only, thus excluding other factors from the analysis. In the framework of the present finite element model, it was the electrode configuration (size, shape, orientation) that was modified most frequently to provide the solution shift associated with the exterior electric field with a point of reference.

2. Numerical tests for ballooning matrices

Before being applied to the interior piezoelectric problems, the superelement matrices obtained from the block balloon recursion were rigorously tested on several three-dimensional electrostatic examples with open-electric boundaries for which solutions by means of alternative numerical methods were available.

Convergence behavior of the solution as a function of the surface mesh size n_S was first studied on the example of a unit (1 m) metallic cube. Because there is no electric field inside the cube, the problem is treated as a purely exterior one. It is represented solely by the equation $\mathbf{S}_{11}\mathbf{\Phi} = 0$, where $\mathbf{S}_{11}$ is the superelement matrix that models the infinite region, and $\mathbf{\Phi} = (\varphi_i)$, $i = 1, ..., n_S$ is the vector of surface potentials. The capacitance is calculated as twice the energy of a cube charged to 1V:

$$C = \mathbf{\Phi}^{\mathrm{T}}\mathbf{S}_{11}\mathbf{\Phi}, \tag{2.1}$$

i.e. $\varphi_i = 1$ for all i. For a mapping ratio $\eta = 1.2$, some seven iterations are quite sufficient for the energy to converge, as demonstrated in Fig. 5.1.

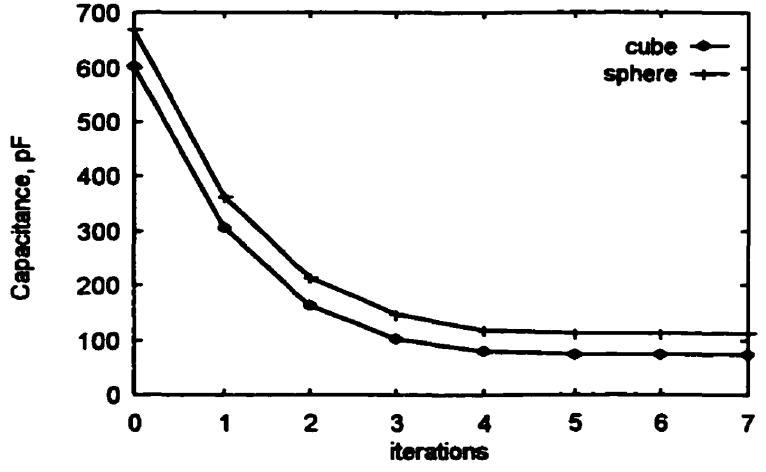

Fig 5.1 Convergence of capacitance of a unit cube problem solved with the scaling ratio $\eta = 1.2$; exact capacitance $C = 4\pi\epsilon_0/(R_1^{-1} - R_2^{-1})$ of a unit spherical capacitor ($2R_1 = 1\mathrm{m}$) with $R_2 = \eta^{2^i} R_1$, where i is the iteration number.

The capacitance of a unit cube has previously been reported by several authors. Lean, Friedman and Wexler (1980) obtained a value of 73.03 pF or 0.6573 e.s.u. (in CGS units) with 31 variables by applying the boundary element method based on elements of second order to the one-eighth of the cube. Jawson and Symm (1977) reported that Laskar (1974) obtained values of capacitance ranging from 0.6538 to 0.6603 e.s.u. for 6 to 66 variables respectively with the same method. Earlier Reitan and Higgins (1951) determined the lower and upper bounds for the capacitance of a unit cube, which are 0.62211 and 0.71055 e.s.u. respectively, and also calculated the value of 0.6555 e.s.u. by the 'method of subareas' (Silvester, 1968). Results obtained in the present work using the ballooning method are summarized in Table 5.1 for different mesh sizes. All ballooning matrices were obtained using elements of second order ($N = 2$) to discretize the bordering region. The most accurate value of capacitance — 73.61 pF or 0.6616 e.s.u. — was obtained with the division into $12 \times 12 \times 12$ bricks or into 8640 tetrahedra.

Table 5.1 Convergence data for the unit cube problem.

FE mesh $E_x \times E_y \times E_z$	No. of surface triangles	No. of surface nodes		Capacitance	
		total n_S	independent n_{oct}	pF	e.s.u.
$2 \times 2 \times 2$	48	98	19	74.70	0.6714
$4 \times 4 \times 4$	192	386	61	74.77	0.6640
$6 \times 6 \times 6$	432	866	127	73.73	0.6626
$8 \times 8 \times 8$	768	1538	217	73.67	0.6621
$10 \times 10 \times 10$	1200	2402	331	73.64	0.6619
$12 \times 12 \times 12$	1728	3458	469	73.61	0.6616

Because the solution in this problem is affected by physical discontinuities at the edges and corners, it is important to represent the field distribution at the vicinity of the cube surface as precisely as possible. The accuracy of the model, apart from the mesh size n_S, is determined by the mapping ratio η, the order of surface triangle elements N_t and the order of line segments in the radial direction ('toblerone' edges) N_s in the bordering region. By varying these parameters, it was found that the order of interpolation on the surface N_t, at least for the present electrostatic problems, was not overly critical: as demonstrated in Fig. 5.2 (*a*), the precision is almost identical for any order starting from $N_t = 2$. It is, however, desirable to use a line segment of high order if large values of scaling ratio η are

employed (Fig. 5.2 (*b*)). Such values allow enlarging the region in fewer iterations; practically, this reduction in the number of iterations is compensated by the amount of additional operations involved in static condensation of interior nodes in $\Omega_{(1)}$ if $N_s > 1$. It was found that for $\eta \leq 1.2$ no significant improvement is reached by setting N_s higher than 2 (Fig. 5.2 (*c*)). Most superelement matrices used in this analysis were obtained with orders of interpolation $N_t = N_s = 2$ and scaling ratio $\eta = 1.2$.

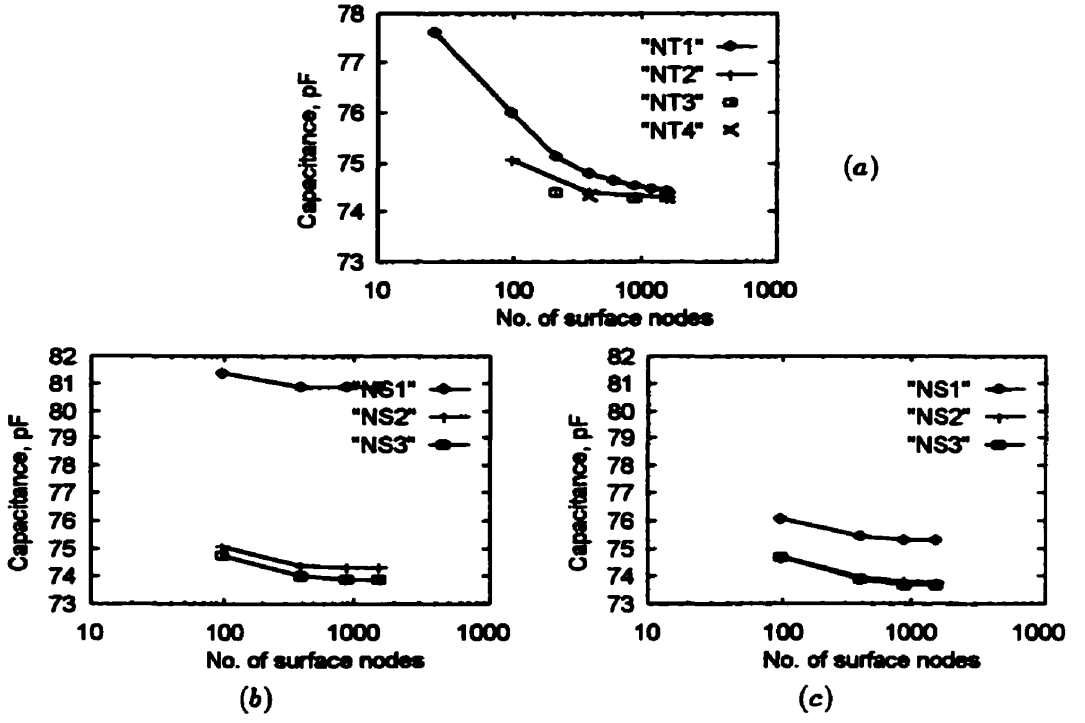

Fig 5.2 Convergence behavior of capacitance of a unit cube for various orders of interpolation on surface triangles N_t and on 'toblerone' edges N_s. (a) Here the scaling ratio $\eta = 1.5$ and $N_s = 2$; (b) $N_t = 2$, $\eta = 1.5$, (c) $N_t = 2$, $\eta = 1.2$.

Matrices $\mathbf{S}_{11}$ were also used to solve two open boundary problems that involve modeling some of the interior space. The first is the electrostatic field due to a thin square plate of unit area, as shown in Fig. 5.3. Because the problem is purely electrostatic, the interface Γ may be placed arbitrary. In this example, the interior region is subdivided into $12 \times 12 \times 4$ 'bricks' (2880 tetrahedra) where the plate

itself is in contact with $10 \times 10 \times 2$ of them. With elements of second order, this yields 5049 variables for the interior problem. The surface mesh consists of 1922 nodes, of which only 269 (N_{oct}) are independent. The calculated capacitance of the square plate is 41.5 pF or 0.373 e.s.u. In their book, Jawson and Symm (1977) reported the values 0.367 and 0.362 e.s.u. for the same configuration: the former was obtained by Noble (1971), and the latter — by Laskar (1974) using the integral equation method with 289 elements and 45 variables. Konrad and Tsukerman (1995) used Harrington's method to obtain 41 pF. Also, to compare, the exact capacitance $C = 2a/\pi$ (Landau and Lifshitz, 1992) of a thin disk of unit diameter ($2a = 1$ m) equals 0.3183 e.s.u.

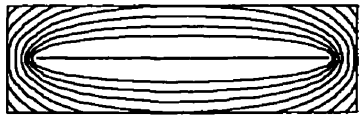

Fig 5.3 Cross-section of electric potential distribution around a square plate.

Closely related to this problem is that of determining the capacitance of a parallel square plate capacitor of unit (1 m) area. The problem was solved with a cubic $12 \times 12 \times 12$ mesh for various plate separations d (Fig. 5.4). At least one layer of elements separated the interface from conductors. The calculated values of capacitance are shown in Fig. 5.4 (*b*).

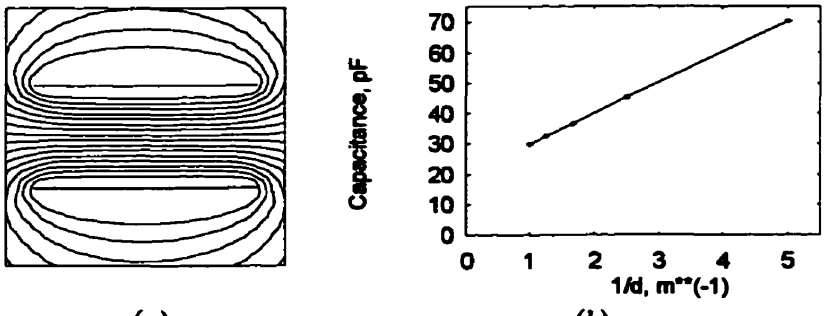

Fig 5.4 Square (1m × 1m) parallel-plate capacitor. *(a)* Cross-section of electric potential distribution; *(b)* capacitance as function of plate separation d.

A similar dependence was obtained by Konrad and Tsukerman (1995) using the method of average potentials. By extrapolating the graphic (Fig. 5.4) to the origin

$(1/d \rightarrow 0)$, the capacitance of the parallel-plate capacitor with infinite separation, can be estimated approximately at 20 pF. This is consistent with the previously obtained value for a single square plate, whose capacitance is two times greater than the capacitance of the system of two infinitely separated plates.

3. Static and modal analyses of piezoelectric structures

To study the effect of the exterior electric field on the characteristics of piezoelectric vibrators in a more or less systematic way, the static and modal analyses should involve various piezoelectric materials, crystal shapes, electrode configurations, and vibrational modes. Because it is difficult to assess the role of these factors using one particular application, the piezoelectric structures in the examples below were subdivided, based on their shape, into four categories within which only a limited number of electrical situations was simulated. Since no 'textbook' problems are available in the case of three-dimensional piezoelectric vibrations, the obtained results were typically checked, when possible, against the one-dimensional estimates or compared to experimental data.

3.1 $Li_2B_4O_7$ *unit cube*

The problem of a lithium tetraborate unit (1 m) cube (Antonova and Silvester, 1997), though artificial, is presented here for its illustrative qualities since both the material and the vibrator shape are favorable to electric flux leakage. This example serves also to introduce the few postprocessing operations involved in the present finite element analysis, to study the convergence behavior of static and motional parameters and to interpret the influence of the exterior electric field on them.

The solution of the static piezoelectric problem is examined in terms of static capacitance C_s, which can be determined in two ways, i.e. either as the ratio of the electrode charge Q and the potential difference $\Delta\varphi = |\varphi_1 - \varphi_2|$ between the electrodes

$$C_s = \frac{Q}{\Delta\varphi}, \tag{3.1}$$

or from the total stored energy U_{total}

$$C_s = \frac{2\mathrm{U}_{total}}{(\Delta\varphi)^2}, \tag{3.2}$$

where $\mathrm{U}_{total} = \frac{1}{2}\mathbf{x}^{\mathrm{T}}\mathbf{K}\mathbf{x}$ is typically calculated as the sum of mechanical and electrical energies over all the elements E, including the superelement S_{11} when the problem is solved with open electric boundaries:

$$\mathrm{U}_{total} = \frac{1}{2}\sum_{e=1}^{E} \mathbf{x}^{(e)\mathrm{T}}\mathbf{K}^{(e)}\mathbf{x}^{(e)} + \frac{1}{2}\boldsymbol{\Phi}_s^{\mathrm{T}}\mathbf{S}_{11}\boldsymbol{\Phi}_s, \tag{3.3}$$

where $\mathbf{x}^{(e)}$ is the vector of nodal displacements $\mathbf{u}^{(e)}$ and potentials $\varphi^{(e)}$ for the element e, and $\boldsymbol{\Phi}_s$ is the vector of surface potentials. To calculate the purely electric part of the capacitance C_s, i.e. the value that can be recovered from the vibration analysis if the static condensation of potential degrees of freedom is used (Eq. (5.12), Chapter 4),

$$C_s^{elect} = \frac{2\mathrm{U}_{elect}}{(\Delta\varphi)^2}, \tag{3.4}$$

only the electrical part U_{elect} of U_{total} is taken into account, i.e.

$$\mathrm{U}_{elect} = \mathrm{U}_{diel} + \mathrm{U}_{ext} = \frac{1}{2}\sum_{e=1}^{E} \varphi^{(e)\mathrm{T}}\mathbf{K}_{\varphi\varphi}^{(e)}\varphi^{(e)} + \frac{1}{2}\boldsymbol{\Phi}_s^{\mathrm{T}}\mathbf{S}_{11}\boldsymbol{\Phi}_s. \tag{3.5}$$

The capacitance obtained from the model with open electric boundaries C_s^{open}, being a more realistic approximation, is considered as a reference value when the relative increase in C_s due to the exterior electric field

$$\Delta C_s = \frac{C_s^{open} - C_s^{closed}}{C_s^{open}} \tag{3.6}$$

is calculated.

In the example problem shown in Fig. 5.5, the values of C_s^{open} were found to be 20.1 and 12.2 % higher than their closed-boundary counterparts C_s^{closed} for the full (4×4) and partial (2×2) electrode plating of the top and bottom surfaces of the cube respectively. The contribution of the exterior field to the total stored energy is clearly of the order of ΔC_s, and constitutes 24 and 13 % for the corresponding electrode configurations. Numerous calculations of C_s^{closed} and C_s^{open} in the framework of convergence study demonstrated that the accuracy of the static capacitance was practically the same, no matter whether derived from (3.1) or (3.2). This is consistent with the static boundary conditions imposed on the electrodes (Table 4.3, Chapter 4), under which C_s is not a stationary quantity.

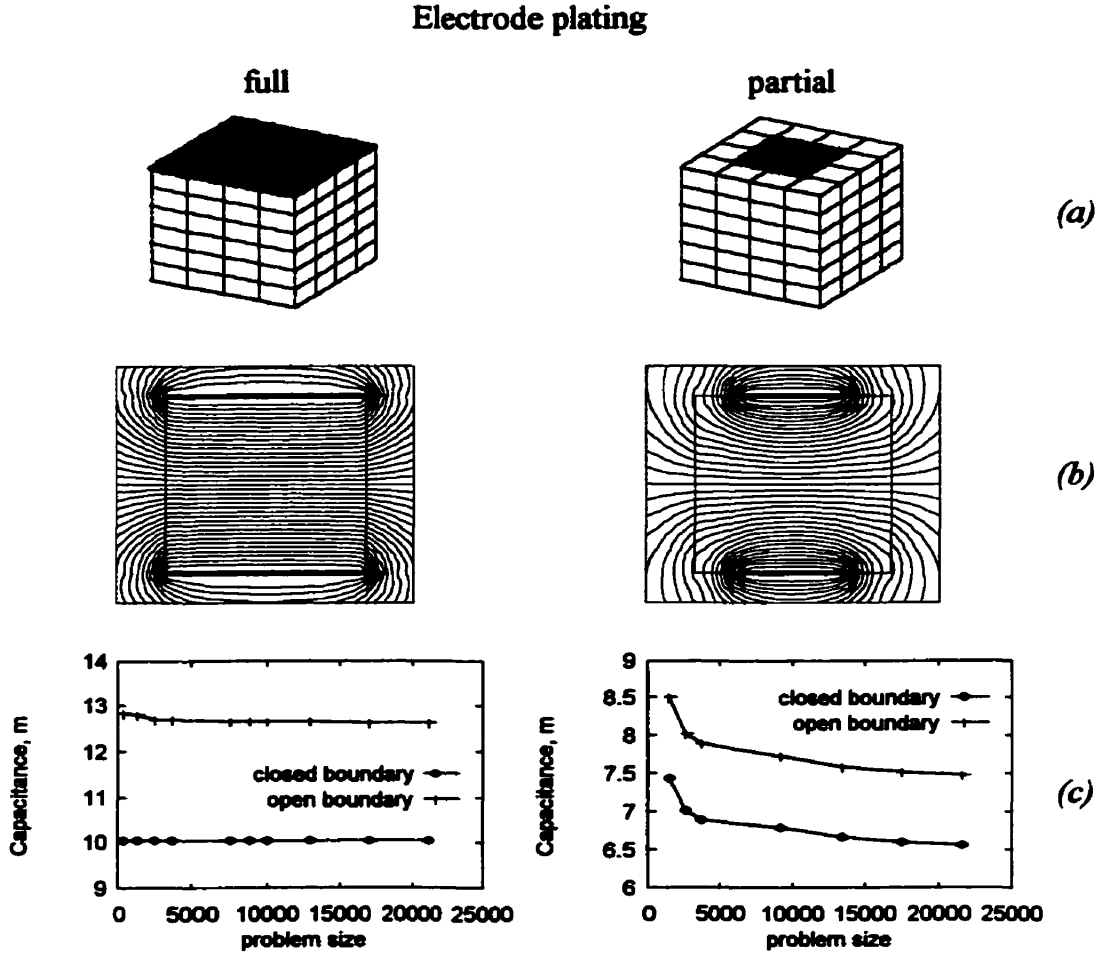

Fig 5.5 Static solution. *(a)* Transducer configuration. *(b)* Cross-section of electric potential distribution. *(c)* Convergence of the static capacitance C_s/ϵ_0.

The values of capacitance obtained with the finest mesh used ($8 \times 8 \times 8$) are summarized in Table 5.2.

Table 5.2 Static capacitance of a unit lithium tetraborate cube.

Electrode plating	Electric boundary			
	closed		open	
	C_s^{elect}/ϵ_0, m	C_s/ϵ_0, m	C_s^{elect}/ϵ_0, m	C_s/ϵ_0, m
full	8.15	10.03	10.76	12.64
partial	5.58	6.61	6.54	7.53

The convergence of C_s is very rapid for the fully covered piezoelectric capacitor (Fig. 5.5*(c)*, left), while the capacitance of the structure with partial electrode stabilizes if the top and bottom surfaces are subdivided in at least 8×8 rectangles (Fig. 5.5*(c)*, right). The latter configuration makes it evident that the cubic shape, with its closely located dielectric corners and electrode edges, constitutes a serious test for the finite element model. Nevertheless, the separation between C_s^{closed} and C_s^{open} was almost independent of the mesh for either electrode shape. This suggests that the shift in the capacitance due to the leakage field is calculated more accurately that the solution (C_s) itself, and can be estimated even by using a coarse mesh of elements.

An important step in the result post-processing is visualizing the fringe electric field around the piezoelectric body. A smooth and physically valid potential distribution not only illustrates the obtained results, but also attests their correctness and accuracy. As mentioned in Chapter 2, the most serious drawback associated with the method of ballooning consisted in its inability to recover potentials in the outer region modeled by the superelement matrix. Attempts to compute the exterior potential distribution by means of the Poisson integral

$$\varphi(P) = \frac{1}{4\pi\epsilon_0} \int_S \frac{\sigma(Q)}{|r_P - r_Q|} \, \mathrm{d}S \tag{3.7}$$

failed since the surface charge density $\sigma(Q) = -\mathbf{n} \cdot \mathbf{D}(Q)$, calculated over the surface of piezoelectric crystal by the direct differentiation of the piecewise continuous approximate solution ($\mathbf{u}$, φ), was too inaccurate to be used with (3.7). To visualize the fringe field, a more direct method was adopted in the present work: the mesh of tetrahedral elements was simply extended one layer beyond the surface of the piezoelectric body to include some of the free space. For example, in the problem shown in Fig. 5.5, the corresponding superelement matrix was added to the $6 \times 6 \times 8$ mesh, made up of the $4 \times 4 \times 6$ discretization of the piezoelectric cube (Fig. 5.5 *(a)*) and of the element-wide free space interface. After solving this larger inhomogeneous problem, the potential distribution shown in Fig. 5.5 *(b)* was obtained by plotting the contour lines of the finite element solution $\varphi(x, y = 0.5, z)$.

It is useful to start the modal analysis with a free unit piezoelectric cube (Table 5.3), thus eliminating for the time being the boundary conditions associated with the electrodes.

Table 5.3 Lowest modes of a free lithium tetraborate cube.

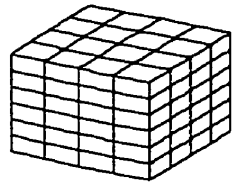

Mesh $4 \times 4 \times 6$
No. of tetrahedra $E_V = 480$
No. of nodes $n = 957$
No. of surface nodes $n_S = 514$
Dimensions of stiffness $n_K = 3828$ and
mass $n_M = 2871$ matrices.

Mode	Mechanical problem	Piezoelectric problem with electric boundaries			
		closed		open	
	f_m, kHz	f_p^c, kHz	U_{diel}/U_{total}, %	f_p^o, kHz	U_{ext}/U_{total}, %
1	1.7488	1.8162	6.93	1.8020	1.16
2	1.7488	1.8162	6.93	1.8020	1.16
3	1.8918	2.0090	0.90	2.0066	0.17
4	1.9992	2.0561	14.4	2.0240	2.43
5	2.1565	2.1566	0.01	2.1566	0.00
6	2.2794	2.3298	4.09	2.3182	0.72
7	2.6094	2.6604	3.07	2.6533	0.53
8	2.6097	2.6621	1.83	2.6570	0.22

The numerical results for the few lowest modes demonstrate a continuous change in the linear resonant frequencies $f = \omega/(2\pi)$ due to, first, the addition of the piezoelectricity to the model, and, second, to the 'opening' of its electric boundaries. The mechanical resonance was obtained by setting the piezoelectric coefficients in the model to zero, and calculating the natural frequencies f_m of the purely elastic structure; the addition of piezoelectric terms increases these resonant frequencies. Table 5.3 demonstrates that the effect of exterior electric field on the piezoelectric vibrations can be viewed as a reduction of the 'effective' piezoelectric coupling for a given material. Although this frequency decrease $f_p^c - f_p^o$ is smaller than the shift due to the piezoelectric effect itself $f_p^c - f_m$, they are nevertheless of the same order of magnitude, and can be approximately correlated to the portion of interior U_{diel}/U_{total} and exterior U_{ext}/U_{total} electric energies in the total energy of the system U, respectively. Therefore, for materials that have a moderate or

strong piezoelectric coupling combined with a relatively low dielectric permittivity ($\epsilon \sim 10\epsilon_0$), including the exterior electrostatic field into the finite element model is almost as important as taking into account the piezoelectric effect itself.

In the next example (Table 5.4), the piezoelectric cube is characterized by two frequencies — resonance f_r and the antiresonance f_a — resulting from the two homogeneous boundary conditions imposed on the pair of electrodes (Table 4.3, Chapter 4).

Table 5.4 Lowest vibrational modes of a unit cube (full electrode plating).

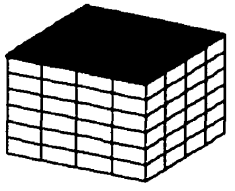

Mesh $4 \times 4 \times 6$ (details in Table 5.3)
Electrodes 4×4 (two sides)
$n_K = 3668, \quad n_M = 2871$

Mode	Electric boundaries							
	closed				open			
	f_r, kHz	f_a, kHz	C_n, pF	k, %	f_r, kHz	f_a, kHz	C_n, pF	k, %
1	1.7663	1.7663	0.0	0.0	1.7650	1.7650	0.0	0.0
2	1.7663	1.7663	0.0	0.0	1.7650	1.7650	0.0	0.0
3	1.9201	2.0552	11.6	38.2	1.9189	2.0208	11.2	33.0
4	2.0009	2.0009	0.0	0.0	2.0008	2.0008	0.0	0.0
5	2.1566	2.1566	0.0	0.0	2.1566	2.1566	0.0	0.0
6	2.2942	2.2942	0.0	0.0	2.2929	2.2929	0.0	0.0
7	2.6311	2.6547	1.17	13.4	2.6307	2.6476	1.14	11.4
8	2.6490	2.6490	0.0	0.0	2.6484	2.6484	0.0	0.0
9	2.6597	2.6597	0.0	0.0	2.6560	2.6566	0.0086	2.1

For the given electrode configuration, only few of the natural frequencies from Table 5.3 become piezoelectrically active, which is indicated by the separation of the resonant frequencies f_r and f_a. Indeed, the matrix of piezoelectric coefficients for lithium tetraborate in the crystallographic, i.e. nonrotated, axes

$$\mathbf{e} = \begin{bmatrix} 0 & 0 & 0 & 0 & e_{15} & 0 \\ 0 & 0 & 0 & e_{15} & 0 & 0 \\ e_{31} & e_{31} & e_{33} & 0 & 0 & 0 \end{bmatrix} \tag{3.8}$$

reveals that the applied electric field $\mathbf{E} = (0, 0, E_3)^T$ is piezoelectrically coupled, through constants e_{31}, $e_{32} = e_{31}$, and e_{33}, to the strain components S_{11}, S_{22}, and S_{33}. Therefore, only extensional vibrations in the direction of three coordinate axes and their overtones may take place under the above electrical conditions.

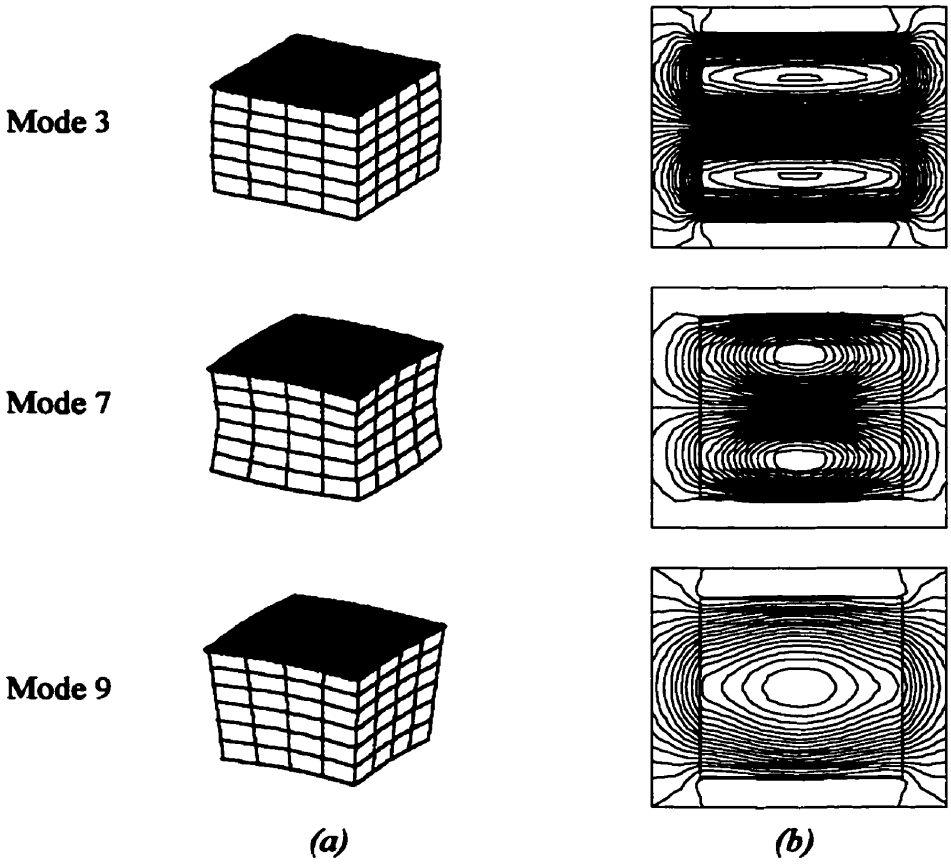

Fig 5. 6 *(a)* Vibrational shapes of the piezoelectric cube with full electrodes. *(b)* Cross-section of electric potential distribution at the resonance frequency f_r.

Two of them (3 and 7) are shown in Fig. 5.6[1] along with the corresponding electric potential distributions. It is interesting to note that some other modes, inactive ($f_r = f_a$) in the closed-boundary model, are excited by the fringe field.

---

[1] The vibrational shapes were visualized by adding the scaled displacements $\overline{\mathbf{U}}_S$, obtained from the finite element model, to the Cartesian coordinates $\mathbf{r}_S$ of the surface, $\mathbf{r}'_S = \mathbf{r}_S + \overline{\mathbf{U}}_S$, and by plotting the deformed surface $\mathbf{r}'_S$ in parametric mode.

For example, mode 9, also shown in Fig. 5.6, appears on the admittance curve corresponding to the problem with open electric boundaries near mode 7 (Fig. 5.7) in the form of a small but clearly visible resonance. Under specific circumstances this unwanted resonance may be amplified and can deteriorate the performance of the resonator. Clearly, such modes 'activated' by the exterior electric field contribute to the family of spurious responses, and should be studied as part of the vibrator model.

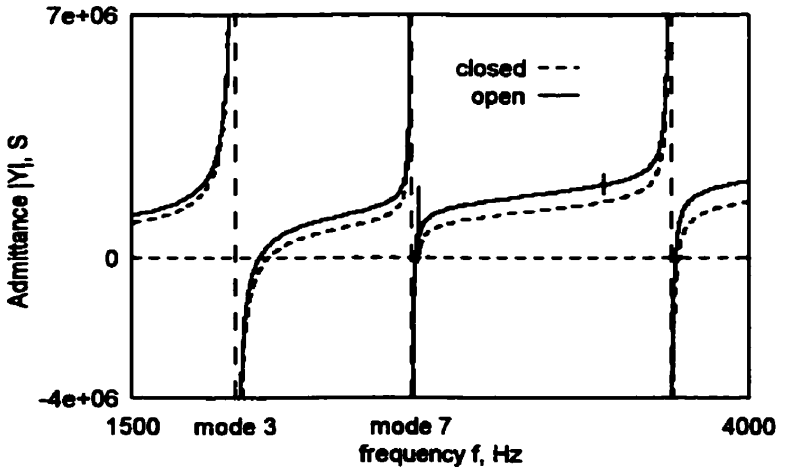

Fig 5. 7 Electrical admittance of the piezoelectric cube in the low frequency range.

As seen from the values of resonant frequencies (Table 5.4) and the admittance curve (Fig. 5.7), the most noticeable influence of the exterior leakage field on the piezoelectric vibrations consists in reducing the effective *separation* of resonant frequencies $\Delta f = f_a - f_r$. The latter is closely related to two other parameters appearing in Table 5.4 — the motional capacitance

$$C_n = \frac{Q_n^2}{\omega_n^2 \mathbf{U}_n^{\mathrm{T}} \mathbf{M} \mathbf{U}_n}, \tag{3.9}$$

where $\mathbf{U}_n$ is the vector of mechanical displacements, and the effective coupling coefficient defined in Eq. (6.37), Chapter 1. The calculation of C_n can be simplified if one recall that in the adopted variant of the Lanczos algorithm the

resulting eigenvectors are M-orthogonal, i.e. $\mathbf{U}_n^{\mathrm{T}}\mathbf{M}\mathbf{U}_n = 1$, so that Eq. (3.9) turns into

$$C_n = \frac{Q_n^2}{\omega_n^2}. \tag{3.10}$$

It is important to note that the separation Δf reduces mainly through the antiresonance frequency f_a, which diminishes for the electrically unbounded problem. A simplified electrical model of the piezoelectric vibrator can help to interpret this observation. In the neighborhood of the well separated nth resonance, the equivalent circuit (Fig. 1.5, Chapter 1) can be approximated by a simple circuit consisting of the shunt capacitor C_0 in parallel with the series circuit L_n and C_n. In this case, the resonant frequencies f_r and f_a are given by expressions

$$f_r = \frac{1}{2\pi}\sqrt{\frac{1}{L_n C_n}} \tag{3.11}$$

and

$$f_a = \frac{1}{2\pi}\sqrt{\frac{1}{L_n C_n}\left(1 + \frac{C_n}{C_0}\right)}. \tag{3.12}$$

The shunt capacitance C_0 (Eq. (7.21), Chapter 1) can generally be derived from the static C_s and motional C_n capacitances as

$$C_0 = C_s - \sum_{n=1}^{\infty} C_n, \tag{3.13}$$

or approximated by C_s

$$C_0 \approx C_s \tag{3.14}$$

for materials with small piezoelectric coupling like quartz. In either case, Eqs. (3.11) and (3.12) demonstrate that among the two resonant frequencies, only the antiresonance f_a depends on the static capacitance C_s. As shown earlier in this section, the latter increases considerably in the presence of exterior field, thus diminishing the antiresonance frequency in (3.12). The motional capacitance C_n, and therefore the resonance frequency f_r, is also affected by the leakage field but

at much lesser degree. This is illustrated by the test problem where the frame S_∞, on which the potential was set to zero, is moved away from the surface of the unit cube (Fig. 5.8).

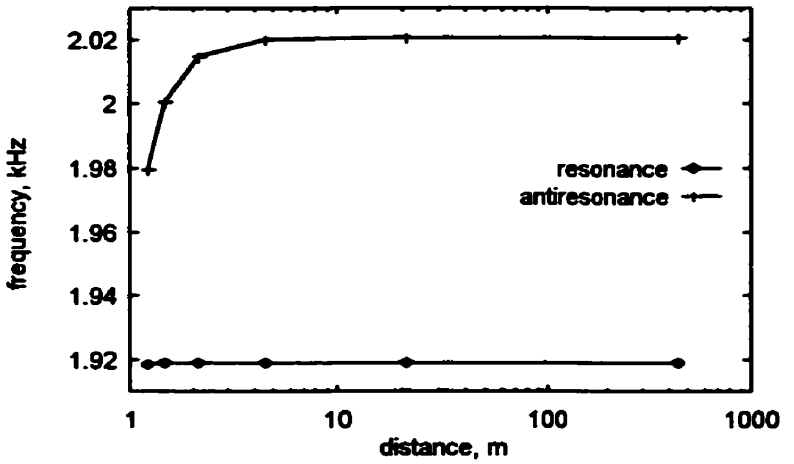

Fig 5. 8 Dependence of the resonant frequencies on the distance between the surface of the piezoelectric cube and the outer boundary S_∞.

Numerically, the curve is similar to the one shown in Fig. 5.1 for the purely static case, and models the convergence of the resonant frequencies (mode 3) to their open-boundary values f_r^{open} and f_a^{open} as the number of recursive condensation steps grows; physically, it corresponds to the increase in resonant frequencies of the piezoelectric cube as a grounded metallic frame is moved away from its surface towards infinity. Its shows clearly that as more free space is added to the system, the antiresonance frequency increases by 40 Hz, while the resonance frequency remains practically unchanged. Note also that the main shift in the antiresonance frequency occurs in the vicinity of the surface, i.e. at the distance of several vibrator sizes from it. This can be used to explains why, in practice, no change in the resonant frequencies is observed when the mounted crystal is sealed in a metallic enclosure. Indeed, since the latter is typically separated from the vibrator major surfaces by no less that a few plate thicknesses, the electrical situation in the finished resonator is well described by the model with open electric boundaries.

The antiresonance frequency, being a global quantity, converges rapidly as the finite element model is refined (Fig. 5.9). Meanwhile, the shift $f_a^{closed} - f_a^{open}$ produced by the leakage electric field converges even faster, so that it is well approximated long before the antiresonance frequency stops changing.

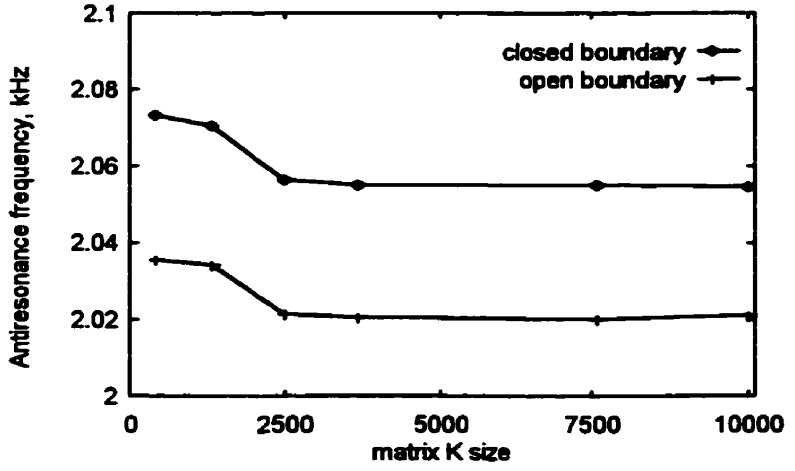

Fig 5. 9 Convergence of the antiresonance frequencies f_a^{closed} and f_a^{open} with mesh refinement.

It follows from Eqs. (3.11) and (3.12) that for small piezoelectric coupling ($C_n/C_0 \ll 1$) the relative separation between the resonant frequencies can be approximated by

$$\frac{\Delta f}{f_r} \approx \frac{1}{2r}, \tag{3.15}$$

where $r = C_0/C_n$ is the *capacitance ratio*. In practice, it is desirable to make the value of r as small as possible, thus increasing the separation (3.15). Having a large Δf is important for many application: it determines the bandwidth of a piezoelectric filter, and allows a transducer or a voltage controlled oscillator (VCO) to be operated over a wide range of frequencies between f_r and f_a. The definition of the capacitance ratio suggests that to make r small, the motional capacitance C_n should be large (which is accomplished by choosing the crystal, cut, and mode of vibration with large piezoelectric coupling), while the shunt

capacitance C_0 should be as small as possible. In this sense, the effect of the exterior electric field is deleterious for the vibrator performance: while preserving the values of C_n (except for modes activated by the fringe field), it considerably increases the values of C_s (and consequently C_0) thus raising r, and diminishing the spacing Δf and the effective piezoelectric coupling factor k of active modes (Table 5.4).

Table 5.5 Motional parameters of the lowest vibrational modes for a unit cube (partial electrode plating).

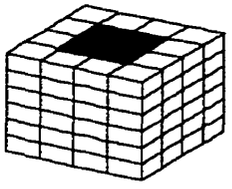

Mesh $4 \times 4 \times 6$ (details in Table 5.2)
Electrodes 2×2 (two sides)
$n_K = 3780, \quad n_M = 2871$

Mode	Electric boundaries							
	closed				open			
	f_r, kHz	f_a, kHz	C_n, pF	k, %	f_r, kHz	f_a, kHz	C_n, pF	k, %
1	1.7964	1.7964	0.0	0.0	1.7876	1.7876	0.0	0.0
2	1.7964	1.7964	0.0	0.0	1.7876	1.7876	0.0	0.0
3	1.9540	2.0560	6.01	32.7	1.9453	2.0237	5.36	28.7
4	2.0074	2.0074	0.0	0.0	2.0055	2.0055	0.0	0.0
5	2.1566	2.1566	0.0	0.0	2.1566	2.1566	0.0	0.0
6	2.3227	2.3227	0.0	0.0	2.3132	2.3132	0.0	0.0
7	2.6528	2.6619	0.33	8.3	2.6469	2.6520	0.226	6.2
8	2.6600	2.6600	0.0	0.0	2.6565	2.6569	0.0042	1.6

Besides depending on the crystal cut and mode of vibration, the resonance separation Δf is affected, through C_n and C_s, by the electrode size and shape. It is therefore natural to compare the reduction in Δf due to electric field leakage to the frequency shift resulting from a change in electrode shape. To this end, the similar analysis of the vibrator with partial electrodes on the top and bottom surfaces (Table 5.5) was carried out for the few lowest modes. All modes obtained with the previous electrode configuration are present here, including the one excited by the exterior electric field (Fig. 5.10). However, their electrical activity, measured by the motional capacitance C_n, is clearly less intense because of smaller electrode area.

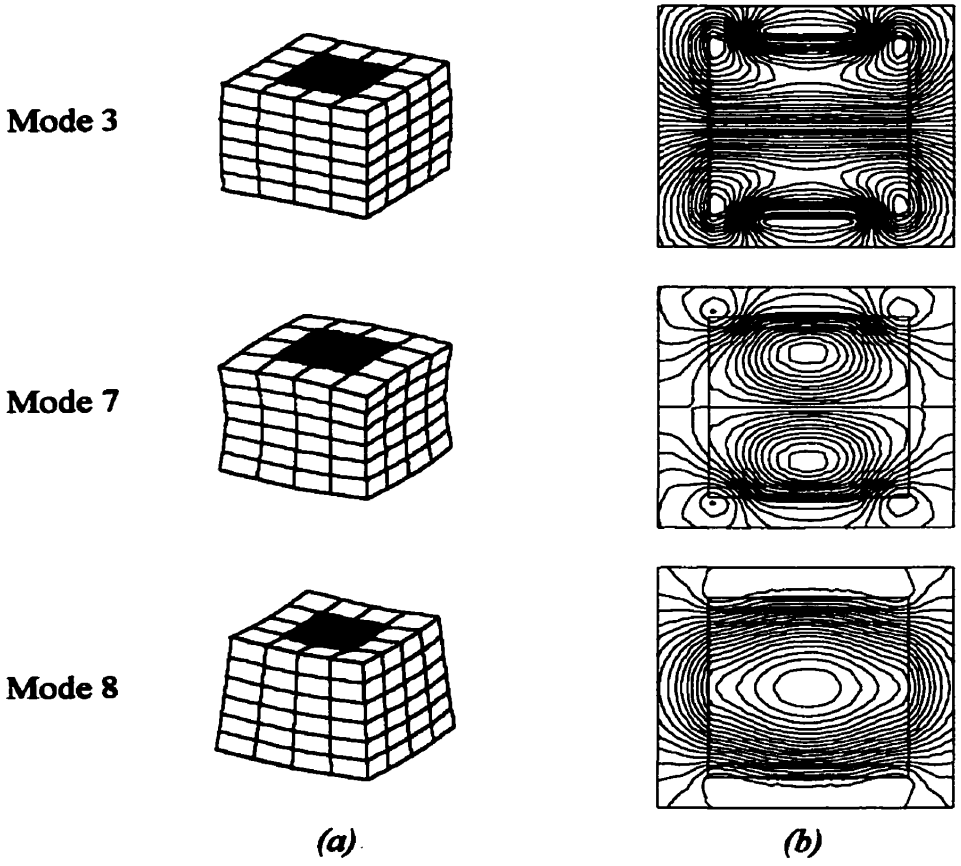

Fig 5. 10 *(a)* **Vibrational shapes of the piezoelectric cube with partial electrodes.** *(b)* **Cross-section of electric potential distribution at the resonance frequency f_r.**

The spacing Δf between the resonances of mode 3 are given in Table 5.6 for various electrical boundary conditions. It shows that for both electrode configurations, the 'effective' separation constitutes only about 75 % of the Δf obtained with a model with closed electric boundaries. It is interesting to note that in the example with full electrodes, adding the exterior electric field diminishes Δf from 135 kHz to 102 kHz, while exactly the same reduction, but this time through the resonance frequency f_r, is achieved within the model with closed electric boundaries as the electrode size is reduced by the factor of two.

Table 5.6 Resonance separation Δf in the piezoelectric cube.

	Electric boundary					
	closed			open		
Electrode	f_r, kHz	f_a, kHz	Δf, Hz	f_r, kHz	f_a, kHz	Δf, Hz
4×4	1.9201	2.0552	135	1.9189	2.0208	102
2×2	1.9540	2.0560	102	1.9450	2.0240	79

3.2 *Square piezoelectric plates*

The square plate geometry (Fig. 5.11) was chosen for the comparative study of static capacitance C_s for different piezoelectric materials. As mentioned in Chapter 4, it is only the interior and electrostatic part C_s^{elect} of the capacitance that is typically calculated by the existing finite element analyses of piezoelectric vibrators. The latter does not take into account either the static mechanical displacement due to the piezoelectric coupling with applied electric field or the exterior leakage field. It is demonstrated below that for many materials C_s^{elect} may be a rough approximation to the piezoelectric static capacitance C_s, particularly the one obtained from the model with open electric boundaries.

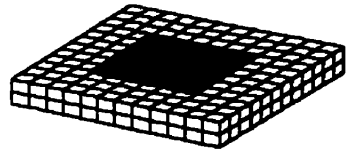

Region $6 \times 6 \times 1$ mm^3
Mesh $12 \times 12 \times 2$
Electrodes 6×6
$n = 2837, \quad n_S = 1538$
$n_K = 11012, \quad n_M = 8511$

Fig 5.11 Square plate resonator configuration and its finite element model.

The materials for capacitance tests (Table 5.7) were selected to have different combinations of dielectric permittivity ϵ and piezoelectric coupling k. Namely, quartz has both low ϵ and small coupling coefficient, lithium tetraborate is a moderate piezoelectric and its permittivity is relatively low, lithium niobate is a very strong piezoelectric and possesses large permittivity. The crystal cuts are the ones used for thickness-shear mode resonators (considered later in this section), though for the present static tests these orientations do not carry any physical meaning. They are described by the rotated coefficient matrices (3.9)–(3.17) of Appendix 2, and the Cartesian axes x_2 is perpendicular to the major surfaces of the plates.

Table 5.7 Electric permittivities and piezoelectric coupling.

Parameter	Quartz	Lithium tetraborate	Lithium niobate
$\epsilon_{22}^S\ (\epsilon_0)$	4.62	8.5	44.0
$\epsilon_{22}^T\ (\epsilon_0)$	4.67	9.6	76.0
k_{st}, %	10.5	34.0	64.0
$\frac{\epsilon_0}{\epsilon_{22}^T+\epsilon_0}$, %	17.6	9.4	1.3
$\frac{\epsilon_{22}^T-\epsilon_{22}^S}{\epsilon_{22}^T+\epsilon_0}$, %	0.9	10.4	41.6

The low permittivity is responsible for the electric field leakage into the outer space, while a high coupling factor efficiently transforms the supplied electric energy into mechanical strain. In either case, the effective static capacitance C_s is larger than its purely electrostatic and closed boundary counterparts because of the additional energy associated with strain and exterior electric field. The anticipated contribution to the capacitance from the exterior electric field and piezoelectrically induced mechanical deformation should be proportional to the ratios $\epsilon_0/(\epsilon_{22}^T+\epsilon_0)$ and $(\epsilon_{22}^T-\epsilon_{22}^S)/(\epsilon_{22}^T+\epsilon_0)$ respectively (Table 5.7), where ϵ_{22}^T is the 'free' dielectric permittivity in the direction of the plate thickness (x_2); the difference between ϵ_{22}^T and ϵ_{22}^S is function of the piezoelectric coefficients, and is given by Eq. (4.4), Appendix 2.

The capacitances, as functions of the electrode size, are presented in Fig. 5.12. For quartz, with its weak piezocoupling, the change in the static capacitance is almost entirely attributed to the exterior electrostatic field. For the electrode configuration shown in Fig 5.11, C_s increases by 8.9 % (Table 5.8) when the latter is taken into account. For lithium tetraborate plate of the same geometry, the contribution from the mechanical and exterior electrical fields to C_s constitutes 11 and 4.7 % respectively. For lithium niobate crystal cut, the high permittivity ϵ_{22}^S makes the leakage field negligible; however, because of strong piezoelectric coupling with mechanical fields, the full static capacitance of the lithium niobate plate surpasses the electrostatic one by 41 %.

Table 5.8 Static capacitances (pF) of piezoelectric square plates.

	Parallel-plate capacitor model	Finite element model with electric boundary			
		closed		open	
Crystal	C_s, pF	C_s^{elect}, pF	C_s, pF	C_s^{elect}, pF	C_s, pF
Quartz	0.373	0.512	0.518	0.563	0.569
Lithium tetraborate	0.77	0.945	1.068	0.997	1.121
Lithium niobate	6.39	4.784	8.143	4.840	8.208

The changes in C_s resulting from the inclusion of the exterior electric field in the finite element model is reflected in the equivalent electrical admittance of piezoelectric plates in the low frequency range (Fig. 5.13). For quartz and lithium tetraborate plates the curve obtained from the model with open electric boundaries is slightly higher than the closed-boundary one. Although for lithium niobate this difference is not visible, its spectrum is 'enriched' by small spurious resonances excited by the fringing field to a much higher degree that in other materials. Indeed, the piezoelectric coupling of lithium niobate is so strong that even a small portion of electric field leaking into the outer space is sufficient to excite many, normally inactive, modes.

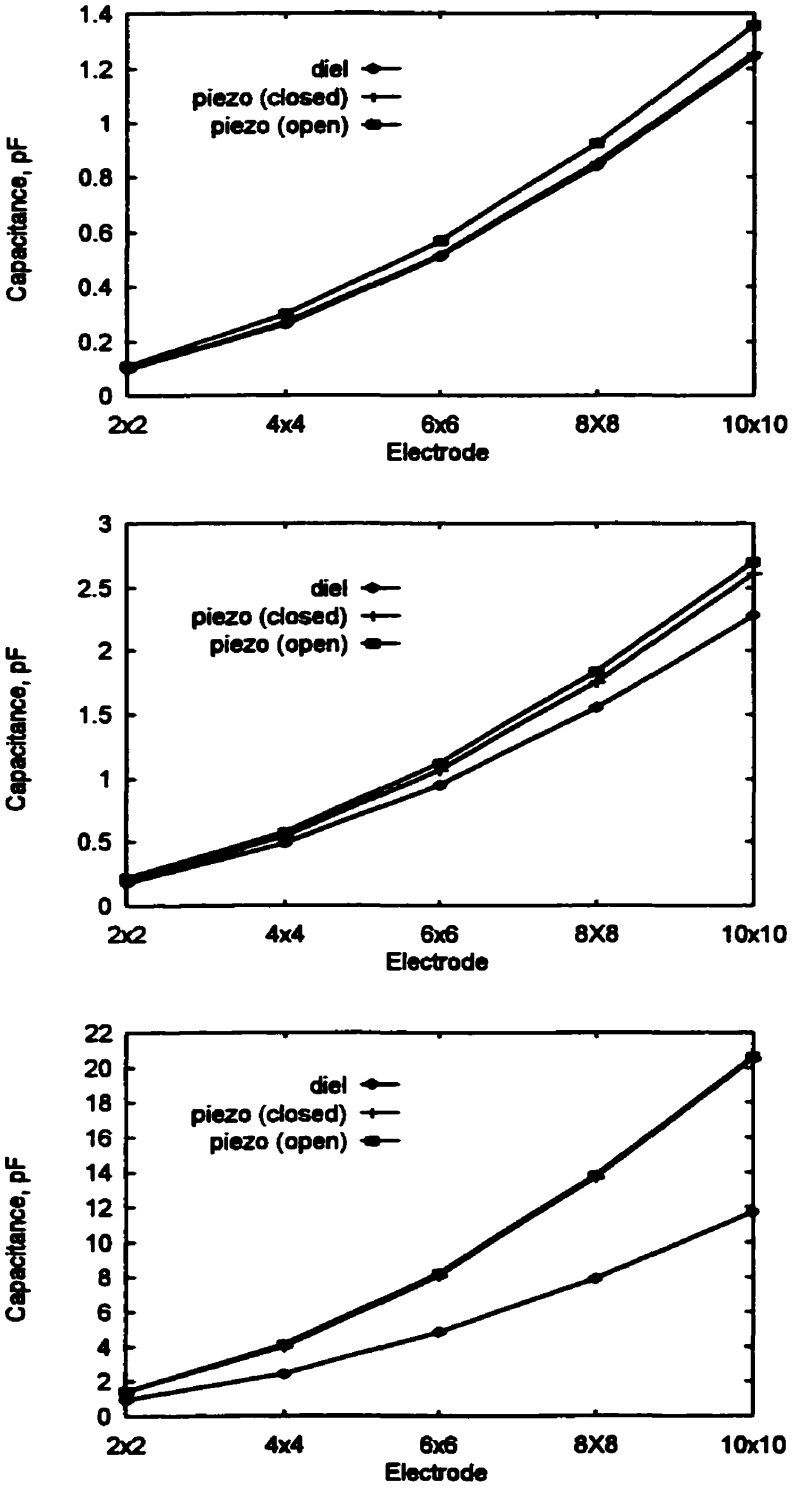

Fig 5.12 Electric and piezoelectric (with closed and open boundaries) static capacitances of square plates with different electrode sizes.

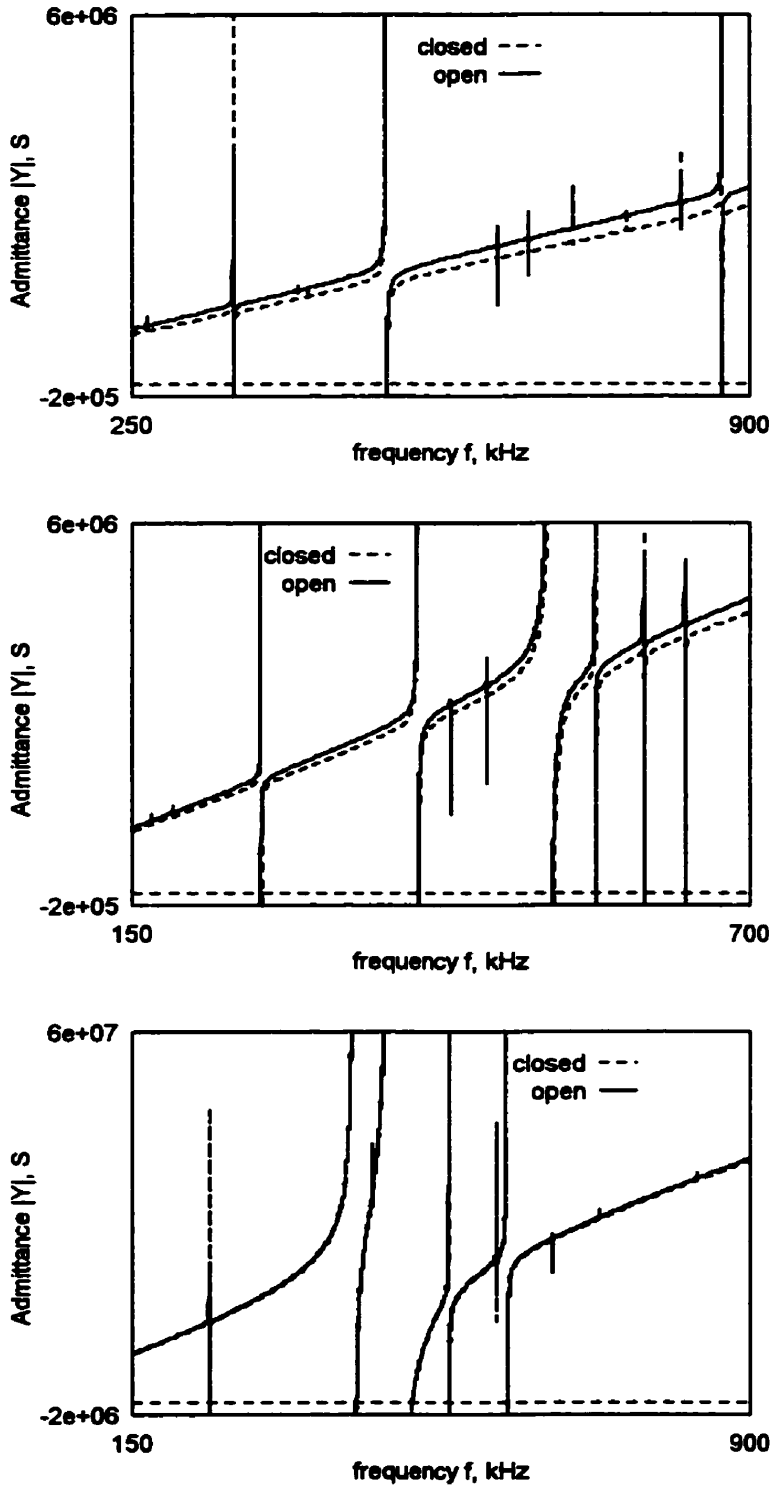

Fig 5.13 Electrical admittance of square piezoelectric plates in the low frequency range.

3.3 *Longitudinal vibrations in* CdS *rods*

In this section, the electric flux leakage associated with extensional vibrations of CdS rectangular rods is determined. Although this problem may seem obsolete (cadmium sulfide is barely used now as a transducer material), it is still considered here since the issue of electric flux leakage from piezoelectric crystals was first raised in connection with these geometrical shapes and material. Ogawa (1969) observed that for some specimens of CdS, the experimental mechanical losses and the dispersion of sound velocity — both proportional to the piezoelectric coupling coefficient k^2 — were smaller than their respective theoretical values. He related the weakening of the effective piezoelectric coupling with the electric flux leakage and the semi-conductive properties of CdS. Because the former had never been taken into account, this led Ogawa to define a generalized depolarization factor which included a correction to the piezoelectric polarization field **P** for geometries favorable to the expansion of electric lines beyond the crystal boundaries. This approach, subsequently adopted by Ikeda (1978, 1996), was briefly discussed in Section 3.1*B* of Chapter 2 as the only systematic attempt to introduce the exterior electric field into the model of extensional vibrations.

The two CdS transducer configurations modeled by finite elements are shown in Fig. 5.14. In both cases, the z-axis is chosen parallel to the hexagonal axis of the CdS (nonrotated) crystal and perpendicular to its top and bottom surfaces covered by electrodes. However, the two geometries correspond to different electrical situations with respect to lengthwise extensional vibrations, characterized by the stress components T_{11}, in the case of a thick bar elongated in the x-direction (Fig. 5.14*a*), and by T_{33} — for the pillar-type transducer (Fig. 5.14*b*). The direction of the former vibration (wave vector **k**) is perpendicular to the applied electric field $\mathbf{E} = (0, 0, E_3)^{\mathrm{T}}$ and excited through the piezoelectric module d_{31} (Eq. (4.6), Appendix 2), while the latter, d_{33}-driven mode is parallel to **E**. Following Ikeda's terminology, these piezoelectric interactions are referred to as transversal (T)- and longitudinal (L)-effects respectively. Because in either case the major surfaces are not shielded, the electric flux leakage has to be considered.

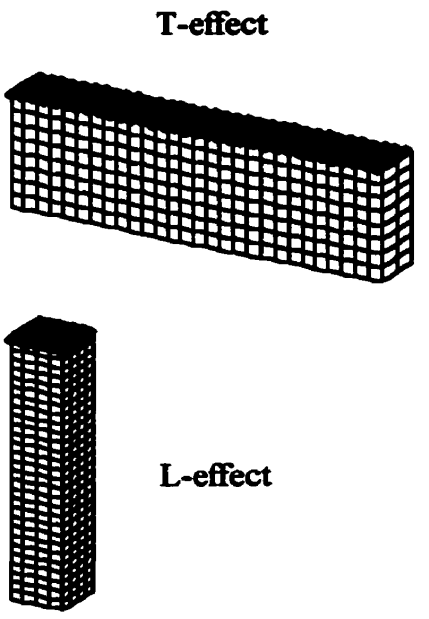

Fig 5.14 CdS transducers and their finite element models. Configurations with transversal *(a)* and longitudinal *(b)* electric field orientations.

The calculated static and motional parameters are presented in Table 5.9. Since the rod length l is considerably greater than its width and thickness, the finite element model with closed electric boundaries is well supported by the one-dimensional simulation of longitudinal modes (Table 5.10), which provides the former with an implicit numerical test. In the latter case, the resonant frequencies and coupling coefficient were computed by substituting the transducers' geometrical dimensions (Fig. 5.14 *a,b*) and the material constants of CdS (Eqs. (4.5)–(4.7), Appendix 2) into the solutions, or first order approximations (Ogawa, 1969) to the solutions, of transcendental equations governing extensional vibrations of piezoelectric bars, briefly outlined in Chapter 2 (Table 2.4). The static capacitances, obtained from the parallel-plate capacitor model, are almost identical to their finite element approximations since, in the case of electrodes completely covering the top and bottom surfaces, no fringe field exists either inside or outside of the piezoelectric.

Table 5.9 Parameters of extensional vibrations in CdS transducers obtained from the finite element model.

Electric boundary	Piezoelectric coupling									
	T-effect					L-effect				
	C_s (pF)	f_r (kHz)	f_a (kHz)	C_1 (fF)	k (%)	C_s (pF)	f_r (kHz)	f_a (kHz)	C_1 (fF)	k (%)
closed	0.213	224.2	225.7	2.76	11.4	0.013	250.7	258.1	0.73	24.4
open	0.295	224.2	225.2	2.74	9.5	0.043	250.0	251.2	0.44	9.7

Table 5.10 Parameters of CdS transducers obtained from the one-dimensional model of extensional vibrations.

T-effect	L-effect
$C_s = \dfrac{\epsilon_{33}^T \epsilon_0 lt}{w}$ $= 0.211$ pF	$C_s = \dfrac{\epsilon_{33}^T \epsilon_0 wt}{l}$ $= 0.013$ pF
$f_r = \dfrac{1}{2l\sqrt{\rho s_{11}^E}}$ $= 226.2$ kHz	$f_r = \left[1 + \left(\dfrac{1}{2} - \dfrac{4}{\pi^2}\right) k_{33}^2\right] \dfrac{1}{2l\sqrt{\rho s_{33}^E}}$ $= 251.1$ kHz
$f_a = \left(1 + \dfrac{4}{\pi^2} k_{31}^2\right) \dfrac{1}{2l\sqrt{\rho s_{11}^E}}$ $= 227.5$ kHz	$f_a = \left(1 + \dfrac{1}{2} k_{33}^2\right) \dfrac{1}{2l\sqrt{\rho s_{33}^E}}$ $= 258.1$ kHz
$k_{31} = d_{31} / \sqrt{\epsilon_{33}^T s_{11}^E}$ $= 11.8\,\%$	$k_{33} = d_{33} / \sqrt{\epsilon_{33}^T s_{33}^E}$ $= 26.2\,\%$

As can be seen from the above tables, the electrical conditions created by the T- and L-effect couplings are very different. Because in CdS the piezoelectric constant d_{33} that governs the L-effect is almost two times greater than d_{31}, the resonant frequency separation Δf and the corresponding electromechanical

coefficient k_{33}, are superior to that of the T-effect. At the same time, the motional and static capacitances (Table 5.10) are smaller for the L-effect transducer since in this case the electrodes occupy the minor surfaces separated by the length. This special configuration is at the origin of a severe electric flux leakage predicted by Ikeda (1996). Indeed, the finite element model shows that 67 % of the electric energy is stored outside of the crystal in the case of the static field distribution thus increasing the static capacitance C_s from 0.013 pF to 0.043 pF, i.e. by almost 70 % (Table 5.9). The antiresonance frequency f_a shifts so close to f_r that their effective separation constitutes only 16 % of the value predicted by the finite element analysis with closed electric boundaries or by the one-dimensional model of longitudinal vibrations. In terms of the piezoelectric strength, the electric flux leakage diminishes the L-effect piezoelectric coupling from 24.4 % to 9.7 % thus reducing it to that of the T-effect.

3.4 *Strip resonators*

Piezoelectric resonators operating in thickness-shear modes are by far the most popular and mass-produced since their frequency range suits best the modern consumer market of electronic equipment controlled by microcomputers to which they serve as a time base (i.e. generate a reference clock signal). The miniaturization and the cost reduction of these devices are largely determined by the miniaturization of the resonators. Using materials with high piezoelectric coupling is one way of reducing the resonator size; another avenue in the process of miniaturization is the design of *strip-type* resonators. Compared to the large conventional quartz resonators made from rectangular or circular plates and requiring a sophisticated individual convex contouring, the strip resonators have small size and simple rectangular shape, and, therefore, lend themselves to the large-scale production as chip components for integrated circuits.

Although some specifications are relaxed for strip resonators, their performance must still be comparable to that of large resonators. If the parameters of the latter are well predicted by one- or two-dimensional models (Section 3, Chapter 2), the optimal design of the miniature strip resonators requires a full three-dimensional analysis. The finite element models are best suited to study the influence of the crystal dimensions and electrode shape (and the associated electric flux leakage) on the resonator spectrum and electrical parameters. The X- and Z-

oriented strips (Fig. 5.15) of Y-rotated cuts of quartz and lithium tetraborate (Eqs. (3.9)–(3.14), Appendix 2) known for their temperature stability are considered in this section.

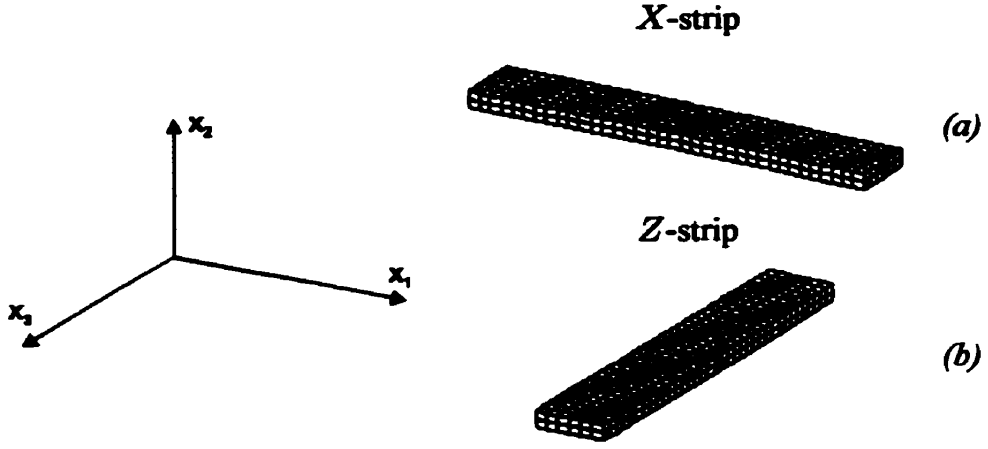

Fig 5.15 Piezoelectric strip orientation in Cartesian coordinate axes. Structures elongated in the direction x_1 *(a)* and x_3 *(b)*.

The specific geometry depends on the design requirements; however, most often the strip length is chosen to be parallel to the displacement in the thickness-shear mode in order to avoid spurious thickness-twist overtones. The displacement **u** can be determined from the one-dimensional model of thickness vibrations (Eq. (3.4), Chapter 2). In the case of a rotated ($\theta = 35°15'$) Y-plate of quartz (AT-cut), the polarization of the shear wave is strictly parallel to the digonal x_1-axis, i.e. $\mathbf{u} = (u_1, 0, 0)^{\mathrm{T}}$, which corresponds to the X-strip configuration. For the rotated ($\theta = 51°$) Y-cut of $Li_2B_4O_7$, the displacement in the slow shear mode (the mode of interest) is predominantly x_3-oriented, which suggests using a Z-strip. Therefore, in the standard notation (Appendix 2), the modeled quartz and lithium tetraborate plates can be designated as $(YXl)\,35°15'$ and $(YZl)\,51°$ respectively[2].

Since the thickness-shear mode is the resonance of a transversal wave traveling in the thickness direction of the plate, the strip thickness t determines the operating

---

[2] According to the convention on the positive sense of crystallographic axes for quartz (IEEE Standard on Piezoelectricity, 1987), the rotational symbol for the AT-cut should read as $(YXl)\,-35°15'$.

frequency of the resonator. The length of the strip plate l is designed to be as small as possible but large enough to keep the resonator series resistance at minimum by not damping the vibration at mounting points. The width w is chosen to separate the main thickness-shear mode from numerous spurious resonances of waves propagating in the width direction (Fujiwara *et al*, 1985). The optimum dimension ratios l/t and w/t are determined by the design and depend, in great part, on the crystal piezoelectric coupling. The electrode shape and size are chosen to make the capacitance ratio r at the main resonance as large as possible, and also to suppress unwanted responses. Since no optimization was aimed in the present analysis, the following dimensions $l = 18$ mm, $w = 3$ mm, and $t = 1$ mm were chosen for both the quartz and lithium tetraborate strips shown in Fig. 5.15. The choice of l, w, and t was based on computational considerations, such as the size of the matrices arising from the finite element discretization, rather than practical strip configurations for which the length to thickness ratio l/t is typically greater. Nevertheless, this geometry allows a pronounced thickness-shear mode, and is, therefore, suitable for studying the influence of the exterior electric field.

To accurately model the mechanical and electrical field variations associated with the high-frequency thickness-shear mode, the strips were subdivided into elements of second order proportionally with l, w, and t, i.e. 36, 6 and 2 elements were distributed along the length, width, and thickness respectively. This discretization produces a large model with a total of $n = 4313$ nodes, of which $n_S = 2402$ lie on the surface (superelement size). The dimension of the stiffness matrix depends on the area occupied by the electrode but does not exceed $n_K = 4n = 17252$ (bare strip); the size of the mass matrix is fixed for all electrode configurations and equals $n_M = 3n = 12939$.

In the first test, the rectangular electrodes (18×4 in terms of elements) cover two thirds of the length and two thirds of the width in the center of the top and bottom surfaces, i.e. one third of the major faces[3]. The analysis of the first 150 vibrational modes in the quartz X-strip (Table 5.11), demonstrates that except for several weak spurious responses, only two strong modes are excited by the applied electric field $\mathbf{E} = (0, E_2, 0)^{\mathrm{T}}$. These modes, identified as face-shear (FS) and

[3] The electrode pattern would normally include some additional metallization to electrically connect the central area with pins. It is neglected by the present model.

thickness-shear (TS), are characterized by the strain components $S_5 = S_{13}$ and $S_6 = S_{12}$ induced through the piezoelectric coefficients e_{25} and e_{26} respectively. The electric response, in terms of motional capacitance C_n and the coupling coefficient k, is almost of the same intensity for both modes since e_{25} and e_{26} have close values (Eq. (3.10), Appendix 2).

Table 5.11 Modes in quartz strip excited by the thickness electric field.

Mode (number)	Shape	Parameters	Electric boundary	
			closed	open
FS_1 (55)		f_r (kHz)	870.7	870.5
		f_a (kHz)	872.2	872.0
		C_n (fF)	3.43	3.51
		k (%)	5.9	5.7
TS_1 (136)		f_r (kHz)	1668.9	1668.2
		f_a (kHz)	1671.7	1670.7
		C_n (fF)	3.36	3.40
		k (%)	5.8	5.5

The resonance frequency predicted by the one-dimensional model of an infinite bare plate

$$f^{FS_1} = \frac{1}{2w}\sqrt{\frac{c_{55}^E}{\rho}} = 850 \text{ kHz}, \tag{3.16}$$

$$f^{TS_1} = \frac{1}{2t}\sqrt{\frac{c_{66}^D}{\rho}} = 1661 \text{ kHz}, \tag{3.17}$$

where c_{66}^D is the 'piezoelectrically stiffened' elastic constant $c_{66}^D = c_{66}^E + e_{26}^2/\epsilon_{22}^S$, are lower than the ones obtained from the finite element model (Table 5.11) since both the face-shear and thickness-shear modes are shaped by the finite lateral dimensions.

The calculated static capacitances for the above electrode configuration are $C_s^{closed} = 0.99$ pF and $C_s^{open} = 1.074$ pF for the closed- and open-boundary models respectively. This 8 % change in the static capacitance increases the

effective capacitance ratio r of the thickness-shear mode from $r^{closed} = 295$ and $r^{open} = 316$. To compare, the experimental value for the AT-cut quartz strip resonator (of different configuration) reported by Fujiwara and Wakatsuki (1987) was $r = 333$, which is fairly close to the value obtained with the finite element model with open electric boundaries. Because the presence of the exterior electric field shifts, in this case, both the resonance ($\Delta f_r = 0.7$ kHz) and antiresonance ($\Delta f_a = 1$ kHz) frequencies, their separation Δf diminishes only slightly, i.e. from 2.8 to 2.5 kHz

The same thickness-shear mode with displacement u_1 can be activated by the lateral (with respect to the thickness direction x_2) electric field E_3 configuration through the piezoelectric coefficient e_{36} (Eq. (3.10), Appendix 2). However, its electric activity is less strong, which is reflected in the resonance separation Δf, motional capacitance C_n, or coupling coefficient k (Table 5.12), which is partly attributed to the fact that constant e_{36} has a smaller absolute value compared to its E_2-field counterpart e_{26}.

Table 5.12 Characteristics of the thickness-shear mode in quartz strip resonator excited by lateral electric field.

TS_1 	Parameters				
	Static	Dynamic			
Electrical boundary	C_s, pF	f_r, kHz	f_a, kHz	C_n, fF	k, %
closed	0.101	1669.6	1671.5	0.429	4.8
open	0.212	1669.1	1670.3	0.429	3.7

As expected, the relative frequency shifts due to open electric boundaries are greater in the case of lateral excitation of the thickness-shear mode since the uncovered major surfaces favor the propagation of electric field into the outer space (Fig. 5.16*b*). The static capacitance C_s doubles in the presence of the exterior electric field (Table 5.12). The resulting shift in the antiresonance frequency $\Delta f_a = 1.2$ kHz is as large as the effective frequency separation

$\Delta f^{open} = 1.2$ kHz which constitutes only 63 % of that predicted by the closed-boundary model $\Delta f^{closed} = 1.9$ kHz.

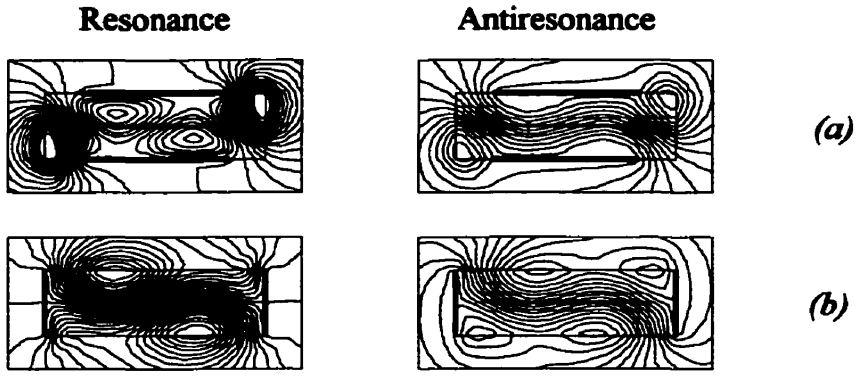

Fig 5.16 Cross section x_2–x_3 of electric potential distribution in the thickness-shear mode of X-strip quartz resonator for *(a)* thickness and *(b)* lateral electric field orientation.

Because of the different structure of the piezoelectric matrix (Eq. (3.13), Appendix 2), four types of vibration can be piezoelectrically excited in the lithium tetraborate Z-strip by the perpendicular electric field $\mathbf{E} = (0, E_2, 0)^{\mathrm{T}}$. These modes are activated through the nonzero piezoelectric coefficients e_{21}, e_{22}, e_{23}, e_{24} and are characterized by mechanical strain components S_{11}, S_{22}, S_{33}, and S_{23} respectively. The first three correspond to extensional motions along the coordinate axes x_i, $i = 1, 2, 3$, with displacement components u_i, while the last is the thickness-shear mode. To help identify modes calculated by the finite element model, their approximate resonance frequencies can be obtained from the one-dimensional extensional and thickness vibrations of the Z-strip:

$$f_r^{E_1} = \frac{1}{2w}\sqrt{\frac{1}{\rho s_{11}^E}} = 1104 \text{ kHz}, \tag{3.18}$$

$$f_r^{TSt_2} = \frac{1}{2t}\sqrt{\frac{c_{22}^E}{\rho}} = 3296 \text{ kHz}, \tag{3.19}$$

$$f_r^{E_3} = \frac{1}{2l}\sqrt{\frac{1}{\rho s_{33}^E}} = 188 \text{ kHz}, \tag{3.20}$$

$$\left.\begin{aligned} &\begin{vmatrix} (c_{22}^E + e_{22}^2/\epsilon_{22}^S) - \rho V^2 & c_{24}^E + e_{22}e_{24}/\epsilon_{22}^S \\ c_{24}^E + e_{22}e_{24}/\epsilon_{22}^S & (c_{44}^E + e_{24}^2/\epsilon_{22}^S) - \rho V^2 \end{vmatrix} = 0, \\ &f^{TS_3} = \frac{V}{2t} = 1654 \text{ kHz}, \end{aligned}\right\} \tag{3.21}$$

The frequency of the extensional vibration in the thickness direction (3.19), denoted here, following Mindlin's nomenclature of modes (Mindlin, 1982), as *thickness-stretch* (TSt), is too high and is beyond the scope of the present modal analysis. The remaining three piezoelectric modes are among the 150 lowest modes of the lithium tetraborate Z-strip, and are shown in Table 5.13. Moreover, two resonances of the width extensional motion with a different number of wavelengths along the strip length — E_1 and $\bar{E}_1$ — are present in the spectrum of Z-strip. As in the case of quartz X-strip, the resonant frequencies calculated by the finite element model which takes into account the lateral dimensions of the plate are higher than their one-dimensional approximations.

The shifts in the resonant frequencies of the thickness-shear mode due to the exterior electric field are $\Delta f_r = 5.4$ and $\Delta f_a = 8.5$ kHz for the resonance and antiresonance respectively. Their cumulative change reduces the resonance spacing Δf by 12.5 %. To calculate the capacitance ratio of the thickness-shear mode, the shunt capacitance C_0 was approximated by the static capacitance C_s ($C_s^{closed} = 2.043$ and $C_s^{open} = 2.148$ pF) less the motional capacitances C_n of the first four active modes (Table 5.13):

$$C_0 \approx C_s - C_9 - C_{61} - C_{64} - C_{131}, \tag{3.22}$$

since lithium tetraborate is a relatively strong piezoelectric. This yields the capacitance ratios $r^{closed} = 29.0$ and $r^{open} = 31.6$ for the closed and open electric boundaries respectively. The experimental value $r = 20.9$ was reported by Fujiwara *et al.* (1985).

The similar parameters for the thickness-shear mode excited by the lateral electric field are shown in Table 5.14.

Table 5.13 Modes in $Li_2B_4O_7$ strip resonators excited by the thickness electric field.

Mode (number)	Shape	Parameters	Electric boundary	
			closed	open
E_3 (9)	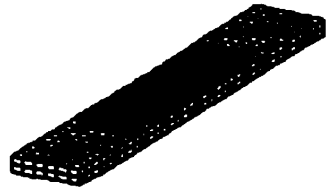	f_r (kHz)	189.9	189.1
		f_a (kHz)	190.5	189.7
		C_n (fF)	13.1	13.4
		k (%)	8.0	7.9
E_1 (61)	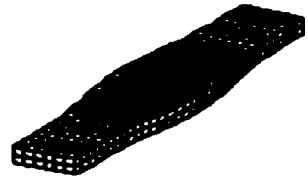	f_r (kHz)	1073.0	1072.7
		f_a (kHz)	1076.3	1075.7
		C_n (fF)	16.0	15.3
		k (%)	7.8	7.4
$\overline{E}_1$ (64)	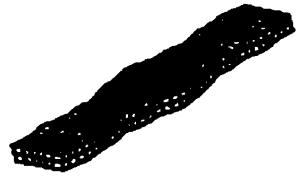	f_r (kHz)	1086.2	1084.7
		f_a (kHz)	1089.6	1088.2
		C_n (fF)	9.72	10.9
		k (%)	7.9	8.1
TS_3 (131)	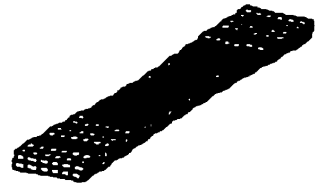	f_r (kHz)	1677.4	1672.0
		f_a (kHz)	1705.3	1696.8
		C_n (fF)	66.7	64.7
		k (%)	18.0	17.0

Table 5.14 Characteristics of the thickness-shear mode in lithium tetraborate strip resonator excited by lateral electric field.

TS_3 (#138) 	Parameters				
	Static	Dynamic			
Electrical boundary	C_s, pF	f_r, kHz	f_a, kHz	C_n, fF	k, %
closed	0.205	1760.7	1778.0	6.23	13.9
open	0.318	1758.6	1771.5	6.46	12.0

Tables 5.11 and 5.13 demonstrated how the resonance frequencies of strip resonators change when the exterior electric field is added to the model. However,

it is not clear, at first sight, whether the change produced by the external field is substantial. As in the example of unit cube, this change is compared to the frequency shift due to the variation of the electrode size. Table 5.15 shows that the frequency shifts due to the leakage of the electrostatic field Δf^{open} are comparable to those resulting from the electrode shortening $\Delta f^{l_e/l}$.

Table 5.15 Shifts in resonance and antiresonance of the thickness-shear mode due to the leakage field for various electrode sizes.

(a) Quartz

Electrode length	Electrical boundary				Shift	
	closed		open		resonance	antiresonance
l_e/l	f_r, kHz	f_a, kHz	f_r, kHz	f_a, kHz	Δf_r^{open}, kHz	Δf_a^{open}, kHz
0.67	1668.3	1671.4	1667.7	1670.5	0.6	0.9
0.5	1668.9	1671.7	1668.2	1670.7	0.7	1.0
0.33	1669.8	1672.0	1668.9	1670.9	0.9	1.1
$\Delta f^{l_e/l}$, kHz	1.5	0.6	1.2	0.4	↵	

(b) Lithium tetraborate

Electrode length	Electrical boundary				Shift	
	closed		open		resonance	antiresonance
l_e/l	f_r, kHz	f_a, kHz	f_r, kHz	f_a, kHz	Δf_r^{open}, kHz	Δf_a^{open}, kHz
0.67	1670.9	1700.5	1667.7	1695.1	3.2	5.4
0.5	1677.3	1705.3	1672.0	1696.8	5.4	8.5
0.33	1687.3	1711.3	1678.4	1697.9	8.9	13.4
$\Delta f^{l_e/l}$, kHz	16.4	10.8	10.7	2.8	↵	

For example, as the electrode length is halved, i.e. changes from $0.67l$ to $0.33l$ (line 1 and 3), the resonance and antiresonance frequencies of the open-boundary quartz strip drop by 1.2 and 0.4 kHz respectively. The corresponding frequency shifts produced by the 'opening' of electric boundaries in the strip with the median electrode (line 2) equal 0.7 and 1.0 kHz. In is interesting to note that in the model with open electric boundaries, the antiresonance frequency f_a is almost constant for various electrode sizes. This is particularly visible for the lithium tetraborate strip (Table 5.15 *(b)*) for which f_a increases only by 2.8 kHz compared to 10.8 kHz for the model with closed boundaries as the electrode length decreases.

Conclusions and further work

As it has been demonstrated in the previous chapter, the exterior electroquasistatic field affects the solution of the static and vibrational piezoelectric problems in several ways. First, it increases the static capacitance C_s, typically by 10–20 %. Second, due to this increase, the effective separation between the resonant frequencies diminishes, mostly through the shift in the antiresonance frequency; in terms of coupling coefficient, this is equivalent to the decrease of the effective piezoelectric coupling. For some special configurations (e.g. L-effect in CdS rods), the leakage from the crystal can be so severe that it almost annihilate the piezoelectric effect. Compared to the influence of other electrical boundary conditions, this shift in the antiresonance frequency is not a negligible quantity. It was shown for both the lower (extensional vibrations of cube) and higher (thickness-shear vibrations in strip-type resonators) modes, that the change in f_a was of the same order of magnitude as the piezoelectric effect itself, which, in the case of a piezoelectric crystal with two electrodes, is measured by the spacing between the two characteristic frequencies (resonance and antiresonance). Moreover, in one of the examples, the shift in the antiresonance frequency due to the electric flux leakage was almost equal to the shift in the resonance frequency due to the halving of the electrode size, so that the same effective resonance separation was observed in both cases. Finally, the exterior electric field excites some of the mechanical modes that were piezoelectrically inactive under the closed-boundary model.

The above suggests that for crystals with a relatively low permittivity ($\epsilon \leq 10\epsilon_0$), including the exterior electric field in the simulation of piezoelectric vibrations is as important as modeling the electrode plating. Although in the present finite element analysis only electrical boundary conditions were considered in order to isolate the effect of the leakage field, it is felt that the described electrical behavior would be reproduced if other perturbations (e.g. electrode mass-loading, acoustic damping, temperature changes, or mounting strains) were included in the simulation. Also, although the limitation on the problem size set by the core memory prevented the modeling of large and complex structures, one can expect that the piezoelectric vibrations in more realistic configurations would react to the exterior electric field in the same manner. Therefore, as the next step of research, it would be tempting to try to verify these assumptions by performing numerical experiments with a superposition of two or more perturbing factors or on resonators with larger dimension ratios. In particular, structures with multiple electrodes (e.g. the model of a monolithic filter) represent a natural continuation of the present series of illustrative example.

Since the electrically unbounded piezoelectric problem has never been considered or solved previously, most of the attention was given to the problem formulation, numerical solution of the finite element equations, and result interpretation, maybe at the expense of efficiency in modeling the infinite exterior region. Initially, the method of ballooning was chosen primarily for the simplicity of implementation and accuracy. In addition, since the superelement matrix can be attached directly to the surface of the piezoelectric, no extra variables are added to the interior model, which is very convenient considering the limited core memory. Although the ballooning algorithm lends itself to considerable memory savings (block recursion for rectangular interfaces, neglect of small entries in the superelement matrix), the generation of the final matrix is still an expensive process from the point of view of computing time and memory. Therefore, trying an alternative method of approximating the exterior electric field, or even carrying out a comparative study of several techniques is essential for the future development of the piezoelectric problem with open electric boundaries. The method of *exterior mapping* (Stochniol, 1992) seems the most promising, provided a more sophisticated meshing program is used.

In contrast to the traditional approach of obtaining the dielectric part of C_s from the modal analysis, the full static capacitance is determined from the solution of a separate piezoelectric static problem. Since both the static and vibrational solutions of the piezoelectric boundary-value problem are required for a complete representation of forced vibrations, both the deterministic and eigenvalue problem are to be solved in the finite element analysis of piezoelectric structures. However, it seems possible to combine these solutions by adopting the approach proposed by Nour-Omid and Clough (1984), who used the **M**-orthogonal Lanczos vectors as an alternative to the mode superposition method for describing the dynamic response. Indeed, the Lanczos vectors are much less expensive to generate that the eigenvectors, and include the static displacement as the first vector.

Finally, some innovations can be introduced in the finite element formulation of the piezoelectric problem. In Chapter 1 Section 2, for the sake of consistency between electromagnetic and elastic equations and boundary conditions, the continuity of the tangential strain across the interface was expressed in symbolic form (Eq. (2.26)), analogous to the continuity condition for the tangential electric field. Taken alone, the former condition is not used explicitly in the present formulation since nodal finite elements preserve the continuity of displacement, not strain. However, it indicates that, by analogy with the edge elements used in computational electromagnetics, a new type of tetrahedra-based elements that preserve the continuity of the tangential components of a dyadic (**S**) across the element faces can be derived. Such elements might be useful if the piezoelectric problem is formulated directly in terms of strain **S** and electric field **E**, i.e. when accurate calculation of the stress and strain is required, for example in composite materials, in smart structure applications, or simply for post-processing purposes.

Appendix 1

Uniform plane waves

In general, both the rotational and irrotational electric fields may accompany the propagation of an acoustic wave in the piezoelectric medium. Among these hybrid acousto-electromagnetic solutions two special cases — when an acoustic wave interacts only with electric field of a particular type (either rotational or irrotational) — are essential for the analysis of coupled wave propagation. The physical difference between these two types of coupled solutions is best illustrated on the example of *uniform plane waves* propagating in an unbounded space.

For linear materials, any mechanical or electromagnetic tensor variable $\mathfrak{X}(\mathbf{r},t)$ in a wave propagating at speed V along the direction given by a unit vector $\mathbf{m}$ depends on time t and position $\mathbf{r}$ as

$$\mathfrak{X}(\mathbf{r},t) = {}^{\circ}\mathfrak{X}\,\mathrm{F}\left(t - \frac{\mathbf{m}\cdot\mathbf{r}}{\mathrm{V}}\right). \tag{1.1}$$

The curl, divergence, and gradient operators acting upon $\mathfrak{X}(\mathbf{r},t)$ may be replaced, respectively, by vector, scalar, and dyadic products of $\mathbf{m}$ and $\mathfrak{X}(\mathbf{r},t)$, times $(-1/\mathrm{V})$; the action of the partial differential operator $\partial/\partial t$ reduces simply to the arithmetic multiplication by unity. Since the solution is sought in the form of (1.1), the acoustic wave equation (3.5) of Chapter 1 simplifies to

$$\left(\mathbf{m}\cdot\mathbf{c}^{E}\cdot\mathbf{m} - \rho\mathrm{V}^{2}\mathbf{I}\right)\cdot\mathbf{u} = -\varphi\,\mathbf{m}\cdot\mathbf{e}\cdot\mathbf{m} + \mathrm{V}\,\mathbf{m}\cdot\mathbf{e}\cdot\mathbf{A}, \tag{1.2}$$

where it has been taken into account that $\mathbf{m}\cdot\mathbf{c}^{E} : \mathbf{mu} = \left(\mathbf{m}\cdot\mathbf{c}^{E}\cdot\mathbf{m}\right)\cdot\mathbf{u}$ due to the symmetry of the stiffness tensor $\mathbf{c}^{E}$.

Before inquiring under what circumstances the propagation of a piezoelectric wave is accompanied by only one type of electric field, it is of interest to determine how vectors **D** and **E**, as well as their rotational and irrotational components, are oriented in this wave. Applying the differential rules mentioned above, Eq. (3.4) of Chapter 1 becomes

$$\mathbf{m} \times \mathbf{m} \times \mathbf{A} = \mathrm{V}^2 \mu_0 \mathbf{D}, \tag{1.3}$$

where the total electric flux density vector **D** is given by (3.11) of the same chapter. Because Eq. (1.3) requires the plane acousto-electromagnetic wave to have **D** in the transverse plane, its $\mathbf{D}^P$, $\mathbf{D}^{E^{(r)}}$ and $\mathbf{D}^{E^{(i)}}$ components must have such directions and magnitudes that their sum is orthogonal to the direction of propagation **m**. The Gauss law (3.13) of Chapter 1, reduced for a uniform plane wave to

$$\mathbf{m} \cdot \mathbf{D}^{E^{(i)}} = -\mathbf{m} \cdot \mathbf{D}^P, \tag{1.4}$$

adds no additional constraint on **D** but implies the solenoidality of $\mathbf{D}^{E^{(r)}}$

$$\mathbf{m} \cdot \mathbf{D}^{E^{(r)}} = 0 \tag{1.5}$$

already prescribed by the gauge condition (3.7) of Chapter 1. The latter implies that the $\mathbf{D}^{E^{(r)}}$ component is also perpendicular to the direction of propagation **m**; at the same time, the corresponding rotational electric field $\mathbf{E}^{(r)}$, or **A**, determined from the solution of (1.3), is not restricted to lie in the transverse plane. In contrast, for the irrotational field this is the orientation of $\mathbf{E}^{(i)}$ that is predetermined by the direction of propagation **m** so that $\mathbf{E}^{(i)}$ is always longitudinal:

$$\mathbf{E}^{(i)} = \frac{\varphi}{\mathrm{V}} \mathbf{m}; \tag{1.6}$$

the orientation of $\mathbf{D}^{E^{(i)}}$ is related to the symmetry of tensor ϵ^S, and, in general, is not parallel to **m**.

Expanding **D** according to (3.11) of Chapter 1, and using the vector identity

$$\mathbf{A} = \mathbf{m}\mathbf{m} \cdot \mathbf{A} + \mathbf{m} \times \mathbf{A} \times \mathbf{m} \tag{1.7}$$

that expresses **A** as the sum of its component along **m** and its component orthogonal to **m**, the plane wave counterpart of Eq. (3.12) of Chapter 1 may be written as

$$\left(\mathbf{I} - \mathbf{mm} - \mathrm{V}^2\mu_0\boldsymbol{\epsilon}^S\right)\cdot\mathbf{A} = -\mathrm{V}^2\mu_0\mathbf{D}^P - \mathrm{V}^2\mu_0\mathbf{D}^{E^{(i)}}. \tag{1.8}$$

It is easily seen from Eq. (1.4) that the right-hand side source vector in (1.8) is orthogonal to **m**; as a consequence, it always generates a rotational field provided $\mathbf{D}^P + \mathbf{D}^{E^{(i)}}$ does not vanish. The same relation (1.4) suggests that the longitudinal electric field $\mathbf{E}^{(i)}$ is induced only if vector $\mathbf{D}^P$ has a nonzero component along **m**. In contrast, when $\mathbf{D}^P$ is perpendicular to **m** (Fig. A1.1a), the irrotational field is not piezoelectrically excited by the propagating acoustic wave, and the $\mathbf{D}^{E^{(i)}}$ term vanishes in (1.8). For this orientation of $\mathbf{D}^P$, the vector potential **A** can be symbolically expressed as

$$\mathbf{A} = \mathrm{V}\mu_0\left(\mathbf{I} - \mathbf{mm} - \mathrm{V}^2\mu_0\boldsymbol{\epsilon}^S\right)^{-1}\cdot(\mathbf{e}\cdot\mathbf{m})\cdot\mathbf{u}, \tag{1.9}$$

where the symmetry of piezoelectric tensor **e** about its two last indices allowed **e** : **mu** to be replaced by $(\mathbf{e}\cdot\mathbf{m})\cdot\mathbf{u}$. This expression can be simplified further if one recall that the ratio between acoustic and electromagnetic velocities V/v is of order of 10^{-5}. Consequently, $\left\|\mathrm{V}^2\mu_0\boldsymbol{\epsilon}^S\right\| \sim \left\|(\mathrm{V}/v)^2\mathbf{I}\right\| \ll 1$ in (1.9), and potential **A** can be approximated by

$$\mathbf{A} \simeq \mathrm{V}\mu_0\left(\mathbf{I} - \mathbf{mm} + \mathrm{V}^2\mu_0\boldsymbol{\epsilon}^S\right)\cdot(\mathbf{e}\cdot\mathbf{m})\cdot\mathbf{u} \simeq \mathrm{V}\mu_0\,(\mathbf{e}\cdot\mathbf{m})\cdot\mathbf{u}. \tag{1.10}$$

Substituting this expression into (1.2) with $\varphi = 0$ and rearranging terms, one obtain the equation for the mechanical displacement **u**:

$$\left\{\mathbf{m}\cdot\left(\mathbf{c}^E - \mathrm{V}^2\mu_0\mathbf{e}\cdot\mathbf{e}\right)\cdot\mathbf{m} - \rho\mathrm{V}^2\mathbf{I}\right\}\cdot\mathbf{u} = 0 \tag{1.11}$$

in an acoustic wave accompanied solely by the rotational field $\mathbf{E}^{(r)}$.

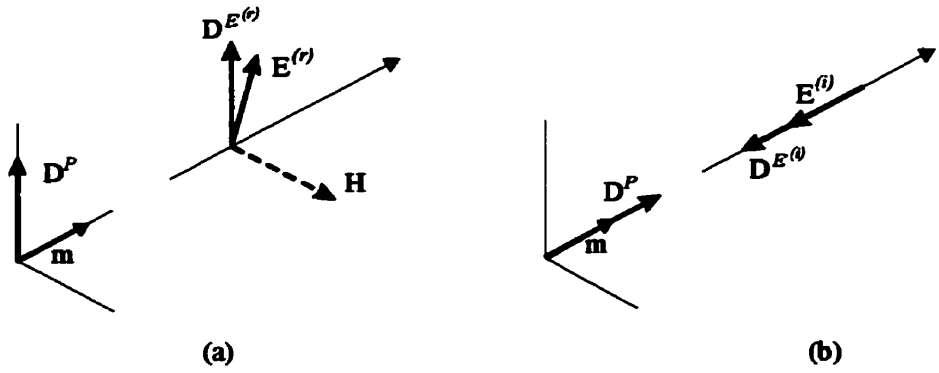

Fig A1.1 Electric flux density orientation in a quasi-acoustic *(a)* and stiffened acoustic *(b)* waves.

Now consider the situation when the propagating acoustic wave is coupled to the irrotational electric field $\mathbf{E}^{(i)}$ but not to the rotational one $\mathbf{E}^{(r)}$. From Eq. (1.3), one can notice that if $\mathbf{D} = 0$ in a plane piezoelectric wave, the electromagnetic wave is not excited. In other words, if the sum of $\mathbf{D}^P$, $\mathbf{D}^{E^{(r)}}$, and $\mathbf{D}^{E^{(i)}}$ is a null vector, the piezoelectric wave propagation is not accompanied by the displacement current and the magnetic field; therefore, the associated electric field can only be potential. This situation can occur, for instance, when $\mathbf{D}^P$ and $\mathbf{D}^{E^{(i)}}$ are directed along $\mathbf{m}$ (Fig. A1.1*(b)*): neither $\mathbf{D}^P$ nor $\mathbf{D}^{E^{(i)}}$ has a component in the transverse plane, i.e. plays no part in the propagation of an electromagnetic wave. Recalling (1.4), one obtain that $\mathbf{D}^P = -\mathbf{D}^{E^{(i)}}$, thus reducing to zero the source term in (1.8). The latter becomes a homogeneous equation in $\mathbf{A}$ — Fresnel equation (Landau, Lifshitz, 1992) — whose solution consists of two purely electromagnetic waves $(v^{(k)}, \mathbf{A}^{(k)})$, $k = 1, 2$ propagating along $\mathbf{m}$. Thus the piezoelectric component of $\mathbf{D}$ — $\mathbf{D}^P$ — does not have the right orientation to excite an electromagnetic field but does induce bound charges along $\mathbf{m}$ characterized by the longitudinal electric field $\mathbf{E}^{(i)}$ or, alternatively, by the scalar potential φ. The bound charge potential distribution can always be expressed in terms of displacement $\mathbf{u}$ by using the plane wave version of (3.8) of Chapter 1:

$$\varphi = \frac{\mathbf{m} \cdot \mathbf{e} \cdot \mathbf{m}}{\mathbf{m} \cdot \boldsymbol{\epsilon}^S \cdot \mathbf{m}} \cdot \mathbf{u}, \tag{1.12}$$

where the symmetry of tensor **e** was exploited once again to rearrange terms. To obtain an equation analogous to (1.11) for the mechanical displacement **u** coupled to $\mathbf{E}^{(i)}$ alone, φ is substituted into Eq. (1.2) with $\mathbf{A} = 0$ in the right side:

$$\left\{\mathbf{m}\cdot\left(\mathbf{c}^{E}+\frac{\mathbf{e}\cdot\mathbf{m}\mathbf{m}\cdot\mathbf{e}}{\mathbf{m}\cdot\boldsymbol{\epsilon}^{S}\cdot\mathbf{m}}\right)\cdot\mathbf{m}-\rho\mathrm{V}^{2}\mathbf{I}\right\}\cdot\mathbf{u}=0. \tag{1.13}$$

It is readily seen that the homogeneous Eqs. (1.11) and (1.13) obtained from the above analysis are amenable to the form of Christoffel equations (Sirotin, 1979):

$$(\mathbf{m}\cdot\mathbf{c}\cdot\mathbf{m}-\rho\mathrm{V}^{2}\mathbf{I})\cdot\mathbf{u}=0, \tag{1.14}$$

if the stiffness tensor **c** is replaced by

$$\mathbf{c}^{(r)}=\mathbf{c}^{E}-\mathrm{V}^{2}\mu_{0}\mathbf{e}\cdot\mathbf{e} \tag{1.15}$$

and

$$\mathbf{c}^{(i)}=\mathbf{c}^{E}+\frac{\mathbf{e}\cdot\mathbf{m}\mathbf{m}\cdot\mathbf{e}}{\mathbf{m}\cdot\boldsymbol{\epsilon}^{S}\cdot\mathbf{m}} \tag{1.16}$$

respectively. For a given direction **m** the solution of Eqs. (1.14) yields three phase velocities $\mathrm{V}^{(k)}$ and, accordingly, three polarization vectors $^{\circ}\mathbf{u}^{(k)}$ $(k=1,2,3)$ of uniform plane acoustic waves propagating in a nonpiezoelectric infinite medium (Fig. A1.2); $\mathrm{V}^{(k)}$ and $^{\circ}\mathbf{u}^{(k)}$ are respectively real eigenvalues and orthogonal eigenvectors of the positive-definite Christoffel tensor $\boldsymbol{\Gamma}=\mathbf{m}\cdot\mathbf{c}\cdot\mathbf{m}$. Additionally, it follows from (1.14) that the acoustic wave velocity V is derived from stiffness **c** as

$$\mathrm{V}=\sqrt{\frac{\mathbf{um}:\mathbf{c}:\mathbf{mu}}{\rho\,\mathbf{u}\cdot\mathbf{u}}}. \tag{1.17}$$

Thus the influence of the piezoelectric effect on V can be attributed to the modification of the stiffness tensor **c**. In other words, the coupling of an acoustic wave with rotational (1.15) and irrotational (1.16) electric fields can be taken into account by substituting effective stiffnesses $\mathbf{c}^{(r)}$ and $\mathbf{c}^{(i)}$ into (1.14) instead of **c**.

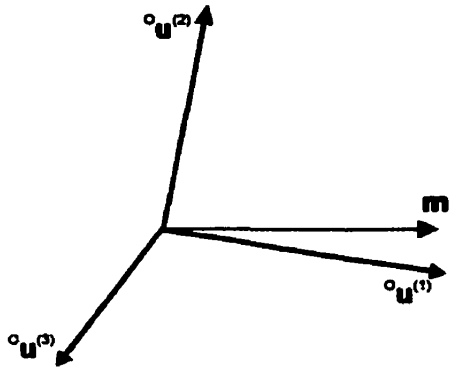

Fig A1.2 A set of orthogonal displacement vectors associated with one quasi-longitudinal ($^{\circ}\mathbf{u}^{(1)}$) and two quasi-shear ($^{\circ}\mathbf{u}^{(2)}$, $^{\circ}\mathbf{u}^{(3)}$) plane acoustic waves propagating along the direction $\mathbf{m}$ in an infinite piezoelectric medium.

It is seen from (1.16) that in the case of piezoelectric coupling with potential electric field the stiffness is increased by the quantity $(\mathbf{e}\cdot\mathbf{m}\mathbf{m}\cdot\mathbf{e})/(\mathbf{m}\cdot\boldsymbol{\epsilon}^{S}\cdot\mathbf{m})$ that varies for different materials and directions of propagation from zero to tens of percent compared to $\mathbf{c}^{E}$. This effect is called *piezoelectric stiffening*, and the plane acoustic wave coupled solely with irrotational electric field is referred to as *stiffened acoustic wave* (Auld, 1990a). Accordingly, the phase velocity of the stiffened acoustic wave is higher than that of the purely acoustic wave. For the sake of comparison with (1.16), (1.15) is better rewritten in the form

$$\mathbf{c}^{(r)} = \mathbf{c}^{E} - \left(\frac{\mathrm{V}}{v}\right)^{2}\frac{\mathbf{e}\cdot\mathbf{e}}{\mathbf{m}\cdot\boldsymbol{\epsilon}^{S}\cdot\mathbf{m}}, \tag{1.18}$$

where the electromagnetic wave velocity v has been approximated by $1/\sqrt{\mu_0\mathbf{m}\cdot\boldsymbol{\epsilon}^{S}\cdot\mathbf{m}}$. Because quantities $(\mathbf{e}\cdot\mathbf{m}\mathbf{m}\cdot\mathbf{e})/(\mathbf{m}\cdot\boldsymbol{\epsilon}^{S}\cdot\mathbf{m})$ and $(\mathbf{e}\cdot\mathbf{e})/(\mathbf{m}\cdot\boldsymbol{\epsilon}^{S}\cdot\mathbf{m})$ are clearly of the same order of magnitude, it follows from (1.16) and (1.18) that the contribution of the rotational electric field to the effective stiffness $\mathbf{c}^{(r)}$ is 10^{5} times smaller than that of the irrotational field. Thus, the piezoelectric coupling with electromagnetic field shifts the stiffness, and, respectively, the phase velocity to a slightly lower value. The corresponding hybrid wave is called *quasi-acoustic* (Auld, 1990a), and represents a slightly perturbed version of a purely acoustic wave.

Appendix 2

Matrices of material coefficients

1. Calculations in compressed notation

The symmetry properties of material tensors, expressed by Eqs. (2.4) of Chapter 1, allow the multi-index tensor components to be arranged in matrices by using special index abbreviations (IEEE Standard on Piezoelectricity, 1987). In the case of elastic and piezoelectric tensors, they simply consist in replacing pairs of interchangeable indices ij and kl $(i, j, k, l = 1, 2, 3)$ in the extended tensor notation by single indices p and q $(p, q = 1, ..., 6)$ in the compressed matrix (i.e. engineering) notation

$$c^E_{ijkl} = c^E_{pq}, \tag{1.1}$$

$$e_{ikl} = e_{ip} \tag{1.2}$$

according to the following rule

$$\begin{aligned} &11 \rightarrow 1,\ 22 \rightarrow 2,\ 33 \rightarrow 3, \\ &\qquad (23 \text{ or } 32) \rightarrow 4,\ (13 \text{ or } 31) \rightarrow 5,\ (12 \text{ or } 21) \rightarrow 6, \end{aligned} \tag{1.3}$$

without recourse to a multiplying factor. Thus, the $3^4 = 81$ components of the elastic stiffness tensor can be compactly stored in the form of a 6×6 symmetric matrix

$$\mathbf{c} = \begin{bmatrix} c_{11} & c_{12} & c_{13} & c_{14} & c_{15} & c_{16} \\ c_{12} & c_{22} & c_{23} & c_{24} & c_{25} & c_{26} \\ c_{13} & c_{23} & c_{33} & c_{34} & c_{35} & c_{36} \\ c_{14} & c_{24} & c_{34} & c_{44} & c_{45} & c_{46} \\ c_{15} & c_{25} & c_{35} & c_{45} & c_{55} & c_{56} \\ c_{16} & c_{26} & c_{36} & c_{46} & c_{56} & c_{66} \end{bmatrix}, \tag{1.4}$$

and the $3^3 = 27$ components of the piezoelectric tensor — as a 3×6 matrix

$$\mathbf{e} = \begin{bmatrix} e_{11} & e_{12} & e_{13} & e_{14} & e_{15} & e_{16} \\ e_{21} & e_{22} & e_{23} & e_{24} & e_{25} & e_{26} \\ e_{31} & e_{32} & e_{33} & e_{34} & e_{35} & e_{36} \end{bmatrix}. \tag{1.5}$$

These matrices will be further symbolically denoted by boldface courier lower-case characters $\mathbf{c}$ and $\mathbf{e}$ respectively to distinguish them from the corresponding tensors. For the second rank tensor ϵ^S the compressed and expanded notations are equivalent, and lead to the symmetric matrix

$$\boldsymbol{\epsilon} = \begin{bmatrix} \epsilon_{11} & \epsilon_{12} & \epsilon_{13} \\ \epsilon_{12} & \epsilon_{22} & \epsilon_{23} \\ \epsilon_{13} & \epsilon_{23} & \epsilon_{33} \end{bmatrix}. \tag{1.6}$$

2. Measured properties of piezoelectric materials

The main advantage of the above notation lye in the possibility to manipulate material coefficients as ordinary two-dimensional matrices. Because the abbreviated indices can also be applied to variables, almost all physical equations, including constitutive relations, can be recast in the matrix form. Therefore, when the fundamental set of elastic, piezoelectric, and dielectric constants is recovered from measurements on a series samples for which the relationship between the variables is as simple as possible (e.g. described by some one-dimensional model), the material coefficients are determined and tabulated directly as components of matrices $\mathbf{c}$, $\mathbf{e}$, and $\boldsymbol{\epsilon}$. Their symmetry properties are derived from the point group of the crystal assuming that the coefficient matrix is invariant under the application of each symmetry element, such as an n-fold axis of rotation or a mirror plane (m), of the group. In the form (1.4)–(1.6), the material matrices corresponds to the least symmetrical class 1 of triclinic system (IEEE, 1987). Since most practical piezoelectric materials belong to the trigonal, tetragonal or hexagonal systems, they are characterized by a higher degree of symmetry, and only few of the 21, 18, and 6 entries of (1.4)–(1.6) respectively are independent. In these categories of symmetry, the z-axis of the Cartesian coordinate system, in which the material tensor is defined, is chosen parallel to the three-, four-, and, respectively, sixfold crystallographic axes. For example, the elastic, piezoelectric and dielectric matrices of quartz (trigonal system, class 32) are given by

$$\mathbf{c} = \begin{bmatrix} c_{11} & c_{12} & c_{13} & c_{14} & 0 & 0 \\ c_{12} & c_{22} & c_{23} & -c_{14} & 0 & 0 \\ c_{13} & c_{23} & c_{33} & 0 & 0 & 0 \\ c_{14} & -c_{14} & 0 & c_{44} & 0 & 0 \\ 0 & 0 & 0 & 0 & c_{44} & c_{14} \\ 0 & 0 & 0 & 0 & c_{14} & c_{66} \end{bmatrix} \tag{2.1}$$

$$\mathbf{e} = \begin{bmatrix} e_{11} & -e_{11} & 0 & e_{14} & 0 & 0 \\ 0 & 0 & 0 & 0 & -e_{14} & -e_{11} \\ 0 & 0 & 0 & 0 & 0 & 0 \end{bmatrix} \tag{2.2}$$

$$\boldsymbol{\epsilon} = \begin{bmatrix} \epsilon_{11} & 0 & 0 \\ 0 & \epsilon_{11} & 0 \\ 0 & 0 & \epsilon_{33} \end{bmatrix} \tag{2.3}$$

respectively. The experimentally determined (Bechmann *et al.*, 1962) independent material coefficients of quartz are summarized in Table A2.1, along with similar sets constants for $Li_2B_4O_7$ (Shorrocks *et al.*, 1981), $LiNbO_3$ (Kovacs *et al.*, 1990), and CdS (Gualtieri *et al.*, 1994), for which the patterns of matrices $\mathbf{c}$, $\mathbf{e}$, and $\boldsymbol{\epsilon}$ can be found in the IEEE Standard on Piezoelectricity, 1987 or practically in any textbook on piezoelectricity.

3. Matrices for rotated crystal cuts

The above sets of independent constants are used to derive material matrices for an arbitrary oriented crystal cut. According to the IEEE Standard, the most general orientation of a rectangular plate is designated as $(YXlwt)\ \Phi/\Theta/\Psi$, by indicating the initial orientation of plate's thickness (along Y) and length (along X), and the axes (length l, width w, or thickness t) and the corresponding angles (Φ, Θ, Ψ) of the three successive rotations. In this convention, an angle is considered positive if the rotation is clockwise looking from the origine toward the positive end of the axis (Fig. A2.1).

Table A2.1 Measured constants of piezoelectric crystals

Material		Quartz	Lithium Tetraborate	Lithium Niobate	Cadmium Sulfide
Formula		SiO_2	$Li_2B_4O_7$	$LiNbO_3$	CdS
Symmetry		32	$4mm$	$3m$	$6mm$
Density (10^3 kg/m^3)	ρ	2.649	2.451	4.628	4.82
Elastic constants c_{pq}^E (10^9 N/m^2)	c_{11}	86.74	126.7	198.39	90.7
	c_{12}	6.99	0.5	54.72	58.1
	c_{13}	11.91	30.0	65.13	51.0
	c_{14}	−17.91	—	7.88	—
	c_{33}	107.2	53.9	227.90	93.8
	c_{44}	57.94	55.0	59.65	15.04
	c_{66}	39.88	46.0	—	16.3
Piezoelectric constants e_{pq} (C/m^2)	e_{11}	0.171	—	—	—
	e_{14}	−0.041	—	—	—
	e_{15}	—	0.36	3.69	−0.21
	e_{22}	—	—	2.42	—
	e_{31}	—	0.19	0.30	−0.24
	e_{33}	—	0.89	1.77	0.44
Dielectric constants ϵ_{pq}^S (ϵ_0)	ϵ_{11}	4.58	8.97	45.6	9.02
	ϵ_{33}	4.70	8.15	26.3	9.53

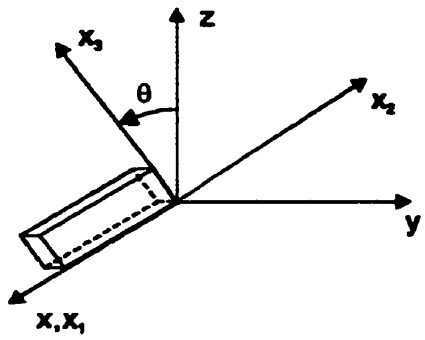

Fig A2.1 Clockwise rotation (YXl) θ of a rectangular plate YX about the x axis.

Most practical crystal cuts are obtained by a single rotation, or more rarely double rotation, of X- and Y-plates, i.e. plates with initial thicknesses along X- or Y-axis respectively. The coordinate transformation corresponding to the single

clockwise rotation through an angle θ about the x axis, as shown in Fig. A2.1, is described by the matrix

$$\mathbf{a} = \begin{bmatrix} 1 & 0 & 0 \\ 0 & \cos\theta & \sin\theta \\ 0 & -\sin\theta & \cos\theta \end{bmatrix}. \tag{3.1}$$

In the rotated coordinate system x_1–x_2–x_3, the components of the elastic, piezoelectric, and dielectric tensors are transformed according to the definition of tensor quantities

$$c'_{ijkl} = a_{im}a_{jn}a_{ko}a_{lp}c_{mnop}, \tag{3.2}$$

$$e'_{ijk} = a_{im}a_{jn}a_{ko}e_{mno}, \tag{3.3}$$

$$\epsilon'_{ij} = a_{im}a_{jn}\epsilon_{mn}. \tag{3.4}$$

However, if the elastic and piezoelectric coefficients are stored in compressed matrix notation, applying coordinate transformations (3.2)–(3.3) would require converting matrices $\mathbf{c}$ and $\mathbf{e}$ to full tensor subscripts, and reconverting the transformed tensors back to the abbreviated notation. The Bond method (Auld, 1990a) overcomes this inconvenience by performing the transformation in the abbreviated notation. It consists in constructing (from components of the transformation matrix $\mathbf{a}$) a 6×6 matrix $\mathbf{M}$ which can be directly applied to a physical variable or a coefficient matrix compressed by means of the rule (1.3). For example, the Bond matrix corresponding to the transformation (3.1) is:

$$\mathbf{M} = \begin{bmatrix} 1 & 0 & 0 & 0 & 0 & 0 \\ 0 & \cos^2\theta & \sin^2\theta & \dfrac{\sin 2\theta}{2} & 0 & 0 \\ 0 & \sin^2\theta & \cos^2\theta & -\dfrac{\sin 2\theta}{2} & 0 & 0 \\ 0 & -\sin 2\theta & \sin 2\theta & \cos 2\theta & 0 & 0 \\ 0 & 0 & 0 & 0 & \cos\theta & -\sin\theta \\ 0 & 0 & 0 & 0 & \sin\theta & \cos\theta \end{bmatrix}. \tag{3.5}$$

Using matrices $\mathbf{a}$ and $\mathbf{M}$, the arrays of material coefficients in the rotated coordinate system are derived from the basic set of matrices $\mathbf{c}$, $\mathbf{e}$, and $\boldsymbol{\epsilon}$ as

$$\mathbf{c}' = \mathbf{M}^{\mathrm{T}}\mathbf{c}\mathbf{M}, \tag{3.6}$$

$$\mathbf{e}' = \mathbf{M}^{\mathrm{T}}\mathbf{e}\mathbf{a}, \tag{3.7}$$

$$\boldsymbol{\epsilon}' = \mathbf{a}^{\mathrm{T}}\boldsymbol{\epsilon}\mathbf{a}. \tag{3.8}$$

The latter equations, with matrices **a** and **M** defined in Eqs. (3.1) and (3.5), were employed to calculate the elastic stiffness, piezoelectric, and dielectric coefficients of the rotated Y-cuts for several piezoelectric material used in numerical examples:

$$SiO_2\ (\theta = +35°15')$$

$$\mathbf{c}' = \begin{bmatrix} 86.74 & -8.25 & 27.15 & -3.66 & 0 & 0 \\ -8.25 & 129.77 & -7.42 & 5.70 & 0 & 0 \\ 27.15 & -7.42 & 102.83 & 9.92 & 0 & 0 \\ -3.66 & 5.70 & 9.92 & 38.61 & 0 & 0 \\ 0 & 0 & 0 & 0 & 68.80 & 2.53 \\ 0 & 0 & 0 & 0 & 2.53 & 29.01 \end{bmatrix} 10^9\ \mathrm{N/m^2} \tag{3.9}$$

$$\mathbf{e}' = \begin{bmatrix} 0.171 & -0.153 & -0.018 & 0.067 & 0 & 0 \\ 0 & 0 & 0 & 0 & 0.108 & -0.095 \\ 0 & 0 & 0 & 0 & 0.076 & 0.067 \end{bmatrix} \mathrm{C/m^2} \tag{3.10}$$

$$\boldsymbol{\epsilon}' = \begin{bmatrix} 4.58 & 0 & 0 \\ 0 & 4.62 & 0.057 \\ 0 & 0.057 & 4.66 \end{bmatrix} \epsilon_0 \tag{3.11}$$

$$Li_2B_4O_7\ (\theta = +51°)$$

$$\mathbf{c}' = \begin{bmatrix} 126.7 & 18.32 & 12.18 & 14.43 & 0 & 0 \\ 18.32 & 106.5 & 6.22 & -22.86 & 0 & 0 \\ 12.18 & 6.22 & 121.7 & -12.75 & 0 & 0 \\ 14.43 & -22.86 & -12.75 & 31.23 & 0 & 0 \\ 0 & 0 & 0 & 0 & 49.57 & 4.40 \\ 0 & 0 & 0 & 0 & 4.40 & 51.44 \end{bmatrix} 10^9\ \mathrm{N/m^2} \tag{3.12}$$

$$\mathbf{e}' = \begin{bmatrix} 0 & 0 & 0 & 0 & 0.227 & 0.280 \\ 0.148 & 0.698 & 0.142 & 0.219 & 0 & 0 \\ 0.120 & 0.112 & 0.568 & 0.274 & 0 & 0 \end{bmatrix} \text{C/m}^2 \tag{3.13}$$

$$\boldsymbol{\epsilon}' = \begin{bmatrix} 8.97 & 0 & 0 \\ 0 & 8.47 & -0.4 \\ 0 & -0.4 & 8.645 \end{bmatrix} \epsilon_0 \tag{3.14}$$

$$\text{LiNbO}_3 \ (\theta = +163°)$$

$$\mathbf{c}' = \begin{bmatrix} 198.39 & 51.20 & 68.65 & 3.62 & 0 & 0 \\ 51.20 & 204.48 & 65.97 & -2.21 & 0 & 0 \\ 68.65 & 65.97 & 220.13 & -12.57 & 0 & 0 \\ 3.62 & -2.21 & -12.57 & 60.49 & 0 & 0 \\ 0 & 0 & 0 & 0 & 65.18 & 10.21 \\ 0 & 0 & 0 & 0 & 10.21 & 67.27 \end{bmatrix} 10^9 \text{ N/m}^2 \tag{3.15}$$

$$\mathbf{e}' = \begin{bmatrix} 0 & 0 & 0 & 0 & -2.82 & 3.39 \\ 2.40 & -0.019 & -1.69 & -3.69 & 0 & 0 \\ 0.42 & -0.45 & -2.24 & -0.70 & 0 & 0 \end{bmatrix} \text{C/m}^2 \tag{3.16}$$

$$\boldsymbol{\epsilon}' = \begin{bmatrix} 45.6 & 0 & 0 \\ 0 & 44.0 & 5.4 \\ 0 & 5.4 & 28.0 \end{bmatrix} \epsilon_0 \tag{3.17}$$

4. Alternate set of material constants

For the finite element formulation adopted in this thesis, the set of matrices $\mathbf{c}$, $\mathbf{e}$, and $\boldsymbol{\epsilon}$, associated with the mechanical strain $\mathbf{S}$ and electric field $\mathbf{E}$, is sufficient to describe the material properties of a piezoelectric. However, in some cases (e.g. one-dimensional models of longitudinal vibrations), it is more convenient to impose the mechanical boundary conditions in terms of stress $\mathbf{T}$, and to use $(\mathbf{T}, \mathbf{E})$ as a pair of independent variables. For linear materials, the corresponding constitutive relations derived from the Gibbs free energy (Eq. (2.17), Chapter 1) are written as follows

$$\begin{cases} \mathbf{S} = \mathbf{s}^E : \mathbf{T} + \mathbf{E} \cdot \mathbf{d}, \\ \mathbf{D} = \mathbf{d} : \mathbf{T} + \mathbf{E} \cdot \boldsymbol{\epsilon}^T, \end{cases} \tag{4.1}$$

where $\mathbf{s}^E$ is the tensor of elastic compliances measured under constant electric field, $\mathbf{d}$ — tensor of piezoelectric coefficients; $\boldsymbol{\epsilon}^T$ is the tensor of dielectric permittivities measured for constant stress $\mathbf{T}$, or 'free' permittivities as compared to the 'clamped' ones $\boldsymbol{\epsilon}^S$. As other material coefficients, tensors $\mathbf{s}^E$ and $\mathbf{d}$ can be recast in compressed notation (1.3) — an operation that would involve, in this case, pre-multiplying the tensor components s^E_{ijkl} and d_{ijk} by some numerical factors (IEEE, 1987). However, by exploiting the relations between different sets of constitutive equations, the elastic compliances, piezoelectric moduli, and free dielectric permittivities can be obtained from $\mathbf{c}^E$, $\mathbf{e}$, and $\boldsymbol{\epsilon}^S$ directly in matrix form:

$$\mathbf{s}^E = \left(\mathbf{c}^E\right)^{-1}, \tag{4.2}$$

$$\mathbf{d} = \mathbf{e}\mathbf{s}^E, \tag{4.3}$$

$$\boldsymbol{\epsilon}^T = \boldsymbol{\epsilon}^S + \mathbf{d}\mathbf{e}^{\mathrm{T}}. \tag{4.4}$$

An example of these matrices is given for the (nonrotated) crystal of CdS (*6mm*):

$$\mathbf{s}^E = \begin{bmatrix} 206.9 & -99.8 & -58.2 & 0 & 0 & 0 \\ -99.8 & 206.9 & -58.2 & 0 & 0 & 0 \\ -58.2 & -58.2 & 170.0 & 0 & 0 & 0 \\ 0 & & 0 & 664.9 & 0 & 0 \\ 0 & 0 & 0 & 0 & 664.9 & 0 \\ 0 & 0 & 0 & 0 & 0 & 613.5 \end{bmatrix} 10^{-13}\ \mathrm{m^2/N} \tag{4.5}$$

$$\mathbf{d} = \begin{bmatrix} 0 & 0 & 0 & 0 & -1.40 & 0 \\ 0 & 0 & 0 & -1.40 & 0 & 0 \\ -0.51 & -0.51 & 1.03 & 0 & 0 & 0 \end{bmatrix} 10^{-11}\ \mathrm{C/N} \tag{4.6}$$

$$\boldsymbol{\epsilon}^T = \begin{bmatrix} 9.31 & 0 & 0 \\ 0 & 9.31 & 0 \\ 0 & 0 & 10.2 \end{bmatrix} \epsilon_0 \tag{4.7}$$

Appendix 3

Calculations on tetrahedral elements

The calculation of element matrices, both in the case of the interior tetrahedron and the exterior bordering element, relies on the properties of simplex elements. Because the latter are well documented (e.g. Silvester and Ferrari, 1996), only the main facts referred to from Chapter 3 are listed here. All properties are given for a tetrahedron; the relations for simplexes of lower orders (line segment and triangle) can be derived as special cases of them.

1. Local coordinates and their properties

A tetrahedron can be regarded as a three-dimensional simplex. A general simplex is defined as the 'the minimal possible nontrivial geometric figure' in N–dimensional space (Silvester and Ferrari, 1996). Other well known simplexes are the line segment ($N = 1$) and triangle ($N = 2$).

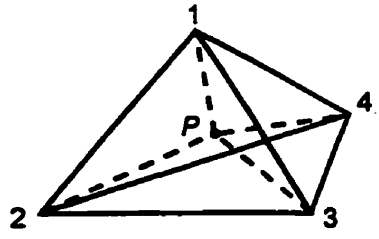

Fig A3.1 Tetrahedral element.

Any interior point $P(x, y, z)$ is uniquely defined in terms of homogeneous or *simplex coordinates*

$$\zeta_m = \frac{V_m}{V}, \qquad m = 1, 2, 3, 4 \tag{1.1}$$

where V is the volume of the main tetrahedron 1-2-3-4, and V_m is the volume of one of the four smaller tetrahedra (subsimplexes). For instance, the volume of the tetrahedron P-2-3-4 is written as

$$V_1 = \frac{1}{3!}\begin{vmatrix} 1 & x & y & z \\ 1 & x_2 & y_2 & z_2 \\ 1 & x_3 & y_3 & z_3 \\ 1 & x_4 & y_4 & z_4 \end{vmatrix}. \tag{1.2}$$

Volumes V_2, V_3, and V_4 are given by similar expressions, where the coordinates x, y, z of point P replace those of vertex 2, 3, 4 respectively. Because point P defines a unique partition of the tetrahedron, i.e. $\sum_{m=1}^{4} V_m = 1$, it follows that

$$\sum_{m=1}^{4} \zeta_m = 1. \tag{1.3}$$

The expansion of volume V_m in (1.1) in terms of Cartesian coordinates x, y, z yields an expression for ζ_m

$$\zeta_m = \frac{1}{3!V}(a_m + b_m x + c_m y + d_m z), \tag{1.4}$$

where numerical coefficients a_m, b_m, c_m, and d_m are the minors of the row $[1 \quad x \quad y \quad z]$ in V_m. An alternative way of obtaining (1.4) is to simultaneously solve for ζ_m, $m = 1, \ldots, 4$, Eq. (1.3) and the system

$$\left.\begin{aligned} x &= x_1\zeta_1 + x_2\zeta_2 + x_3\zeta_3 + x_4\zeta_4, \\ y &= y_1\zeta_1 + y_2\zeta_2 + y_3\zeta_3 + y_4\zeta_4, \\ z &= z_1\zeta_1 + z_2\zeta_2 + z_3\zeta_3 + z_4\zeta_4, \end{aligned}\right\} \tag{1.5}$$

which describes the tetrahedron shape in terms of ζ_m and vertex coordinates x_m, y_m, z_m. It follows from (1.3) that

$$\sum_{m=1}^{4} a_m = 1, \quad \text{and} \quad \sum_{m=1}^{4} b_m = \sum_{m=1}^{4} c_m = \sum_{m=1}^{4} d_m = 0. \tag{1.6}$$

To set up the finite element matrices, the Jacobians $\partial(x,y,z)/\partial(\zeta_1,\zeta_2,\zeta_3)$ and $\partial(\zeta_1,\zeta_2,\zeta_3)/\partial(x,y,z)$ of the coordinate transformations, which map Cartesian coordinates x,y,z into local independent coordinates ζ_1,ζ_2,ζ_3 and vice versa, need be known. Eliminating one of the local variables (e.g. ζ_4) using (1.3), and differentiating (1.5), one obtain for the direct transformation

$$\mathbf{J} = \begin{bmatrix} \frac{\partial x}{\partial \zeta_1} & \frac{\partial y}{\partial \zeta_1} & \frac{\partial z}{\partial \zeta_1} \\ \frac{\partial x}{\partial \zeta_2} & \frac{\partial y}{\partial \zeta_2} & \frac{\partial z}{\partial \zeta_2} \\ \frac{\partial x}{\partial \zeta_3} & \frac{\partial y}{\partial \zeta_3} & \frac{\partial z}{\partial \zeta_3} \end{bmatrix} = \begin{bmatrix} x_1 - x_4 & y_1 - y_4 & z_1 - z_4 \\ x_2 - x_4 & y_2 - y_4 & z_2 - z_4 \\ x_3 - x_4 & y_3 - y_4 & z_3 - z_4 \end{bmatrix}. \tag{1.7}$$

For simplex elements the Jacobian of the inverse transformation is easily derived from (1.4) so that a numerical inversion of (1.7) is not required:

$$\mathbf{J}^{-1} = \begin{bmatrix} \frac{\partial \zeta_1}{\partial x} & \frac{\partial \zeta_2}{\partial x} & \frac{\partial \zeta_3}{\partial x} \\ \frac{\partial \zeta_1}{\partial y} & \frac{\partial \zeta_2}{\partial y} & \frac{\partial \zeta_3}{\partial y} \\ \frac{\partial \zeta_1}{\partial z} & \frac{\partial \zeta_2}{\partial z} & \frac{\partial \zeta_3}{\partial z} \end{bmatrix} = \frac{1}{6V} \begin{bmatrix} b_1 & b_2 & b_3 \\ c_1 & c_2 & c_3 \\ d_1 & d_2 & d_3 \end{bmatrix}. \tag{1.8}$$

2. Lagrangian interpolation functions

The scalar approximating functions associated with the tetrahedron are the Lagrangian interpolation polynomials of order N defined on a set of $M = (N+1)(N+2)(N+3)/3!$ regularly distributed nodes with coordinates $\zeta_1 = i/N$, $\zeta_2 = j/N$, $\zeta_3 = k/N$, and $\zeta_4 = l/N$, where $i,j,k,l = 0,\ldots,N$ and $i+j+k+l = N$. The approximating functions are best expressed as products of auxiliary polynomials $R_i(N,\zeta)$

$$\alpha_{ijkl}(\zeta_1,\zeta_2,\zeta_3,\zeta_4) = R_i(N,\zeta_1)\,R_j(N,\zeta_2)\,R_k(N,\zeta_3)\,R_l(N,\zeta_4), \tag{2.1}$$

each depending on only one local coordinate ζ:

$$\left.\begin{aligned} R_m(N,\zeta) &= \prod_{k=0}^{m}\left(\frac{\zeta-\frac{k}{N}}{\frac{m}{N}-\frac{k}{N}}\right) = \frac{1}{m!}\prod_{k=0}^{m}(N\zeta-k), \\ & \qquad\qquad\qquad\qquad m = 1,\ldots,N \\ R_0(N,\zeta) &= 1 \end{aligned}\right\}. \tag{2.2}$$

Therefore, for any order of N the approximating functions $\alpha_{ijkl}(\zeta_1,\zeta_2,\zeta_3,\zeta_4)$ are practically calculated as follows

$$\begin{array}{l} \text{for } i = N,\ldots,0 \\ \quad\left[\begin{array}{l} \text{for } j = N-i,\ldots,0 \\ \quad\left[\begin{array}{l} \text{for } k = N-i-j,\ldots,0 \\ \quad\left[\begin{array}{l} l = N-i-j-k \\ \zeta_1 = \dfrac{i}{N},\ \zeta_2 = \dfrac{j}{N},\ \zeta_3 = \dfrac{k}{N},\ \zeta_4 = \dfrac{l}{N} \\ m = m+1 \\ \alpha_m = R_i(N,\zeta_1)\,R_j(N,\zeta_2)\,R_k(N,\zeta_3)\,R_l(N,\zeta_4) \end{array}\right. \end{array}\right. \end{array}\right. \end{array} \tag{2.3}$$

The algorithm (2.3) also serves to establish the correspondence between multi- and single-index notations $(i,j,k,l) \rightarrow m = 1,\ldots,M$.

3. Differentiation in local coordinates

Setting up stiffness matrices for tetrahedral elements implies the evaluation of approximating function derivatives with respect to Cartesian coordinates:

$$\nabla\alpha_i = \left[\frac{\partial\alpha_i}{\partial x} \quad \frac{\partial\alpha_i}{\partial y} \quad \frac{\partial\alpha_i}{\partial z}\right]^{\mathrm{T}}. \tag{3.1}$$

Because polynomials α_i themselves are functions of local coordinates, this is accomplished by applying the chain rule of differentiation and taking into account relations (1.4):

$$\nabla\alpha_i = \begin{bmatrix} \sum_{m=1}^{4} \frac{\partial\alpha_i}{\partial\zeta_m}\frac{\partial\zeta_m}{\partial x} \\ \sum_{m=1}^{4} \frac{\partial\alpha_i}{\partial\zeta_m}\frac{\partial\zeta_m}{\partial y} \\ \sum_{m=1}^{4} \frac{\partial\alpha_i}{\partial\zeta_m}\frac{\partial\zeta_m}{\partial z} \end{bmatrix} = \frac{1}{3!V}\sum_{m=1}^{4} \begin{bmatrix} b_m \\ c_m \\ d_m \end{bmatrix} \frac{\partial\alpha_i}{\partial\zeta_m}. \tag{3.2}$$

One of the local variables in Eq. (3.2) can be eliminated using (1.3). Therefore, another way to express the gradients $\nabla\alpha_i$ is by invoking the Jacobian of the inverse transformation given by (1.7):

$$\nabla\alpha_i = \mathbf{J}^{-1}\nabla_{\zeta_1\zeta_2\zeta_3}\alpha_i. \tag{3.3}$$

Taking into account (1.3), the transformation of Eq. (3.3) leads to

$$\begin{aligned} \nabla\alpha_i &= \begin{bmatrix} b_1 & b_2 & b_3 \\ c_1 & c_2 & c_3 \\ d_1 & d_2 & d_3 \end{bmatrix} \begin{bmatrix} \frac{\partial\alpha_i}{\partial\zeta_1} - \frac{\partial\alpha_i}{\partial\zeta_4} \\ \frac{\partial\alpha_i}{\partial\zeta_2} - \frac{\partial\alpha_i}{\partial\zeta_4} \\ \frac{\partial\alpha_i}{\partial\zeta_3} - \frac{\partial\alpha_i}{\partial\zeta_4} \end{bmatrix} \\ &= \frac{1}{3!V}\sum_{m=1}^{3} \begin{bmatrix} b_m \\ c_m \\ d_m \end{bmatrix} \left(\frac{\partial\alpha_i}{\partial\zeta_m} - \frac{\partial\alpha_i}{\partial\zeta_4}\right). \end{aligned} \tag{3.4}$$

For practical reasons, it is convenient to express the partial derivatives $\partial\alpha_i/\partial\zeta_m$ in terms of auxiliary polynomials. Again, this can be done by applying the chain rule of differentiation to the product (2.1), where the derivatives of the auxiliary polynomials are given by

$$\left.\begin{aligned} \frac{\partial R_m(N,\zeta)}{\partial\zeta} &= \frac{N}{m!}\sum_{j=0}^{m-1}\prod_{k=0}^{j-1}(N\zeta - k)\prod_{k=j+1}^{m-1}(N\zeta - k), \\ &\qquad\qquad m = 1, \ldots, N \\ \frac{\partial R_0(N,\zeta)}{\partial\zeta} &= 0. \end{aligned}\right\} \tag{3.5}$$

4. Integration in local coordinates

From the definition of the scalar triple product, the absolute value of the determinant of the Jacobian matrix (1.7) is readily recognized as being the volume of the parallelepiped constructed on the edges 4-1, 4-2, and 4-3 (Fig. A3.1). The parallelepiped can be broken down into six equal tetrahedra of volume V, where V is the volume of tetrahedron 1-2-3-4. Hence, the Jacobian $|\mathbf{J}|$ is equal to $6V$, leading to the following transformation of the element of volume $\mathrm{d}x\mathrm{d}y\mathrm{d}z$:

$$\mathrm{d}x\mathrm{d}y\mathrm{d}z = |\mathbf{J}|\mathrm{d}\zeta_1\mathrm{d}\zeta_2\mathrm{d}\zeta_3 = 6V\mathrm{d}\zeta_1\mathrm{d}\zeta_2\mathrm{d}\zeta_3 \tag{4.1}$$

An arbitrary function f can be integrated in simplex coordinates by premultiplying the integral with respect to $\zeta_1, \zeta_2, \zeta_3$ by the factor $6V$:

$$\int_{V_e} f\,\mathrm{d}x\mathrm{d}y\mathrm{d}z = 6V\int_0^1 \mathrm{d}\zeta_1\int_0^{1-\zeta_1}\mathrm{d}\zeta_2\int_0^{1-\zeta_1-\zeta_2} f\,\mathrm{d}\zeta_3. \tag{4.2}$$

Appendix 4

Tables for element matrices

1. Weighting coefficients for the stiffness matrix

The elements of the weighting coefficient matrix $\mathbf{W}^{(mn)}$, defined in Chapter 3 as

$$\mathbf{W}^{(mn)} = \mathbf{g}^{(m)} \cdot \mathbf{t} \cdot \mathbf{g}^{(n)} = \begin{pmatrix} b_m \\ c_m \\ d_m \end{pmatrix} \cdot \mathbf{t} \cdot \begin{pmatrix} b_n \\ c_n \\ d_n \end{pmatrix}, \tag{1.1}$$

are given her in closed form, suitable for machine implementation. They combine the geometric parameters b_i, c_i, d_i of the tetrahedral element (Appendix 3), and the components of the material tensors $\mathbf{c}^E$, $\mathbf{e}$, $\boldsymbol{\epsilon}^S$, denoted in (1.1) by a generic tensor $\mathbf{t}$. The following expressions for the elastic, piezoelectric, and dielectric weighting coefficients $\mathbf{W}^{(mn)}$ have been obtained by expanding the scalar products in (1.1) for $\mathbf{c}^E$, $\mathbf{e}$, $\boldsymbol{\epsilon}^S$ respectively:

$$W_{ij}^{(mn)} = g_j^{(m)} c_{ikjl}^E g_l^{(n)}, \quad i,j,k,l = 1,2,3, \tag{1.2}$$

$$W_j^{(mn)} = g_i^{(m)} e_{ijk} g_k^{(n)}, \quad i,j,k = 1,2,3, \tag{1.3}$$

$$W^{(mn)} = g_i^{(m)} \epsilon_{ij}^S g_j^{(n)}, \quad i,j = 1,2,3, \tag{1.4}$$

and exploiting the symmetry of tensors $\mathbf{c}^E$, $\mathbf{e}$, $\boldsymbol{\epsilon}^S$, which is reflected in their compressed matrix notation (Appendix 2).

A. Elastic weighting matrix for $\mathbf{K}^{uu}$

$$
\begin{aligned}
W_{11}^{(mn)} &= b_m c_{11} b_n + b_m c_{15} d_n + b_m c_{16} c_n + d_m c_{15} b_n + d_m c_{55} d_n \\
&\quad + d_m c_{56} c_n + c_m c_{16} b_n + c_m c_{56} d_n + c_m c_{66} c_n \\
W_{12}^{(mn)} &= b_m c_{12} c_n + b_m c_{14} d_n + b_m c_{16} b_n + d_m c_{25} c_n + d_m c_{45} d_n \\
&\quad + d_m c_{56} b_n + c_m c_{26} c_n + c_m c_{46} d_n + c_m c_{66} b_n \\
W_{13}^{(mn)} &= b_m c_{13} d_n + b_m c_{14} c_n + b_m c_{15} b_n + d_m c_{35} d_n + d_m c_{45} c_n \\
&\quad + d_m c_{55} b_n + c_m c_{36} d_n + c_m c_{46} c_n + c_m c_{56} b_n \\
W_{21}^{(mn)} &= c_m c_{12} b_n + c_m c_{25} d_n + c_m c_{26} c_n + d_m c_{14} b_n + d_m c_{45} d_n \\
&\quad + d_m c_{46} c_n + b_m c_{16} b_n + b_m c_{56} d_n + b_m c_{66} c_n \\
W_{22}^{(mn)} &= c_m c_{22} c_n + c_m c_{24} d_n + c_m c_{26} b_n + d_m c_{24} c_n + d_m c_{44} d_n \\
&\quad + d_m c_{46} b_n + b_m c_{26} c_n + b_m c_{46} d_n + d_m c_{66} d_n \\
W_{23}^{(mn)} &= c_m c_{23} d_n + c_m c_{24} c_n + c_m c_{25} b_n + d_m c_{34} d_n + d_m c_{44} c_n \\
&\quad + d_m c_{45} b_n + b_m c_{36} d_n + b_m c_{46} c_n + b_m c_{56} b_n \\
W_{31}^{(mn)} &= d_m c_{13} b_n + d_m c_{35} d_n + d_m c_{36} c_n + c_m c_{14} b_n + c_m c_{45} d_n \\
&\quad + c_m c_{46} c_n + b_m c_{15} b_n + b_m c_{55} d_n + b_m c_{56} c_n \\
W_{32}^{(mn)} &= d_m c_{23} c_n + d_m c_{34} d_n + d_m c_{36} b_n + c_m c_{24} c_n + c_m c_{44} d_n \\
&\quad + c_m c_{46} b_n + b_m c_{25} c_n + b_m c_{45} d_n + b_m c_{56} b_n \\
W_{33}^{(mn)} &= d_m c_{33} d_n + d_m c_{34} c_n + d_m c_{35} b_n + c_m c_{34} d_n + c_m c_{44} c_n \\
&\quad + c_m c_{45} b_n + b_m c_{35} d_n + b_m c_{45} c_n + b_m c_{55} b_n
\end{aligned}
\tag{1.5}
$$

B. Piezoelectric weighting vector for $\mathbf{K}^{u\varphi}$

$$
\begin{aligned}
W_1^{(mn)} &= b_m e_{11} b_n + b_m e_{21} c_n + b_m e_{31} d_n + d_m e_{15} b_n + d_m e_{25} c_n \\
&\quad + d_m e_{35} d_n + c_m e_{16} b_n + c_m e_{26} c_n + c_m e_{36} d_n \\
W_2^{(mn)} &= c_m e_{12} b_n + c_m e_{22} c_n + c_m e_{32} d_n + d_m e_{14} b_n + d_m e_{24} c_n \\
&\quad + d_m e_{34} d_n + b_m e_{16} b_n + b_m e_{26} c_n + b_m e_{36} d_n
\end{aligned}
$$

$$W_3^{(mn)} = d_m e_{13} b_n + d_m e_{23} c_n + d_m e_{33} d_n + c_m e_{14} b_n + c_m e_{24} c_n + c_m e_{34} d_n + b_m e_{15} b_n + b_m e_{25} c_n + b_m e_{35} d_n \quad (1.6)$$

C. Dielectric weighting constant for $\mathbf{K}^{\varphi\varphi}$

$$W^{(mn)} = b_m \epsilon_{11} b_n + b_m \epsilon_{12} c_n + b_m \epsilon_{13} d_n + c_m \epsilon_{12} b_n + c_m \epsilon_{22} c_n + c_m \epsilon_{23} d_n + d_m \epsilon_{13} b_n + d_m \epsilon_{23} c_n + d_m \epsilon_{33} d_n \quad (1.7)$$

Note that in the present analysis the abbreviated, also referred to as compressed or engineering, notation comes into play only through matrices of material coefficients $\mathbf{c}$, $\mathbf{e}$ and $\boldsymbol{\epsilon}$ when expanding (1.2)–(1.4). If the whole finite element formulation is carried out in this notation, as it is customary the case (Zienkiewicz, 1989), an alternative way of arriving at (1.5)–(1.7) is to symbolically evaluate the following matrix products:

$$\mathbf{W}_{uu}^{(mn)} = \mathbf{B}_u^{(m)\mathrm{T}} \mathbf{c} \mathbf{B}_u^{(n)}, \quad (1.8)$$

$$\mathbf{W}_{u\varphi}^{(mn)} = \mathbf{B}_\varphi^{(m)\mathrm{T}} \mathbf{e}^{\mathrm{T}} \mathbf{B}_u^{(n)}, \quad (1.9)$$

$$W_{\varphi\varphi}^{(mn)} = \mathbf{B}_\varphi^{(m)\mathrm{T}} \boldsymbol{\epsilon} \mathbf{B}_\varphi^{(n)}. \quad (1.10)$$

Matrices

$$\mathbf{B}_u^{(m)} = \begin{bmatrix} b_m & 0 & 0 \\ 0 & c_m & 0 \\ 0 & 0 & d_m \\ 0 & d_m & c_m \\ d_m & 0 & b_m \\ c_m & b_m & 0 \end{bmatrix}, \quad \mathbf{B}_\varphi^{(n)} = \begin{bmatrix} b_m \\ c_m \\ d_m \end{bmatrix}, \quad (1.11)$$

arise from the finite element approximation of mechanical strain S and electric field E, when the former is recast into a one-dimensional array of six elements by applying the index abbreviation rules employed in applied mechanics.

2. Universal matrices for piezoelectric tetrahedra

The integrals (3.14) and (3.15) of Chapter 3, that define the numerical matrices $\mathfrak{C}$ and $\mathfrak{T}$, have been evaluated by means of the symbolic algebra package *MAPLE*. The calculation has been carried out for tetrahedra up to the fourth order. The entries of universal matrices represent rational numbers, and, therefore, can be stored in an integer format after a common denominator has been established. This is illustrated below on the example of matrices $\mathfrak{T}$ and $\mathfrak{C}^{(12)}$ for tetrahedra of second order.

$$\mathfrak{T} = \frac{1}{2520}\begin{bmatrix} 6 & -4 & -4 & -4 & 1 & -6 & -6 & 1 & -6 & 1 \\ -4 & 32 & 16 & 16 & -4 & 16 & 16 & -6 & 8 & -6 \\ -4 & 16 & 32 & 16 & -6 & 16 & 8 & -4 & 16 & -6 \\ -4 & 16 & 16 & 32 & -6 & 8 & 16 & -6 & 16 & -4 \\ 1 & -4 & -6 & -6 & 6 & -4 & -4 & 1 & -6 & 1 \\ -6 & 16 & 16 & 8 & -4 & 32 & 16 & -4 & 16 & -6 \\ -6 & 16 & 8 & 16 & -4 & 16 & 32 & -6 & 16 & -4 \\ 1 & -6 & -4 & -6 & 1 & -4 & -6 & 6 & -4 & 1 \\ -6 & 8 & 16 & 16 & -6 & 16 & 16 & -4 & 32 & -4 \\ 1 & -6 & -6 & -4 & 1 & -6 & -4 & 1 & -4 & 6 \end{bmatrix} \tag{2.1}$$

$$\mathfrak{C}^{(12)} = -\frac{1}{30}\begin{bmatrix} 3 & -4 & -1 & -1 & 1 & 1 & 1 & 0 & 0 & 0 \\ -1 & 4 & 4 & 4 & -3 & -4 & -4 & 0 & 0 & 0 \\ -1 & 0 & 8 & 4 & 1 & -8 & -4 & 0 & 0 & 0 \\ -1 & 0 & 4 & 8 & 1 & -4 & -8 & 0 & 0 & 0 \\ 0 & 0 & 0 & 0 & 0 & 0 & 0 & 0 & 0 & 0 \\ 0 & 0 & 0 & 0 & 0 & 0 & 0 & 0 & 0 & 0 \\ 0 & 0 & 0 & 0 & 0 & 0 & 0 & 0 & 0 & 0 \\ 0 & 0 & 0 & 0 & 0 & 0 & 0 & 0 & 0 & 0 \\ 0 & 0 & 0 & 0 & 0 & 0 & 0 & 0 & 0 & 0 \\ 0 & 0 & 0 & 0 & 0 & 0 & 0 & 0 & 0 & 0 \end{bmatrix} \tag{2.2}$$

The metric matrix $\mathfrak{T}$ is identical to matrix **T** tabulated by Silvester (1972) along with another well-known fundamental symmetric matrix **Q**, defined as

$$\mathbf{Q}_{ij}^{(mn)} = -6\int \left(\frac{\partial \alpha_i}{\partial \zeta_m} - \frac{\partial \alpha_i}{\partial \zeta_n}\right)\left(\frac{\partial \alpha_j}{\partial \zeta_m} - \frac{\partial \alpha_j}{\partial \zeta_n}\right) d\zeta_1 d\zeta_2 d\zeta_3.^{1} \tag{2.3}$$

Both $\mathfrak{T}$ and $\mathbf{Q}$ have been employed to discretize the scalar Helmholtz equation in isotropic media. The relationship between the present matrix $\mathfrak{C}$ and $\mathbf{Q}$ is the following:

$$\mathbf{Q}^{(mn)} = 6\left(\mathfrak{C}^{(mn)} + \mathfrak{C}^{(nm)}\right), \quad m \neq n. \tag{2.4}$$

In principle, matrices $\mathbf{Q}^{(mn)}$ could have been used to assemble the dielectric element stiffness matrix $\mathbf{K}^{\varphi\varphi}$, for the symmetry of the associated scalar weighting coefficient $W_{\varphi\varphi}^{(mn)} = W_{\varphi\varphi}^{(nm)}$ allows the pair of matrices $\mathfrak{C}^{(mn)}$ and $\mathfrak{C}^{(nm)}$ to be combined as in (2.4). Unfortunately, the arrays of mechanical and piezoelectric weighting factors $\mathbf{W}_{uu}^{(mn)}$ and $\mathbf{W}_{u\varphi}^{(mn)}$ do not enjoy the same property; therefore, both $\mathfrak{C}^{(mn)}$ and $\mathfrak{C}^{(nm)}$ are required to build $\mathbf{K}^{uu}$ and $\mathbf{K}^{u\varphi}$. Although the use of $\mathbf{Q}$-matrices would have sped up the computation of $\mathbf{K}^{\varphi\varphi}$, from the memory saving considerations and for the sake of consistency, only one type of universal matrices — $\mathfrak{C}$ — has been retained in the present finite element analysis.

3. Permutation arrays for rotations about tetrahedral ζ_1- and ζ_2-axes

The permutation matrices $\mathbf{R}_1$ and $\mathbf{R}_2$ defined in Section 3 of Chapter 3 have been derived up to the fourth order for the specific tetrahedron node labeling used in the present work. The permutation operations have been performed on the multi-index numbering of interpolation nodes by exchanging the last three subscripts (rotation). When remapped back using the single-index notation (Eq. (2.3), Appendix 3), the relabeled node indexes are stored in the form of one-dimensional arrays R_1 and R_2 as shown in Fig. A4.1 for the tetrahedron of second order. Note that array R_1 is the subset of the array ITET2 tabulated by Silvester (1982b).

---

[1] In the 1972 paper by Silvester the factor 6 was missing, which was corrected subsequently in Silvester and Ferrari (1990).

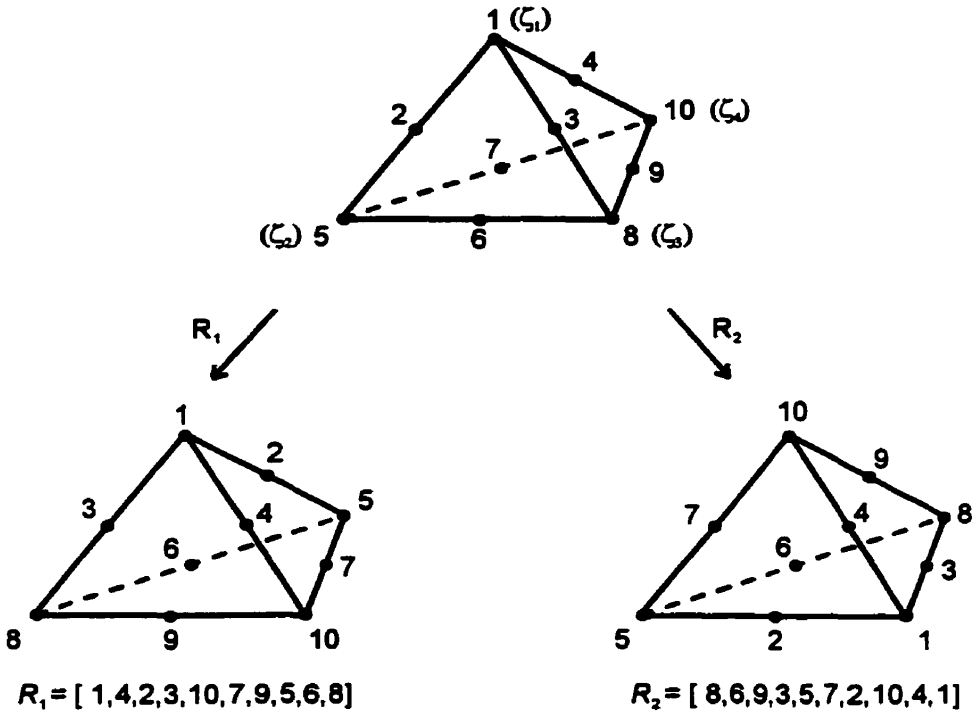

Fig A4.1 Vertices relabeling in a second-order tetrahedron after right-handed rotations about ζ_1- and ζ_2-axes.

4. Gaussian integration on line segment and triangle

Notation:

I_s – number of integration points over a line segment;

I_t – number of integration points over a triangle;

p – highest order of polynomial which is exactly integrated;

n – multiplicity of an integration point.

Table A4.1 Gaussian quadrature points for a line segment

I_s	p	Weight w_i^s	Coordinates $\pm x_i$	n
3	5	0.888888889	0.000000000	1
		0.555555556	0.774596669	2
4	7	0.652145155	0.339981044	2
		0.347854845	0.861136312	2
5	9	0.568888889	0.000000000	1
		0.478628670	0.906179846	2
		0.236926885	0.538469310	2

Table A4.2 Gaussian integration points for a triangle (Dunavant, 1985)

I_t	p	Weight w_i^t	Coordinates α_i	β_i	γ_i	n
6	4	0.223381590	0.108103018	0.445948491	0.445948491	3
		0.109951744	0.816847573	0.091576214	0.091576214	3
12	6	0.116786276	0.501426510	0.249286745	0.249286745	3
		0.050844906	0.873821971	0.063089014	0.063089014	3
		0.082851076	0.053145050	0.310352451	0.636502499	6
16	8	0.144315608	0.333333333	0.333333333	0.333333333	1
		0.095091634	0.081414823	0.459292588	0.459292588	3
		0.103217371	0.658861385	0.170569308	0.170569308	3
		0.032458498	0.898905543	0.050547228	0.050547228	3
		0.027230314	0.008394777	0.263112830	0.728492393	6
25	10	0.090817990	0.333333333	0.333333333	0.333333333	1
		0.036725958	0.028844733	0.485577633	0.485577633	3
		0.045321059	0.781036849	0.109481575	0.109481575	3
		0.072757917	0.141707219	0.307939839	0.550352942	6
		0.028327243	0.025003535	0.246672561	0.728323905	6
		0.009421667	0.009540815	0.066803251	0.923655934	6

Bibliography

1. Ajiz, M.A. and Jennings, A. (1984), 'A robust incomplete Cholesky-conjugate gradient algorithm,' *International Journal for Numerical Methods in Engineering*, **20**, pp. 949–66.
2. Allik, H. and Hughes, T.J.R. (1970), 'Finite element method for piezoelectric vibration,' *International Journal for Numerical Methods in Engineering*, **2**, pp. 151–57.
3. Allik, H., Webman, K.M., and Hunt, J.T. (1974), 'Vibrational response of sonar transducers using piezoelectric finite elements,' *Journal of Acoustical Society of America*, **56**, pp. 1782–91.
4. Antonova, E.E. and Silvester, P.P. (1997), 'Finite Elements for Piezoelectric Vibrations with Open Electric Boundaries,' *IEEE Transactions on Ultrasonics, Ferroelectrics, and Frequency Control*, **UFFC-44**, pp. 548–57.
5. Auld, B.A. (1981), 'Wave propagation and resonance in piezoelectric materials,' *Journal of the Acoustical Society of America*, **70**, pp. 1577–85.
6. Auld, B. A. (1990a), *Acoustic Fields and Waves in Solids*. 2nd. edn. Vol. 1. New York: John Wiley & Sons. x + 435 pp.
7. Auld, B. A. (1990b), *Acoustic Fields and Waves in Solids*. 2nd. edn. Vol. 2. New York: Jonh Wiley & Sons. x + 421 pp.
8. Baranski, K.N. (1991), *Fizicheskaya akustika kristallov*. Moskva: Izdatelstvo Moskovskogo Gosudarstvennogo Universiteta. 143 pp. In Russian.
9. Bathe, K.J. and Wilson, E.L. (1973), 'Solution method for eigenvalue problems in structural mechanics,' *International Journal for Numerical Methods in Engineering*, **6**, pp. 213–26.
10. Bechmann, R., Ballato, A. and Lukaszek, T.J. (1962), 'Higher Order Temperature Coefficients of the Elastic Stiffnesses and Compliances of Alpha-Quartz,' *Proceedings IRE*, **50**, pp. 1812–22.

11. Boucher, D., Lagier M., and Maerfeld, C. (1981), 'Computation of the Vibrational Modes for Piezoelectric Array Transducers using a Mixed Finite Element–Perturbation Method,' *IEEE Transactions on Sonics and Ultrasonics*, **SU-28**, pp. 318–30.
12. Campbell, C.F. and Weber, R.J. (1992), 'Two dimensional finite difference method for the analysis of piezoelectric devices,' *Proceedings of the 1992 Ultrasonics Symposium*, pp. 477–81.
13. Challand, P. (1990), 'Optimizing Ultrasonic Transducers Based on Piezoelectric Composites Using a Finite-Element Method,' *IEEE Transactions on Ultrasonics, Ferroelectrics, and Frequency Control*, **UFFC-37**, pp. 135-40.
14. Chen, T. and Lin, F.Z. (1995), 'Boundary integral formulations for three-dimensional anisotropic piezoelectric solids,' *Computational Mechanics*, **15**, pp. 485-96.
15. Chou, P.C. and Pagano, N.J. (1967), *Elasticity — tensor, dyadic, and engineering approaches*. Princeton, N.J.: Van Nostrand, xiv + 290 pp.
16. Cowdrey, D.R. and Willis, J.R. (1974), 'Application of the finite element method to the vibrations of quartz plates,' *Journal of the Acoustical Society of America*, **56**, pp. 94–8.
17. Dasgupta, G. (1984), 'Computation of exterior potential fields by infinite substructuring,' *Computer Methods in Applied Mechanics and Engineering*, **46**, pp. 295–305.
18. Decarpigny, J.N., Debus, J.C., Tocquet, B. and Boucher, D. (1985), 'In-air analysis of piezoelectric Tonpilz transdusers in a wide frequency band using a mixed finite element-plane wave method,' *Journal of Acoustical Society of America*, **56**, pp. 1499–1507.
19. Decarpigny, J.N., Hamonic, B.F. and Debus, J.C. (1991), 'Computation of the equivalent modal impedance matrix of a multiple degree of freedom electroelastic structure using antiresonance modes,' *Journal of Acoustical Society of America*, **90**, pp. 2891–94.
20. Détaint, J. and Lançon, R. (1976) 'Temperature characteristics of high frequency lithium tantalate plates,' *Proceedings of the 30th Annual Symposium on Frequency Control*, pp. 132–40.
21. Détaint, J. and Lefèvre, R. (1987) 'Les dispositifs piézoélectriques à ondes de volume,' *L' Écho des Recherches*, **128**, pp. 21–38.
22. Dieulesaint, E. and Royer D. (1974), *Ondes élastiques dans les solides: application au traitement du signal*. Paris: Edition Masson. xvi + 407 pp. In French.
23. Dunavant, D.A. (1985), 'High degree efficient symmetrical Gaussian quadrature rules for the triangle,' *International Journal for Numerical Methods in Engineering*, **21**, pp. 1129–48.
24. Eer Nisse, E.P. (1967), 'Variational Methods for Electroelastic Vibration Analysis,' *IEEE Transactions on Sonics and Ultrasonics*, **SU-14**, pp. 153–60.

25. Emson, C.R.I. (1988), 'Methods for the solution of open-boundary electromagnetic-field problems,' *IEE Proceedings-A*, **135**, pp. 151–58.
26. Ericsson, T. and Ruhe, A. (1980), 'The Spectral Transformation Lanczos Method for the Numerical Solution of Large Sparse Generalized Symmetric Eigenvalue Problems,' *Mathematics of Computation*, **34**, pp. 1251–68.
27. Farnell, G.W. (1970), 'Properties of Elastic Surface Waves, ' In *Physical Acoustics: principles and methods* (W.P. Mason and R.N. Thurston, eds). Vol. 6, Chap. 3. New York: Academic Press.
28. Freeman, E.M. and Lowther, D.A. (1989), 'An open boundary technique for axisymmetric and three dimensional magnetic and electric field problems,' *IEEE Transactions on Magnetics*, **MAG-25**, pp. 4135–37.
29. Fried, I. (1970), 'A gradient computational procedure for the solution of large problems arising from the finite element discretization method,' *International Journal for Numerical Methods in Engineering*, **2**, pp. 477–94.
30. Fried, I. (1972), 'Bounds on the extremal eigenvalues of the finite element stiffness and mass matrices and their spectral condition number,' *Journal of Sound and Vibration*, **22**, pp. 407–18.
31. Fried, I. (1973), 'Bounds on the spectral and maximum norms of the finite element stiffness, flexibility and mass matrices,' *International Journal of Solids and Structures*, **9**, pp. 1013–34.
32. Fujiwara, Y., Ono, M., Sakai, M., and Wakatsuki, N. (1985), 'Strip type resonators of lithium tetraborate,'*Proceedings of the 39th Annual Symposium on Frequency Control*, pp. 351-55.
33. Fujiwara, Y. and Wakatsuki, N. (1987), '$LiTaO_3$ and $LiNbO_3$ Strip-Type Resonators,' *IEEE Transactions on Sonics and Ultrasonics*, **SU-34**, pp. 39–44.
34. Gantmacher, F.R. (1988), *Teoriya matrits*. Moskva: Nauka. 548 pp. In Russian.
35. Golub, G.H. and Van Loan, C.F. (1989), *Matrix Computations*. 2nd edn. Baltimore: The Johns Hopkins University Press. xix + 642 pp.
36. Gould, S.H. (1957), *Variational methods for eigenvalue problems: an introduction to the methods of Rayleigh, Ritz, Weinstein, and Aronszajn*. Toronto: University of Toronto Press. xii + 179 pp.
37. Greenbaum, A. and Rodrigue, G.H. (1989), 'Optimal preconditioners of a given sparsity pattern,' *BIT*, **29**, pp. 610–634.

38. Grimes, R. G., Lewis, J.G. and Simon, H.D. (1994), 'A shifted block Lanczos algorithm for solving sparse symmetric generalized eigenproblems,' *SIAM Journal on matrix analysis and applications.*, **15**, pp. 228–272.
39. Gualtieri, J.G., Kosinski, J.A., and Ballato, A. (1994), 'Piezoelectric Materials for Acoustic Wave Applications,' *IEEE Transactions on Ultrasonics, Ferroelectrics, and Frequency Control*, **UFFC-41**, pp. 53–8.
40. Guo, N., Cawley, P., and Hitchings, D. (1992), ' The finite element analysis of the vibration characteristics of piezoelectric discs,' *Journal of Sound and Vibration*, **159**, pp. 115–38.
41. Hammer, P.C., Marlowe O.J., and Stroud, A.H. (1956), 'Numerical Integration over Simplexes and Cones,' *Mathematics Tables Aids Comp.*, **10**, pp. 130-37.
42. Hermann, J. (1975) 'Determination of the electromechanical coupling factor of quartz bars vibrating in flexure or length-extension,' *Proceedings of the 29th Annual Symposium on Frequency Control*, pp. 26–34.
43. Hildebrand, F.B. (1965), *Methods of applied mathematics*. 2nd edn. Englewood Cliffs, N.J.: Prentice-Hall, Inc. ix+362 pp.
44. Holland, R. and Eer Nisse, E.P. (1969), *Design of resonant piezoelectric devices*. Cambridge: M.I.T. Press. x + 258 pp.
45. Hossack, J.A. and Hayward, G. (1991), 'Finite Element Analysis of 1-3 Composite Transducers,' *IEEE Transactions on Ultrasonics, Ferroelectrics, and Frequency Control*, **UFFC-38**, pp. 618-29.
46. Huang, D. and Boucher, S. G. (1991), 'New 1-3 type piezoelectric composite material for kilohertz frequency range transducers,' *Proceedings of the 1994 Ultrasonics Symposium*, **UFFC-38**, pp. 973-78.
47. Hurwitz, H., Jr. (1984), 'Infinitesimal scaling — a new procedure for modeling exterior field problems,' *IEEE Transactions on Magnetics*, **MAG-20**, pp. 1918–23.
48. *IEEE Standard on Piezoelectricity* (1987). New York: Institute of Electrical and Electronics Engineers, Inc.
49. Ikeda, T. (1996), *Fundamentals of Piezoelectricity*. 2nd edn. Oxford: Oxford University Press. xi + 263 pp.
50. Ikeda, T. and Inawashiro, S. (1978) 'Depolarizing-Field Effect in a Piezoelctric Rod under the Longitudinal-Effect Extensional Vibration, ' *Journal of the Acoustical Society of Japan*, **34**, pp. 223–33.
51. Ingebrigtsen, K.A. (1969), 'Surface waves in piezoelectrics,' *Journal of Applied Physics*, **40**, pp. 2681–86.

52. Jawson, M.A. and Symm, G.T. (1977), *Integral equations methods in potential theory and elastostatics*. New York: Academic Press. xiv + 287 pp.
53. Jones, M.T. and Patrick, M.L. (1993), 'The Lanczos algorithm for the generalized symmetric eigenproblem on shared-memory architectures,' *Applied Numerical Mathematics*, **12**, pp. 377–89.
54. Johnson, M. P. (1990), 'Equivalent modal impedance matrix of multiple degree of freedom electroelastic structures,' *Journal of the Acoustical Society of America*, **88**, pp. 1–6.
55. Kagawa, Y. and Gladwell, G. M. L. (1970), 'Finite Element Analysis of Flexure-Type Vibrators With Electrostrictive Transducers,' *IEEE Transactions on Sonics and Ultrasonics*, **SU-17**, pp. 41–49.
56. Kagawa, Y. (1971), 'A New Approach to Analysis and Design of Electromechanical,' *Journal of the Acoustical Society of America*, **49**, pp. 1348–56.
57. Kagawa, Y. and Yamabuchi, T. (1974), 'Finite Element Simulation of Two-Dimensional Electromechanical Resonators,' *IEEE Transactions on Sonics and Ultrasonics*, **SU-21**, pp. 275–83.
58. Kagawa, Y., Arai, H., Yakuwa K., and Shirai, K. (1975), 'Finite element simulation of energy-trapped electromechanical resonators,' *Journal of Sound and Vibration*, **39**, pp. 317–35.
59. Kagawa, Y. and Yamabuchi, T. (1976), 'Finite Element Approach for a Piezoelectric Circular Rod,' *IEEE Transactions on Sonics and Ultrasonics*, **SU-23**, pp. 379–85.
60. Kagawa, Y., Maeda, H. and Nakazawa, M. (1981), 'Finite Element Approach to Frequency-Temperature Characteristic Prediction of Rotated Quartz Crystal Plate Resonators,' *IEEE Transactions on Sonics and Ultrasonics*, **SU-28**, pp. 257–64.
61. Kagawa, Y., Tsuchiya, T., and Kawashima, T. (1996), 'Finite Element Simulation of Piezoelectric Vibrator Gyroscopes,' *IEEE Transactions on Ultrasonics, Ferroelectrics, and Frequency Control*, **UFFC-43**, pp. 509–18.
62. Kantor, V.M. (1977), *Monolitniye piezoelectricheskie filtry*. Moskva: Sviaz. 152 pp. In Russian.
63. Konrad and Tsukerman, I.A. (1995) 'Application of Integral and Differential Methods to Electromagnetic Field Problems,' In *Finite Elements, Electromagnetics and Design* (S.R.H. Hoole ed.) , Amsterdam: Elsevier Science B.V., xviii + 650 pp.
64. Kostek, S. and Randall, C.J. (1994), 'Modeling of a piezoelectric transducer and its application to full waveform acoustic logging,' *Journal of the Acoustical Society of America*, **95**, pp. 109–22.

65. Kovacs, G., Anhorn, M., Engan, H.E., Visintini, G. and Ruppel, C.C.W. (1990), 'Improved Material Constants for $LiNbO_3$ and $LiTaO_3$,' *Proceedings of the 1990 Ultrasonics Symposium*, pp. 435–38.

66. Landau, L.D. and Lifshitz, E.M. (1987), *Teoreticheskaya fizika*. Vol. VII: *Teoriya uprugosti*. 4th edn. Moskva: Nauka. 246 pp. In Russian.

67. Landau, L.D. and Lifshitz, E.M. (1992), *Teoreticheskaya fizika*. Vol. VIII: *Elektrodinamika sploshnyzh sred*. 3rd edn. Moskva: Nauka. 661 pp. In Russian.

68. Lean, M.H., Friedman, M. and Wexler, A. (1980), 'Application of the boundary element method in electrical engineering problems, ' In *Finite Elements in Electric and Magnetic Field Problems* (M.V.K. Chari and P.P. Silvester, eds). , Chap. 9. Chichester: John Wiley. xii + 219 pp.

69. Lee, J.F. and Cendes, Z.J. (1987), 'Transfinite elements: A highly efficient procedure for modeling open field problems,' *Journal of Applied Physics*, **61**, pp. 3913–15.

70. Lee, P.C.Y., Zee C., and Brebbia, C.A. (1982), 'Thickness shear, thickness twist, and flexural vibrations of rectangular AT-cut quartz plates with patch electrodes,' *Journal of Acoustical Society of America*, **72**, pp. 1855–62.

71. Lee, P.C.Y. and Tang, M.S.H. (1987), 'Acceleration effect on the thickness vibrations of doubly rotated crystal resonators,' *Proceedings of the 41st Annual Frequency Control Symposium*, pp. 277–81.

72. Lee, P.C.Y. (1988), 'Electromagnetic radiation from an AT-cut quartz plate under lateral-field excitation,' *Proceedings of the 1988 Ultrasonics Symposium*, pp. 407–411.

73. Lee, P.C.Y. (1990), 'A variational principle for the equations of piezoelectromagnetism in elastic dielectric crystals,' *Proceedings of the 1990 Ultrasonics Symposium*, pp. 565–68.

74. Lee, P.C.Y. and Guo, X.(1991), 'Acceleration Sensitivity of Crystal Resonators Affected by the Mass and Location of Electrodes,' *IEEE Transactions on Ultrasonics, Ferroelectrics, and Frequency Control*, **UFFC-38**, pp. 358–65.

75. Lerch, R. (1990), 'Simulation of Piezoelectric Devices by Two- and Three-Dimensional Finite Elements,' *IEEE Transactions on Ultrasonics, Ferroelectrics, and Frequency Control*, **UFFC-37**, pp. 233–47.

76. Lerch, R. (1992), 'CAE tools for piezoelectric sensors,' *International Journal of Computer Applications in Technology*, **5**, pp. 191–7.

77. Lewis, J.A. (1961), 'The Effect of Driving Electrode Shape on the Electrical Properties of Piezoelectric Crystals,' *Bell System Technical Journal*, **40**, pp. 1259–80.

78. Lloyd, P. and Redwood, M. (1965), 'Finite-Difference Method for the Investigation of the Vibrations of Solids and the Evaluation of the Equivalent-Circuit Characteristics of Piezoelectric Resonators. I,II,' *Journal of the Acoustical Society of America*, **39**, pp. 346–61.
79. Lloyd, P. (1967), 'Equations Governing the Electrical Behavior of an Arbitrary Piezoelectric Resonator Having *N* Electrodes,' *Bell System Technical Journal*, **46**, pp. 1881–1900.
80. Lobitz, D. W., Mnick, F.L., and Reese, G.M. (1990), 'Finite element analysis of a quartz rotation sensor,' *AIAA*, pp. 1941–44.
81. Love, A.E.H. (1927), *A treatrise on the mathematical theory of elasticity*. 4th edn. New York: Dover Publications, Inc. xviii + 643 pp.
82. Manteuffel, T.A. (1980), 'An Incomplete Factorization Technique for Positive Definite Linear Systems,' *Mathematics of computation*, **34**, pp. 473–97.
83. Marcus, M. and Minc, H. (1964), *A survey of matrix theory and matrix inequalities*. Boston: Prindle, Weber & Schmidt, Inc. xii + 180 pp.
84. Milsom, R.F., Elliott, D.T., Terry-Wood, S., and Redwood, M. (1983), 'Analysis and Design of Coupled-Mode Miniature Bar Resonators and Monolithic Filters,' *IEEE Transactions on Sonics and Ultrasonics*, **SU-30**, pp. 140–55.
85. McDearmon, G.F. (1984), 'The addition of piezoelectric properties to structural finite element programs by matrix manipulations,' *Journal of Acoustical Society of America*, **76**, pp. 666–69.
86. McDonald, B.H. and Wexler, A. (1972), 'Finite-Element Solution of Unbounded Field Problems,' *IEEE Transactions on Microwave Theory and Techniques*, **MTT-20**, pp. 841–47.
87. Mindlin, R.D. (1973) 'Electromagnetic radiation from a vibrating quartz plate,' *International Journal of Solids and Structures*, **9**, pp. 697–702.
88. Mindlin, R.D. (1982) 'Third overtone quartz resonator,' *International Journal of Solids and Structures*, **18**, pp. 809–817.
89. Mindlin, R.D. and Spencer, D.C. (1967) 'Anharmonic, Thickness-Twist Overtones of Thickness-Shear and Flexural Vibrations of Rectangular, AT-Cut Quartz Plates,' *Journal of the Acoustical Society of America*, **42**, pp. 1268–77.
90. Meeker, T.R., Shreve, W.R., and Cross, P.S. (1985) 'Theory and Properties of Piezoelectric Resonators and Waves,' In *Precision Frequency Control* (Ballato, A. and Gerber E.A. eds.), Vol. 1, Orlando: Academic Press, Inc. xxii + 434 pp.
91. Mochizuki, Y. (1978), 'A new method to analyse vibrations of resonators by the combination of plate equations and finite element method,' *Proceedings of the 1978 Ultrasonics Symposium*, pp. 120–33.

92. Moetakef, M.A., Lawrence, K.L., Joshi, S. P., and Shiakolas, P.S. (1995), 'Closed-Form Expressions for Higher Order Electroelastic Tetrahedral Elements,' *AIAA Journal*, **33**, pp. 136–42.

93. Morgan, R.P. (1985), *Surface-Wave Devices for Signal Processing*. New York: Elsevier.

94. Nadeau, G. (1964), *Introduction to Elasticity*. New York: Holt, Rinehart and Winston, Inc. xii + 285 pp.

95. Naillon, M., Coursant, R.H., and Besnier, F. (1983), 'Analysis of piezoelectric structures by a finite element method,' *Acta Electronica*, **25**, pp. 341–62.

96. Nour-Omid, B., Parlett, B.N., and Taylor, R.L. (1983), 'Lanczos versus subspace iteration for solution of eigenvalue problems,' *International Journal for Numerical Methods in Engineering*, **19**, pp. 859–71.

97. Nour-Omid, B. and Clough, R. (1985), 'Block Lanczos method for dynamic analysis of structures,' *Earthquake Engineering and Structural Dynamics*, **13**, pp. 271–75.

98. Nour-Omid, B., Parlett, B.N., Ericsson, T. and Jensen, P.S. (1987), 'How to Implement the Spectral Transformation,' *Mathematics of Computation*, **48**, pp. 663–73.

99. Ogawa, T. (1969) 'Effect of Depolarization Field on Electromechanical Properties of Piezoelectric Semiconductors (Theory), ' *Japanese Journal of Applied Physics*, **8**, pp. 227–35.

100. Onoe, M. and Jumonji, H. (1965) 'Analysis of piezoelectric resonators vibrating in trapped-energy modes, ' *Electronics and Communications in Japan*, **48**, pp. 84–93.

101. Ostergaard, D.F. and Pawlak, T.P. (1986), 'Three-dimensional finite elements for analyzing piezoelectric structures,' *Proceedings of the 1986 Ultrasonics Symposium*, pp. 639–42.

102. Parlett, B.N. (1980), *The Symmetric Eigenvalue Problem*. Englewood Cliffs, N.J.: Prentice-Hall, Inc. xx + 348 pp.

103. Parlett , B. N. (1984), 'The software scene in the extraction of eigenvalues from sparse matrices,' *SIAM Journal on Scientific and Statistical Computing.*, **5**, pp. 591–604.

104. Parlett , B. N. and Nour-Omid, B. (1985), 'The Use of a Refined Error Bound When Updating Eigenvalues of Tridiagonals,' *Linear Algebra and its Applications*, **68**, pp. 179–219.

105. Parlett , B. N. and Nour-Omid, B. (1989), 'Towards a black box Lanczos program,' *Computer Physics Communications*, **53**, pp. 169–179.

106. Parton, V.Z. and Kudryavtsev, B.A. (1988), *Elektromagnitouprugost piezoelectricheskikh i elektroprovodnikh tel*. Moskva: Nauka. 472 pp. In Russian.

107. Pissanetsky, S. (1984), *Sparse Matrix Technology*. Orlando, Fl.: Academic Press, Inc. xiii + 321 pp.

108. Press, W.H., Teukolsky, S.A., Vetterling, W.T. and Flannery, B.P. (1992), *Numerical Recipes in FORTRAN. The Art of Scientific Computing*. 2nd edn. Cambridge: Cambridge University Press. xxvi + 963 pp.

109. Raoelijaona, F. and Dulmet, B. (1994), 'Finite element analysis using trigonometric interpolations for quasi-thickness piezoelectric resonators,' *Proceedings of the 1994 Ultrasonics Symposium*, pp. 965–68.

110. Reitan, D.K., Higgins, T.J. (1951), 'Calculation of the electrical capacitance of a cube,' *Journal of Applied Physics*, **22**, pp.

111. Saad, Y. (1988), 'Preconditioning techniques for nonsymmetric and indefinite linear systems,' *Journal of Computational and Applied Mathematics*, **24**, pp. 89–105.

112. Scott , D. S. (1982), 'The advantages of inverted operators in Rayleigh-Ritz approximations,' *SIAM Journal on Scientific and Statistical Computing.*, **3**, pp. 68–75.

113. Sekimoto, H., Watanabe, Y., and Nakazawa, M. (1990), 'Two-dimensional analysis of thickness-shear and flexural vibrations in rectangular AT-cut quartz plates using a one-dimensional finite element method,' *Proceedings of the 44th Annual Symposium on Frequency Control*, pp. 358–62.

114. Sekimoto, H., Watanabe, Y., and Nakazawa, M. (1992), 'Forced vibrations of thickness-flexure, face-shear and face-flexure in rectangular AT-cut quartz plates,' *Proceedings of the 46th Annual Symposium on Frequency Control*, pp. 532–36.

115. Shockley, W., Curran, D.R., and Koneval, D.J. (1967), 'Trapped-Energy Modes in Quartz Filter Crystals,' *Journal of the Acoustical Society of America*, **41**, pp. 981–93.

116. Shorrocks, N.M., Whatmore, R.W., Ainger, F.W. and Young, I.M. (1981), 'Lithium tetraborate — a new temperature compensated piezoelectric substrate material for surface acoustic wave devices,' *Proceedings of the 1981 Ultrasonics Symposium*, pp. 337–40.

117. Shulga, N.A. and Bolkisev, A.M. (1990), *Kolebaniya piezoelektricheskikh tel*. Kiev: Naukova Dumka. 228 pp. In Russian.

118. Silvester, P.P. (1968), *Modern Electromagnetic Fields*. Englewood Cliffs: Prentice-Hall. xiv + 332 pp.

119. Silvester, P.P. and Ferrari, R.L. (1990), *Finite elements for electrical engineers*. 2nd edn. Cambridge: Cambridge University Press. xii + 344 pp.

120. Silvester, P.P. and Ferrari, R.L. (1996), *Finite elements for electrical engineers*. 3rd edn. Cambridge: Cambridge University Press. xviii + 494 pp.

121. Silvester, P.P. (1993), *Data Structures for Engineering Software.* vi + 182 pp.

122. Silvester, P.P. and Pelosi, G. (1994), *Finite elements for wave electromagnetics.* New York: IEEE Press. ix + 534 pp.

123. Silvester, P.P., Lowther, D.A., Carpenter, C.J. and Wyatt, E.A. (1977), 'Exterior finite elements for 2–dimensional field problems with open boundaries,' *Institution of Electrical engineers Proceedings*, **124**, 1267–70.

124. Silvester, P.P. (1969), 'High-order polynomial triangular finite elements for potential problems,' *International Journal for Engineering Science*, **7**, pp. 849–61.

125. Silvester, P.P. and Hsieh, M.-S. (1971), 'Finite element solution of 2-dimensional exterior-field problems,' *Proceedings IEE*, **118**, pp. 1743-47.

126. Silvester, P.P. (1972), 'Tetrahedral polynomial finite elements for the Helmholtz equation,' *International Journal for Numerical Methods in Engineering*, **4**, pp. 405–13.

127. Silvester, P.P, Minhas, F.U., and Csendes, Z.J. (1981) 'Tetrahedral finite element matrix primitives,' *Computer Physics Communications*, **24**, pp. 173–79.

128. Silvester, P.P. (1982a), 'Universal finite element matrices for tetrahedra,' *International Journal for Numerical Methods in Engineering*, **18**, pp. 1055–61.

129. Silvester, P.P. (1982b), 'Permutation rules for simplex finite elements,' *International Journal for Numerical Methods in Engineering*, **18**, pp. 1245–59.

130. Simon, H. (1984), 'Analysis of the symmetric Lanczos algorithm with reorthogonalization methods,' *Linear Algebra and its Applications*, **61**, pp. 101–131.

131. Sirotin, Y.I. and Shaskolskaya, M.P. (1979), *Osnovy kristallofiziki.* 2nd edn. Moskva: Nauka. 639 pp.

132. Smith, R.R., Hunt, J.T., and Barach, D. (1973), 'Finite element analysis of acoustically radiating structures with applications to sonar transducers,' *Journal of Acoustical Society of America*, **54**, pp. 1277–1288.

133. Söderkvist, J. (1990), 'Electric Equivalent Circuit for Flexural Vibrations in Piezoelectric Materials,' *IEEE Transactions on Ultrasonics, Ferroelectrics, and Frequency Control*, **UFFC-37**, pp. 577–86.

134. Söderkvist, J. (1998), 'Using FEA To Treat Piezoelectric Low-frequency Resonators,' *IEEE Transactions on Ultrasonics, Ferroelectrics, and Frequency Control*, **UFFC-45**, pp. 815–25.

135. Stochniol, A. (1992), 'A General Transformation for Open Boundary Finite Element Method for Electromagnetic Problems,' *IEEE Transactions on Magnetics*, **MAG-28**, pp. 1679–81.

136. Stone, G.O. (1973), 'High-Order Finite Elements for Inhomogeneous Acoustic Guiding Structures,' *IEEE Transactions on Microwave Theory and Techniques*, **MTT-21**, pp. 538–42.

137. Tiersten, H.F. (1969), *Linear piezoelectric plate vibrations*. New York: Plenum Press. xv + 212 pp.

138. Tomikawa, Y., Miura H. and Dong, S. B. (1978), 'Analysis of Electrical Equivalent Circuit Elements of Piezo-Tuning Forks by the Finite Element Method,' *IEEE Transactions on Sonics and Ultrasonics*, **SU-25**, pp. 206–12.

139. Trümpy, K. and Zingg, W. (1993), 'Finite Element Analysis of AT Strip Quartz Resonators,' *7th European Frequency and Time Forum, Neuchâtel.*

140. Vekovischeva, I.A. (1971), 'Variatsionnie printsipi v teorii elektrouprugosti,' *Prikladnaya mekhanika*, **7**, pp. 129–33. In Russian.

141. Washizu, K. (1968), *Variational methods in elasticity and plasticity*. Oxford: Pergamon Press. x + 348 pp.

142. Watkins, D.S. (1991), *Fundamentals of Matrix Computations*. New York: John Wiley & Sons. xiii + 449 pp.

143. Webb, J.P. (1995), 'Application of the finite-element method to electromagnetic and electrical topics,' *Reports on Progress in Physics*, **58**, pp. 1673–1712.

144. Yamada, T. and Niizeki, N. (1971), 'A New Formulation of Piezoelectric Plate Thickness Vibration,' *Review of the Electrical Communication Laboratories*, **19**, pp. 705–13.

145. Yamada, Y. and Sato, M. (1998), 'Application of Extended Finite-Difference Time-Domain Method to Two-Dimensional Dynamic Analysis of a Piezoelectric Vibrator,' *Japanese Journal of Applied Physics*, **37**, pp. 255–56.

146. Yong, Y. K. (1987a), 'On the use of 1-D finite elements for the temperature behavior of a contoured and partially plated SC-cut resonator,' *Proceedings of the 1987 Ultrasonics Symposium*, pp. 353–58.

147. Yong, Y.-K. (1987b), 'Three-Dimensional Finite-Element Solution of the Lagrangean Equations for the Frequency-Temperature Behavior of *Y*-Cut and *NT*-Cut Bars,' *IEEE Transactions on Ultrasonics, Ferroelectrics, and Frequency Control*, **UFFC-34**, pp. 491–99.

148. Yong, Y.-K. and Stewart, J.T.(1991), 'Mass-Frequency Influence Surface, Mode Shapes, and Frequency Spectrum of a Rectangular *AT*-Cut Quartz Plate,' *IEEE Transactions on Ultrasonics, Ferroelectrics, and Frequency Control*, **UFFC-38**, pp. 67–73.

149. Yong, Y.-K. and Zhang, Z. (1993), 'A Perturbation Method for Finite Element Modeling of Piezoelectric Vibrations in Quartz Plate Resonators,' *IEEE Transactions on Ultrasonics, Ferroelectrics, and Frequency Control*, **UFFC-40**, pp. 551–62.

150. Yong, Y.-K. and Zhang, Z. (1994), 'Numerical Algorithms and Results for SC-Cut Quartz Plates Vibrating at the Third Harmonic Overtone of Thickness Shear,' *IEEE Transactions on Ultrasonics, Ferroelectrics, and Frequency Control*, **UFFC-41**, pp. 685–93.

151. Yong, Y.-K. and Cho, Y. (1994), 'Algorithms for eigenvalue problems in piezoelectric finite element analyses,' *Proceedings of the 1994 Ultrasonics Symposium*, pp. 1057–62.

152. Yu, Y.Y. (1996), *Vibrations of Elastic Plates: Linear and Nonlinear Dynamical Modeling of Sandwiches, Laminated Composites, and Piezoelectric Layers*. New York: Springer-Verlag. xiii + 228 pp.

153. Zelenka, J. (1986), *Piezoelectric resonators and their applications*. New York: Elsevier 301 pp.

154. Zienkiewicz, O.C. and Taylor, R.L. (1989), *The Finite Element Method*. 4th edn. Vol. 1 of 2 vols. London: McGraw-Hill. xix + 648 pp.

155. Zienkiewicz, O.C. and Morgan, K. (1983), *Finite elements and approximation*. New York: John Wiley & Sons. xii + 328 pp.